Multiscale Modeling of Two-Dimensional Materials: Structures, Properties, and Designs

by

Gang Seob Jung

B.S., Physics
University of Tsukuba (2006)
S.M., Physics
University of Tokyo (2008)

Submitted to the Department of Civil and Environmental Engineering
in partial fulfillment of the requirements for the degree of

Doctor of Philosophy

at the

MASSACHUSETTS INSTITUTE OF TECHNOLOGY

June 2019

Signature redacted

Author .....
Department of Civil and Environmental Engineering
May 17, 2019

Certified by ..... Signature redacted .....
Markus J. Buehler
Jerry McAfee Professor of Civil and Environmental Engineering
Thesis Supervisor

Accepted by ..... Signature redacted .....
Heidi Nepf
Donald and Martha Harleman Professor of Civil and Environmental Engineering
Chair, Graduate Education Committee

Multiscale Modeling of Two-Dimensional Materials: Structures, Properties, and Designs

by

Gang Seob Jung

Submitted to the Department of Civil and Environmental Engineering
on May 17, 2019, in partial fulfillment of the
requirements for the degree of
Doctor of Philosophy

Abstract

Multiscale modeling undertakes to describe a system with multiple models at different scales. In principle, quantum mechanics provides sufficient information. However, the development of a scaled-up model, *e.g.*, molecular dynamics, from quantum mechanics, should be validated against the experiments. Two-dimensional (2D) materials provide excellent platforms to verify theoretical models by directly comparing atomic structures and properties with advanced transmission electron microscopy (TEM) techniques due to their high crystallinity and thin nature.

In this thesis, molecular dynamics (MD) models have been developed for the 2D transition metal dichalcogenides (TMDs) such as MoS_2, WS_2, $MoSe_2$, and WSe_2 from density functional theory (DFT) by focusing on their nonlinearity and failure strains. The structures, crack-tip behaviors, and fracture patterns from the models are directly compared with atomic level *in-situ* TEM images. The models have revealed atomic scale mechanisms on the crack-tip behaviors in the single crystals such as roles of sulfur vacancies, geometric interlocking frictions, and the directions of crack propagation.

The models have been further validated with more complicated structures from grain boundaries in the WS_2 bilayer and lateral heterostructures, *e.g.*, MoS_2-WSe_2, by the images from ADF-STEM. Also, a method for generation of grain boundary has been proposed for well-stitched grain boundaries based on experimentally observed dislocations and defects. The models and methods have been utilized to understand the chemical reactions for MoS_2 channel growth in WSe_2 and fracture toughness of polycrystalline graphene.

Finally, the validated models and methods are utilized to predict the atomic structures of 2D materials with three-dimensional (3D) surfaces, *e.g.*, triply periodic minimal surfaces (TPMS) and corrugated surfaces with non-zero Gaussian curvatures. The mechanics, failure behaviors, and thermal properties of TPMS graphene are systematically studied from the predicted structures. A recent experiment shows the predicted scaling laws of Young's modulus and strengths agree well with the measurements.

Thesis Supervisor: Markus J. Buehler
Title: Jerry McAfee Professor of Civil and Environmental Engineering

Author's Declaration

I am the author of all the work presented in this thesis. Part of the work presented here has been published:

1. **G.S. Jung** and M.J. Buehler. *Annual Review Biomedical Engineering*, **2017**

2. J. Yeo, **G.S. Jung**, F.J. Martín-Martínez, S. Ling, G.X. Gu, Z. Qin, M.J. Buehler. *Physica Scripta*, **2018**

3. J. Yeo*, **G.S. Jung***, F.J. Martín-Martínez*, J. Beem, Z. Qin, M.J. Buehler *Advanced Materials*, **2019**

4. S. Wang*, Z. Qin*, **G.S. Jung**, F.J. Martín-Martínez, K. Zhang, M.J. Buehler, J.H. Warner, "Atomically Sharp Crack Tips in Monolayer MoS_2 and Their Enhanced Toughness by Vacancy Defects", *ACS Nano*, **2016**

5. **G.S. Jung***, S. Wang*, Z. Qin, F.J. Martin-Martinez, J.H. Warner, M.J. Buehler, "Interlocking Friction Governs the Mechanical Fracture of Bilayer MoS_2," *ACS Nano*, **2018**

6. **G.S. Jung***, S. Wang*, Z. Qin, S. Zhou, M. Danaie, A.I. Kirkland, J.H. Warner, M.J. Buehler, "Anisotropic Fracture Dynamics Due to the Local Lattice Distortions," *ACS Nano*, **2019**

7. **G.S. Jung**, Z. Qin, M.J. Buehler, "Molecular mechanics of polycrystalline graphene with enhanced fracture toughness," *Extreme Mechanics Letters*, **2015**

8. J. Chen, **G.S. Jung**,G.H. Ryu, R.J. Chang, S. Zhou, Y. Wen, M.J. Buehler, and J.H. Warner, "Atomically Sharp Dual Grain Boundaries in 2D WS_2 Bilayers," **in revision**

9. Y. Han*, M.-Y. Li*, **G.S. Jung***, M.A. Marsalis, Z. Qin, M.J. Buehler, L.J. Li, and D.A. Muller, "Sub-nanometre channel embedded in two-dimensional materials," *Nature Materials*, **2017**

10. **G.S. Jung** and M.J. Buehler, "Multiscale Mechanics of Triply Periodic Minimal Surfaces of Three-Dimensional Graphene Foams," *Nano Letters*, **2018**

11. Z. Qin*, **G.S. Jung***, M.J. Kang, M.J. Buehler, "The mechanics and design of a lightweight three-dimensional graphene assembly", *Science Advances*, **2017**

12. **G.S. Jung**, J. Yeo, Z. Tian, Z. Qin, M.J. Buehler,"Unusually low and density-insensitive thermal conductivity of three-dimensional gyroid graphene", *Nanoscale*, **2017**

13. Y. Zhou, S.G. Sarwat, **G.S. Jung**, M.J. Buehler, H. Bhaskaran, and J.H. Warner, "Grain Boundaries as Electrical Conduction Channels in Polycrystalline Monolayer WS_2", *ACS Applied Materials and Interfaces*, **2019**

Acknowledgments

First and foremost, I would like to express my appreciation and gratitude to my advisor, Professor Markus J. Buehler, who supported, guided, inspired, and encouraged me during the past years. He provides me priceless advice about my research, presentations, and future career. Words cannot express how thankful I am to have had excellent experience and opportunities in his lab. I would also like to thank my committee members, Professor Xuanhe Zhao, and Professor Admir Masic. I am incredibly grateful for their expertise and guidance and for providing valuable comments on the contents and presentation of this dissertation. Their advice and help were essential to the completion of this dissertation.

My Ph.D. study started in the Laboratory for Atomistic and Molecular Mechanics (LAMM) in the fall of 2013. I learned interesting concepts and methods every day and met incredible and passionate people along the way. This thesis is the end of this journey. I would like to thank all of those who helped make this thesis possible and my Ph.D. an unforgettable experience.

I would like to thank all my collaborators: Professor Jamie Warner, Professor David Kaplan, Professor David Muller, Professor Pupa Gilbert, Professor Jiwoong Park, Professor Jing Kong, Professor Zhitin Tian, and Professor Jeff Wiess. Also, Zhao Qin, Francisco Martin-Martinez, Jingjie Yeo, Shangshang Wang, Yimo Han, Jun Chen, Joonki Suh, Yingqiu Zhou, Jared Zitnay, Chun-Teh Chen, Anna Tarakanova, Shengjie Ling, Grace Gu, and Yimin Qiu. It was a great honor and privilege to work with all of them. Especially, I would like to thank Professor Jamie Warner for many exciting research topics, valuable comments, discussions, and incredible work with advanced TEM.

In my daily work, I have been blessed with my labmates who helped me personally and professionally: Kai Jin, Baptiste Depalle, Tristan Giesa, Leon Dimas, Dieter Brommer, Shu-Wei Chang, Chia-Ching Chou, Max Solar, Diego Lopez Barreiro, Zaira Martin Moldes, Isabelle Su, Ta lal Al-Mulla, Flavia Libonati, Kassu Gebresellasie, Davoud Ebrahimi, Reza Mirzaeifar, Mario Milazzo, Jonny Yu, and Eesha Khare.

Also, I would like to thank Marygrace Aboudou for keeping the lab in line, specifically, helping me secure the times and dates for my milestones on this journey.

I would also like to thank valuable supports from Professor Shinji Tsuneyuki, Professor Hideo Aoki, Professor Atsushi Oshiyama, Professor Shinya Aoki, Professor Shiraishi Kenji, Professor Susumu Okada, Professor Yoshihide Yoshimoto in Japan for me to build up insight and knowledge on physics. Also, I appreciate Kwang Jin Oh, Jihoon Kang, Hoonju Myung, Okyung Kwon, Heung-Sik Kim in Korea for me to learn the knowledge about high-performance computing and parallel coding.

This research was funded by the MIT Presidential Fellowship (Edward H. Linde), AFOSR (DOD-MURI, Grant No. FA9550-15-1-0514), ONR (Grant No. N00014-16-1-233), NSF (Grant No. CMMI-1300649), and NIH (Grant No. U01EB014976; 5U01EB016422). Their support is much appreciated.

Finally, I would like to express my greatest thanks and appreciation to my family. I am greatly indebted to my wife, SangMi, and our parents for the tremendous support and encouragement they have provided me in every stage of my life.

Contents

Chapter 1

Introduction

This chapter briefly summarizes the history of two-dimensional materials with respect to synthesis and characterization methods. Then, the motivations and objectives of the study are introduced followed by the thesis outline. Part of the review presented in this chapter has been published [1].

1.1 Two-dimensional materials

After the initial development of transistors in 1948 at Bell Laboratory [2], electronic devices have changed our life significantly. At the fundamental level, most electronic devices are designed to control system or process information by controlling electrical currents through the applied external voltage to open a current channel in semiconducting materials. Therefore, electronic properties of materials, such as their band structures, density of states, electron transport, resistance, and conductivity, are key factors that have to be considered in the manufacture and implementation of electronic devices. The applied voltage experiences a process of screening that is inherent to the bulk structure of the constituent material. This screening is diminished if the thickness is reduced and the electrons are confined in at least one of the spatial directions. Accordingly, thin structured materials are ideal for the development of electronic devices. This effect is maximized in atomically thin two-dimensional (2D) materials. The confinement helps to reduce the screening of the applied voltage.

Among the 2D materials, graphene is specially known for its extremely intriguing properties, such as high mobility of electrons, which were predicted theoretically [3, 4]. Informed by previous theoretical research, graphene was isolated and characterized for the first time in 2004 [5] by Andre Geim and Konstantin Novoselov who designed an innovative way of obtaining graphene samples from graphite. Since graphite is an allotrope of carbon that consists of stacked graphene layers by $\pi - \pi$ interactions, Geim and Novoselov were able to exfoliate single-layered graphene from graphite by using Scotch tape. This simple but innovative technique can produce high quality micron-sized samples while also being equally applicable to other 2D materials that are multilayered bulk systems. In the case of graphene, its mechanical, electrical, and thermal properties are found to be exceptional: the thermal conductivity is estimated to be 5,000 W/mK [6]; the electron mobility is approximately 15,000 $cm^2/V \cdot s$ at room temperature [5]; the high elastic modulus is around 1 TPa and its high intrinsic strength is around 130 GPa [7]. These properties have placed graphene as one of the leading materials for innovation in the field of condensed matter physics and materials science.

Although graphene is well known for its ballistic transport and high electron mobility, it has no band gap. Possessing a band gap is vital for various electronic applications, such as transistors [11]. It is possible to open the band gap of graphene by processing them in the form of nano-ribbons [12] or applying uniaxial mechanical strain [13]. However, the mobility drops significantly to around $100 \sim 200$ $cm^2/V \cdot s$ for a 150 meV bandgap because the high mobility of electrons in graphene is a direct consequence of not having a band gap. Thus, researchers have expanded their attention to other two-dimensional materials, such as molybdenum disulfide (MoS_2) and their transition metal dichalcogenide (TMD) family, hexagonal boron nitride (h-BN), black phosphorous, and many other 2D materials. In particular, monolayer MoS_2 has attracted significant attention due to its excellent electron transport with intrinsic direct bandgap (1.8 eV) [14]. Figure 1-1(a) shows some representative two-dimensional materials of graphene, MoS_2, h-BN, and their band structures.

The properties of graphene devices are strongly affected by their substrates as they

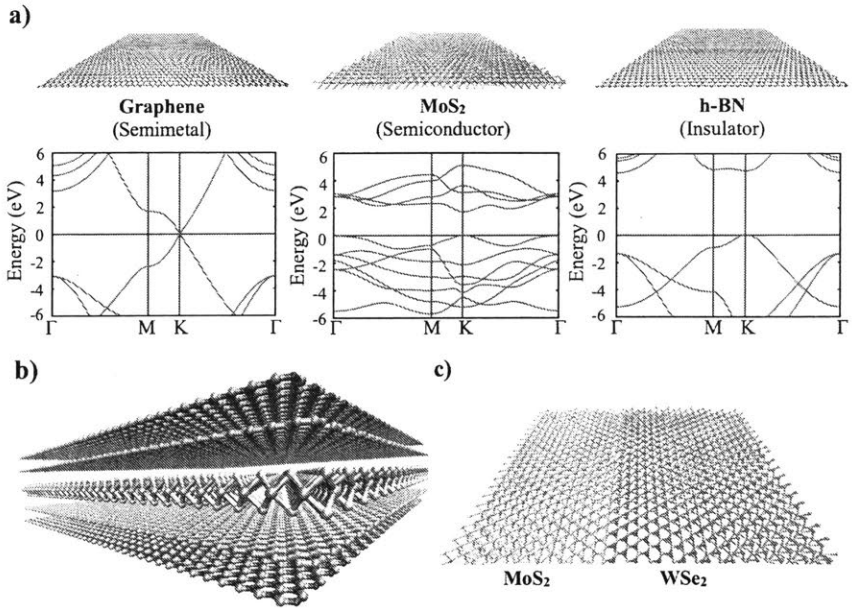

Figure 1-1: (a) Atomic structures of 2D materials, including graphene, MoS_2, and h-BN, and their band structures. Band structures are obtained with DFT calculations in the Quantum-Espresso package [8] using the Perdew-Burke-Ernzerhof (PBE) functional [9] and norm-conserving type pseudopotential [10]. (b) Heterostructures with van der Waals interaction: hBN-Graphene-MoS_2-Graphene-hBN. (c) Lateral heterostructure of MoS_2-WSe_2.

are atomically thin, which limits their integration with conventional silicon-based devices. Utilizing h-BN as a substrate for graphene devices improved the mobility by approximately an order of magnitude as compared to devices with SiO_2 substrates [15]. This research inspired other studies of new material systems with van der Waals heterostructures, including graphene, h-BN, MoS_2, and WSe_2 [16, 17] as shown in Figure 1-1(b) [18], which are emerging candidates for the next generation of electronic devices. Moreover, wafer-scale heterostructures of WS_2, MoS_2, and MoS_2 were reported [19]. Alternatively, instead of weak binding by stacking vertically, laterally bonded structures between h-BN and graphene show great promise for atomically thin circuits [20]. Subsequently, in combination with the TMD family, various lateral heterostructures were proposed [21, 22, 23]. Through epitaxial growth, atomically sharp interfaces between MoS_2-WSe_2 lateral junction was also reported and this is illustrated in Figure 1-1(c) [24]. Through permutations of these atomically thin graphene and other two-dimensional materials with lateral and vertical heterostructures, highly efficient and flexible devices can be realized.

1.2 Chemical vapor deposition for synthesis

Chemical vapor deposition (CVD) is one of the most successful way for large scale production [25]. The nucleation of carbon atoms on a metallic substrate (Ni or Cu) initiates the growth of graphene flake into large domains. Due to the grain boundaries of the metal substrates, the graphene produced by CVD also has grain boundaries where the boundaries are well-stitched with pentagon and heptagon defects [26, 27]. The grain boundary affects the various properties of graphene based on their atomistic arrangements. However, the grain size obtained from CVD has improved significantly to produce inch-sized single-crystalline graphene [28].

1.3 Atomic structures and dynamics from TEM

Transmission electron microscopy (TEM), a technique where electron beams are transmitted into the samples to visualize their images, was developed in early 1930s. However, the Nobel Prize in Physics was only awarded several decades later to the developer, Ernst Ruska, in 1986. TEM utilizes the short wavelength of electrons rather than light or UV, which allows much higher resolutions than optical microscopy because the wavelength of electrons is much shorter than visible light or UV. The electron beam can generate diffraction patterns from crystals (selected area diffraction patterns), which is a useful tool for studying the crystallinity of materials. Various versions of TEM have been developed for higher resolutions and better image quality, such as scanning TEM, cryo-TEM, and aberration corrected (AC)-TEM. Currently, sub-Angstrom resolutions are achievable, thus playing a critical role in studying atomic structures and charge redistribution of chemical bonds.

1.4 Motivation and objective

Different from the traditional modeling focusing on one scale, the multiscale modeling undertakes to describe a system with the multiple models at different scales. This new paradigm of modeling becomes more critical when the available macroscale models are not accurate enough, but microscale models are not efficient enough; usually limited by the system size. One of the most common approaches is to derive parameters required for the larger scale models from the higher resolution method. For examples, forcefields of molecular dynamics can be computed and fitted from first principle calculation of quantum mechanics. However, the process is not so simple and can vary because one should decide what information to be discarded by the reasonable approximation, which requires comprehensive and multidisciplinary insight. While quantum mechanics already provides principles sufficient for chemistry, material science, and biology [29], the way of connecting different scale models should be validated and tested.

The first isolation of graphene from graphite in 2004 has brought extensive interest in this atomically thin material for technologies particularly for flexible and wearable technologies and energy due to its high carrier mobility, broad-band absorption, and high transparency. Another class of two-dimensional materials called the transition metal dichalcogenides (TMDs) are a group of semiconductors with intrinsic bandgaps that have gained traction for ultrathin semiconductor technologies. There are many other 2D materials including h-BN, black -phosphorus, and graphyne, etc. With the advanced CVD methods, some of them can be synthesized as a wafer scale film with an atomically thin thickness. Therefore, these materials have intrinsically multiscale features. Different from bulk materials, the single atomic level defects, and dislocations in grain boundaries can change the entire properties of the film, which makes the 2D materials as the challenging but intriguing testbed for multiscale modeling [30]. Especially the thin nature of 2D materials can provide atomic resolution structures with various optoelectronic properties, which can be directly compared with DFT and MD calculations. By comparison between atomic level features, 2D materials provide lots of opportunities for improvements in terms of accuracy and efficiency of theoretical models

The first objective of this thesis is to develop reactive MD models by focusing on their nonlinearity with experimental validations of structures, crack-tip behaviors, and fracture patterns from atomic level *in-situ* TEM images. The second objective is a systematical understanding of atomic structures, chemical reactions, and mechanical behaviors with crack propagation of 2D materials. The final goal is to propose new atomic-scale design in 3D space based on the validated models and methods, *e.g.*, triply periodic minimal surfaces (TPMS) and corrugated surfaces with non-zero Gaussian curvatures with predictions of properties such as mechanics, failure behaviors, and thermal conductivity. The understanding atomic-scale mechanisms, as well as the development of models and methods can open avenues of systematic and reliable bottom-up approach from quantum mechanics to continuum theory through MD simulations. The core bridge developed in this thesis eventually works for combining synthesis process and characterization with computational multiscale modeling

paradigm.

1.5 Thesis outline

This thesis is organized into introducing the methodology and three main applications, focused on distinct topics of 2D materials science applications, *e.g.*, graphene and transition metal dichalcogenide (TMD) materials. The main topics will be categorized into 1) single crystalline system, 2) heterostructures and polycrystalline system, and 3) new designs with three-dimensional surfaces. Each chapter was written based on published work in peer-reviewed journals. The multiscale modeling and simulations unveil the structure-properties relation of 2D materials and show how the 3D designs by utilizing a curved surface can bring a new class of materials with mechanical and thermal properties.

In Chapter 2, I introduce computational models and methods utilized in the thesis: density functional theory (DFT), molecular dynamics (MD), reactive molecular dynamics, and continuum theory for brittle fracture of materials. The details of REBO forcefield for reactive MD, the effects of the switching functions, and parameterizations based on DFT calculation are discussed. Also, methods developed for the grain boundaries, topological defects for curved surfaces of graphene and TMD materials are introduced.

Chapter 3 deals with the mechanics of the single crystalline MoS_2 and WS_2 including a bilayer system. It shows how the lattice of a crystal can interact with a sharp crack tip and defects. The mechanisms unveiled by MD simulations will be discussed through the comparison with the atomic structures and crack behaviors in TEM images.

In Chapter 4, I report the studies with the polycrystalline, grain boundaries, and heterostructures. The out-of-plane deformation in polycrystalline graphene plays a crucial function in controlling the toughening mechanisms for the fracture toughness. The developed MD models describe the complex geometries (*e.g.*, defects, dislocations, and out-of-plane deformation) from dual grain boundary of a WS_2 bilayer as

well as their mechanical stability. In the last section, the catalytic role of the 5|7 dislocation between MoS_2 and WSe_2 unveils through MD simulations, which provide a chemical synthesis process of MoS_2 1D channel embedded in WSe_2 without dangling bonds or misfit.

Chapter 5 continues the study of 2D materials but with new designs of 3D surfaces. By utilizing topological defects such as pentagon or heptagon, 2D materials can sustain positive or negative curvatures. Firstly, I build systems with triply periodic minimal surfaces to understand their mechanical and thermal properties, and derive scaling laws. This can provide a way of modeling for designing a new class of materials with high surface area and low-density materials. Also, the grain distributions based on non-negative Gaussian curvatures will be discussed.

The last chapter of this thesis, Chapter 6, summarizes the key findings and their significance, discusses the results, and proposes possible future directions.

Chapter 2

Methodology

This chapter introduces different modeling methods and theory from the density functional theory (DFT) to the fracture mechanics. Molecular dynamics (MD) and forcefields for thermal and mechanical properties are mainly discussed in half of the chapter. Then, the REBO parameterizations based on DFT for two-dimensional materials are discussed. This chapter contains the parts of contents in the published journal articles: [31, 32, 33, 34, 35, 36, 37, 38, 39, 40]. The codes, parameters developed here and visualizations of data are further described in the Appendix F.

2.1 Density functional theory (DFT)

The most fundamental scale within the multiscale paradigm is the atomistic scale. Components of the muscular-skeletal system are continuously growing and occasionally damaged. Both growth and failure initiate from atomistic scale through chemical bonding and breaking [41]. The interactions between atoms are governed by the distribution and states of their electrons. Quantum simulations allow us to predict the behavior of electrons and understand their corresponding properties, such as light absorptions, band structures and electromagnetic characteristics. In principle, for a given geometry of atoms, quantum simulation does not require experimentally fitted parameters [42]. Thus, we can model the system with a bottom-up approach and develop modeling-driven material designs.

Electrons have discrete energy values based on their quantum states and their behavior can be derived from the Schrödinger equation. However, solving the equations for all electrons in even small systems is almost impossible. Approximations simplifying the many-body interaction to non-interacting electrons in an effective potential are adopted in density functional theory (DFT) [43, 44]. DFT enables handling more atoms in systems and has been successfully applied to solid-state physics [9]. However, DFT is not sufficiently accurate enough to deal with transition states or van der Waals (vdW) interactions. *Ab initio* quantum chemistry calculation is another approach to deal with electrons based on the Hartree-Fock (HF) method. Many extensions of HF have been proposed for better accuracy [45]. However, the computation cost increases significantly as the accuracy increases, hence the method should be chosen carefully based on the properties to be studied. At present, the mechanical properties and structures of materials at the ground state, which are well described by either DFT or *ab initio* calculations. The properties and structures derived from quantum simulations can be utilized to develop unknown input parameters in MD for materials.

2.2 Molecular Dynamics (MD)

2.2.1 Classical molecular dynamics

Since the number of atoms the quantum simulation can handle is extremely limited, further simplifications are necessary to deal with a greater number of atoms. Classical MD is a way to deal with the atoms or molecules based on their interactions where the electronic structures of atoms are not changed. Instead, force-fields or potentials are adopted for the effects of electron states. After Alder and Wainwright performed the first MD simulation with hard spheres in the late 1950's, various potential forms have been developed and used in MD simulations [46]. The most fundamental potential that includes repulsive and attractive terms is Lennard Jones (LJ) potential,

commonly expressed as

$$V_{LJ}(r) = 4\epsilon \left[\left(\frac{\sigma}{r}\right)^{12} - \left(\frac{\sigma}{r}\right)^{6} \right] \tag{2.1}$$

where ϵ is the depth of the potential, σ is the distance where the potential value is zero and r is the distance between particles, which had great success in describing the behavior of noble gases such as argon [47]. This potential is widely used in describing VdW interaction in various systems. For biomolecules such as lipids and protein systems, an empirical force-field known as CHARMM is proposed [48]. The basic form of the force-field is

$$V_{System} = V_{Bond} + V_{Angle} + V_{Dihedral} + V_{Improper} + V_{VdW} + V_{Coulomb} \tag{2.2}$$

Other force-fields such as AMBER [49] and GROMOS [50] have also been proposed with similar constituent terms to describe proteins. The force-fields commonly have terms for torsion, bond stretching, angle and non-bonded interactions in Figure 2-1(a).

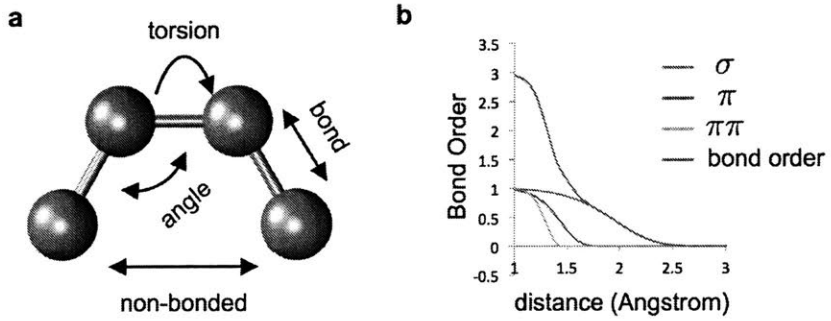

Figure 2-1: The basic term of the classical MD and the concept of the bond orders in the reactive MD. (a) The classical potential of MD commonly has terms for torsion, bond stretching, angle and non-bonded interactions. (b) Based on the distance bond-order allow to distinguish single, double, triple bonds of carbons. The potential energy between carbon atoms changes and goes to zero when it reaches bonds' breaking points.

From these force-fields, the Hamiltonian of a system is defined as $H = K + E$,

where K is the kinetic energy term, E is the potential energy term described by the force-fields, p_i and q_i are momentum and position of ith particles, respectively. From the Hamiltonian, the time derivatives of position and momentum can be derived, and the trajectories of atoms are obtained by numerical integration [51]. The system is described as a microcanonical ensemble representing all possible states of a mechanical system having the same total energy. Since the controllable macroscopic variables are the number of particles (N), total volume (V) and energy (E), the microcanonical ensemble is also termed as the NVE ensemble. However, NVT (canonical), and NPT (isobaric-isothermal) ensembles are generally adopted in MD simulations because temperature or pressure is usually utilized as macroscopic variables in experiments [52, 53, 54].

A proper time step should be chosen for the conservation of the total Hamiltonian to ensure the appropriate sampling of the correct ensemble. In biomolecular systems, a time step of 1femtosecond is sufficient for unconstrained atomistic systems, while a larger time step of 2 femtoseconds can be utilized together with H-bond constraints [55]. The short integration time steps prevent attaining simulation time-scales beyond microseconds in MD simulations. This would require more than a billion steps, a significant task even for modern supercomputers.

2.2.2 Reactive molecular dynamics

The deformation and mechanical responses of biomolecules are mainly governed by changes in H-bond networks [56]. However, the breaking of covalent bonds is also critical to understanding the mechanisms of protein unfolding and failure [41, 57]. Nonreactive force-fields such as CHARMM are only capable of describing atoms near their ground states because these force-fields ignore quantum chemical states as an approximation. In contrast, reactive force-fields can capture the changes in bonding by considering bond-orders that are estimated from the relative distances and angles between particles. The bond-orders enable to approximate quantum chemical states of particles for the formation or breakage of bonds in the systems in Figure 2-1(b) [58]. Although the reactive force-field captures the change of quantum states and is

less computationally expensive than quantum simulations, the number of atoms in the system is still limited to tens of thousands, which is much less than classical MD simulations (over billions) [59]. Thus, a hybrid concept can be utilized for efficiency, which uses the reactive force-field only for highly reactive parts of the system [60]. Classical MD with CHARMM-like forcefields can successfully reveal the failure mechanisms of biomolecules, including silk, collagen, intermediate filaments and amyloids as well as characterize the effects of nano-confinement on the biomaterials' mechanical properties. However, modeling the deformation and crack propagation of graphene, graphyne, or any other graphene-based carbon allotropes require MD forcefields that can capture the breaking of covalent bonds. As the breaking of chemical bonds rely on the changing states of electrons, classical MD methods are inadequate for modeling these phenomena as the chemical bonds in classical MD are typically pre-defined and not dynamically changeable.

2.2.3 Tersoff potential

The Tersoff potential is a three-body potential expressed as [61]

$$E_b = f_c(r_{ij})[V_R(r_{ij}) + b_{ij}V_A(r_{ij})] \tag{2.3}$$

where r_{ij} is the atomic distance between atom i and j; V_R the repulsive term; V_A the attractive term; b_{ij} the bond order parameter; and f_C the switching function. The original form of the Tersoff potential utilized an analytical form of the bond order parameter, b_{ij}, to model the properties of materials derived from carbon, silicon, and germanium. The term of b_{ij} represents many-body effects with an analytic form,

meaning that the strengths of bonds change due to the local environments.

$$b_{ij} = \frac{1}{(1+\beta^n \zeta_{ij}^n)^{1/2n}}, \tag{2.4}$$

$$\zeta_{ij} = \sum_{k \neq i,j} f_C(r_{ij}) g(\theta_{ijk}) e^{[\lambda_3^3 (r_{ij} - r_{ik})^3]}, \tag{2.5}$$

$$g(\theta) = 1 + \frac{c^2}{d^2} - \frac{c^2}{d^2 + (h - \cos\theta)^2}. \tag{2.6}$$

In this thesis, Tersoff potential is utilized for the thermal conductivity of graphene and three-dimensional graphene because the phonon dispersion is well matched with experimental measurements.

2.2.4 REBO (Reactive Empirical Bond Order) forcefield

Brenner proposed a more flexible form of b_{ij} by adding a correction term for the bond order. This correction term resolved the over-binding of Tersoff types in the intermediate bonding states [62]. Stuart *et al.* extended Brenner's Reactive Empirical Bond Order (REBO) potential to include dihedral, torsional and LJ terms, called Adaptive Intermolecular Reactive Empirical Bond Order (AIREBO) [63]. Both the repulsive and attractive terms, V_R and V_A, are Morse-type potentials of the mathematical form, $Ae^{-\lambda r}$. The Morse-type potential has some disadvantages when dealing with collisions relating to the compressive force and thus, the second generation REBO was proposed with a modified $(1+Q/r)Ae^{-\lambda r}$ term to resolve these issues [64]. Currently, this modified AIREBO potential is one of the most popular reactive force fields for studying the mechanical behaviors of graphene and various carbon allotropes. The salient feature of this potential is that the bond order term only depends on the local coordination without the need to consider explicit charges and long-range Coulombic interactions, allowing for excellent computational performance as fast Fourier transforms (FFT) calculations are not needed. However, the cutoffs of the switching functions in the REBO terms must be carefully selected and this is discussed later.

Van Duin *et al.* proposed a different type of reactive force field for hydrocarbon systems called ReaxFF that included Lennard-Jones (LJ) and Coulombic interac-

tions [58]. ReaxFF is fundamentally different from the REBO and other Tersoff-type potentials. First, the bond order parameter in ReaxFF is a function of the distance between interacting atoms. Second, the ReaxFF calculates the atomic charges with the Electron Equilibrium Method (EEM) [65, 66] method that is similar to the Charge Equilibration (QEq) method [67] that inspired another type of reactive force field known as the Charge-Optimized Many-Body (COMB) potential [68]. The atomic charges in ReaxFF are dynamically optimized during the simulations, thus ReaxFF is more transferable and suitable for complex chemical reactions. Therefore, the force field theoretically can handle the interactions between graphene or graphyne with other molecules in various environments. While several studies reported the elastic properties of graphene based on the ReaxFF, the measured properties strongly depended on the version of ReaxFF parameters that was used because the parameters were fitted from specific training data sets. Jensen *et al.* [69] investigated the difference in elastic properties from ReaxFFC-2013 and ReaxFFCHO. The ReaxFFC-2013 parameters were based on a data set that included graphite and diamond, thereby showing significant improvements in reproducing the fundamental physical properties of graphene compared to ReaxFFCHO. Many early studies of graphynes were based on the ReaxFFCHO, which might have some discrepancies from the later versions of ReaxFFC-2013 and DFT calculations. There are other many-body potentials for modeling graphene, such as the Gaussian Approximation Potential (GAP) [70] and Tersoff potentials [71], which were also utilized for modeling the failure and determining the strength of graphene.

2.2.5 Thermal properties

There are two common ways to predict thermal conductivities from MD simulations: equilibrium (Green-Kubo relation) and non-equilibrium MD methods. Both methods have been extensively utilized for determining thermal conductivities of graphene [72, 73] and porous materials [74]. From kinetic theory, thermal conductivity can be

expressed as [75]

$$\lambda = \frac{1}{3}\sum_{\omega} c(\omega)vl(\omega) = \frac{1}{3}c(\omega)\tau(\omega), \tag{2.7}$$

where $c(\omega)$, v, $l(\omega)$, and $\tau(\omega)$ are the phonon-specific heat, group velocity, MFP, and relaxation time, respectively.

Non-equilibrium Molecular Dynamics (NEMD)

In NEMD, the heat flux is imposed in the NVE ensemble for the steady state after the system fully relaxed. Then from the heat flux energy and temperature gradient, the thermal conductivity is simply obtained from Fourier's Law:

$$\lambda = -\frac{j}{\partial T/\partial x}, \tag{2.8}$$

where j and $\partial T/\partial x$ are the heat flux and the temperature gradient respectively.

Equilibrium Molecular Dynamics (EMD)

Thermal conductivity in the direction i is given by [76, 77],

$$\lambda_i = \frac{1}{k_B V T^2}\int_0^{\infty} \langle J_i(t)J_i(0)\rangle dt, \tag{2.9}$$

where k_B, t, V, J_i and are the Boltzmann constant, time, volume, heat current vector in the i direction and the heat current autocorrelation function (HCACF). The detailed expression of the heat current vector is expressed as [73]

$$J = \sum_i e_i v_i + \frac{1}{2}\sum_{i<j}(f_{ij}\cdot(v_i + v_j))x_{ij}, \tag{2.10}$$

where e_i, v_i, f_{ij} and x_{ij} are the energy, velocity of atom i, forces and distance between atom i and j, respectively.

The typical HCACF data and thermal conductivity for graphene as a function of time are shown Figure 2-2.

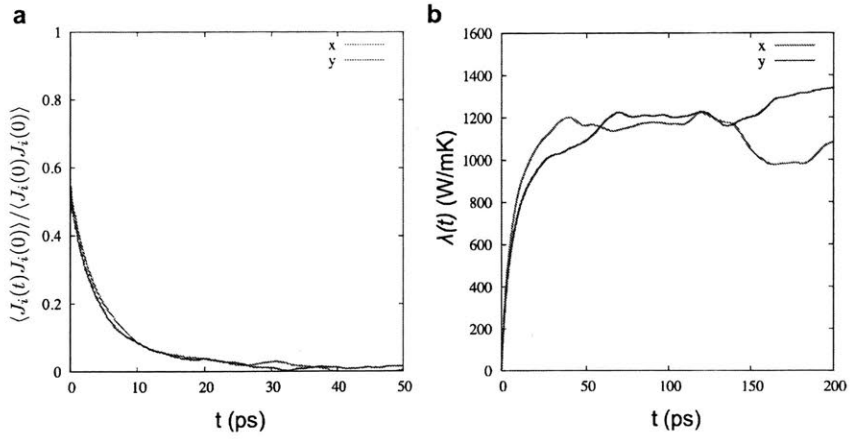

Figure 2-2: The HCACF (a) and thermal conductivity (b) and from EMD (Green-Kubo) of graphene (10nm x 10nm).

Phonon density of state (PDOS)

The vibrational density of state (vDOS) can be determined from the Fourier transform of the velocity autocorrelation function (VACF) as [78]

$$g(\omega) = \frac{1}{\sqrt{2\pi}} \int e^{i\omega t} \frac{\langle v(t)v(0)\rangle}{\langle v(0)v(0)\rangle}. \tag{2.11}$$

The phonon density of states (PDOS) is calculated from PDOS $= [g(\omega)]^2$. The noise of PDOS depends on the number of atoms in systems and sampling time. In the thesis, More than 20,000 atoms are utilized by repeating the unit cell if it is necessary for graphene and 3D graphene, and 5 ps sampling with 0.25 fs time step. From the PDOS ($D(\omega)$), the specific heat can be obtained by

$$C_V = b_B \int \left(\frac{\hbar\omega}{k_B T}\right)^2 \frac{e^{\hbar\omega/k_B T}}{[e^{(\hbar\omega/k_B T)} - 1]^2}. \tag{2.12}$$

2.2.6 Mechanical properties

Elastic constants

In this section, the process to obtain elasticity of 2D materials and 3D graphene with cubic symmetry. First, the structures obtained from the refinement are fully relaxed.

After energy minimization, model is relaxed with the NPT ensemble for 50 ps at 10K with 1fs time step. Then, the elastic constants are measured based on an orthotropic symmetry by calculating $C_{11}, C_{22}, C_{33}, C_{12}, C_{13}, C_{23}, C_{44}, C_{55}$, and C_{66}. The deformation strain is set to $\pm$ 0.1%. There are nonlinear responses in small strain ranges of 3D graphene. The behaviors are observed in the polycrystalline graphene due to the out of plane deformation around the topological defects. The 3D graphene models have the same essential features as polycrystalline. Therefore, it is natural to have such a region in the small strain range as the lattice size increases due to the defect distributions. The same deformation level obtained from the pristine graphene (Table E.27) is utilized to measure the elastic constants of the models. The components for the cubic crystal (C_{11}, C_{12}, C_{44}) are obtained by averaging corresponding values.

From the compliance matrix, Young's modulus (E_x, E_y, E_z) and Poisson's ratios $(\nu_{xy}, \nu_{yx}, \nu_{zx})$ can be calculated and averaged based on the cubic symmetry. Poisson's ratio is obtained by $\nu = C_{12}/(C_{11} + C_{12})$.Two shear moduli are identified based on the symmetry. The cubic shear modulus C_{44} represents the resistance to shear deformation across the (100) plane in the [010] direction while $(C_{11}-C_{12})/2$ represents the resistance to shear deformation across the (110) plane in the $[1\bar{1}0]$ direction [79].

Voigt and Reuss bounds of Young's modulus, Bulk modulus, shear modulus and Poisson's ratios to estimate the upper and lower bounds of the elastic constants [80]:

$$E_V = \frac{(C_{11} - C_{12} + 3C_{44})(C_{11} + 2C_{12})}{2C_{11} + 3C_{12} + C_{44}}, G_= \frac{C_{11} - C_{12} + 3C_{44}}{5}, \nu_V = \frac{C_{11} + 4C_{12} - 2C_{44}}{4C_{11} + 6C_{12} + 4C_{44}}, \tag{2.13}$$

$$E_R = \frac{5}{3S_{11} + 2S_{12} + S_{44}}, G_R = \frac{5}{4S_{11} - 4S_{12} + 3S_{44}}, \nu_V = -\frac{2S_{11} + 8S_{12} - S_{44}}{6S_{11} + 4S_{12} + 2S_{44}}. \tag{2.14}$$

Then, the macroscale effective moduli are estimated from the Voigt-Reuss-Hill approach as following

$$E_{VRH} = \frac{E_V + E_R}{2}, G_{VRH} = \frac{G_V + G_R}{2}, \nu_{VRH} = \frac{E_{VRH}}{2G_{VRH}} - 1. \tag{2.15}$$

Also, the bulk modulus is as following11:

$$B_V = \frac{C_{11} + 2C_{12}}{3}, B_R = \frac{1}{3}\frac{1}{S_{11} + 2S_{12}}, B_{VRH} = \frac{B_V + B_R}{2}. \tag{2.16}$$

The bulk modulus of the cubic crystal is isotropic ($B_V \sim B_R$). Two indexes are utilized to characterize the elastic anisotropy of models. The ratio between the shear moduli is a Zener ratio as

$$A_z = \frac{2C_{44}}{C_{11} - C_{12}}. \tag{2.17}$$

As the value approaches one, the material is isotropic. However, the Zener ratio lacks universality because one can choose the index as 1/A. A universal anisotropy index has been proposed to eliminate this ambiguity as [79]:

$$A_U = 5\frac{G_V}{G_R} + \frac{B_V}{B_R} - 6. \tag{2.18}$$

The zero value of A_U indicates isotropic elasticity.

2.3 Continuum theory

The continuum approach is the most common method to describe systems at the macroscale and this is a very successful way to describe the many structural problems of homogenous materials. In this approach, a system is modeled as a continuous material rather than being composed of particles, without explicitly accounting for a materials internal structure. The fundamental concept of continuum mechanics is Hooke's relation where the elongation of elements is proportional to the applied external force. When a force F is applied to a beam of length L and cross sectional area A, the extension is given as Δu in Figure 2-3.

The equation, $F = k\Delta u$ can be normalized by the unit volume ($V = AL$) as

$$\sigma = \frac{F}{A} = \frac{Lk}{A}\frac{\Delta u}{L}E\epsilon, \tag{2.19}$$

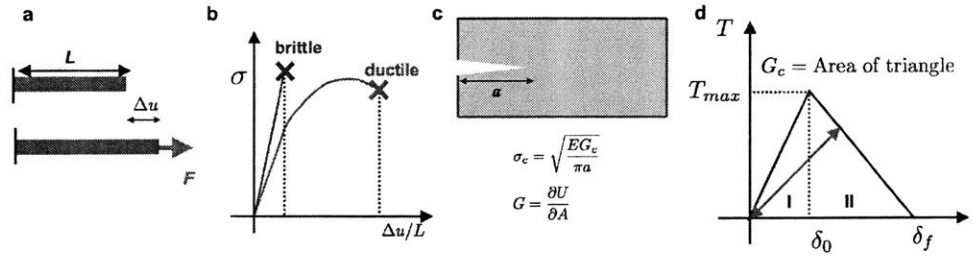

Figure 2-3: Concepts of the continuum theories (a) Elongation of a homogenous bar (length: L) under a tensile force F is given as Δu (b) Brittle and ductile materials show different stress-strain behaviors. (c) Griffith criterion and energy release rate in a homogenous materials with a crack are given by the equation in the panel. (d) The basic concept of a cohesive zone model: The deformation in the region I is reversible without damages. Once stress reaches the T_{max}, the element gets damaged and the elastic behavior changes to red arrow. When the extension reaches δ_f, the element totally breaks and the required energy is the total area of the triangle, characterized as the critical energy release rate.

where σ, E and ϵ are defined as stress, Young's modulus, and strain, respectively. This linear relation between stress and strain governs the behavior of brittle materials in the elastic regime where the deformation is reversible. However, generally the deformation of materials such as metals has a plastic deformation regime where irreversible deformation occurs.

2.3.1 Griffith's model

Griffith and Irwin developed linear elastic fracture mechanics (LEFM) [81, 82]. The Griffith criterion states that failure of materials with a flaw occurs when the stored strain energy is large enough to create two new surfaces under uniaxial loading. The energy release rate G, which represents the dissipation of stored strain energy per unit of newly created surface area during the crack propagation, is defined by

$$G = \frac{\partial U}{\partial A} \tag{2.20}$$

where U is stored strain energy available for crack propagation, and A is surface area. A small crack can propagate when $G = 2\gamma$, where γ is surface energy (the energy

necessary to create new surfaces; two new surfaces are created as the crack advances). The failure strength of a linear system with a small crack is given by $\sigma_c = \sqrt{\frac{EG}{\pi a}}$, where E and a are Young's modulus and size of the crack length, respectively. LEFM can describe the failure of brittle and homogenous material such as glass [81].

In brittle materials, Young's modulus and energy release rate can be simply obtained from atomistic simulation by calculating the corresponding materials' elastic constants and surface energy. However, the energy release rate is not simply 2γ when the dissipated energy constitutes a large portion of the energy release rate such as in heterogeneous materials. A better expression under this situation would be $G = 2\gamma + G_{diss}$. The energy release rate of inhomogeneous materials can be obtained from atomistic simulations by measuring the total external work for failure of the systems [31]. The deformations and damages of biological systems and polycrystalline 2D materials are locally inhomogeneous, which is challenging to be described with LEFM. The cohesive zone model is widely adopted for describing the damages based on the critical energy release rate. Each element can take damage based on their local stress and the history of damages. The basic elastic properties and the energy release rate are keys to connecting the particle-based simulation (QM, MD, and CGMD) to continuum theory (FEM). However, a more systematic framework needs to be developed to bridge these disparate methods.

2.3.2 Lukás model for a circular hole as a crack

The circular void follows the different behaviors due to the different stress concentration factor. We utilize the Lukás model for the small crack with the elliptical hole [83, 84]. Although the circular model does not have the small crack, we assume the discretized atomic position can play as a small crack with a constant size. The solution for an elliptical hole is [83, 84]

$$K_I = \sigma\sqrt{\pi l}\frac{1.122(1+2\frac{a}{b})}{\sqrt{1+4.5\frac{al}{b^2}}} \tag{2.21}$$

where a and b are the major and minor axes of an ellipse; l represents the length of crack. For the circular hole ($a = b = R$), we obtain

$$K_I = \sigma\sqrt{\pi l}\frac{3.366}{\sqrt{1+4.5\frac{l}{R}}} \tag{2.22}$$

We assumed that l is a constant value related to the discretized atomic positions.

2.4 REBO for failure of 2D materials

2.4.1 Switching functions in REBO

Properly formulating the switching function in REBO-based potentials is critical for describing the failure of carbon systems. The switching function utilized has the same form as the function from the Tersoff potential in eq(2.3)

$$f_C(r_{ij}) = \begin{cases} 1 & r_{ij} < R_{min} \\ \frac{1}{2}\left(1+\cos\left[\frac{\pi(r_{ij}-R_{min})}{R_{max}-R_{min}}\right]\right), & R_{min} < r_{ij} < R_{max} \\ 0 & r_{ij} > R_{max} \end{cases} \tag{2.23}$$

where the switching function varies from 1 to zero over the range of R_{min} to R_{max}. Since the cutoff radius is very short (R_{max} = 2 Å for carbon in the AIREBO potential), the attractive and repulsive potential terms (V_A and V_R in eq(2.3)) have very large values at the point where the bonds are breaking, *i.e.*, the potential is highly discontinuous when bonds break. This problem with discontinuity in the switching function can simply solved by smoothly varying the value of the potential at R_{min} to zero at R_{max}. However, an unusual behavior of this switching function was reported in a study on the fracture of polycrystalline diamond [85]. They observed unphysical and high stresses due to the switching function, and proposed adjusting R_{min} to alleviate the problem.

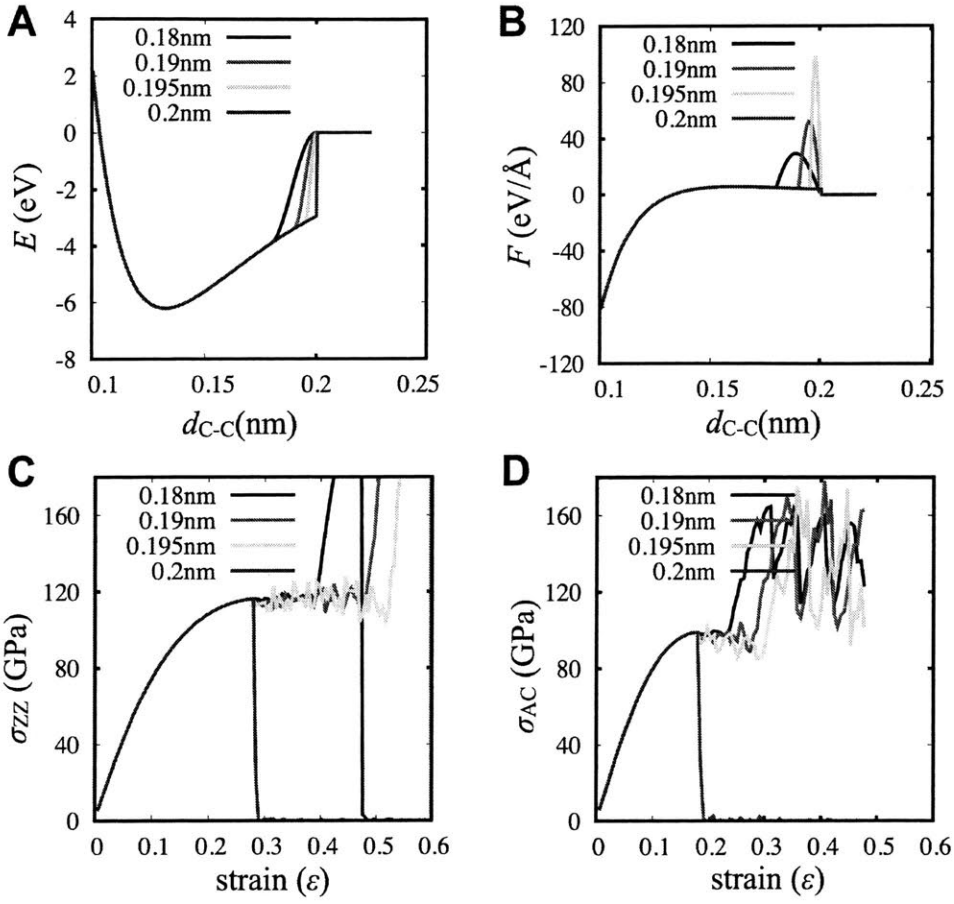

Figure 2-4: (a, b) The effects come from the modified potential energy (a) and force (b). (c, d) The effects of radius cutoff of AIREBO on the stress-strain behaviors under loadings in the zigzag direction (c) and armchair direction (d). They clearly show that only turning off switching function provides reliable stress-strain curves.

2.4.2 AIREBO for graphene monolayer

Two methods of adjusting the switching functions were proposed, although there were no clear explanations of how these methods could reproduce the failure of graphene. Firstly, two representative studies utilized the switching functions but with a cutoff of 1.92 Å for R_{min} instead [86, 87]. Wei *et al.* obtained stress-strain curves of pristine graphene with the AIREBO potential and compared these curves with results obtained from DFT calculations [87] This study showed that there were no stiffening effects from the switching function if R_{min} was larger than 1.92 Å. Many subsequent studies utilized this adjustment in R_{min}. However, without considering the exact role of the switching function, adjusting R_{min} in this arbitrary manner is problematic, especially when examining the effects of grain boundaries or defects on the mechanical properties of graphene. These issues become clearer when the changes in the potential energy and force between interacting pairs of C-C atoms is examined closely in Figure 2-4 (a) and (b).

The basic role of switching function is to smoothly vary the potential from a non-zero value to zero smoothly, implying that a stronger force than the original potential is applied to remove the discontinuity between the two points of R_{min} and R_{max}. The stiffening effects do not disappear with smaller ranges of the switching function, which can artificially increase the strength of graphene with grain boundaries or 5-7 defects. Since the C-C bonds in 5-7 defects can have longer bond lengths than in pristine hexagonal graphene, the stiffening effects appear when one of these longer bonds is within the range of the switching function. The observed stress-strain behaviors depend on the loading rate because the stiffening effect can be missed. if the loading rate is too fast and the stress is not sampled adequately. While not observed in the stress-strain curve of pristine graphene, the stiffening effects still exist and can lead to wrong conclusions, especially for systems with 5-7 ring defects. The stiffening effects can still appear even with a low R_{min} value of 1.95Å and at low temperature (10 K) and loading rate (0.02 Å/ps) (Figure 2-4 (c) and (d)). The stiffening artifacts worsen as R_{min} decreased, as demonstrated by the spike in forces between C-C atoms (Figure

2-4(b)). Thus, the previous AIREBO or REBO studies showing strengthening with defects and grain boundaries using $R_{min} = 1.92$ Å should be re-examined to confirm whether the strengthening is an artifact of the switching functions because this effect is completely unphysical and undesirable.

The second method to adjust the switching function is to set both R_{min} and R_{max} to be 2 Å to completely disable the switching function completely. This method was originally proposed for modeling the fracture of diamond by Brenner *et al* [85]. As shown in Figure 2-4 (blue lines), equal values of R_{min} and R_{max} completely remove the stiffening effects and show reliable stress-strain curves of graphene with brittle failure. Although this setting solves the unphysical stiffening, there is still a discontinuity in the potential, and the graphene simulation becomes unstable easily as the temperature increases. The temperature dependence is due to kinetic vibrations that may cause a C-C bond length to exceed 2 Å temporarily, resulting in a broken bond. Thus, carefully setting the loading and performing the analysis are required to understand the failure behaviors with AIREBO or REBO. This choice of cutoffs was utilized by various studies to examine flaw insensitive fracture in nano-crystalline graphene [88] and toughness enhancement in graphene ruga [89].

The REBO potential has a relatively simple analytical form compared to other reactive FFs. This simplicity allows easy removal of unphysical stiffening and obtaining reliable stress-strain curves that are comparable with DFT calculations. However, charge-based reactive FFs are comparatively too complicated to easily circumvent undesirable stiffening and optimize parameters for failure behaviors with proper stress-strain curves. To improve these potentials, not only the data of equilibrium states must be included in the training data set, but also data near the failure of the material.

2.4.3 REBO for MoS_2 monolayer

Tuning a reactive force field for MoS_2 modeling

For the mechanics of MoS_2 and other TMD materials, I utilize the reactive many-body force field (FF) [90, 91]. The force field can describe nonlinear behaviors of MoS_2

and simulate breaking and reforming bonds of materials and deal with the effects of sulfur vacancies. The failure strains of the system under the uniaxial loading depend on the radius cut-off distances among the atoms. I tune the parameters of the original FF based on DFT calculations, since the original FF was not tuned for the failure of MoS_2 system and had a problem with the artificial stiffening from the switching function as the same as the REBO potential for graphene in Figure 2-5. To the best of my knowledge, I firstly provide the parameters for the stress-strain behaviors comparable with the results from DFT. The stress-strain curves are obtained in the armchair and zigzag directions from DFT calculations by Quantum-Espresso package [8] using Perdew Burke Ernzerhof (PBE) functional [9] and norm-conserving type pseudopotential [10]. The rectangular shape cell contains 6 atoms with the periodic boundary condition. To model MoS_2 single layer, the vacuum space of 12Å in the z direction is inserted to avoid interactions between periodic images. The energy cutoff for the wave functions is 80 Ry and 10x10x3 grids are adopted for the K space sampling.

The obtained failure engineering strains are 0.36 and 0.26 for the x and the y direction respectively, which shows good agreement with the previous DFT calculations [93, 92, 94]. Then, I prepare the monolayer pristine MoS_2 in 5x5nm for the tensile tests with MD simulations by using the reactive force field. Based on the various combination tests of radius cut-offs, I obtain close failure engineering strains, 0.35 and 0.27 in the x and y direction, respectively. The cut-offs (R_{min}, R_{max}) of Mo-Mo, Mo-S and S-S are set to (4.5, 5.0) Å, (2.85, 2.85) Å and (1.1, 2.8) Å, respectively. The radius cut-offs are carefully selected not only to match the failure strains but also remove artificial stiffening effects due to the switching function [85]. In another 2D system, graphene, these tuning processes have been widely adopted in both pristine and defected graphene to describe the failure and crack propagations [31, 87]. Next, the repulsion and attraction coefficients are rescaled simultaneously to match the stress-strain points under the uniaxial tensile strain 0.1 in DFT calculation. The failure strain and strengths of MoS_2 are mainly considered to tune the parameters because these factors are most critical to describe the failure correctly, which causes

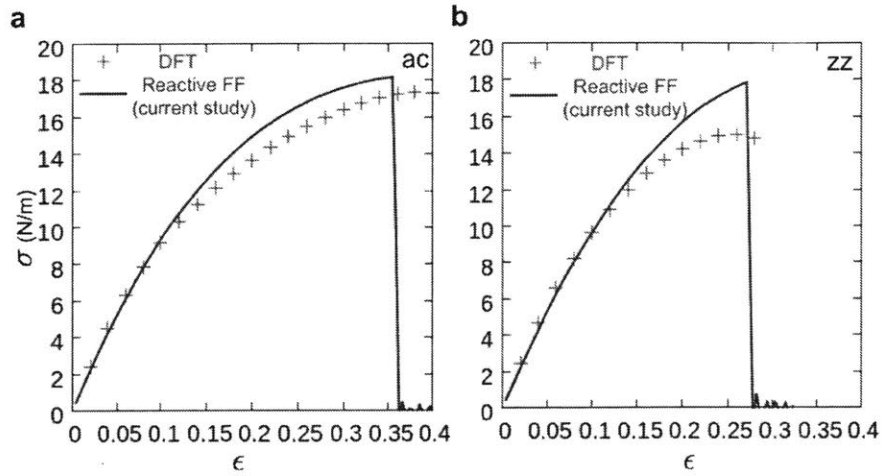

c

	Reactive FF (original)	Reactive FF (current study)	DFT
Mo-Mo	3.17	3.17	3.18
Mo-S	2.44	2.44	2.45
S-S	3.17	3.17	3.18
t(S_{top}-S_{bottom})	3.24	3.24	3.20

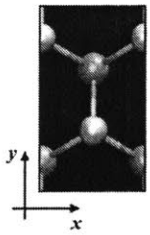

d

Properties	Reactive FF (original)	Reactive FF (current study)	DFT(Xiong, S.)
C_{11}(N/m)	149.0	115.1	123.3
C_{12}(N/m)	41.9	34.1	32.9
C_{22}(N/m)	149.0	115.1	124.3
E (N/m)	137.0	105.1	114.5

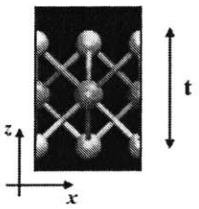

Figure 2-5: (a, b) The stress-strain curves of the MD used (blue line) and DFT calculation (red points) in the armchair and zigzag directions. The original potential has artificial stiffening due to the switching functions as the same as the REBO potential for graphene. The new parameters remove the stiffening effects and can describe the failure strains for both zigzag and armchair directions. (c) The equilibrated geometries of MoS_2. (d) The elastic constant and Young's modulus of the current study and DFT calculation [92]. The reactive FF used in the current study well describes geometries, mechanical properties and failure behaviors of MoS_2.

an error around 10 % of elastic constants from DFT results.

2.4.4 REBO for MoS_2/WSe_2 heterostructures

Development of reactive MD parameters

To model the interactions among Mo-W-S-Se atoms in the atomically sharp MoS_2-WSe_2, WS_2-WSe_2, and MoS_2-$MoSe_2$ lateral heterojunctions, I developed W-Se, W-S, and Mo-Se REBO with the same bond-order parameters of Mo and S but different ionic radiuses on the basis of their chemical and structural similarities. The REBO force field has the form

$$E_b = \frac{1}{2}\sum_{i \neq j} f_{ij}^C(r_{ij}) \left[\left(1 + \frac{Q}{r_{ij}}\right) A^{-\alpha r_{ij}} - b_{ij} B e^{-\beta r_{ij}} \right] \tag{2.24}$$

where E_b is the binding energy, f_{ij}^C is a switching function, b_{ij} is bond-order term, and r_{ij} is the interatomic distance between atom i and j. The parameters, Q, α, and β, are related to geometries such as equilibrium distances, A and B are related to the energy of attractive and repulsive terms. The radius cutoffs of the switching functions are critical to realistic bond breaking and forming because the functions can cause artificial forces near the failure points.

I obtained the geometric parameters for MoS_2, $MoSe_2$, WS_2, and WSe_2 from the DFT calculations by Quantum-Espresso package using PBE functional and norm-conserving type pseudopotential [95]. A rectangular shape cell containing 6 atoms is utilized with the periodic boundary condition in x (along the zigzag edge) and y (along the armchair edge) directions. To model each 2D material, the vacuum space of 15 Å in the z direction is inserted to avoid unphysical interactions between periodic images. The energy cutoff for the wave functions is 60 Ry and 11x11x1 grids are adopted for the K space sampling. Table 2.1 shows the results of the geometric parameters of four different monolayers. The equilibrium distances between Mo-S and W-S are very similar (2.09 and 2.08 Å from our DFT calculations, respectively). In the REBO forms for MoS_2, the equilibrium distance between sulfides does not affect

Table 2.1: The geometric parameters obtained from DFT calculations.

DFT(Å)	MoS_2	WS_2	MoSe2	WSe2
Mo/W - Mo/W	3.18	3.23	3.32	3.36
Mo/W - S/Se	2.45	2.45	2.55	2.58
S/Se - S/Se	3.18	3.23	3.32	3.36
t(top-bottom)	3.20	3.19	3.35	3.40

Table 2.2: The geometric parameters obtained from REBO potential

REBO(Å)	MoS_2	WS_2	MoSe2	WSe2
Mo/W - Mo/W	3.17	3.24	3.28	3.33
Mo/W - S/Se	2.46	2.46	2.55	2.56
S/Se - S/Se	3.17	3.24	3.28	3.33
t(top-bottom)	3.23	3.21	3.41	3.38

the lattice constants of monolayers. The difference of lattice parameters between WS_2 and MoS_2 mainly comes from the larger ionic radius of W than Mo. Thus, we parameterized Q, and in eq(2.24) of W-W to fit WS_2 lattice constants, while for the FF parameters of W-S we use the same Q, α and β of Mo-S.

Based on the obtained new parameters of W-W, Q, α and β of W-Se are parameterized to match the lattice parameters of WSe_2. In the same way, Q, α and β of Mo-Se are parameterized. We used Q, α and β of S-S for the parameters of Se-Se because Se-Se/S-S interaction are not important for the lattice constants of the monolayers. Table 2.2 shows the geometric parameters obtained from new REBO force field, which describes the difference between four different monolayers well. I re-parameterized A and B, which are related to repulsive and attractive terms. I followed the same strategy of the previous study [35], adjusting radius cut-offs, and rescaling A and B simultaneously to match stress-strain curves of monolayers, which were obtained from our DFT calculations (All conditions are the same as those for geometric parameters). The radius cutoffs of the switching functions ($f_{ij}^{C}(r_{ij})$) are adjusted to match the failure strains, and rescaled A and B in eq(2.24) to match the stresses at 0.1 strains in the y direction. The elastic constants from DFT and

Table 2.3: Elastic constants and Young's modulus (averaged in the x and y directions) from DFT calculations

DFT(N/m)	MoS_2	WS_2	MoSe2	WSe2
C_{11}	129.9	129.3	104.7	113.1
C_{22}	130.2	132.6	105.6	112.2
C_{11}	29.25	30.15	24.9	25.8
E	123.5	124	99.2	106.7

Table 2.4: Elastic constants and Young's modulus (averaged in the x and y directions) from the current REBO potential

REBO(N/m)	MoS_2	WS_2	MoSe2	WSe2
C_{11}	115.1	118.3	90.1	96.3
C_{22}	115.1	118.3	90.1	96.3
C_{11}	34.1	34.8	26.7	28.6
E	105.0	108.1	82.2	87.8

REBO are shown in Table 2.3 and 2.4. The new parameters well describe the relative differences of four different monolayers.

Finally, I extended the code from handling two atom types (Mo-S) to four different atom types (Mo-S-W-Se). For Mo-W and S-Se interactions, Tersoff potential mixing rules [61] for α, β, A, B and radius cutoffs of the switching functions are utilized.

2.4.5 REBO for MoS_2 bilayer

DFT calculation for binding energy of MoS_2 bilayer

Lennard-Jones (LJ) parameters of REBO [90, 91] were tuned for van der Waals (vdW) interaction of MoS_2 bilayers from DFT calculations by Quantum-Espresso package using PBE functional and norm-conserving type pseudopotential. Grimme's DFT-D2 correction was applied for vdW interaction between the two layers [96]. A hexagonal unit cell for DFT calculation contains 6 atoms with the periodic boundary condition in a and b directions as shown in Figure 2-6(a). The energy cutoff for the wave functions was 60 Ry and 11x11x1 Monkhost-Pack grids were adopted for the K space sampling.

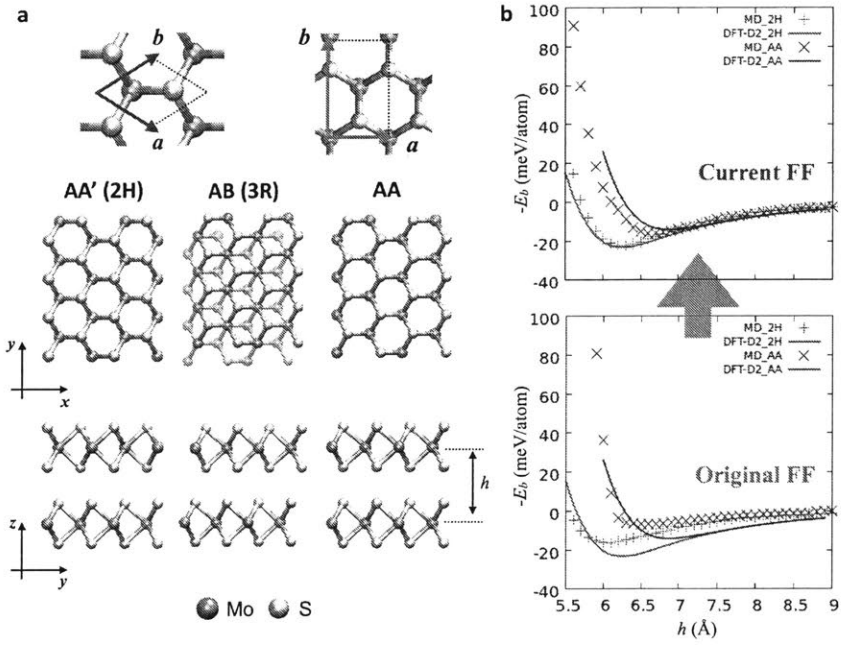

Figure 2-6: (a) Three representative stacking geometries of MoS_2 bilayer. (b) Formation energy profiles comparison between original FF and current FF, showing DFT and MD results for binding energy of bilayer MoS_2 as a function of the interlayer distance (h).

Table 2.5: The binding energy obtained from DFT calculation with Grimme's D2 correction and MD with both original and optimized reactive FFs. The difference of the binding energy between 2H and 3R are improved.

E_b (meV/atom)	AA	AA' (2H)	AB(3R)
DFT-D2	14.1	24.1	23.8
Original FF	11.6	16.2	16.3
Optimized FF	15.6	22.0	21.7

Table 2.6: The equilibrium distance obtained from DFT calculation with Grimme's D2 correction and MD with both original and optimized reactive FFs. The difference of the equilibrium distance between 2H and 3R are improved.

h_{equil} (meV/atom)	AA	AA' (2H)	AB(3R)
DFT-D2	6.7	6.2	6.3
Original FF	6.5	6.1	6.1
Optimized FF	6.7	6.3	6.3

The formation energy ($E_{form} = E_{bilayer} - 2E_{monolayer}$) per atom as a function of the interlayer distance (h) was obtained by structural relaxation, ranging from 5.5 Å to 9 Å with 0.1 Å spacing in Figure 2-6(b).

To model the 2D system, 32 Å vacuum was inserted to avoid undesirable interaction between periodic images. The vacuum space allowed more than 15 Å between layers, which is enough to ignore the interaction from the periodic images. Our calculations of the equilibrium interlayer distance (h_{equil}) and the binding energy ($E_b = -E_{form}$) for AA'(2H), AB(3R), and AA stacks show good agreement with previous studies, [97, 98], as shown in Table 2.5 and 2.6. There are mainly two different types of interlayer interactions. Type I, AA'(2H) and AB(3R), has high binding energy with shorter equilibrium distance than Type II, AA, as shown in Figure 2-6. The difference between the two types is the key to describe the interaction of bilayer MoS_2, which is not captured in the original FF as shown in Figure 2-6(b). Thus, the LJ parameters were optimized mainly based on the energy profiles of AA'(2H) and AA from DFT calculations.

Parameter optimization for vdW binding energy

To evaluate the binding energy, a rectangular unit cell was prepared containing 12 atoms with periodic boundary conditions in both x and y directions as shown in Figure 2-6(a). The system has enough vacuum space (more than 30 Å) for the same reason that the vacuum is inserted in the DFT calculations to avoid the interaction between periodic images. The LJ parameters were obtained to match the formation energy profiles from MD to those from DFT. The parameters for Mo-S interaction, σ_{MS} and ϵ_{MS}, were explicitly applied for Mo-S interaction instead of the conventional mixing rules used in the original form. Also, the shorter radius cutoff, $r_{cutMS} \sim 1.5\sigma_{MS}$ was applied (originally $r_{cutMS} = 2.5\sigma_{MS}$). This shorter r_{cutMS} is helpful to describe the difference between the two stacks while too short r_{cutMS} results in non-continuous formation energy profiles. The formation energy profiles from the original and optimized FFs are shown in Figure 2-6(b), which shows significant improvement for the layer-to-layer interaction.

Parameter optimization for mechanical properties of monolayer MoS_2 (REBO)

The optimized LJ parameters slightly affected the mechanical properties of MoS_2 monolayer. Thus, tuning other parameters related to covalent bonds was required after modification of LJ parameters. From the stress-strain curves from the previous DFT calculations, and the same strategy is applied to tune the parameters in sections 2.4.3 and 2.4.4. Firstly, I fitted the failure points of stress-strain curves of MD to DFT results by adjusting radius cutoffs of switching functions. We completely turned off the switching function by setting $R_{min} = R_{max}$ for Mo-S interaction as utilized in the REBO for hydrocarbon system, which is very important to describe realistic bond breaking and forming without nonphysical stiffening. For the stress-strain curves of MoS_2 monolayer with MD simulation, MoS_2 monolayer with 5 nm x 5 nm was prepared to perform tensile tests in both the zigzag (ZZ) and armchair (AC) directions under a plane strain condition and the periodic boundary condition. The strain rate was set to 0.2 Å/ps (20m/s) for dynamics loadings with NVT ensemble with a low

temperature (~10K) to ignore temperature effects. Then, the attractive and repulsive terms are rescaled to fit the stiffness of MD to that of DFT. Next, the elastic constants (C_{11}, C_{12}, C_{22}) were obtained by calculating the stresses with 0.5% strains in both DFT and MD calculations. The previous DFT/MD calculation [92], and experiment [99] used the unit, N/m, for strength and stiffness to ignore the uncertainty of the thickness of MoS_2. The reported stiffness and strength of monolayer MoS_2 from nano-indentation were 180 ± 60 N/m and 15 ± 3 N/m, respectively. The values show good agreement with the mechanical properties obtained from our DFT calculations. As

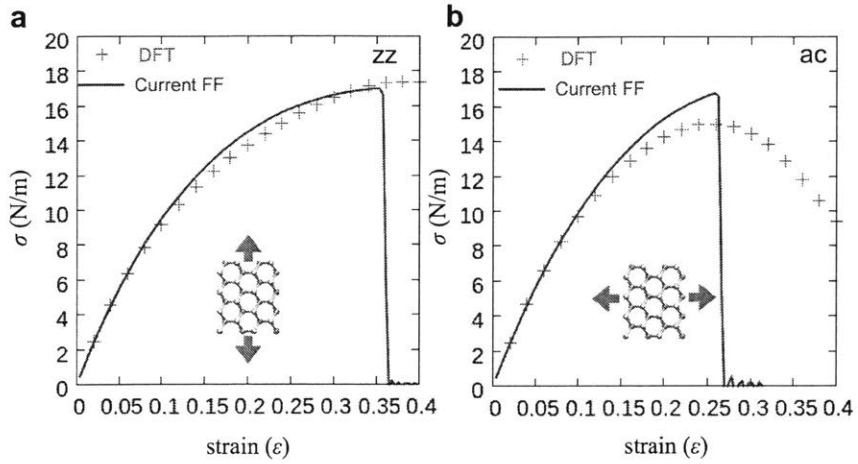

Figure 2-7: The stress-strain curves under the uniaxial tensile loadings in the zigzag (a) and armchair directions (b) with a plane strain condition. The failure strain and strength from the current REBO are well matched with those from DFT calculations. The stress unit (N/m) is used to ignore the uncertainty of the thickness of MoS_2 as the previous experimental and theoretical studies used [92, 99].

shown in Figure 2-7, the mechanical properties and geometric parameters from the MD simulations show good agreement with those from DFT calculations

2.4.6 REBO for WS_2 bilayer

DFT and MD simulations for mechanics of WS_2

I utilize the previous setting to obtain the stress-strain curves of WS_2 from DFT with Quantum-Espresso package using PBE functional and norm-conserving type pseudopotential. A rectangular unit cell for DFT contains six atoms with periodic

boundary conditions as shown in Figure A-1(b). Then, strains in the x (zz) or y (ac) direction are applied to measure the stress. The energy cutoff for the wave functions is 60 Ry, and 11x11x1 Monkhost-Pack grids are adopted for the K space sampling. For modeling the slab system, 15 Å vacuum is inserted to avoid undesirable interaction between periodic images.

The parameters were initially developed for MoS_2 interatomic interactions. First, the ionic radius is determined by adjusting parameters to match relaxed lattice parameters [36]. Second, the cutoffs of switching functions of W-S is selected to describe the failure strains obtained from DFT calculations. A pristine WS_2 monolayer with 5 nm x 5 nm is prepared to perform tensile tests in both zz and ac loading directions under a plane strain condition and the periodic boundary conditions for stress-strain curves. The strain rate is set to 0.02 Å/ps (2 m/s) for dynamics loadings with NVT ensemble with a low temperature (~10K) to ignore temperature effects. I completely turn off the switching function by setting $R_{min} = R_{max}$ for W-S interaction as utilized, which is very important to describe realistic bond breaking and forming with REBO style potentials. Finally, the repulsive and attractive terms are adjusted for elastic modulus. In the previous bilayer MoS_2 study, It was found that adjusting vdW parameters improves the non-linearity, which alleviates the underestimation of elastic properties and the overestimation of strengths. Thus, I utilize the previous setting for the vdW interactions and apply the suggested adjustments only for W-S parameters. Then, the elastic constants (C_{11}, C_{12}) are obtained from both DFT and MD and compared. As shown in Figure A-1, the mechanical properties including failure strains and strengths from our MD simulations show good agreement with those from DFT calculations.

2.5 Grain boundary generation

2.5.1 Polycrystalline graphene

The iterative algorithm is utilized to construct atomistic models of polycrystalline graphene. Building reliable polycrystalline structures is critical to study grain boundary effects in our work. The defects of polycrystalline graphene are mainly pentagon-heptagon ring pairs to reduce the total energy and the tensions of defects, as shown in the previous studies [100]. Since the models of polycrystalline graphene in previous studies have many voids and considerable non-pentagon-heptagon defects [101, 88], we need to develop a better algorithm to generate irregular polycrystalline graphene with mainly pentagon-heptagon defects.

I employ the Voro++ library [102] to generate initial grain shapes by randomly distributing the Voronoi seeds in a system as shown in Figure 2-8(a), where the number of seeds is determined by the average size of grains. Then, the pristine graphene is randomly rotated at each grain, and is sliced to fit its shape with the initial Voronoi cell. After checking neighbor bond lists of all atoms (bond length = 1.6 Å), I obtain the initial grains by removing atoms not having three bonds (Figure 2-8(b)). From the initial grains, we update the bond lists again and add atoms based on the bond number. To be specific, we want additional atoms to form hexagonal geometry; the length of bond varies from 0.6 to 1.2 Å (the range could be arbitrary). This bond length is chosen randomly based on a random number generator, allowing system to find favorable geometry by following energy minimization and MD runs using LAMMPS. In this process, I apply the REBO potential [64] not the AIREBO potential [63] to reduce the computational time. After the relaxation, I iteratively perform the same process from building new bond lists until the system configuration converged as shown in Figure 2-8(c). In the algorithm, I can select any undesirable atom to be removed and make the system form other energetically favorable geometry by MD runs. For example, I remove atoms forming bond angle above 170 degrees and under 90 degrees. The algorithm could be improved to remove all defects except 5-7 rings but not implemented in the present study. The convergence time strongly

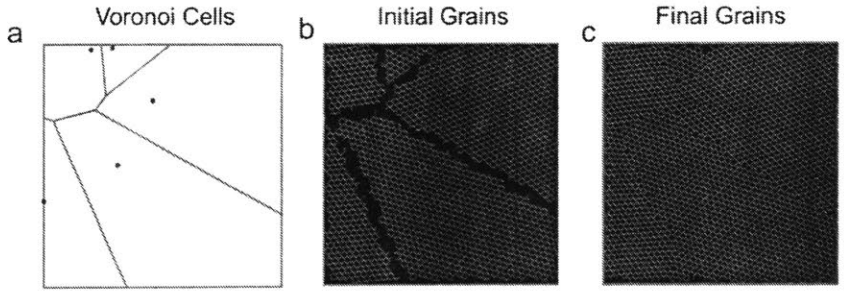

Figure 2-8: The process of a building polycrystalline graphene and the evaluation of our models. From randomly generated Voronoi cells (a), the randomly rotated initial grains form the initial geometry (b). The final geometry is obtained after about 1500 times of iterations with mainly pentagon-heptagon defects (c).

depends on the grain sizes and on the complexity of the initial geometry. In the present simulations, the number of iterations varies from 1,000 to 10,000.

I build a C++ code to use the Voro++ and LAMMPS as libraries for effective iterations, switching between MD runs and geometric modifications. I make use of the Massage Passing Interface (MPI) to use the parallel version of LAMMPS and the cell-linked list is applied to reduce the time to build the bond lists.

Ratios of defects in polycrystalline graphene

The ratios of defects are obtained in our models by counting all rings in the system. There are 4 different rings: 5,6,7 and 8 rings as shown in Figure A-2(b). In general, as the grain size decreases the number of octagon defects increases but it is a relatively small ratio, under 0.5% in Model IrreG and under 0.1% in Model RegG. Since the pentagon-heptagon defects appear in pairs, the ratio between pentagon and heptagon defects is critical to evaluate the model. In our models, the averaged difference in the ratio between pentagon and heptagon defects is only about 0.5%. The algorithm can be utilized with arbitrary grain angles and grain shapes of polycrystalline graphene and have great potential for other applications.

2.5.2 Three-dimensional graphene with triply minimal surface

Gyroid graphene

To understand the mechanical properties of the idealized 3D graphene I utilize the gyroid structure that has minimum surface area in a given volume, called minimal surface. The shape follows the equation

$$V_G = \sin(\frac{2\pi}{L}x)\cos(\frac{2\pi}{L}y) + \sin(\frac{2\pi}{L}y)\cos(\frac{2\pi}{L}z) + \sin(\frac{2\pi}{L}z)\cos(\frac{2\pi}{L}x) \tag{2.25}$$

where L is a parameter for dimension of a unit cell. First, the external potential to Lennard-Jones particle system is introduced as

$$E_{effect} = \sum E_{LJ} + \lambda \sum V_G^2 \tag{2.26}$$

to build a triangular template for the initial geometry. It is found that the shorter equilibrium distance of LJ potential $E_{LJ} = 4\epsilon\left[\left(\frac{\sigma}{r_{ij}}\right)^{12} - \left(\frac{\sigma}{r_{ij}}\right)^{6}\right]$ than graphene bond (~ 1.42Å) is better for the later process to refine geometry and ϵ has little effects on the geometry if strength of the external potential λ is strong enough to bind atoms on the surface. In our model, the parameters are set to ϵ=0.25 kcal/mol, $\sigma = 1.15$ Å, r_{cut}=3.0 Å and $\lambda = 460$ kcal/mol.

After I obtain the external potential term for each LJ potential, we apply this constraint on LJ particles having only less than 60 kcal/mol. The value is carefully set to make sure one dense gyroid surface. If the value is too large, double layers of gyroid form, while a small value results in sparse geometry that requires more number of iterations in the next step. The initial geometry of LJ particles is chosen as fcc solid with 5.8 Å lattice constant as shown in Figure 2-9(a). Then, the system is heated up to 1000K from 350K for 100ps. After the system is cooled down to 10K for another 100ps, the initial triangular geometry of the gyroid is obtained as shown in Figure 2-9 (b) and (c).

Second, I remove atoms based on the bond number for hexagonal geometry because the triangular geometry is not applicable for the refining algorithm. Figure 2-9

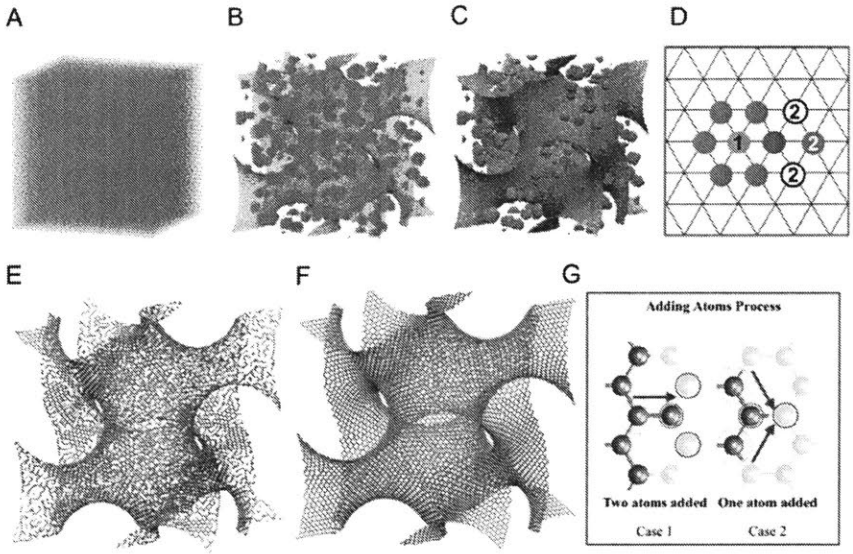

Figure 2-9: The processes of building gyroid structure from three steps: (a-c) generation of triangular gyroid structure with Lennard-Jones potential and the external potential, (d-e) modification from triangular to hexagonal gyroid based on our algorithm, (f-g) refinement of the geometry based on the iterative algorithm.

(d) shows the schematic figure of the deleting algorithm. After obtaining the bond number of all atoms based on the distance criteria (here set to 2 Å), the atoms having more than 6 bonds are removed. After recalculation of the bond number, an atom having 6 bonds is selected (green dot) and deleted. In order to search next atoms to be deleted, all neighbors of green dot (one of them is blue dot) are checked. Three candidates are easily found (white and red with number 2) by excluding the sharing atoms with green dot. For the hexagonal geometry, two white dots should be removed and one red dot should be remained. We distinguish them based on the bond number again: white dot shares two atoms with the green dot but red dot only share the blue dot with green dot. I remove all atoms under the conditions until there is no atom having six bonds. After removing atoms having 4 and 5 bonds, we obtain the hexagonal geometry for the next process as shown in Figure 2-9(e).

Finally, I extend the previous the algorithm to generate polycrystalline graphene to refine the geometry obtained from the previous processes in 2.5.1. Atoms are added based on the bond number and relaxed the structure with energy minimization and

short MD runs.

$$E = \sum E_{AIREBO} + \lambda \sum V_G^2 \tag{2.27}$$

I utilize the modified potential based on eq(2.27) for gyroid graphene with the same parameters for the LJ potential. After removing atoms not satisfying three bonds, the code adds atoms to make hexagonal structures as shown in Figure 2-9(g). Iteratively, this process is repeated until there is no update anymore, and the final geometry of gyroid graphene structure is generated as shown in Figure 2-9 (f). The quality of grain boundary is similar with the previous polycrystalline graphene models, which have mostly 5-7 rings and few 8 rings for the defects.

Triply periodic minimal surface of P and D types

To build the TPMS D and P types with different lattice sizes, two equations are utilized:

$$V_P = \cos(x') + \cos(y') + \cos(z'), \tag{2.28}$$

$$\begin{aligned} V_D = {} & \sin(x')\sin(y')\sin(z') + \sin(x')\cos(y')\cos(z') \\ & + \cos(x')\sin(y')\cos(z') + \cos(x')\cos(y')\sin(z'). \end{aligned} \tag{2.29}$$

where x', y' and z' are expressed with real coordinates (x, y, z) and the system size L as $2\pi x/L$, $2\pi y/L$, and $2\pi z/L$ for P and D types, respectively. The P and D types satisfy $V_P = 0$ and $V_D = 0$, respectively.

Three steps to build 3D graphene with P and D types are shown in Figure 2-10. Firstly, an external potential to the Lennard-Jones (LJ) system is used to obtain a triangular template for the initial geometry with a potential form as

$$E_X = \sum E_{LJ} + \lambda \sum V_X^2, \tag{2.30}$$

where X represents P and D for the targeted surfaces. In our models, the parameters for the LJ potential and external potential are set to ϵ=0.01 eV, σ=1.25 Å, r_{cut} =3.0,

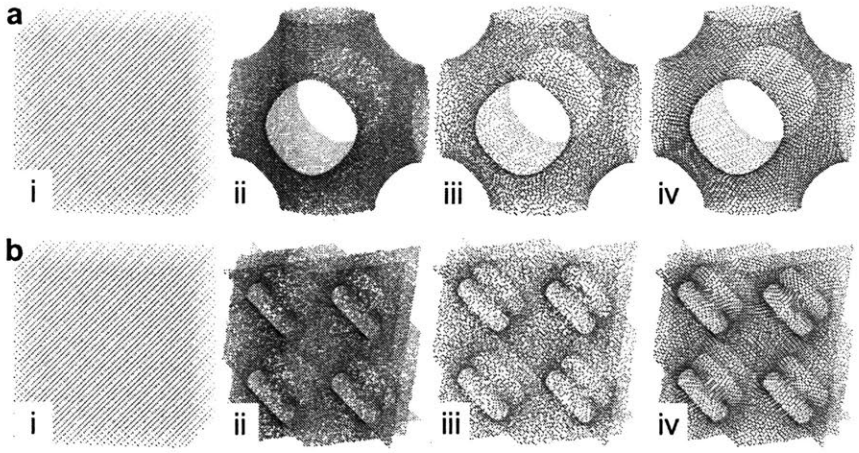

Figure 2-10: Generation of atomic TPMS P(a) and D(b) types, representing key steps including (i) Lennard-Jones (LJ) particles distributed with fcc structure, (ii) generation of TPMSs with triangular LJ lattice with external potentials ($\lambda(V_X)^2$, X = P and D), (iii) transformation from triangular lattice to hexagonal one, and (iv) refinement of the geometries for all carbons to have sp^2 bonds.

and λ=50 eV. From the LJ solid with a face-centered-cubic (fcc) crystal structure in Figure 2-10 (i), the system was heated to 1000K from 350K for 100ps. It is cooled to 10K for 50ps, and then, the initial triangular template is obtained after energy minimization in Figure 2-10 (ii). Secondly, the obtained triangular geometry was transformed to the hexagonal geometry. After removing the atoms having more than three bonds, the remained atoms are carefully selected to ensure hexagonal lattice of graphene as shown in Figure 2-10 (iii). Finally, the graphene flakes are refined by our previous algorithm to generate well-stitched polycrystalline graphene. The interatomic potentials are changed to

$$E_X = \sum E_{AIREBO} + \lambda \sum V_X^2, \tag{2.31}$$

where all carbon atoms interact through AIREBO potential with a constraint from the external potential V_X. The obtained structures are described by the equations 2.25,2.28,2.29 as shown in Figure 2-10 (iv). The algorithm guarantees well-stitched structures without any insufficient bonds (bond number satisfies three for all carbon atoms in the systems) with mainly pentagon and heptagon defects. During the refine-

ment, the radius cutoff of switching function for C-C bonds in REBO is set to 2 Å for both R_{min} and R_{max} to turn off the switching function for C-C bonds completely. Removing unphysical stiffening is critical for natural bonding and breaking from REBO type forcefields. The periodic lattice size, L, controlled the different porosities, and the relaxed structures for five porosities for all types are shown in Figure 2-11.

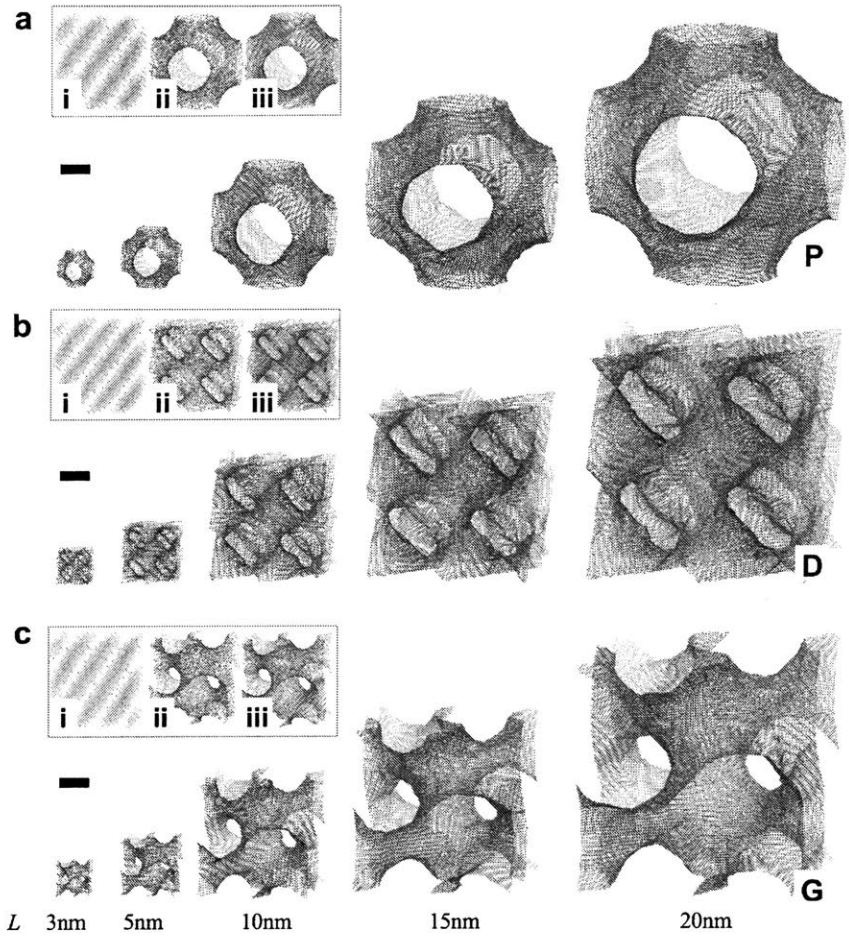

Figure 2-11: (a-c) Five different models of P, D, and G types with different lattice sizes of L=3, 5, 10, 15, 20 nm. Scale bar, 2.5 nm. Inset panels present a summary of three-steps process, including (i) generation of initial template from FCC solid structure of LJ particles with external potentials, (ii) transformation from triangular LJ lattice to hexagonal carbon lattice, and (iii) refinement of geometries by adding and removing atoms based on bond number. The randomly oriented grains and boundaries with topological defects (mainly pentagons and heptagons) shape the curved surfaces.

Chapter 3

Single Crystals

3.1 Introduction

This chapter discusses the crack propagation in single crystalline MoS_2 and WS_2. The first section shows that the crack propagation in MoS_2 monolayer is affected by sulfur vacancies. The second section presents the crack propagation in bilayer MoS_2 and the atomic scale interlocking frictional mechanisms. The last part examines the propagation anisotropy due to the loss of inversion symmetry in the transition metal dichalcogenides. The works presented here are the collaboration with Jamie H. Warner's group in Oxford University and based on the published articles [35, 37, 103].

3.2 Crack propagation in MoS_2 monolayer and sulfur vacancies

3.2.1 Introduction

We combine *in-situ* transmission electron microscopy and large-scale molecular dynamics simulations to investigate brittle fracture in 2D monolayer MoS_2, revealing that cracks propagate with a tip of atomic sharpness through the preferential direction with least energy release. We find that sparse vacancy defects cause crack deflections, while increasing defect density shifts the fracture mechanism from brittle

to ductile by the migration of vacancies in the strain fields into networks. The fracture toughness of defective MoS_2 are found to exceed that of graphene due to interactions between the atomically sharp crack tips and vacancy clusters during propagation. These results show monolayer 2D materials are ideal for revealing fundamental aspects of fracture mechanics not previously possible with thicker materials, similar to studies of dislocation behavior in 2D materials.

3.2.2 Methods

Monolayer MoS_2 model for molecular dynamics simulations

The MD simulations in this method section are designed and conducted by Dr. Zhao Qin with the forcefield I developed. For MoS_2 model in mechanical penetration test in molecular dynamics simulations, we use monolayer MoS_2 in size of 50 x 50 nm with an initial circular hole at the center of the sample. The hole is of 10 nm in diameter and it has two initial triangular cracks at its periphery of two opposite points. Each initial crack has 30° sharpness for its crack tip and 2 nm in length. We incorporate the cohesion between the bottom layer of S atom in MoS_2 and the substrate by using a Lennard-Jones intermolecular potential with the 9-3 form of

$$E(Si_3N_4) = \epsilon[2/15(\sigma/r)^9 - (\sigma/r)^3], \tag{3.1}$$

where r is the distance from a S atom to the surface of substrate, and σ and ϵ are parameters that relates to the equilibrium distance $r = 0.858\sigma$ and adhesion energy 1.054ϵ per S atom. It is noted that this potential is derived by integrating over a 3-dimensional half-lattice of LJ 12-6 particles, which is suitable to describe the interaction with the Si_3N_4 substrate. In simulations we use σ=2.3 Å and it gives the equilibrium distance of 2.0 Å same as the van der Waals radius of the S atom. We test the mechanical strength of the MoS_2 by varying adhesion energy from 0.238 eV/ nm^2 to 7.15 eV/ nm^2, which correspond to ϵ=0.02 to 0.6 eV in our model and find that for $\epsilon > 0.24$ eV, increment in ϵ does not affect the strength of the monolayer MoS_2 anymore. We thereafter use ϵ=1.0 eV through our simulations to ensure the in-plane

deformation of the MoS_2 under mechanical loading to study the intrinsic strength and fracture toughness of MoS_2 without some effects from ripples, which agree with what is observed in all the experiments.

Fracture tests on monolayer MoS_2 by mechanical force

The time step used for time integration is 0.5 fs in the dynamics simulations. We create different ratio of defects in the MoS_2 model simply by randomly removing the S atoms with certain amount that corresponds to the defect ratio throughout the material at the beginning of the simulation. Before we conduct the mechanical penetration tests, the system is fully equilibrated with elevated temperature from 1 K to 300 K by using a Langevin thermostat. The dynamics simulation is run in an NVT ensemble (constant number of particles, volume and temperature) with the temperature controlled by a Nose-Hoover thermostat. We use a cylindrical nanoindenter model with stiffness of K=0.5 eV/Å^3 to apply force on the inner layer of the round hole (force on an atom is given by $F(R) = -K(R - R_0(t))^2$ as R is the distance from the central axis of the indenter and $R_0(t)$ is the radius of the indenter at the current time) in the monolayer MoS_2 by increasing the radius of the nanoindenter R_0 in a quasi-static way. For each increment, we linearly increase R_0 from initially 50 Å by $\Delta R_0 = 1$Å within 10,000 steps, following by equilibrating the system by both energy minimization and equilibration for 20,000 steps by keeping the R_0 at constant value.

We note that we perform energy minimization and relaxation at every quasi-static step, which allow us to describe the deformation of MoS_2 without the strain rate effect. By repeating the increment process, we are able to deform and fracture the entire MoS_2 model with the cracks propagate from the initial triangular cracks. We compute the total potential energy of the system after fully fracture as E_{end} and before mechanical loading as E_{init} and calculate the energy release rate via

$$G_C = (E_{end} - E_{init})/(L - L_0) \tag{3.2}$$

where L=50 nm is the length of the sample and L_0 = 14 nm is the total length of

the round hole and 2 triangular cracks. We find that reducing ΔR_0 does not alter the $E_{release}$ value. We repeat the penetration test for pristine MoS_2 for 4 times for initial cracks along different material directions (armchair versus zigzag) by changing the initial velocity distribution and measure $E_{release}$ for each of the simulations.

3.2.3 Results and Discussions

Figure 3-1b shows a low magnification TEM image of the region where the electron beam has popped the MoS_2 membrane by sputtering a hole, indicated with the yellow dashed boxed area, and the cracks that emanated into the surround area of the MoS_2 that had not been subjected to electron beam irradiation. The region of the crack tip is indicated with the white dashed box, Figure 3-1(b), and the inset shows a magnified view of this area. The cracks were found to have zigzag edge terminations, as shown in figure 3-1(c), that are long and straight and indicative of brittle fracture along the crystallographic plane. Large scale MD simulations also predict the presence of cracks propagating from the end of an elliptical hole, Figure 3-1(d) and (e), along the zigzag direction with similar zigzag edge terminations. Snapshots from the MD simulations reveal that the crack can narrow to an apex tip with atomic sharpness and in some cases have reconstructed tips that contain atomic chains bridging the gap, Figure 3-1(f)-(h). Analysis of AC-TEM images for several different crack tips showed excellent agreement with the MD calculations (Figure 3-1(f),(g)), with the two different types of sharp tips (atomically sharp and reconstructed) observed, Figure 3-2(a)-(d). The AC-TEM image in figure 2b shows the crack narrows all the way down to a single Mo-S bond at its tip, indicated with an arrow. This confirms that crack tips with atomic sharpness can exist in monolayer MoS_2. Figure 3-2(f)-(j) presents a schematic illustration based on experimental observations that indicates the movement of atoms required to form the reconstructed tip. The difference in strain fields of the reconstructed tip, Figure 3-3 (a), and atomically sharp tip, Figure 3-3(f), were evaluated using geometric phase analysis of the AC-TEM images. This method is effective at identifying dislocations from their strain profile and understanding rotation effects in the lattice. The strain maps from the reconstructed crack tip, Figure 3-3(b)-(e), show

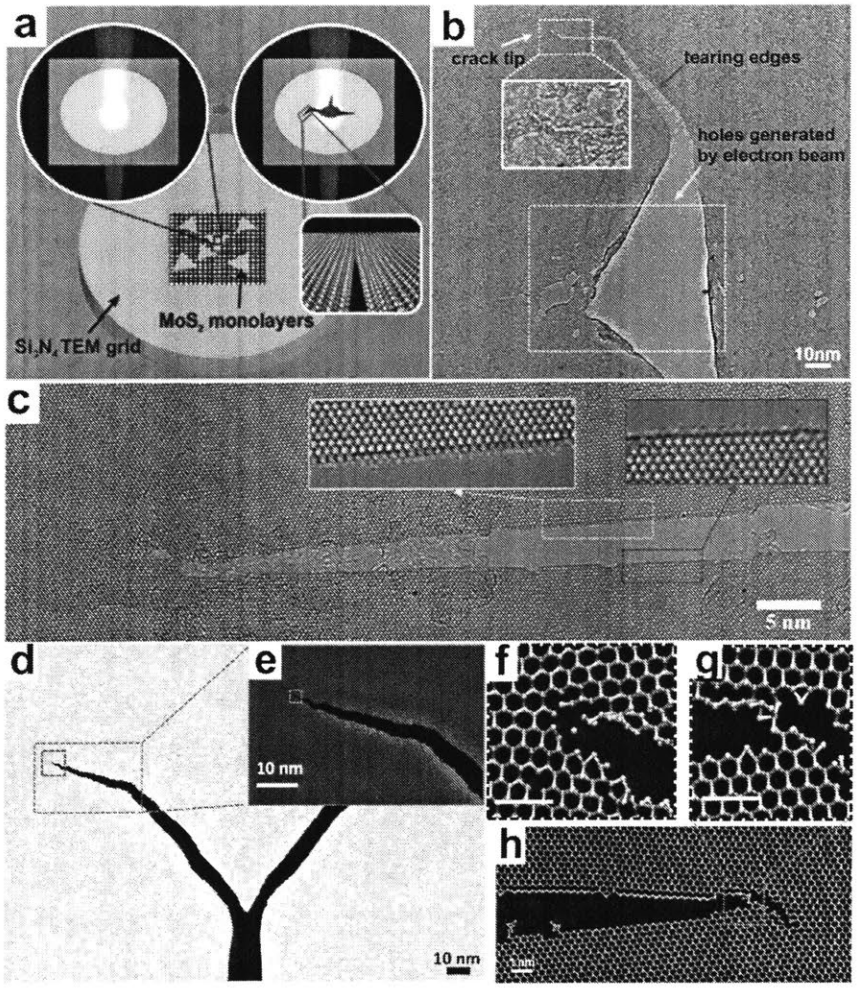

Figure 3-1: (a) Schematic illustration showing CVD-grown triangular-shaped monolayer MoS_2 domains with the size of $\sim$15 μm transferred on to a Si_3N_4 TEM grid with arrays of 2 micron holes. Each domain can completely cover several holes. The zoomed-in image of the circular window showing the crack generation process by the focused e-beam on the suspended monolayer MoS_2 membrane covered on one TEM hole. (b) TEM image showing the crack microstructure. The crack was developed from a hole created by continuous focused e-beam irradiation, marked by the yellow box. A typical crack propagated along a certain lattice direction can be seen, leaving long and straight teared edges, highlighted by the red arrow. The white dashed box shows the crack morphology in its final propagation stage including the crack tip with a higher magnification image below as an inset. (c) Montage of AC-TEM images stitched together to show the long range atomic sharpness of the edges of the crack. (g)-(h) A snapshot of MD simulation of the crack propagating from the end of an elliptical hole in a piece of MoS_2 model of 200 by 200 nm^2 under mechanical stretching force. The crack tip shows an atomic sharpness feature. (i)-(j) A MD simulation snapshot of a different crack propagation by creating a smooth crack edge before creating a step and breaking bonds in front of an intact Mo-S bond, leaving a residue chain behind the crack tip.

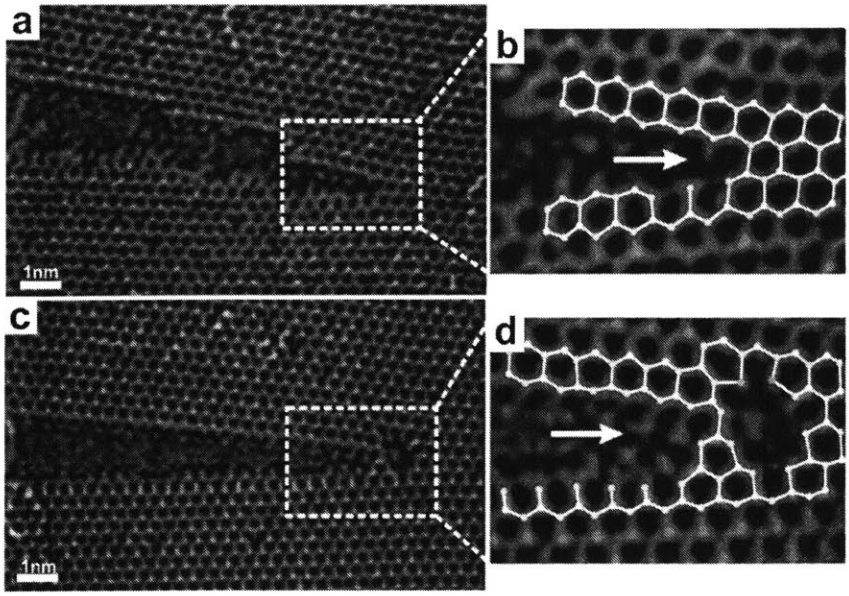

Figure 3-2: (a) AC-TEM image of an atomically sharp crack tip in MoS_2 and (b) a magnified image with atomic model overlay. (c) AC-TEM image of a reconstructed sharp tip in MoS_2 and (d) a magnified image with atomic model overlay. (e) AC-TEM image of a reconstructed crack tip, from panel d, with atomic model overlay to indicate the position of atoms relative to the non-reconstructed form. (f)-(j) Schematic atomic models illustrating the step by step process to transform the tip into a reconstructed form.

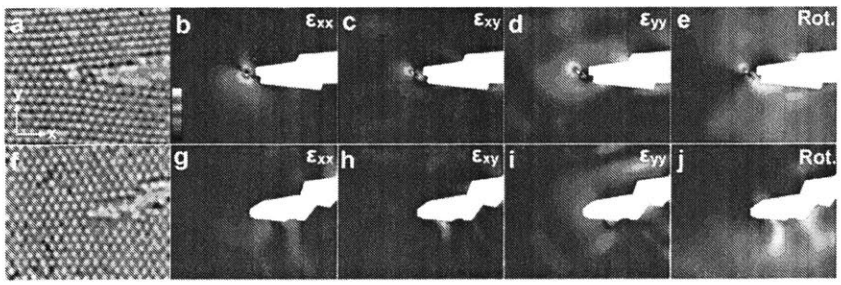

Figure 3-3: AC-TEM images of crack tips (a) reconstructed with dislocation and (f) non-reconstructed and dislocation free. (b)-(e) Strain components, ϵ_{xx}, ϵ_{xy}, ϵ_{yy} and Rotation (radians), extracted by geometric phase analysis (GPA) from AC-TEM image in (a). Red arrow indicates strain feature associated with dislocation core. Scale bar in (b) ranges from -1 to 1 and is used all components except rotation. (g)-(j) Strain components, ϵ_{xx}, ϵ_{xy}, ϵ_{yy} and rotation (radians), extracted by geometric phase analysis (GPA) from AC-TEM image in (f).

the typical pattern in the ϵ_{xx} and ϵ_{yy} strain maps (Figure 3-3(b),(d)) for a dislocation at the front of the reconstructed region, which is not observed in the atomically sharp crack tip strain maps, Figure 3-3(g),(i). The magnitude of the rotation strain appears larger for the reconstructed tip, Figure 3-3(e), compared to the atomically sharp tip, Figure 3-3(j). The use of GPA in Figure 3-3 clearly shows the difference between the two types of tip structures. Crack propagations in MoS_2 can be straight for up to 1μm, forming atomically smooth edges of over nanoscale distances (Figure 3-4(a)-(d)). Very tiny (sub-nm) crack deflections are observed across one or two rows of lattice, Figure 3-4(a). Interestingly, different from graphene, for which cracks occur along both armchair and zigzag lattice directions, in monolayer MoS_2 cracks predominantly occur along the zigzag lattice direction. The cracks have complementary atomic edge terminations, indicative of cleaving the Mo-S bond along the zigzag direction, as shown in Figure 3-4(b)-(d) (Figure B-25, Figure B-26). Occasional 60° direction changes of the cracks following zigzag orientations are observed, Figure 3-4(e), and the near-perfect unzipping along all directions demonstrates brittle fracture. MD simulations show that cracks heading in the zigzag direction have smooth propagation with tiny deflections, while a crack heading in the armchair direction propagates with more deflections of 60°, Figure 3-4(g) and (h). The computed energy release from MD simulations along the zigzag direction is 2.09±0.13 eV/Å, lower than the armchair direction of 2.48±0.16 eV/Å, agreeing with previous DFT calculations of 2.21 eV/Å for zigzag directions (Figure 3-4(i)). Such difference in energy release explains the predominant zigzag crack propagation direction. The ratio of the energy release is very close to the ratio of the total crack length (cos(30°)), suggesting that the increment in the crack path length for the atomic crack tip mainly contributes to the delayed crack propagation along the armchair direction.

Exposing the crack tip region to the e-beam causes propagation within a fixed location (Figure B-27(a)-(c)). A fracture speed of $\sim$ 0.2 nm/s was found under the conditions, Figure 3-5(a)-(c), and is slow enough to capture the dynamics with atomic resolution in AC-TEM. The e-beam introduces S vacancies into the MoS_2 lattice, causing crack path deflections, Figure 3-5(d)-(f). The crack structures studied in

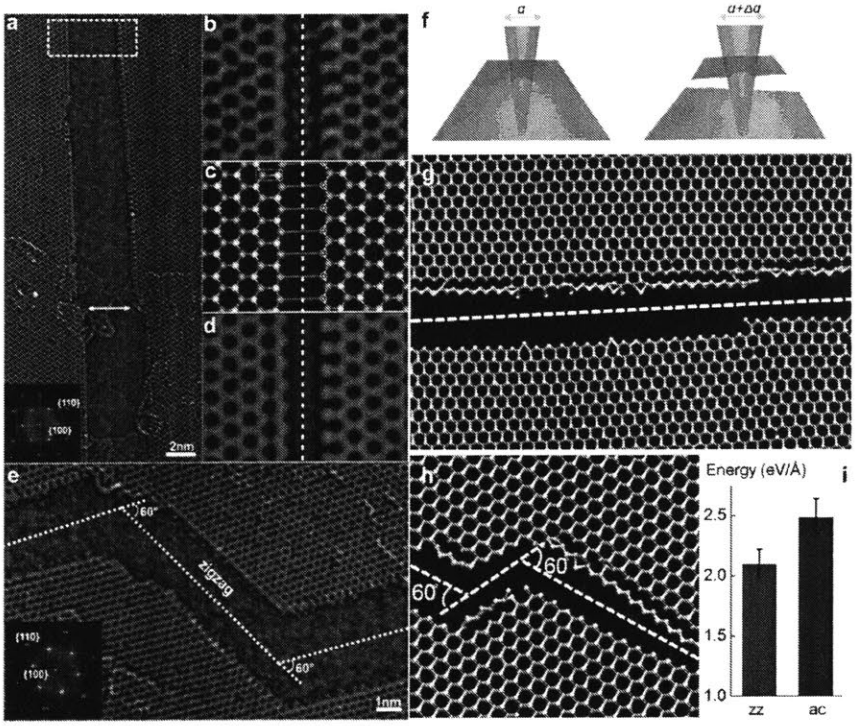

Figure 3-4: (a) AC-TEM image of long and straight zigzag crack edges. The inset is the Fourier transform of the image with labels of two main families of 2D MoS_2 crystal planes, 100 and 110. (b) Detailed structure of the MoS_2 edges from the region indicated by the white dashed box in panel a. (c) Atomic model of the edge structure in panel b. The blue, yellow and orange spheres represent the single Mo atom, double S atoms and the single S atom, respectively. The yellow circles represent the missing S atoms, and the series of horizontal blue dashed lines are drawn to help showing the alignment between these two edges. (d) Multi-slice image simulation using the atomic model in panel c in a supercell. (e) AC-TEM image showing direction changes of crack direction along the zigzag lattice direction. The inset is the Fourier transform of the image, confirming the zigzag direction of each edge. (f) Simulation snapshots of the MoS_2 model before and after loading by penetrating with a rigid cylindrical beam as schematically shown. Each model is initially built with a circular hole of 10 nm in diameter and two initial cracks with 30° sharpness and 2 nm in length. Increment in the diameter of the beam generates the driving force for the crack to propagate. We test models of different lattice directions (zigzag versus armchair) respect to the direction of the initial cracks. Snapshots of the crack edges after rupturing along the zigzag (g) and armchair (h) directions. (i) Energy release after crack propagation in two different directions.

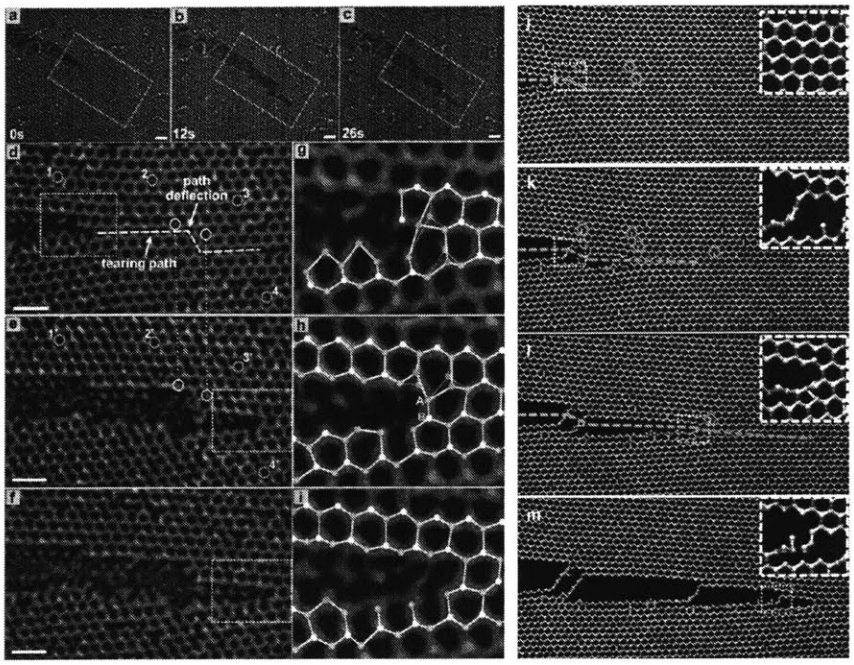

Figure 3-5: (a)-(c) A time series of AC-TEM images showing crack movement through a mildly-defective region, having a low concentration of S vacancies. (d)-(f) AC-TEM images showing the detailed propagation of the crack tip, marked in the region of the white dashed boxes in panel a, b and c, respectively. The white circles in panel d indicate two S vacancies close to the crack path. However, these two vacancies disappeared after the crack tip passing through, as two locations where sitting S vacancies were replaced by regular double stacked S atoms, marked by two white circles in panel e. The yellow dashed line in panel d represents the tearing path of the crack front with a white arrow indicating the path deflection point, situating between two S vacancies. The green circles numbered from 1 to 4 are used to show four S vacancy defects located farther away from the tearing path, compared to those two vacancies marked by white circles. Their locations in panel e are labelled by green circles with corresponding numbers from 1' to 4', respectively. (g)-(i) AC-TEM images of the crack tip region marked in white boxes in panels d, e and f, respectively, with atomic models overlaid. The blue, yellow and orange circles represent the single Mo atom, double S atoms and the single S atom, respectively. All scale bars are 1 nm. (j)-(m) Simulation snapshots of the crack propagation in a MoS_2 model with 1% S atom missing, showing the crack pathway is deflected by the defects near the crack tip.

Figures 3-1-3-4 had fast propagation in pristine regions of the MoS_2 that were not exposed to the e-beam and therefore had minimal defect density. Simulations with 1% S vacancies under the same loading condition, Figure 3-4(f), show different crack propagation compared to pristine MoS_2, Figure 3-5(j) to (m), in agreement with the experimental results. Deflection occurs at a region between the two S vacancies, and once the crack front passes through the two S vacancies disappear, Figure 3-5(e), due to vacancy migration induced by stress concentration around the crack tip. Because of the mobility of vacancies in the stress field, the location of the crack deflection point is not simply determined by the position of static defects, but instead is an evolving dynamic process of vacancy migration and crack propagation by bond unzipping.

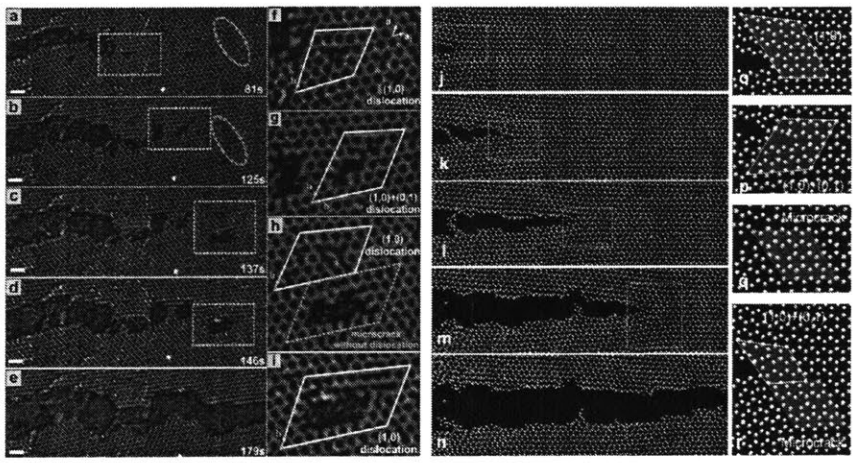

Figure 3-6: Time series of AC-TEM images showing the *in-situ* crack propagation within a moderately defective MoS_2 region containing an increased number of vacancy defect. (a)-(e) A time series of AC-TEM images of crack propagation across an area with a medium concentration of S vacancies, showing the creation of dislocations and micro-cracks ahead of the crack tip marked by white dashed rectangles. The yellow ellipses in panels a and b show the aggregation of some S vacancies into line defects, which subsequently evolve into dislocation pools in panel c as the crack tip approaches. (f)-(i) AC-TEM images of regions marked in white dashed boxes in panels a to d, respectively. Dislocations with corresponding Burgers' vectors, labelled by green arrows, are shown by drawing Burgers' circuits in white. Dislocation-free micro-crack is marked by green dashed lines. All scale bars are 1 nm. (j)-(r) Simulation snapshots of the crack propagation in a MoS_2 model with 20% S atom missing, showing various types of dislocations form at the crack tip. The dislocations interact with the crack propagation by deflecting the crack path and making the crack tip less sharp than material samples with lower defect rates.

In addition, stress concentrated at the crack tip induces lattice distortions, causing the regularly stacked double S atoms in the (001) crystal orientation to split, Figure 3-5(g) and (h), as well as Figure 3-5(j) and (k) in simulations. However, there is no obvious lattice reconstruction in the tip region. The crack typically propagates by directly unzipping the Mo-S bond (marked by A and B in Figure 3-5(h)) perpendicular to the tearing path along the zigzag direction. Once the crack tip passes, the distortion in the bonding is reduced, but with some of the S atoms on the S-terminated edge lost or reconstructed to out-of-plane positions.

Increasing the vacancy defect concentration in front of a crack tip results in distinctly different crack propagation behavior, with some of the single S vacancies agglomerating into line defects followed by the formation of dislocations and micro-cracks ahead of the tip and small regions of dislocation-free lattice trapped between, Figure 3-6(a)-(e). Simulations show similar dislocation formation when increasing S vacancy density up to 20%, Figure 3-6(j)-(n). The Burgers vector of the dislocation region shows two types, (1,0) dislocation and (1,0) + (0,1) dislocation, constructed from two $|b(1,0)| = 3.1$ Å dislocations of (1,0) and (0,1), Figure 3-6(f)-(i). All these dislocation forms can be identified in the simulation snapshots at the crack tip as shown in Figure 3-6(o)-(r) for moderately defective samples. The continuous creation of dislocations ahead of the crack front decreases the vacancy density in this region (comparing Figure 3-6(a) with (d) and (e)), indicating that the dislocations are partly generated by the aggregation of vacancy defects. Furthermore, large-area dislocation pools are formed by the coalescence of small dislocation cores with dislocation-free micro-crack, Figure 3-6 (h) and (i). A fracture velocity of $\sim$0.07 nm/s, in this moderately defective region is the lowest speed measured, compared to the pristine and mildly defective regions.

3.2.4 Conclusions

In summary, our findings enable validation of many theoretical and computational studies that form the foundation of fracture mechanics, but which were previously too difficult to observe at the single atom level in thick materials. Crack tips remained

atomically sharp during propagation and in dislocation nucleation. The atomically sharp crack does not have infinitely large stress at the tip because the interactions between defects and crack tip can lead to deflections, crack blunting and plastic yielding by rearranging of the defects. Increasing the density of defects in MoS_2 leads to enhanced fracture toughness, as crack tips become blunt and the propagation speed reduces dramatically, which is associated with increased fracture toughness.

3.3 Crack propagation in bilayer MoS_2

3.3.1 Introduction

Fundamental fracture mechanics is of crucial concern for materials engineering and subsequent applications, which requires understanding the underlying mechanisms governing crack propagation in a broad range of scientific disciplines [104, 105, 106]. As a post-graphene material, molybdenum disulfide (MoS_2) monolayer is a two-dimensional (2D) material from the transition metal dichalcogenide (TMD) family that has attracted considerable attention due to its electronic and optoelectronic properties [107, 108, 14, 109]. These 2D materials show distinct mechanical behaviors [110] and their atomically thin structures provide opportunities for observing atom dynamics [111, 112] and manipulating atomic configurations [113]. Differently from bulk materials, a single bond breaking in these 2D structures can result in crack propagation due to their atomic thinness. Therefore, the behavior of crack-tip in 2D materials is strongly affected by atomic scale features near the crack-tip, *e.g.*, defects and grain boundaries [35, 31].

Furthermore, there are emerging applications and fundamental engineering arising from the addition of more layers to the system, *e.g.*, electro-mechanics [114, 115, 116] and van der Waals (vdW) heterostructures [5, 17, 19] where the interlayer interaction becomes more crucial for their fracture. Thus, characterizing interlayer interactions and understanding their roles in the mechanical stability and failure are of great importance for the development of devices based on the combination of 2D materials.

To understand the multilayer 2D systems, the stacking geometries and binding energies of differently stacked bilayer MoS_2 systems have been reported [97, 98]. Despite these previous initiatives, the atomic-scale mechanics of crack-tip behaviors in multilayer MoS_2 systems have been elusive so far due to the challenges associated with its direct experimental observation and development of predictive atomic-scale models. Specifically, it is quite elusive how the interlayer interaction of MoS_2 may interplay with the crack-tip behaviors in one of the layers.

Our previous study has demonstrated that *in-situ* aberration-corrected transmission electron microscopy (AC-TEM) and molecular dynamics (MD) simulations are efficient tools to investigate the dynamics of crack-tip behaviors and fracture of MoS_2 monolayer. By utilizing these tools, we report here the dynamics of crack propagation in suspended bilayer MoS_2 and address questions related to the effects of the uncracked layer on crack propagation in the cracked layer. Our finding reveals atomic-scale features and interlayer interactions of the multilayer system with 2D materials, which impacts the bottom-up design of vdW heterostructures and applications of electro-mechanics.

3.3.2 Methods

Crack blocking: Crack propagation into stacked finite bilayer regions

We prepared a 30 x 50 nm rectangular MoS_2 layer (bottom layer) for the crack region with a circular layer (top layer) with a 14nm radius for the uncracked region as shown in Figure B-2(a). The circular regions were stacked in six different ways: 0° (3R), 15°, 30°, 45°, and 60° (2H) rotated. In the beginning, the systems were stretched with 3.2% tensile strain in the x direction, which allowed crack propagation and broke the monolayer layer as shown in Figure B-2(b). After energy minimization, the system was relaxed with NVT ensemble at low temperature 10K for 100ps with 1 fs time step. At this point, the bottom layer was still pre-stretched but the top layer was fully relaxed without rotation. Then, NVE ensemble was applied to ignore the undesired effects from the thermostat before a crack insertion in the bottom layer.

After a sharp crack (l_c = 15nm) was inserted in the bottom layer and the crack propagation was observed as shown in Figure B-2(b).

Coherent fracture: Crack propagation into stacked semi-infinite bilayer regions

Instead of a finite circular layer, a semi-infinite top layer that is large enough to be pre-stretched with the bottom layer was modeled. A square layer (30 x 30 nm) was stacked on the bottom layer with different angles: 0° (3R), 15°, and 60° (2H). The bottom layer was 30 x 40 nm and the entire system was relaxed with NVT ensemble at 10K for 100ps after energy minimization. The ensemble was changed from NVT to NVE and the major crack (l_c = 8nm) in the bottom layer was inserted. Different flaws were introduced in the top layer from 0 to 3nm crack (l_{c2}) on the crack-path in the bottom layer as shown in Figure B-4(a). The flaw lengths were too short to allow the crack propagation in the top layer with the applied pre-strain (~5%).

Crack branching: Cracks in 2H stacked bilayer MoS_2

From the experimental observation in Figure 3-11, we prepared the 40 x 40 nm square layer for the top and bottom layer with 2H-stacked condition as shown in Figure B-5(a). First, different ratios of defects were introduced in the defect region of the top layer where the width is 2nm and the length is 40 nm. Each model was relaxed with 4% pre-strain in the x direction. After energy minimization, the system was relaxed with NVT ensemble at 10K for 100ps. The ensemble was changed from NVT to NVE and a crack ($l_c \sim$ 8nm) was introduced in the bottom layer. The stored strain energy allowed the crack start to propagate, and the natural behaviors of both layers were observed. The left and right boundaries were fixed in the x direction and top and bottom boundaries were fixed in the y direction with a non-periodic boundary condition, mimicking the main features from the experimental structure in Figure 3-11.

3.3.3 Results and Discussions

One of the most promising methods to produce high-quality and large-area MoS_2 is chemical vapor deposition (CVD). By adjusting the synthesis parameters properly, the MoS_2 samples contain regions of both monolayer and bilayer. In our experimental setup, cracks are introduced into MoS_2 by popping a strained MoS_2 membrane with a focused high-energy electron beam in Figure 3-7(a) to cause fractures that enable the observation of the crack-tip behaviors with AC-TEM. The cracks that initially appear in the monolayer regions then propagate into the bilayer domains in Figure 3-7(b) (i-iv). The single atom resolution of AC-TEM and the application of Fast Fourier Transformation (FFT) to TEM images, which enables the extraction of specific lattice information in the reciprocal space to successfully reconstruct the atomic details of each layer in the bilayer MoS_2 as demonstrated in Figure 3-7(b) (v-viii).

To obtain a reliable forcefield for performing MD simulations that are able to reproduce the behavior of crack-tips in bilayer MoS_2 system, REBO parameters are utilized by using dispersion-corrected DFT calculations to describe both mechanical properties of intralayer and interlayer interactions of MoS_2 (See 2.4.5 in Chapter 2). The binding energy between the two layers and mechanical properties of monolayer MoS_2 are critical for MD simulations to provide reliable insights into the mechanisms behind the observed behaviors of the crack-tips. For the binding energy, we chose the two representative stacks, AA and 2H(AA'), as a reference to tune the vdW parameters. Then, we tuned the interatomic REBO parameters for the mechanical properties of monolayer MoS_2. The elasticity and strength of monolayer MoS_2 from our MD show good agreement with those from our DFT calculation, and the previous studies [99, 92]. Also, the crack behavior in the bilayer region is well captured in Figure 3-7(c). Then, the subsequent MD simulations allow us to systematically measure the friction between the two layers with different stacks and loading directions as shown in Figure 3-8(a). The magnitude of the friction significantly depends on the stacking and loading conditions (Figure 3-8(b)). The results show that frictions in $\pm$ armchair (AC) directions with 2H and 3R stacks can reach 10 times higher than

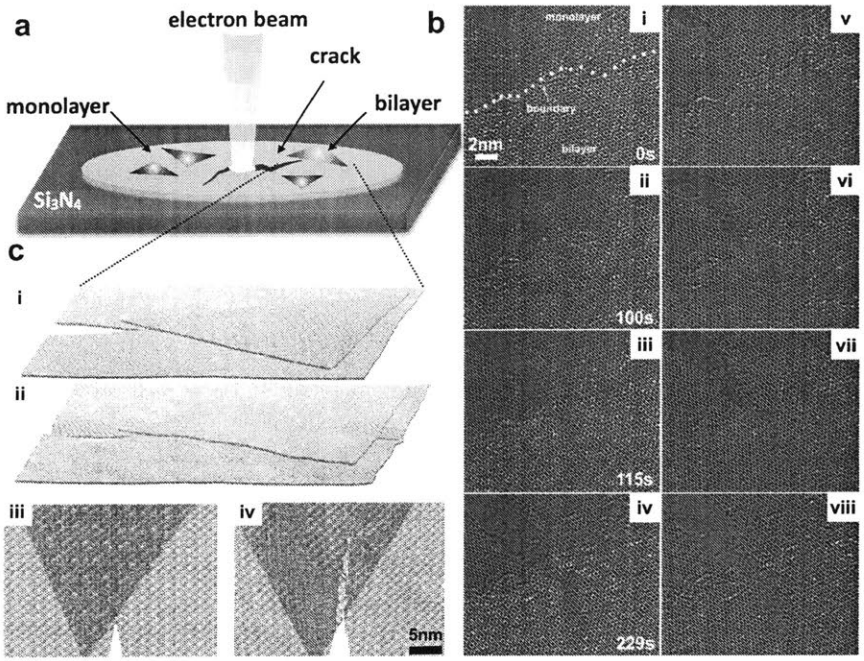

Figure 3-7: (a) Schematic illustration showing CVD grown mono- and bi-layer MoS_2 on Si_3N_4 TEM grid. The focused e-beam on the suspended layers generates a hole and cracks. (b) A time series of AC-TEM images (i-iv) showing a crack going from the monolayer into the turbostratically-stacked bilayer region. The color of these AC-TEM images is inverted to give a higher visual contrast so that atoms are in white. The crack is restricted to one layer even in the bilayer region. (v-viii) A time series of reconstructed AC-TEM images after filtering out the uncracked layer. (c) The snap shots of MD simulation before (i) and after (ii) crack propagation into the triangular bilayer region. The atomic bond breaking and moiré pattern coming from bilayer can be well captured with reactive MD simulations (iii, iv).

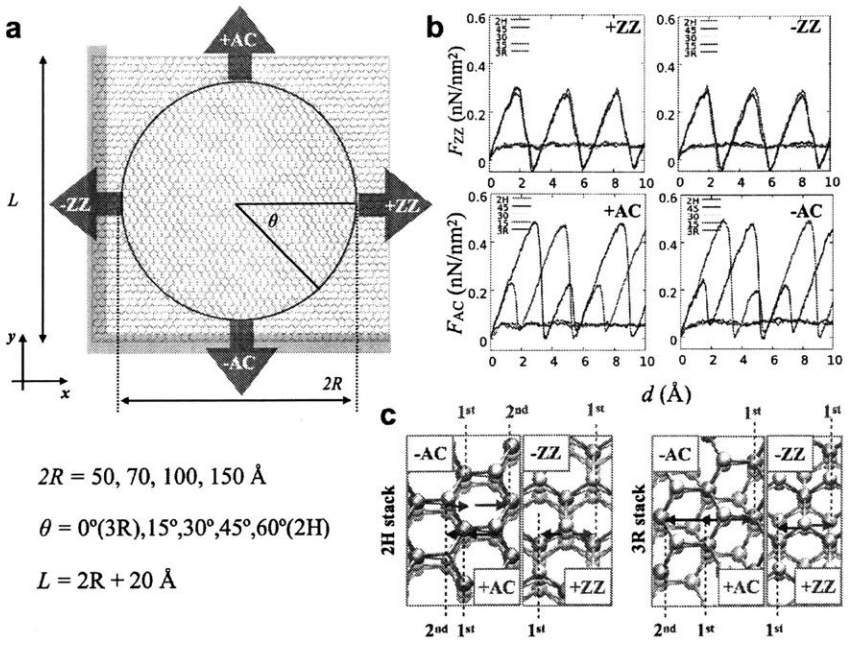

d

	0°(3R)	15°	30°	45°	60°(2H)
+ZZ	0.37	0.071	0.064	0.065	0.34
-ZZ	0.33	0.055	0.056	0.056	0.35
+AC	0.52/0.15	0.056	0.057	0.060	0.24/0.52
-AC	0.25/0.52	0.067	0.064	0.065	0.53/0.14

(nN/nm²)

Figure 3-8: (a) Schematic depiction of MD simulations for interlayer frictional forces per area (eV/nm^3) with four different loading directions: positive and negative zigzag (+ZZ and -ZZ) and armchair directions (+AC and -AC). (b) The forces obtained from the system size of $2R$ =150Å (c) The relative positions of sulfurs of top and bottom layers. Considering the small difference from the weak vdW interactions, the 10 times higher friction force is counterintuitive. (d) A table for the averaged frictions (nN/nm^2). The two values in the ±AC represent the two peaks of the frictions. The forces and directional dependence can be explained with the relative distance and position of sulfur atoms, suggesting the friction is originated from the geometrical interlocking. The detailed values are listed in Table E.5 - E.8.

turbostratically-stacked systems. The origin of the difference for 2H and 3R with respect to turbostratically-stacked systems is expected to come from different binding energies as shown inTable E.1 and E.2. However, the binding energies of 2H or 3R stacking are only $\sim$ 1.5 times larger than those of AA stacking (See Figure 2-6 and Table E.1). Instead, analyzing the relative positions of sulfur atoms in the top and bottom layers indicate a geometric effect on the friction. As shown in Figure 3-8(c), sulfur positions in $\pm$ zigzag (ZZ) directions are highly symmetric while sulfur positions in $\pm$ AC directions are asymmetric. In fact, the peaks of friction forces occur when the sulfur atoms of the top layer align with the sulfur atoms of the bottom layer. Our results show that the slopes are equal to all peaks due to the geometry and number of interacting sulfur atoms per unit length. Therefore, we conclude that such large difference results not from the vdW interaction itself but geometrical interlocking between two layers.

The friction per unit area of the stacked bilayer is likely to decrease as the stacked areas increase (See Tables E.4 -E.8) because local ripples and deformation facilitate the sliding as the stacked areas increase in Figure B-2. Also, We have evaluated the loading rate dependence. The results show that the friction values are likely to decrease as the loading rate decreases as shown in Figure B-1. However, the friction values of 2H and 3R systems are less sensitive to the loading rate compared to turbostratically-stacked layers, which means that the friction from well-stacked layers can be relatively much stronger than the friction coming from turbostratically-stacked layers at the slow loading rate limit. This geometrically interlocking friction of MoS_2 allows us to understand complicated crack-tip behaviors observed with *in-situ* AC-TEM.

Crack tips in turbostratically-stacked bilayer MoS_2 region: crack blocking

Figure 3-9 shows the experimental observation of crack propagation in turbostratically-stacked bilayer regions with AC-TEM, together with MD results. In turbostratically-stacked systems one of the layers can be removed in AC-TEM images by using a mask in Fourier space to study the crack in detail without the interference of the second

layer. The AC-TEM images reconstructed by these means show the atomic structures of both the cracked and uncracked regions separately, which can be directly compared to the simulation results. Both AC-TEM images and MD simulations reveal that the crack prefers the zigzag direction for propagating, and as a consequence the sliding of the cracked layer with respect to the uncracked one generates different moiré patterns in Figure 3-9(a)-(f). The asymmetric moiré patterns along the crack result from asymmetric friction from the other layer.

To see how the friction from the different stacking can disturb the crack propagation, we performed MD simulations with a circular bilayer with different stacking conditions (Figure B-1(a)). Due to the elastic energy, a crack naturally propagates into the circular bilayer regions. The propagation of the crack is drastically disturbed and finally stops at the center of the circular region with 0° (3R) and 60° (2H). However, the other stacks (*e.g.*, 15°, 30°, and 45°) cannot disturb the cracks enough as shown in Figure B-3(b). Figure 3-9 and Figure B-4 show that the interlocking friction strongly interacts with the crack-tip with 0° (3R) and 60° (2H).

Crack propagation through the entire bilayer region: coherent fracture

Figure 3-10 shows two distinct fracture behaviors in suspended MoS_2 with 60° (2H) that are generated by puncturing the membrane with the electron beam irradiation in a monolayer region. The crack on the left propagated too fast to be captured with the AC-TEM imaging technique, while the crack on the right propagated slowly enough to be tracked. Despite the fast propagation of the first crack, the image shows a complete fracturing of both layers, while the slow crack is confined in one layer without any interruption of the second layer. Although friction force from fast crack propagation should be higher than that from slow propagation, this loading rate dependence is not sufficient to explain this coherent fracture. To probe whether the uncracked layer breaks due to the crack propagation in the second layer, we performed MD simulations of a 30 x 40 nm rectangular-shaped bottom layer with an 8 nm length initial crack. To evaluate the differences coming from the stacking conditions, 30 x 30 nm square-shaped top layer is stacked with 0° (3R), 60° (2H), and

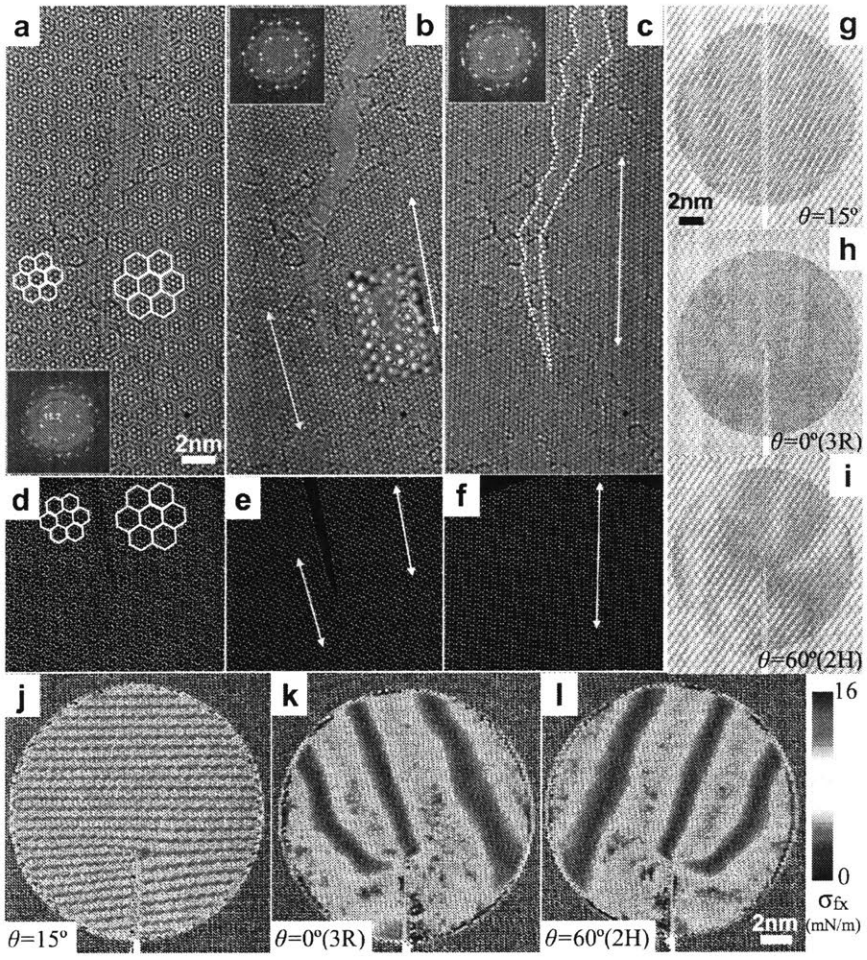

Figure 3-9: (a) AC-TEM image showing a crack propagating in one layer of a turbostratically-stacked bilayer MoS_2. (b) Reconstructed AC-TEM image. It highlights the lattice configuration of the fractured layer. The crack tip region is zoomed-in with atomic models overlaid, which shows atomic sharpness. The blue and yellow spheres represent Mo and S atoms, respectively. (c) The yellow outline indicates the region that has a crack on the other layer. (d) The MD simulation of crack propagation into finite bilayer region that is turbostratically stacked by 15 degrees. The white hexagons indicate the size of moiré patterns (e) Crack-tip image in the cracked region showing atomic sharpness as AC-TEM image (f) Image of the un-cracked finite layer region without any structural change. The arrows indicate the zigzag lattice direction in both AC-TEM images and MD simulations. (g)-(h) The MD results of crack propagation with different stacking. 2H (60°) and 3R (0°) stacks block the crack propagation while the other stacks allow the crack to propagate through entire layers. (j)-(l) The friction distribution from vdW of the two sulfurs in the top and bottom layers, showing the regions of highly activated interlocking friction. 2H and 3R stacks show stronger interaction between the friction and the crack tips than the stack with 15°. The region with high friction provides driving force to dominate the fracture of the top layer and its discontinuous distribution associate with the stacking geometry with the two layers after deformation.

15°. The top layer is assumed to be semi-infinite with periodic boundary conditions (Figure B-5(a)). The top layer does not break even if the pre-strain increases in both layers, which corresponds to faster propagation due to higher elastic energy. The crack propagations cause local ripples in the cracked layer and the propagation disturbed the coherent behaviors (consisting 2H stack) as shown in Figure 3-10(e) and Figure B-6, significantly reducing the coherency of the friction. Once the 2H stack is distorted, it does not recover its alignment due to the mismatching strains at both layers. However, this behavior changes drastically if the top layer has a small flaw on the crack propagation path. Due to this flaw, the regions near the flaw are not well stacked in 2H anymore before the crack propagation, showing highly activated interlocking friction in Figure 3-10(g)-(i), allowing coherent movement to cause effective tensile stress near the crack tip after initial crack passed as shown in Figure 3-10(f). Therefore, the small flaw becomes a crack-tip following the first crack path. It is important to note that this flaw is too small to break along itself. Also, the coherent fracture happens with 3R, but not with turbostratically-stacked layer as shown in Figure B-5(b).

Cracks in 2H-stacked bilayer MoS_2: crack branching

Figure 3-11(a) shows a region in the bilayer MoS_2 where the 1st crack tip is in the monolayer region and the 2nd crack goes through both layers. There is lattice distortion along the 1st crack path, which could be a result from defects and grain boundaries. As shown in Figure 3-11(e), moiré patterns are observed at the front of the 1st crack. Although these irregular moiré patterns could be thought to arise from a local ripple of one layer, the remaining tensile strain of the other layer prevents the local ripple from appearing with such extremely confined width and non-straight shape [117]. Also, if this comes from grain boundaries, well-aligned 2H phase in overall regions is not possible. Thus, it is reasonable to conclude that the distortion comes from local defects. These specific structures are able to appear when two separated triangles with 2H stack on monolayer MoS_2 combine during CVD growth-process. Furthermore, the 1st crack path is on the defect region of the 2nd layer, which can

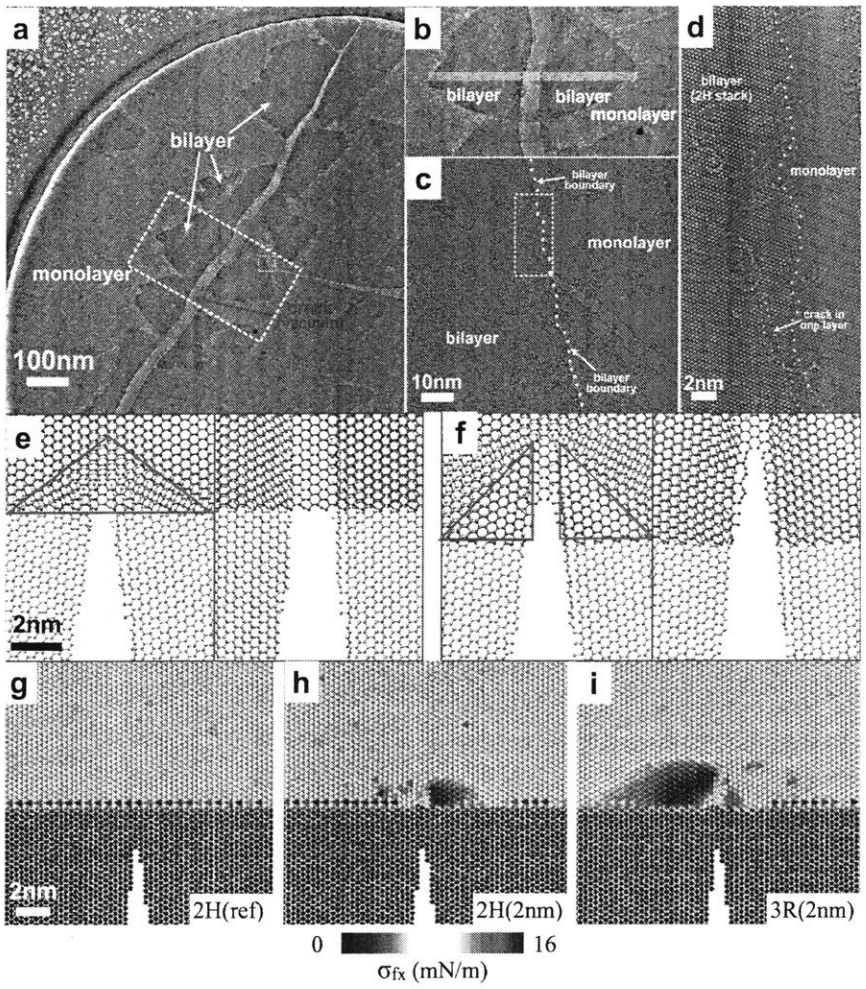

Figure 3-10: (a) Low-mag TEM image showing two cracks on a suspended MoS_2 region. Most areas of this suspended MoS_2 region are monolayer, with some small bilayer/multilayer islands distributed on it, as marked by yellow arrow. The red arrow on the left indicates one of them, and the other one is on the right. (b) Zoom-in TEM image of the region marked by the dashed white box on the left crack in panel a. (c) Zoom-in TEM image of the region marked by the dashed yellow box at the tip region on the right crack of panel a. (d) Zoom-in TEM image of the region in the cyan dashed box in panel c.(e-f) Snap shots of MD simulations. (e) The crack passes through in the bottom layer without breaking the other layer because the interlayer friction reduces significantly by disturbed stacking alignment. (f) Coherent fracture occurs when both layers move coherently during the crack propagation. The red triangle indicates the regions where the effective tensile stress locally occurs due to the high friction from 2H stack alignment. The top layer breaks after the crack pass through in the bottom layer. (g-h) The distribution of the friction from vdW atomic stress of the two sulfurs in the top and bottom layers before the crack propagation. 2H stack without a small flaw shows no activated friction while 2H and 3R stacks with a small flaw show highly activated friction regions near the small flaw, which causes effective tensile stress near the crack tip.

result from weakening friction in the non-coherent 2H-stacked regions. Surprisingly, the 1st crack branches into highly complicated paths in Figure 3-11(f), in contrast to the other observed cracks.

To understand this complex crack-tip behavior in the system, we derived three critical factors to model the systems. First, the entire system is considered as a 2H-stacked bilayer. Second, a thin defected region is prepared in the uncracked 2nd layer. Finally, the system is constrained not only in the crack propagation direction but also in the direction perpendicular to the crack propagation, which implies fixing all boundaries. Within these settings, we simulated a 40x40 nm bilayer system with an initial crack inserted in the 1st layer. The 2nd layer has 2nm-width defect regions with different defect ratios, as shown in Figure B-7(a). As the defect ratio increases, the crack path becomes more disturbed and eventually branches when 10% defects ratio is reached (Figure B-7(b) and Figure 3-11(i)). The boundary condition is essential to provide driving force for the branched crack to propagate into the different direction from the initial direction.

The branched directions of the crack also show good agreement with AC-TEM images. One crack is likely to pass straight following a zigzag edge direction, and the other crack is deflected to the armchair edge direction as shown in Figure 3-11(f) and (i). The asymmetry of friction force due to non-2H stack in Figure 3-11(l) controls the direction of the branches. Also, the branching point in both AC-TEM images and MD snap shots show non 2H-stacked moiré patterns, where the asymmetric force can occur. While one of cracks eventually propagates the entire region with MD simulations, AC-TEM images show that the branched cracks run parallel and leave islands behind. This behavior is not mechanically driven but by sulfur vacancies induced by electron beams because the islands become smaller by losing atoms without sliding (without changing moiré patterns).

3.3.4 Conclusions

In summary, we combine *in-situ* AC-TEM and DFT-based reactive MD to investigate crack-tip behaviors in bilayer MoS_2, revealing the sulfur-to-sulfur geometrical

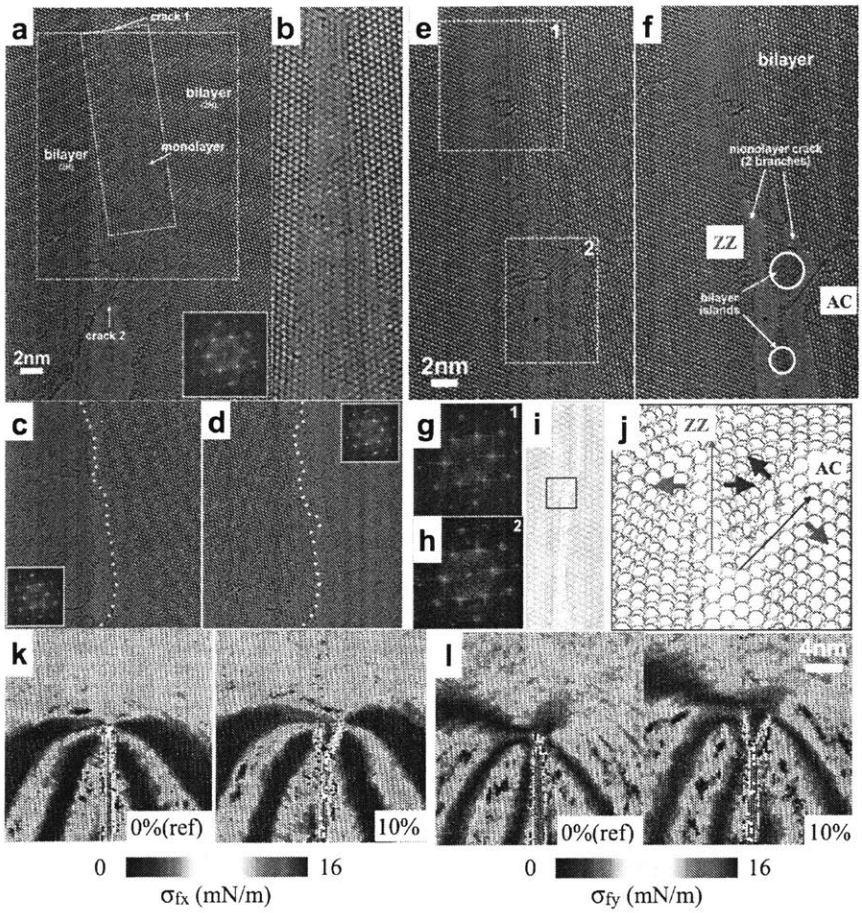

Figure 3-11: (a) AC-TEM image showing cracks in a 2H-stacked bilayer MoS_2 region. In this case, cracks happen in both layers, with a crack in one layer going beyond the other. (b) Zoom-in AC-TEM image of the region in the white dashed box in panel a, showing that the lattice in the monolayer region is deformed as indicated by the red region. (c) Reconstructed AC-TEM image after applying a mask to one set of the FFT spots, as indicated by the cyan spheres of the inset. (d) Reconstructed AC-TEM image after applying a mask to the other set of the FFT spots, as indicated by the yellow spheres of the inset. (e) AC-TEM image showing 1st crack in panel a branches off into two cracks, leaving some bilayer islands in between. Two cracks are highlighted by adding half-transparent white masks, as shown in panel (f). The FFT patterns 1 and 2 are shown in (g) and (h), respectively. (i)A crack branches in MD simulations due to the introduced defects in uncracked layer. The red arrows indicate lower frictions while the blue arrows show the activation of high frictions due to geometric interlocking. (k) The distributions of friction in the x direction from vdW of the two sulfurs in the top and bottom layers with 0 and 10% sulfur vacancies. (l) The distributions of friction in the y direction from vdW of the two sulfurs in the top and bottom layers with 0 and 10% sulfur vacancies.

interlocking mechanism. Both stacking and loading conditions significantly affect the interlayer friction where 2H and 3R stacks show extremely high static friction compared to turbostratically-stacked layers. Complex crack-tip behavior in bilayer MoS_2 is governed by highly variable interlayer friction. 1) A crack can either propagate or be blocked. 2) a crack propagation in the first layer can induce breaking in the other 2H- or 3R-stacked layer when small flaws in the second layer are located in the first crack path. 3) A crack in the first layer branches due to the existence of defects or atomic configuration in the other layer. The observed complex behaviors can be explained by the principles we derived:

1. Higher friction from sulfur-to-sulfur interlocking of 2H and 3R stacks

2. Lower friction of turbostratic stacks

3. Loading-directional dependence of asymmetric frictions

These essential insights into the complex fracture of bilayer MoS_2, can also apply to other transition metal dichalcogenide (TMD) materials, which further increases the relevance of this scientific contribution.

3.4 Anisotropic crack propagation in monolayer WS_2

3.4.1 Introduction

Understanding fracture mechanics is essential for developing correct models of failure due to crack propagation [104, 105, 106, 118, 119], and improvements to materials synthesis to enhance their strength. In brittle crystalline materials, cracks propagate rapidly along low energy directions, which typically match a specific crystal plane, when stress is applied to the materials [81]. Many theories by assuming a linear elasticity of materials are capable of predicting the failure and initiation of crack propagation [120, 121, 122]. However, the elastic linearity is only valid with infinitesimally small deformation, and the materials at the crack experience severe

deformation. The non-linearity of materials or elasticity at large strains, called hyperelasticity, are more dominating on the dynamics of fracture such as crack speed, the onset of instability, and fracture faces [104, 118, 123, 124, 125]. Also, the lattice structure front to the crack tip is a key to understand the crack propagation in crystals such as silicon [105, 126, 127, 128] because the crack tip can be atomically sharp and propagates by further bond breaking one at a time [129, 130]. Thus, a single atomic level deformation and its non-linearity can play a critical role in the dynamics of fracture despite the lack of evidence. Two-dimensional (2D) materials have emerged as ideal materials for studying the atomic structures of cracks, defects, and grain boundaries, due to their thin nature and straightforward interpretation of the 2D structure [131, 132, 133, 134]. In monolayer MoS_2, when electron beam irradiation pops it, the residual tension in the film results in rapid crack emission along the zigzag directions. The force from the additional electron beam applied to around the crack tip allows that the propagation speed is relatively slow, and this makes it possible to track the crack movement in real time. It has also been shown that the crack tips in monolayer MoS_2 retain their atomic sharpness even when entering into a turbostratically stacked bilayer region. By utilizing the first-principle based molecular dynamics, it was revealed that the behavior of cracks in bilayer MoS_2 is influenced by the interlayer locking of S atoms, associated with the 3D structure of the 2D crystals. In this study, we show that single atomic deformation from the different types of atoms regulates the dynamics of fracture from the triangular faceted voids with sharp edges in suspended WS_2 monolayer rather than randomly generated edges from a hole that is popped into transition metal dichalcogenide (TMD) films by electron beams. We also present that the atomic deformation can solely regulate the initiation of crack propagation in spite of the same crack geometries, elasticity, and cleavage surface, which is inexplicable in linear theory.

3.4.2 Methods

MD for crack from triangular voids

MD simulations are performed via LAMMPS package. REBO forcefield (FF) is utilized for the interatomic interactions of tungsten and sulfide. A WS_2 monolayer (50 nm by 50 nm) is prepared with the triangular void that has the same edge structures in experiments. The size of the equilateral triangular, R, is defined as the distance from the centroid to the vertex and R is selected as 6 nm. After energy minimization, the structure is relaxed with NPT ensemble at 10K and 0 bar in the x and y directions for 50 ps and then, with NVT ensemble at 10K for another 50 ps. The pre-strains in both x and y directions (ϵ_{xx}, ϵ_{yy}) are applied after the structural relaxation to mimic the loading conditions from the *in-situ* STEM. Then, the boundary is fixed, and temperature increases from 10 to 100K after additional energy minimization. Although the effect of the temperature on the strength is overestimated with the REBO style, we can add kinetic energy by increasing temperature to break the bonds and cause crack propagations under the certain pre-strains.

MD for propagation anisotropy

To compare the strengths and crack propagation among the triangular and half-circular voids under the tensile loading in the zz direction for both crack directions V_A and $-V_A$, a WS_2 monolayer (30 nm by 50 nm) is prepared with different voids. All void sizes as a crack are set to 5nm (l_c = 5nm). There is enough space in the lateral directions to ignore the interaction between image cells due to the periodic boundary conditions. The structures are relaxed with NPT ensemble at 10K and 0 bar in the x directions for 50 ps after energy minimization. Further relaxation is applied with NVT ensemble at 10K for another 50 ps. Then, the box is stretched in the zz direction with constant velocity, 0.02Å/ps (2m/s), for 1.5ns, and the stress along the zz direction is recorded with strains in. The loading speed is slow enough to ignore the strain rate effect on the strength. However, we check the strain rate effect differently by utilizing the simulation set-ups from the previous study. From

the pre-stretched (~5% in the zz direction) and relaxed system, a designed void shape is introduced. Then, we trace the crack propagation with completely turning off damping effects from the thermostat by using NVE ensemble, which allows us to record the crack propagation purely driven by the mechanical strain energy. We confirm that the distinct crack patterns between the V_A and $-V_A$ directions are not affected by the strain rate.

MD for strengths and stress distributions

A pristine WS_2 monolayer (50 nm by 50 nm) is prepared with different sizes of R from 1 nm to 8 nm. The structural relaxation is applied as the previous sections. After structural relaxation, the box is stretched with constant velocity, 0.02Å/ps (2m/s), for 2.5ns in the zz (x) and ac (y) loading directions. The failure strengths are fitted with equations based on the LEFM. The same tests are performed with different triangles with different crack directions and edge termination.

For the stress distributions from the different geometries of voids in monolayer WS_2, the atomic stress under a tensile strain is obtained by utilizing the equation of virial stress. Unlike monoatomic systems such as graphene, careful atomic stress analysis is required for the multi-atomic system. The atomic stress has useful meaning when we consider the WS_2 unit because the only stress of each W or S atom has a non-zero value even when the system is fully relaxed. The summation of atomic stress from WS_2 unit describes the trend of the far field stress. Firstly, we build a bond list of sulfide atoms near a W atom. Then, we add the atomic stress of the S atom to the W atom with a factor 1.0/6.0, which corresponds to the two sulfide atoms' contribution without any defect. Visualizing the atomic stress of W atoms describes reasonably the stress concentration near the crack tip and the crack initiated from the concentrated stress region.

Stress intensity factor for triangular and circular voids.

Due to the different geometries of holes to compared, we utilize empirical stress intensity factor from FEM simulations for triangular void:

$$K_We = \sigma\sqrt{\pi R}F(\phi) \tag{3.3}$$

where where R is the radius of crack; $\phi = R/L$, and $F(\phi)$ given by fitted data. For the zz loading direction, the empirical solution is

$$F_{zz}(\phi) = 1.041 - 0.60223\phi. \tag{3.4}$$

For the ac loading direction, the empirical solution is

$$F_{ac}(\phi) = 1.341 - 1.138\phi. \tag{3.5}$$

On the other hand, the stress intensity factor for circular voids from the solution for the elliptical hole with eq(2.22).

3.4.3 Results and Discussions

Atomic structures and dynamics of cracks

Aberration corrected annular dark field scanning transmission electron microscopy (ADF-STEM) is utilized to resolve the atomic structure. Low magnification imaging of the samples reveals many triangular faceted voids in the WS_2 monolayer are present, Figure 3-12(a)-(c), and range in size from 20 to 100 nm. They are all typically aligned in the same direction, indicating they all have the same crystallographic orientation. Figure 3-12(c) shows the triangular nanovoid having sharp vertices, and near equilateral geometry. Figure 3-12(d) shows the atomic resolution ADF-STEM image of the vertex region of a triangular nanovoid in monolayer WS_2. The edges are along the S zigzag direction, and the magnified inset region reveals this more clearly. The S atoms at the very edge of the zigzag lattice may be missing in many cases,

either as intrinsic or they are sputtered away easily by the electron beam. The vertex region in Figure 3-12(d) is atomically sharp, and the edges are also very smooth with terracing across only a few atoms across the 20 nm region. Figure 3-12(e) shows a low magnification ADF-STEM image of WS_2 that was transferred to a SiN grid with two microns rectangular slit. Small triangular nanovoids are seen in the WS_2 film below the slit and to the right of it, and the red arrow to the left of the slit shows where a fracture has gone through one of these faceted void regions. In many cases, the nanovoids were not perfectly triangular, with some faceted of the vertex regions to produce truncated triangles. In this case, the tips were no longer atomically sharp, but contained some lattice along the armchair direction, as shown in Figure 3-12(f). The higher magnification ADF-STEM image in Figure 3-12(g) shows that some of the edges have missing S atoms (green arrow), but some S atoms are present.

Sseveral occasions where cracks had formed from the edge of one of the faceted nanovoids, and molecular dynamics (MD) simulations demonstrate a crack can propagate from the vertex in Figure 3-13(a),(b) due to the residual strains.

It is rare to find cracks in monolayer TMD films that have no voids, and prior work needed to introduce holes in MoS_2 to generate crack emission. Here, the existence of voids from the growth conditions means that they can act as sites for crack generation during the mechanical handling and processing of the material. Figure 3-13(c) shows the vertex region of a triangular nanovoid that contains a crack emanating downwards into the bulk lattice of WS_2. In Figure 3-13(c), the green lines indicate the zigzag lattice direction, the yellow lines indicate a 6° angle, and the red line shows the center of the crack. A higher magnification ADF-STEM image of the crack mouth area, Figure 3-13(d), shows it is mainly along the zigzag direction, before kinking to the right along a non-crystallographic direction, green lines. The tip of the crack is located in a pristine clean area of the WS_2, Figure 3-13(e), and further imaging only caused further propagation of the tip region by a couple of nanometers over 20 minutes. This process is entirely different from the prior work, where crack tip propagation was continuous across a long range when imaging due to the residual tension in the film. The crack here in Figure 3-13 has exhausted the strain energy

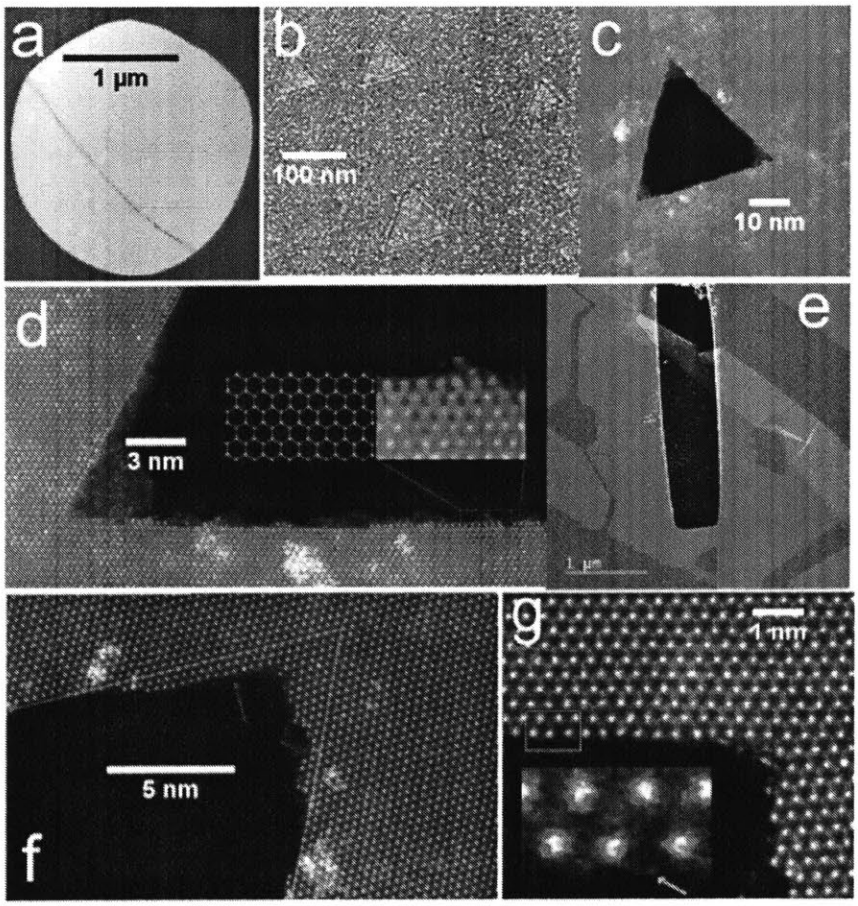

Figure 3-12: (a) STEM shadow image at the low magnification of monolayer WS_2 suspended across 2 micron hole in SiN membrane TEM grid. (b) Magnified view of the green boxed area in (a), showing triangular nanovoids (c) Low magnification ADF-STEM image of a triangular nanovoid. (d) Higher magnification ADF-STEM image of the atomically sharp apex region of a triangular nanovoid with zigzag termination. The inset shows the magnified view of the red boxed area, and the atomic lattice to its left shows the relative orientation of the W and S lattice sites. Green lines indicate zigzag lattice directions. (e) Low magnification ADF-STEM image of a WS_2 monolayer transferred across SiN TEM grid with rectangular slits, showing triangular nanovoids, and also cracked regions indicated with a red arrow. (f) Atomic resolution ADF-STEM image of an apex region of a triangular nanovoid that is not atomically sharp. Green lines indicate zigzag lattice directions. Red arrow indicates the region studied in (g) Higher magnification ADF-STEM image (rotated and false color LUT) of the WS_2 edge region, showing the missing S atoms at the edge (inset), green arrow.

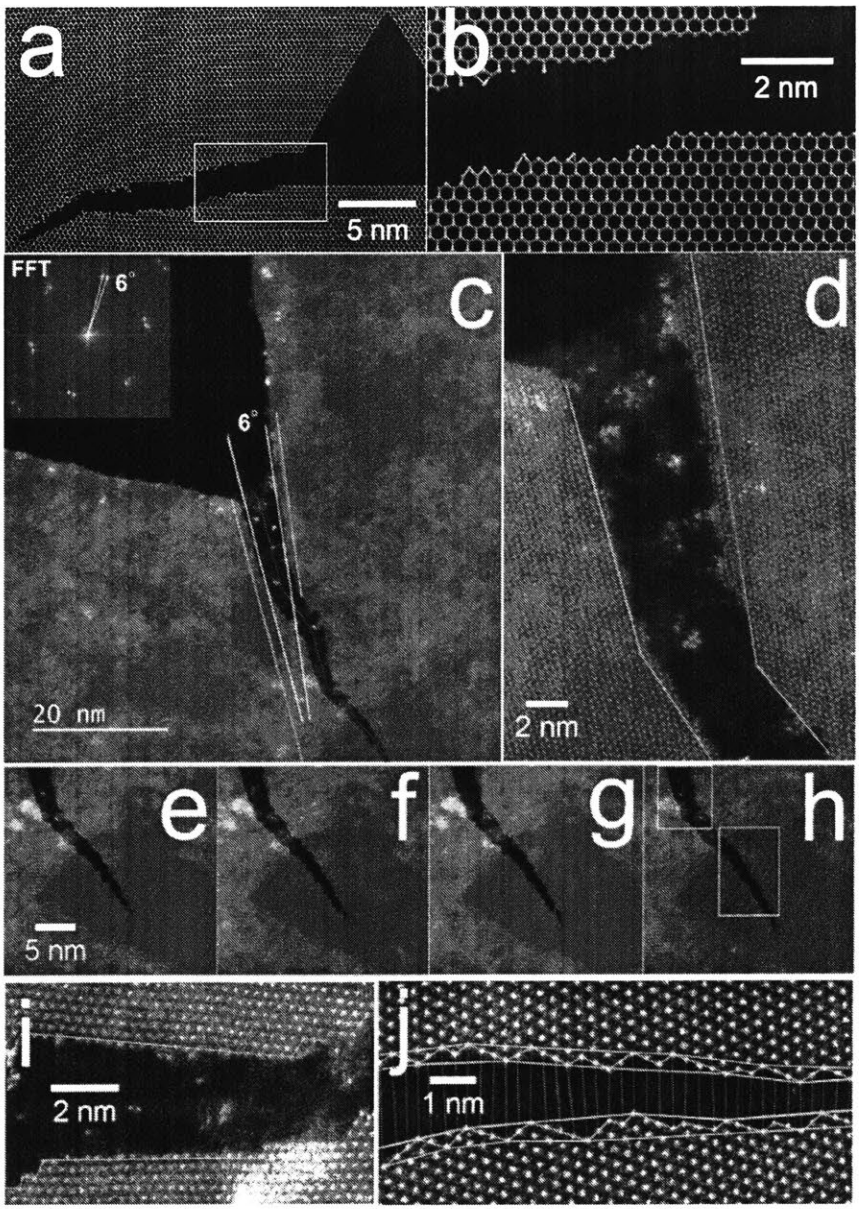

Figure 3-13: (a) Structures and dynamics of cracks emanated from the triangular voids and (b) Snapshots of atomic models for triangular faceted nanovoids in monolayer WS_2 with crack emissions. (c) ADF-STEM image of a crack emanated from the edge of a triangular nanovoid. Green lines indicate zigzag direction; red line indicates the center of crack; yellow lines indicate 6° angle. Inset shows the fast Fourier transform power spectrum (FFT) from the image with two sets of spots at 6° rotation. (d) Higher magnification ADF-STEM image of the crack mouth region (crack: void interface), green lines indicate crack edge pathways. Visible contrast in the crack region is due to residual carbon surface material from the transfer process. (e)-(h) Time series of ADF-STEM images (false color LUT), showing small-scale propagation of crack tip in the clean WS_2 region during imaging. Some surface carbon residue is also visible. (i) ADF-STEM image from the top left white boxed region in (h) showing zigzag edge terminations. (j) ADF-STEM image from the bottom right white boxed region in (h), showing zigzag sawtooth edge terminations. Green lines indicate boundary region of sawtooth oscillations, and white lines indicate edge atoms and their connecting lattice lines on the other side of the crack.

from the residual strains, and no more driving force is left for large-scale movement. However, there was sufficient small residual strain energy left when coupled with the electron beam to observe slow progress and track the atomic level reconstruction. Figure 3-13(i), shows the crack edge structure in the middle region, the top white box in Figure 3-13(h), and shows zigzag edges that are smooth and uniform. However, the part closer to the crack tip, Figure 3-13(j), from the bottom white box in Figure 3-13(h), has significantly different direction and edge termination. The direction of the crack in Figure 3-13(j) is non-crystallographic, and the edges adopt a sawtooth structure with zigzag terminations. The green lines in Figure 3-13(j), indicate the terracing width of the sawtooth edges, showing they are typically 1-2 atoms deep. The actual size of each sawtooth is between 1-4 atoms of W.

Propagation anisotropy

Notably, straight crack propagation along the armchair directions are observed in both ADF-STEM and MD simulations while we mainly found the zigzag patterns in the previous study. We further investigate the mechanisms that make the distinct patterns with MD simulations. For simplicity, we define the directions of crack propagations from the hexagonal unit lattice vectors a and b (Figure B-10(a)) as $V_Z = a$ (along with the zigzag direction, [100]) and $V_A = a+b$ (along with the armchair direction, [110]). We only distinguish the directions V_A and $-V_A$, but do not differentiate between V_Z and $-V_Z$. Also, we define the loading directions in the x and y direction (Figure B-10(b)) as 'zz' (zigzag) and 'ac' (armchair), respectively to distinguish the crack directions and the loading directions. The different fracture patterns can be identified with the defined crack directions, and MD simulations show that local strains affect the fracture patterns in Figure B-11. We find that cracks with different directions (V_A and $-V_A$) generated from different triangular vertices show different behaviors even under the same loading in the x direction are shown in Figure 3-14(a) and (f). Our results indicate that the atom type at the crack tip determines the next bond breaking after a bond at the crack tips breaks in Figure 3-14(c) and (h). In the V_A crack direction, the W-S bond along the zigzag direction is more elongated and

breaks in Figure 3-14(d) and (e). The crack propagates more, and it redirects in the 60° to another zigzag lattice direction due to the applied strain in the x direction. Alternating the redirections leaves entirely zigzag traces behind. On the other hand, the W-S bond along the armchair direction is more stretched and therefore the crack straightly propagates with the $-V_A$ crack direction in Figure 3-14(i) and (j). The different deformation between W and S atoms is a key to understand the propagation anisotropy based on the coordination number around the W atom at the tip. When the W atom loses two S atoms by bond breaking, the coordination number changes from six to four, which results in the softening of the angular stiffness between W-S bonds. The W atom at the crack tip with the V_A crack direction (circled in Figure 3-14(c)) becomes more deformable and protects the closest bond from breaking. Instead, the coordination number of the S atom changes only from three to two and the deformation does not drastically change as the W atom. Thus, the protective role is not activated with the S atom at the crack tip with the $-V_A$ crack direction. Next, we demonstrate why the straight crack propagation along the armchair direction ($-V_A$) was not captured when electron beam popped the membrane. Figure 3-15(a) shows the stress-strain curves for triangular voids and half-circular voids with the same crack length with both V_A and $-V_A$ crack directions (Figure B-12). The crack propagation from half-circular voids also depends on the crack directions in Figure 3-15(b). The triangular voids have similar strength with both crack directions while the half-circular void with the $-V_A$ crack direction has higher strengths than that with the V_A crack direction. The difference comes again from the different atomic-scale deformation between W and S atoms in Figure 3-15(c) and (d). The deformation of the hexagonal unit with the S atom edge in Figure 3-15(c) is more restricted than the hexagonal unit with W atom edge in Figure 3-15(d) as the same reason we discuss in the previous section. The W atoms with the lower coordination number allow more strain, $\epsilon_{xx} = 0.105$ $(-V_A) > \epsilon_{xx} = 0.085$ (V_A), which results in a higher strength but the same stiffness. Therefore, we conclude that generating a hole in a tensioned membrane is more likely to allow crack propagation in the V_A direction so that the zigzag crack edges were mostly observed from generating a hole in the

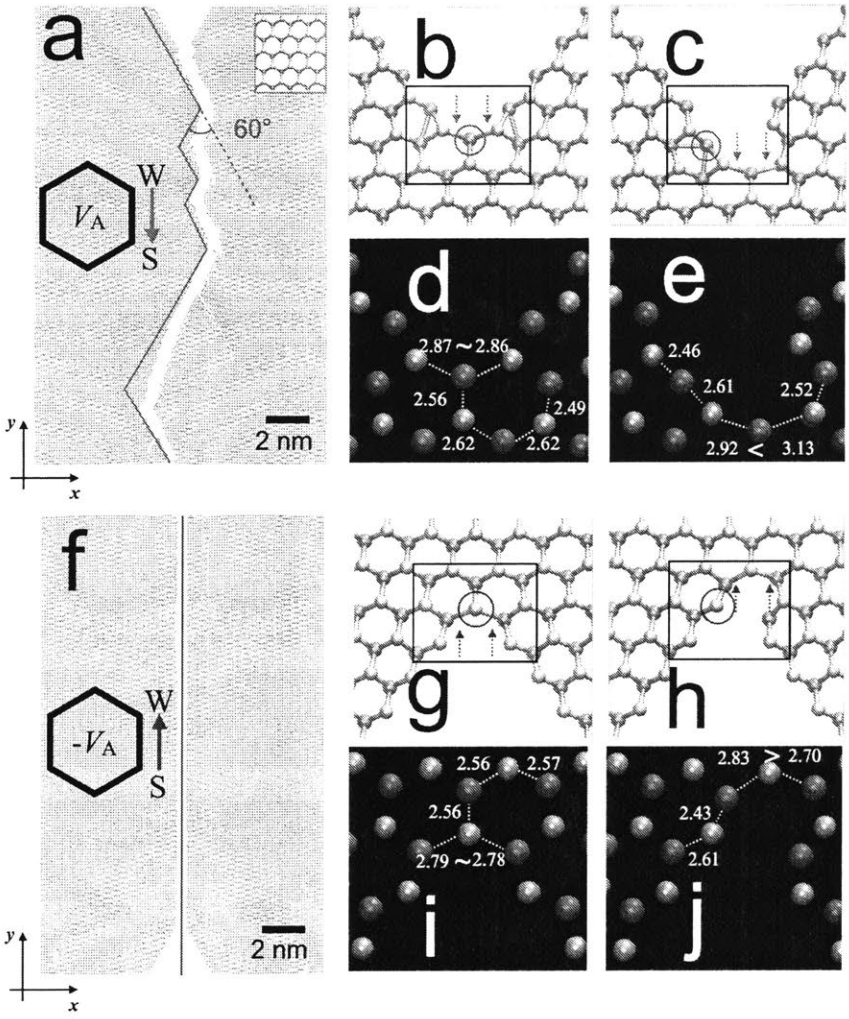

Figure 3-14: Zigzag and straight crack propagation along the armchair lattice directions (a) Crack propagation in the V_A direction from a triangular nanovoid under the tensile loading in the x (the zz loading direction). (b), (c) Snapshots near the crack tip before and after a bond break in the V_A direction. (d), (e) the lengths of W-S bonds near the crack tip. (f) Crack propagation in the $-V_A$ direction from a triangular nanovoid (g), (h) Snapshots near the crack tip before and after a bond break in the $-V_A$ direction. (i), (j) the lengths (Å) of W-S bonds near the crack tips.

membrane.

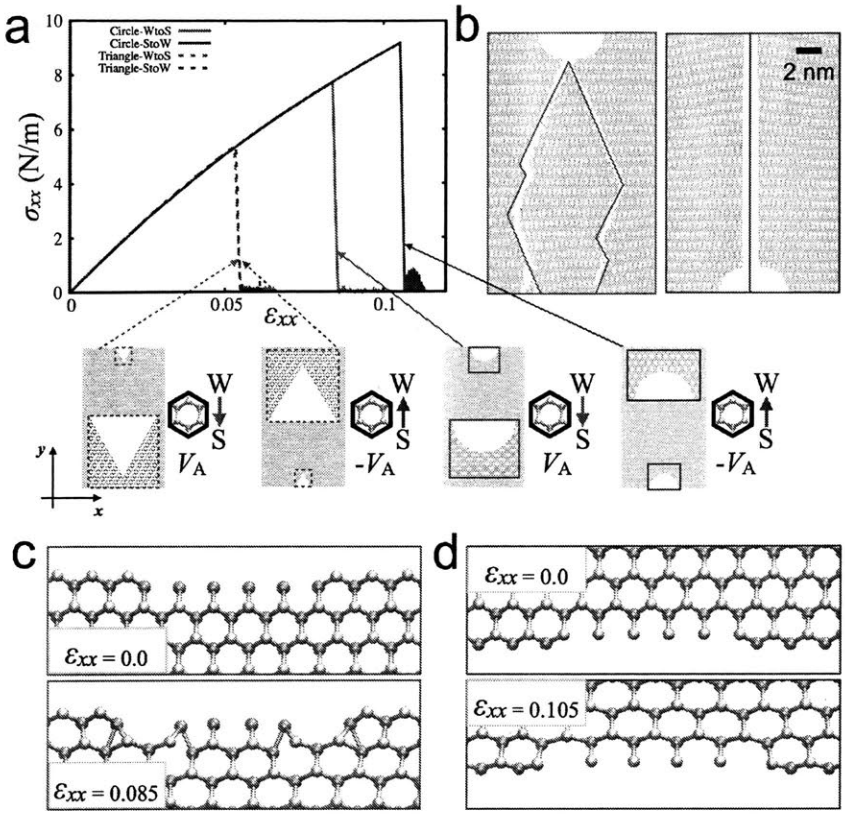

Figure 3-15: Strengths and dynamic fractures from different void shapes (a) Stress-strain curves along of WS_2 monolayer with triangular and half-circular cracks under the tensile loading in the zz (x) direction. (b) Snapshots of fracture patterns from half-circular cracks after crack propagated. (c)-(d) Different deformation between W and S atoms atom at the crack tip. The W atoms allow higher critical strains than the S atoms.

Slow process of crack propagation and dislocation

Upon ADF-STEM imaging, we did observe the small-scale movement of cracks, from 2 to 5 nm over an imaging time of 20-30 minutes typically. Figure 3-16(a)-(d) shows a series of ADF-STEM images from the first image captured of the crack tip, and then imaging every 20 seconds. The crack tip has bridging atoms across it, Figure 3-16(a)-(c), that are sputtered out by the electron beam and cause opening of the crack tip and allow it to reach atomic sharpness in Figure 3-16(d). The frame-by-frame details

of this process are displayed in more detail in Figure 3-16(e)-(h). In Figure 3-16(a), the bridging atom (orange circle) pushes the atoms above and below further apart, and this opens the gap to create the dislocation and establishes a crack tip with a certain angle. Without the bridging atom, the strain would instead be distributed to W-S bonds at the crack tip. The green line indicates the local dislocation region, and the white dots indicate the positions of where W atoms should be for perfect re-stitching, and the blue dots indicate current W positions in the crack area. Red lines show where W atoms should move to for re-stitching. By the next frame, Figure 3-16(f), the top bridging atom is lost, and only one remains, indicated with blue solid dot and green circle. Within the local crack tip region in Figure 3-16(f), there is only one vacant site, white dot green circle, matching the single extra atom that is in the bridging site, providing local W atomic number conservation. In the next frame, Figure 3-16(g), the only difference is the breaking of W-S bonds and the crack tip moving further down, before the final frame, Figure 3-16(h), where the final bridging atom is lost, and the crack opens out. At this final stage of Figure 3-16, the crack tip has propagated 7-8 atomic zigzag rows further downwards and sharped to a single atomic W-S bond. The very apex of the crack tip region shows curved sides throughout Figure 3-16(a)-(d). After reaching atomic sharpness, the next phase of the crack tip dynamics showed blunting of the tip.

Enhancement of strengths from modification of edge structures

Finally, we explore whether the unveiled atomic-scale mechanisms can be utilized to enhance the strengths of monolayer WS_2 by MD simulations. Figure 3-17(a) and (b) show the strengths of both triangular and circular voids with different sizes, R, from 1 nm to 8 nm in WS_2 monolayer (50 nm by 50 nm). The strengths of circular voids are less sensitive to the void size. Also, the stress concentration of a circular void has reduced than a triangular void in Figure 3-17(c). The results predict the strength of the circular void with $R = 50$ nm is as around 4.8 N/m, which is more than three times higher than the strength of triangular voids with the same size ($\sim$ 1.3 N/m). We also investigate the effects of the different edge terminations and shapes in Figures

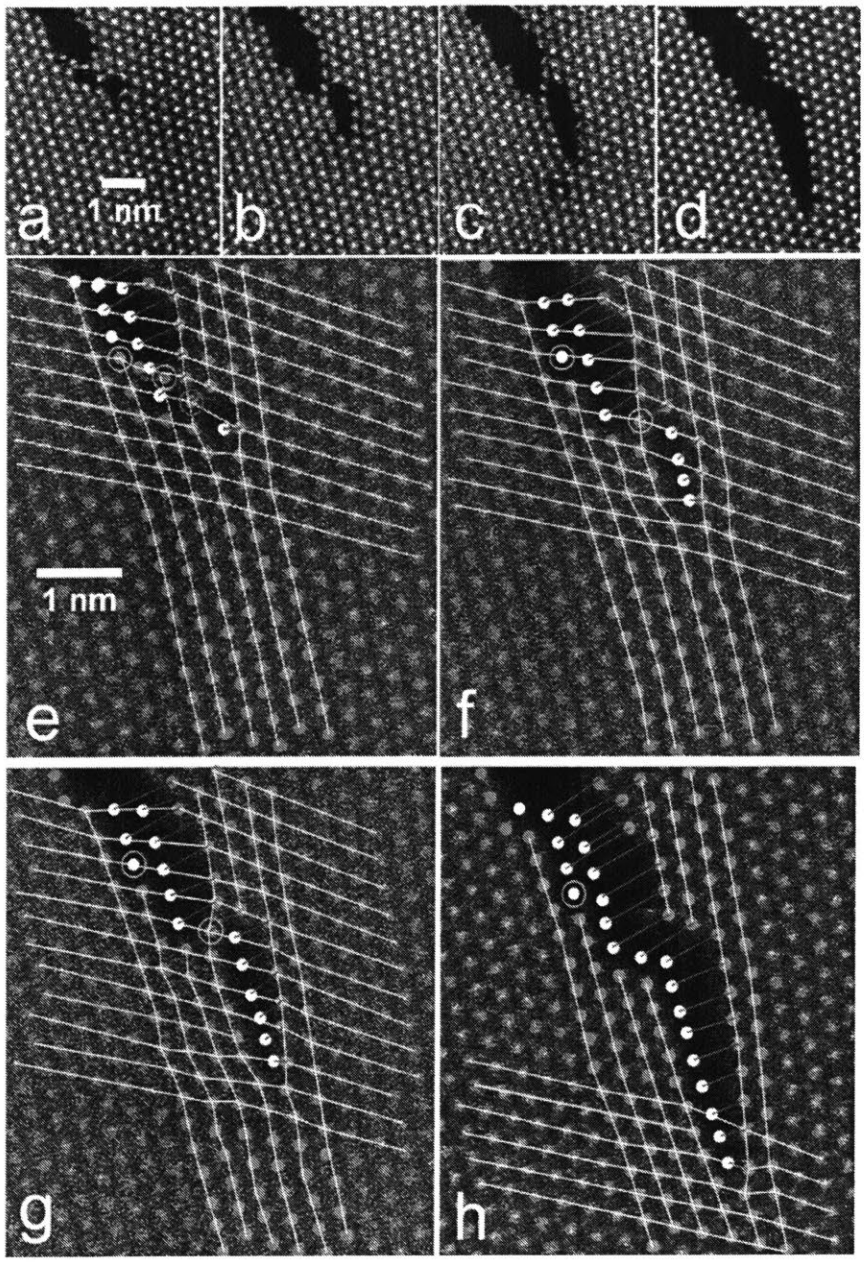

Figure 3-16: (a)-(d) Time series of ADF-STEM images showing the atomic scale propagation of the crack tip during imaging. False color LUT used. (e)-(f) Magnified views of the crack tip areas from (a)-(d) respectively.Blue dots indicate W positions. White dots indicate W positions if no crack was present, red lines show connecting W atoms to W lattice sites if no crack was present. Green lines indicate apparent local dislocation sites. (e) Two W atoms circled in green are sputtered away by the next frame. (f) Green circles indicate one W vacant site and one excess W atom that is the bridging atom. (g) Shows unzipping of W-S bonds as atomically sharp crack tip propagates. Total atom number is the same as in (f). (h) The bridging atom is sputtered away and the atomically sharp crack tip breaks further W-S bonds to propagate further and eliminate reconstructed geometry.

B-13 and B-14. The strengths of triangular voids with the S atom termination under the tensile loading in the ac and zz directions are similar, but the strengths with the W atom termination under the zz loading higher than those under the ac loading. However, the circular void shows the reversed tendency when the size, R, is larger than 4 nm in Figure 3-17(b). The different edge structures regulate this reverse transition. Unlike triangular voids, the circular void generates the edge with the W and S pairs along with the ac direction as indicated by dotted circles in Figure 3-17(d) while the other edges along with the zz direction are likely to be terminated with W or S atoms in Figure 3-15(c) and (d) (See details in Figure B-15). As the number of the W-S pair increase with the size of circles, the pairs allow more strains compared to the other edge. The classical Griffith criterion, $K_{IC} \propto \sigma_C\sqrt{R}$, works well with the data from MD simulations for triangular voids as in Figure 3-17(a) while the values of fracture toughness deviate from more accurate estimations by the finite element method (FEM) due to the geometric factor. On the other hand, the criterion fails to describe the behaviors of circular voids. We need to assume that the discretized atomic positions play as a small crack with the circular voids based on Lukás' model [83, 84] (See 2.3.2). The obtained fracture toughness from triangular to circular voids increases by approximately 30% and 50% in the ac and zz directions, respectively.

3.4.4 Conclusions

The excellent agreement of fracture patterns between the models and STEM observation strongly supports the unveiled the governing mechanism for the propagation anisotropy. Conventional conditions from fracture mechanics such as surface energy, lattice geometries, and elasticity cannot account for the observation because this kind of anisotropy has not been considered as a parameter in traditional theories. The atomic deformation mechanism is entirely different from those of previous studies. The propagation anisotropy of silicon is explained with bond or lattice trapping because of the different two-dimensional arrangement in front of the crack tip, coming from three-dimensional structures by rotation around the axis of the cleavage plane. Thus, cracks on the same cleavage surface (110) with [001] and $[1\bar{1}0]$ crack

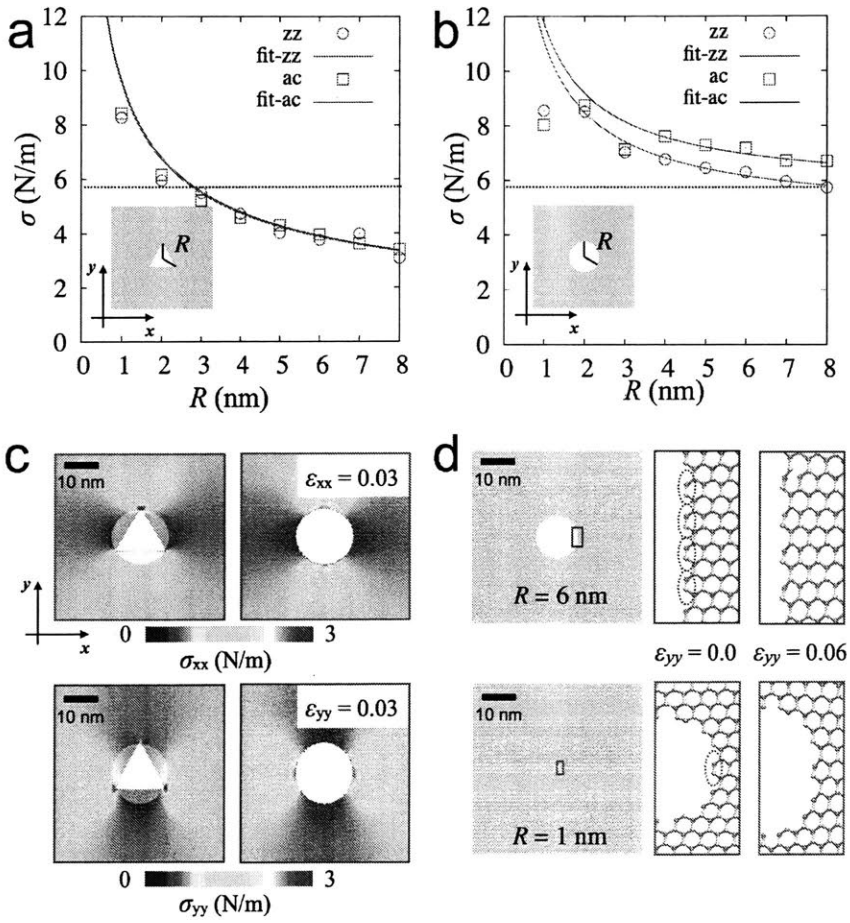

Figure 3-17: Enhancement of strengths by introducing circular voids (a)-(b) Strengths of WS_2 monolayer with triangular and circular voids under the loadings in both armchair and zigzag directions with the plane strain conditions. The obtained values are fitted for the equations from the linear elastic fracture mechanics. (c) The atomic stress distributions of triangular and circular voids under the same strain in both the x (along with the zigzag, top) and the y direction (along with the armchair, bottom). We remove the circular regions in the left panels and relaxed the structures, which results in reduced stress concentration with the hole shown in the right panels. (d) Snapshots with different strains, $\epsilon_{yy} = 0$ and 0.06. There are W atoms with coordination number four in a circled pair. As the number of the W-S pair increase, the pairs allow more strain compared to the other edge, especially terminated with S atoms is restricted to be deformed.

directions experience different bond stretching under the tensile loading, which results in different fracture toughness [127]. On the other hand, the lattice structure of WS_2 monolayer in front of both crack tips (V_A and $-V_A$) is hexagonal, and the propagation anisotropy does not show different failure strengths as in Figure 3-15(a). Another example, potassium bichromate, has alternating AB layered structures along (001) direction. Different cleavage directions, [100] and [$\bar{1}$00], invert termination of surfaces from the layered system where the separated surface is regulated by the P symmetry with the inversion center in the middle of the A and B layers [129, 135].

The fast fracture process from triangular voids of WS_2 monolayer by residual strains during the transferring or handling samples is likely to be brittle while the slow process of crack propagation shows some ductile behaviors such as dislocation movement and crack blunting. As the crack propagates by exhausting the residual strain energy, the alternating paths between $-V_A$ and V_Z are more frequently observed, which can be related to the low-speed crack instability observed in silicon. Reconstruction of crack tip structures with bridging atoms or rotating S atoms at the crack tip requires lower energy than simultaneously breaking two W-S bonds. The atomic simulation shows S atoms at the crack tip more likely to be rotated to open the crack tip wide as the crack close to the fixed boundaries, allowing opportunities to alternate the crack directions. The alternation causes sawtooth edges in Figure 3-13(j).

The simulations results expands current knowledge of the effects coming from the atomic deformation on crack propagation, propagation anisotropy, low-speed crack instability, and bond trapping, which is of great importance for understanding fracture mechanics and improving the strength of materials.

Chapter 4

Grain Boundary and Heterostructures

4.1 Introduction

This Chapter represents the study of polycrystals, grain boundary, and lateral heterostructures of 2D materials. The first section introduces models of polycrystalline graphene with different grain sizes, extensively examining the relation between grain sizes and fracture toughness. The second part shows that atomically sharp dual grain boundary of WS_2 bilayer. The accurate structures are identified by comparing MD simulations and ADF-STEM images. Also, mechanical stability is investigated by MD simulations. The last section reveals the atomic scale mechanism of 1D MoS_2 channel growth embedded in WSe_2 by unveiling the role of the catalytic 5|7 dislocation located along MoS_2-WSe_2 heterojunction. Density functional theory reveals the electronic band structures of the heterostructures. The works presented here are the collaboration with Jamie H. Warner group in Oxford University and David A. Muller Group in Cornell University based on the published articles [31, 36] and unpublished one (ACS Nano, *in revision*).

4.2 Fracture toughness of polycrystalline graphene

4.2.1 Introduction

Graphene is an ultrathin material composed of only a single layer of carbon atoms. Pristine graphene represents the strongest tensile strength of 130 GPa [7], making it ideal for applications under extreme mechanical, thermal and electronically conditions with exceptional performance [7, 136]. For example, it can be imbedded in matrix materials for enhanced mechanical strength and thermal and electrical conductivity [137]. It is critical to precisely measure its strength before using it in applications. Comparing to mechanical exfoliation of graphene, which provides small flakes during peeling, chemical vapor deposition (CVD) is a much more promising technique for large-scale production [5]. However, graphene produced by this means is polycrystalline, having pentagon-heptagon defects distributed along the grain boundary as well as different chirality for neighboring grains [138], as illustrated in Figure 4-1 (a) and (b). Those defects may cause stress concentration, initiate crack propagation and weaken the material strength [139, 140]. Yet it is also known that the existence of a grain boundary may influence the movement of crack and enhance the fracture toughness. It is intriguing how the fracture properties of graphene can be affected by the different geometries of grain boundaries.

Former studies mainly have been focused on the strength of a single graphene grain boundary [139]. Theoretical and computational studies have found that the strength is affected by the arrangement of defects, and it can have values as low as 33 GPa. The results of indenting tests show that the strength of a well stitched polycrystalline graphene consistently exhibits high values above 90 GPa, which is slightly smaller than that of the pristine graphene but much larger than the prediction of the strength of polycrystalline graphenes [140]. These results suggest that the weak grain boundary does not have a significant effect on the fracture strength of a large piece of graphene. This finding is aligned with what is observed in several biological materials, such as nacre and bone, which are composed of mineral plates and weak interfacial protein materials but have high fracture toughness [141, 142].

Modeling of polycrystalline graphene and systematic analysis of how its strength and toughness alter with its geometry are crucial to understand its failure mechanism under extreme loading conditions. Based on the high-resolution transmission electron microscopy data, the shapes of grains are generally irregular, and the defects are mainly 5-7 ring pairs to reduce the total energy and the tensions of defects [100]. However, previously suggested models are limited to mimic the geometry revealed by experiments because the model has limited shape of regular grains or the grain boundaries have numerous voids with irregular grains [139, 101]. In this work, we report an innovative algorithm that is applied to generate well-stitched polycrystalline graphene with any grain shape and any grain orientation, showing mainly 5-7 ring pairs without any voids.

In polycrystalline metals, the grain size plays a key role in their strength [143]. It is also reported that the strength of polycrystalline graphene depends on its grain size in MD simulation [139, 101]. However, since defects generally exist in polycrystalline graphene, its fracture toughness is more critical for the applications and the mechanical strength measurement in experiments [144]. It is not understood how grain size and geometry affect the fracture toughness of polycrystalline graphene. Although some experiments have measured the fracture toughness of polycrystalline graphene, their experimental samples are not well characterized for grain size. Thus, the results provide a range of fracture toughness values, making the dependence of fracture toughness on grain size still elusive [145]. The knowledge of the fracture toughness is vital for the application of CVD to generate graphene with reliable mechanical performance as the grain sizes are sensitive to the growing conditions [138].

4.2.2 Methods

To understand the mechanical effect on grain boundary in graphene, it is crucial to obtain a fully equilibrated structure that mimics the grain boundaries obtained in CVD experiments. Here, a method is developed to generate an entire piece of graphene sample composed of multiple grains. This method allows us to control the shape, size and crystal orientation of each grain and it automatically reconstructs

the boundary by removing and adding atoms. Since the models of polycrystalline graphene in previous studies have voids and considerable non-pentagon-heptagon defects [101, 88], our algorithm works well to generate with lower number of non 5 and 7 ring defects. By using the method, any two neighboring grains of different crystal orientations are always connected by a lattice that includes mainly pentagon, hexagon and heptagon, and a small number of octagon rings (under 0.2% in average) without any other defects or voids. The polycrystalline graphene models are generated with

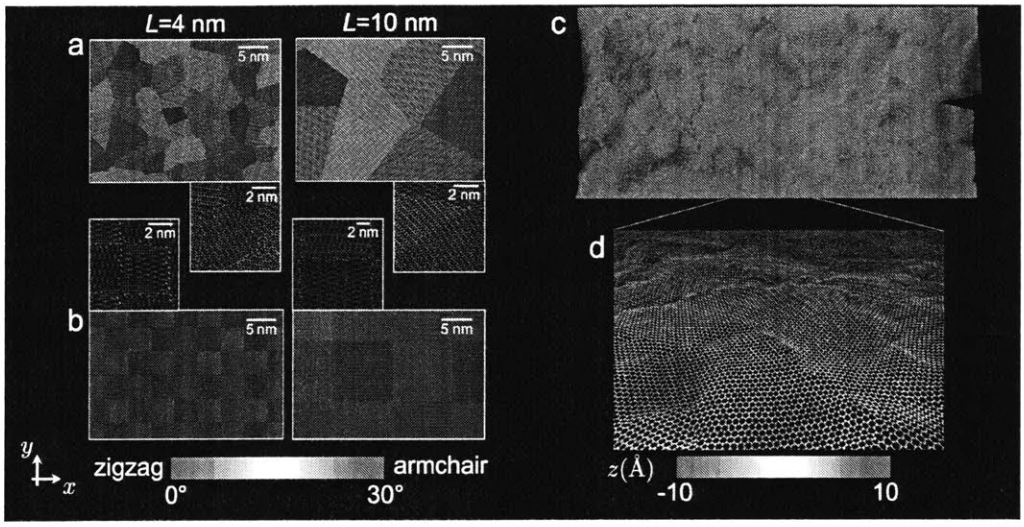

Figure 4-1: Geometry of rectangular and random polycrystalline graphenes; grain boundaries are generated by Voronoi tessellation, and reconstructed based on the coordinate numbers of atoms at boundaries. Colors represent the chiral angle of graphene at the center of the initial grains from 0 (zigzag) to 30 (armchair). The filled rings in the smaller box show the pentagon defects at grain boundaries. The pentagon defects exist with heptagon defects to compensate for their stress. After a sharp crack is inserted, the system is relaxed. The relaxed structures have the out-of-plane deformation due to the defects (c, d).

regular grain (Model RegG) and irregular grain (Model IrreG) shapes with different characteristic sizes as shown in Figure 4-1 (a) and (b). These models are demonstrated to be stable as shown in Figure 4-1(c) and (d). Moreover, the out-of-plane deformation near the grain boundary is distinct after structure relaxation. As shown in previous studies [100, 146, 134, 147], this deformation at the grain boundary is the nature of polycrystalline graphene.

4.2.3 Results and Discussions

Using the polycrystalline graphene models, MD simulation is performed to measure the fracture toughness of the polycrystalline graphene as a function of the grain size, as shown in Figure 4-2. The polycrystalline graphenes show larger energy release rates than that of the pristine graphene. Interestingly, the energy release rate increases as the grain size decreases. This trend is clear for both the Model RegG and Model IrreG, as shown in Figure 4-2(b) and (c). The obtained fracture toughness ranges from K_{IC}=3.1$\sim$4.5 MPa m$^{1/2}$, and these results show good agreement with the results of the recent experiment, K_{IC}=4.0 ($\pm$0.6) MPa m$^{1/2}$ by Zhang *et al.* [145]. They performed MD simulations with pristine graphene and obtained the energy release rate as G_C=11.8$\sim$12.5 Jm^{-2} from the Griffith equation [145, 81] :

$$G_C(2\gamma) = \frac{\sigma_C^2 \pi a_0}{E}, \tag{4.1}$$

where σ_C, a_0 and E are the critical stress of the fracture, half of the central crack length and Young's modulus, respectively. This result is consistent with our result of pristine graphene (G_C = 10.3$\sim$12.4 Jm^{-2}). However, the value is still lower than their experimental results (G_C=16 $\pm$ 4.5 Jm^{-2}) and, as they mentioned, the discrepancy comes from not considering polycrystalline structures or crack deflection. Here, our results are important and counterintuitive. They suggest that the fracture toughness of polycrystalline graphene is larger than that of pristine graphene. Also, they explain that the wide distribution of the experimental measurement comes from the polycrystalline grains. The external work is slightly underestimated because of the cut-off of the force field.

We further explore the mechanism of the higher energy release rate of polycrystalline graphene by looking into the stress distribution in front of the crack tip. Figure 4-3a shows the atomic stress distributions of pristine graphenes and Model IrreGs before fracture. The stress-strain curve for each of model under loading is shown in Figure 4-3(b), and highlight the point where each snapshot in Figure 4-3(a) is taken. It is shown that the multiple grain boundaries near the crack tip help to distribute the

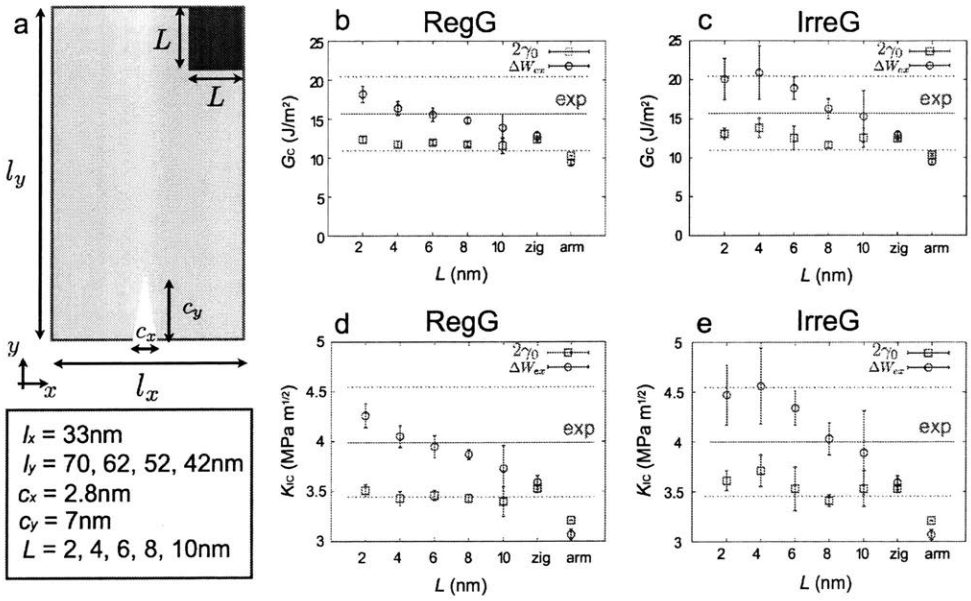

Figure 4-2: (a) Parameters of our models and simulation results. The energy release rates (b, c), and fracture toughness (d, e) of Model RegGs and Model IrreGs as a function of grain size (L). The energy release rates and fracture toughness are calculated by the total external work (ΔW_{ex}) and the surface energy ($2\gamma_0$). The error bars are obtained from the different system lengths (l_y) and the initial crack tip position.

stress, making a larger area of material in deformation instead of highly concentrated at the crack tip. We statistically analyze the distribution of the atomic stress (Figure 4-3(c)) at the critical loading points and it clearly shows that the stress distribution in polycrystalline graphene is much broader and atoms of maximum stress carry more stress (by 10~20%) than the atoms in the pristine graphene. Such stress distribution explains the higher critical loading stress (by 25%) before crack propagation (Figure 4-3(b)). The complex stress distribution in the polycrystalline graphene also makes cracks difficult to propagate, as many of them get arrested after the propagation is initiated, as shown in Figure 4-3(a) and (b). Using the simulation tool, it is possible

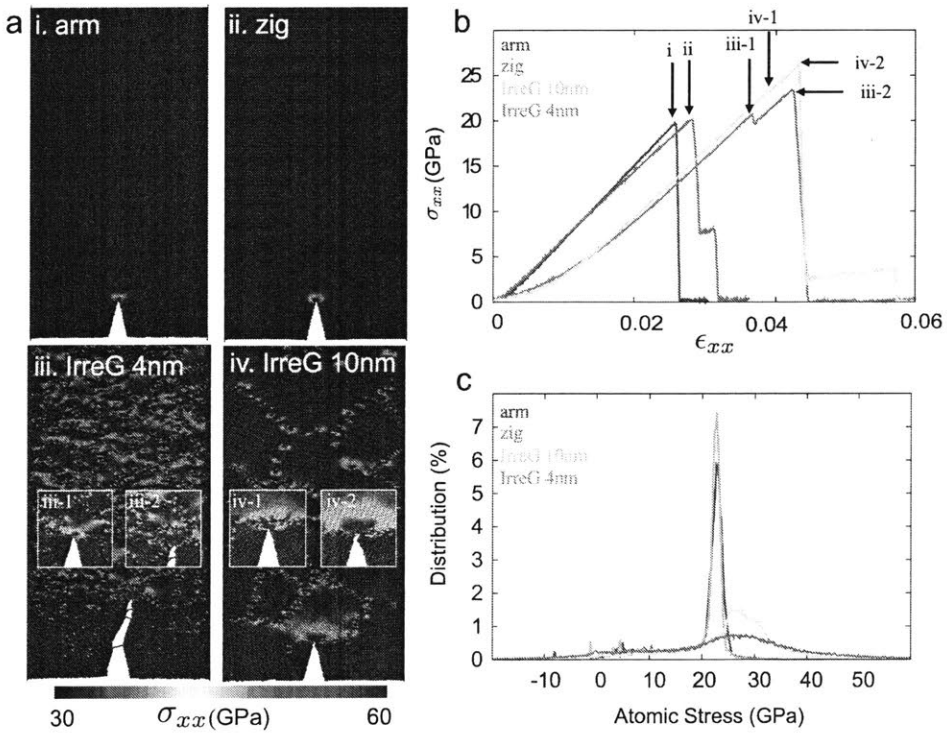

Figure 4-3: Stress distributions and stress-strain curves of pristine graphene and polycrystalline graphene. The stress distributions of polycrystalline graphene are not localized like that of pristine graphene. In order to visualize the difference, we choose the stress range from 30 to 60 GPa. Typically the atomic stress distribution at the fracture point ranges from -70 to 130 GPa. The distribution of atomic stress is calculated at the point before the final fracture by counting the number of atoms at each bin (bin size = 0.2 GPa) and normalized by the total number of atoms.

to follow the crack tip and investigate the effect of grain boundary on crack propaga-

tion. Figure 4-4 summarizes a series of snapshots taken close to the region near the crack tip. With each atom colored by its atomic potential energy, it is more clearly shown how deformation energy is dissipated. Several bonds of defects near the crack tip break (at ϵ=5.4%) and some of them develop into several branches (at ϵ=5.41%), and one of them actually becomes a new crack path (at ϵ=5.42%). Since making branches of cracks and breaking bonds requires more energy, the energy release rate becomes greater in the polycrystalline graphene. Some bonds of branches recovered after crack propagation, and the recovered bonds' energy is not shown in the surface energy ($2\gamma_0$) but in the external work (ΔW_{ex}). Last, the out-of-plane deformation

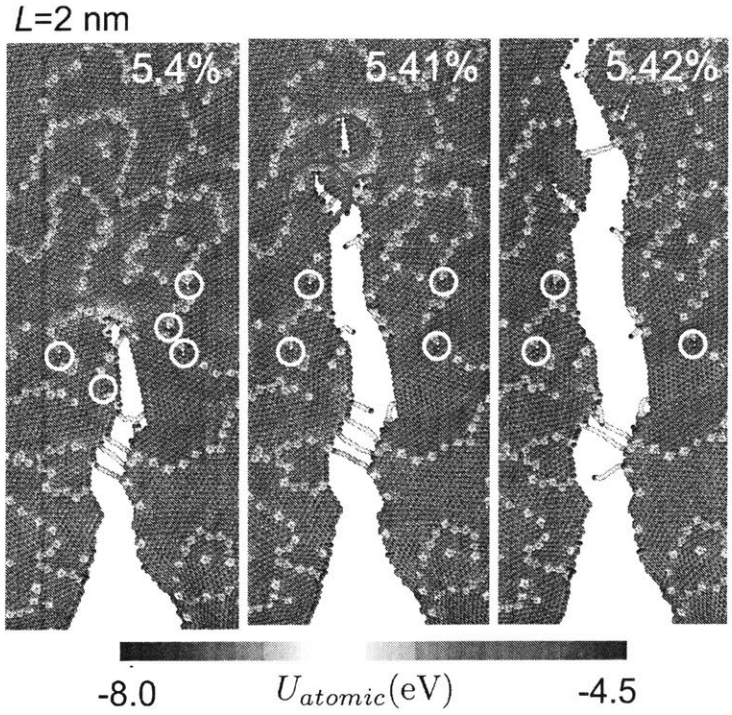

Figure 4-4: Atomic energy distribution of Model IrreG as the crack propagates. Since the pentagon-heptagon defects break easier than the hexagon ring, several bonds of the defects break near the crack tip. Several branches of crack tips are generated from the bond breaking. Some of them remain, others are recovered, and one of them develops to the final crack path. The recovered bonds energy is not shown in the surface energy ($2\gamma_0$) but it is shown in the external work (ΔW_{ex}) before catastrophic failure.

due to the defects plays a key role in governing the enhancing mechanism. In the initial stage of stretching, there is a softened region of polycrystalline graphene (Figure

4-3(b)) as the previous studies reported [145, 88]. The stress-strain curve becomes linear after the deformation is fully stretched. In order to find the role of this out-of-plane deformation, we test several samples with the same conditions except constraint on the movement in the z direction. The results show that the energy release rates of most polycrystalline samples drop to the level of those of the pristine graphene (G_C=12$\sim$14 Jm^{-2})). Figure 4-5 shows how the stress-strain curve is changed when the movement in the z direction is not allowed. The maximum stress decreases by 18%, and the energy release rate decreases by 40%. The shape of stress-strain curve and stress distribution lose their characteristics of polycrystalline graphenes. Interestingly, the enhancing mechanism is not fully activated without the free movement of the deformation although the other conditions are fully met. The strength of polycrystalline metals increases as the grain size decreases, which is known as the Hall-Petch effect. The effect mainly comes from less mobile dislocation in the small grains [143]. Since graphene is typically a brittle material without significant plastic deformation, it is intriguing that the behavior of fracture toughness of polycrystalline graphene as a function of grain size shows similar trends. From our simulation results, we believe that the defects form grain boundaries, and mediate tensile deformation and reduce the stress concentration near the crack tips. The mechanism is enhanced as the density of defects increases. This counterintuitive result is important as it points out that the defects at the grain edge in the polycrystalline graphene can help to dissipate more energy than those in the pristine graphene.

However, the effect showing higher critical stress in Model IrreGs does not depend on the grain size, as depicted in Figure 4-3. The variation of grain areas and the specific geometry appears to be more important and has a higher critical stress than the averaged grain sizes. It could be an interesting future study to discover the role of other conditions such as the orientation of grains and area ratio between grains, and how those affect or maximize the critical stress.

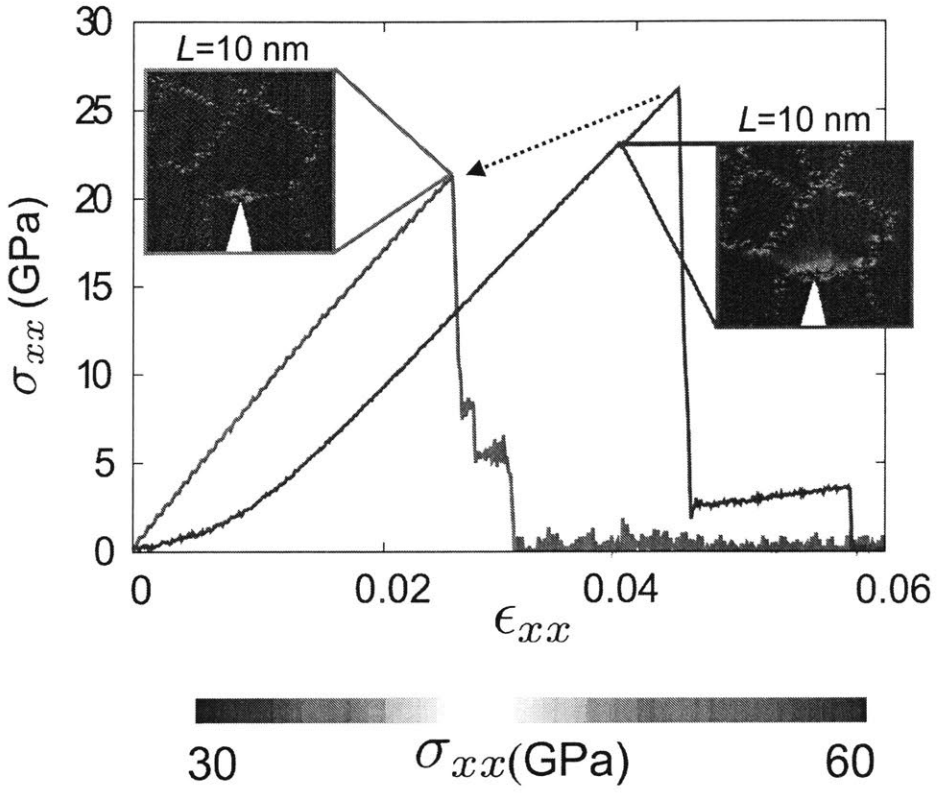

Figure 4-5: The stress-train curves of Model IrreG (10 nm) with and without the fixed movement in the z direction. The critical stress decreases by 18%, and the energy release rate decreases by 40% with the z direction restriction. The enhancing mechanism of grain boundaries does not work for reduction of stress concentration, and the stress strain behavior becomes more like that of pristine graphene in Figure 4-3(b).

4.2.4 Conclusions

Using full atomistic simulations, we investigated the fracture mechanics of polycrystalline graphene under external tensile force. Combining an innovative algorithm with classical MD simulation, we manage to systematically build the well-stitched polycrystalline graphene models with regular and irregular grain boundaries and measure their fracture toughness as a function of the mean grain size. We found that the mean grain size plays a critical role in affecting the fracture toughness of polycrystalline graphene. This result is reproduced many times in our study for both different regular and irregular grain shapes, suggesting the fracture toughness of polycrystalline graphene can have a range of values that depend on its grain size. Indeed, we found the fracture toughness of polycrystalline increases by 20% to 35% compared to that of the pristine graphene. This result is qualitatively confirmed by many recent experimental measurements of the fracture toughness of polycrystalline graphene, which revealed the same range of fracture toughness as we computed here.

Besides good agreement with experiments for the toughness result, our work theoretically reveals the toughening mechanism of polycrystalline graphene, which is distinct from the mechanism of polycrystalline metals in two ways. First, compared with pristine graphene, the polycrystalline graphene features a reduced stress concentration built up at the crack tip, which is caused by the distributed stress at the grain boundaries that involves more area of materials in deformation and less concentration. Second, the grain boundaries cause crack branches and thereby create complex pathways during crack propagation through the entire material, causing greater dissipated energy. We also identified that these two mechanisms strongly rely on the single-atom thickness of graphene, as the out-of-plane deformation significantly affects the mechanical behavior and toughness of polycrystalline graphene. A constraint of such deformation renders its mechanical behavior similar to what is observed in pristine graphene.

This study demonstrates that instead of weakening due to the defects, the existence of grain boundaries can make polycrystalline graphene tougher than pristine

graphene. Thereby, the material toughness is strongly controlled by the grain size, providing a simple theoretical rule of thumb to make reliable CVD grown graphene with predictable toughness. However, it is still not completely clear how the out-of-plane deformation, which closely relates to the nanoconfinement of polycrystalline graphene in its possible working environment, affects the stress concentration and branching behavior of crack propagation. Since the toughening mechanism may depend on the adhesion energy between graphene and its environment, the effects of the out-of-plane deformation on graphene-based composite materials such as a graphene embedded in a polymer or adhered to various substrates. A systematic investigation of these issues could be interesting topics for future work. More theoretical and experimental studies are needed to explore these aspects.

4.3 Grain boundary of TMD in monolayer and bilayer

4.3.1 Introduction

The tilt grain boundaries (GBs) in bilayer 2D crystals of the transition metal dichalcogenide WS_2 can be atomically sharp, where top and bottom layer GBs are located within sub-nm distances of each other. This expands the current knowledge of GBs in 2D bilayer crystals, beyond the established large overlapping GB types typically formed in chemical vapor deposition growth, to now include atomically sharp dual bilayer GBs. By using MD simulations and atomic-resolution annular dark-field scanning transmission electron microscopy (ADF-STEM) imaging, we distinguish different atomic structures in the dual GBs, considering bilayers with 3R (AB stacking)/2H (AA' stacking) interface as well as bilayers with 2H/2H boundaries. An *in-situ* heating holder is used in ADF-STEM and the GBs are stable to at least 800 °C, with negligible thermally induced reconstructions observed. Normal dislocation cores are seen in one WS_2 layer, but the second WS_2 layer has different dislocation structures not seen in freestanding monolayers, which have metal-rich clusters to accommodate

the stacking mismatch of 2H:3R interface. These results reveal the competition between maintaining van der Waals bilayer stacking uniformity and dislocation cores required to stitch tilted bilayer GBs together.

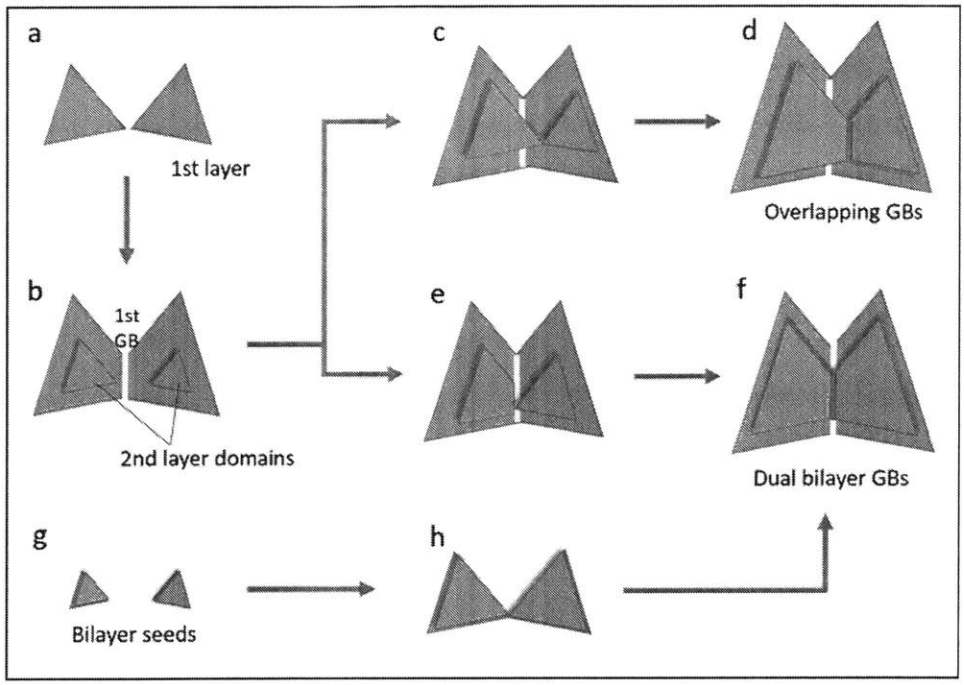

Figure 4-6: Schematic illustration of possible bilayer grain boundaries (GBs) and their different formation processes during growth.

Figure 4-6 depicts three possible configurations of the bilayer GBs in TMDs and their different formation processes during growth. In the first step (Figure 4-6(a)-(b)), a tilt GB within TMD monolayers is produced when two separate monolayer domains with tilt angle grow and meet together, as reported in many literatures before [148, 149, 150, 151]. Meanwhile, a secondary TMD domain nucleates on the top of each 1st-layer grain with crystallographic stacking (2H or 3R) in Figure 4-6(b). As the secondary seeds grow, they either form an overlapping GB (Figure 4-6 (c)-(d)), where one of the secondary layers grows across the GB and these two domains merge to form a new GB at a random place related to the seeding positions of the second layers and their growth rate. In this case, the GBs within each layer are independent to each other, and the bottom-layer GB interferes little on the growth of the secondary domains. The other possibility is the dual GBs, where the secondary domains stop

growing when they reach the location of the GB already formed in the underlying monolayer, Figure 4-6(e)-(f). Eventually both layers connect at the same site as the monolayer GB to form the dual GB. The final mechanism for dual GB formation is that two bilayer TMD domains nucleate and grow as a unified bilayer domain with constant area of top and bottom layers. When two bilayers TMD grow together from bilayer seeds and then merge together, they could also form the dual-GB, Figure 4-6 (g)-(h)-(f).

4.3.2 Methods

To investigate the mechanical stability of dual grain boundaries observed in WS_2, we perform structural relaxation and tensile tests of the geometries obtained from STEM. Unlike the monolayer system, the interlayer interaction may play a critical role in the bilayer system. The previous density functional theory (DFT) study [97] indicates that the difference of binding energy of WS_2 and MoS_2 has only 10meV/atoms with dispersion correction DFT-D and almost same with vdW-DF. Also, the interlayer distance of 2H (AA') is the same. Therefore, instead of further tuning of vdW parameters for WS_2, the vdW parameters developed for MoS_2 bilayer system is utilized, which describes well the binding energy profile as a function of the interlayer distance between two layers.

For the atomic models, the geometries is relaxed from STEM through MD simulations. During the relaxation, the boundaries are fixed because the boundaries of models with a finite size are not well bounded and can change due to residual strains coming from the mismatching lattice parameters between TEM and MD. Then, we take one of the unit cells to rebuild the systems for Type1, Type2i, and Type2ii. The model for the stepped boundary (Type 3) is just cut out with a rectangular shape for the following tensile tests. We further relax atomic structures of the rebuilt models at 10K for 150 ps with the relaxation of the periodic unit length along the y direction except for the Type 3 because the periodic boundary condition in the y direction does not apply to Type 3. Instead, we insert a space between periodic images along the y direction. The periodic boundary condition along the z direction with enough

space is applied to all models to avoid the unphysical interactions between imaginary layers. The non-periodic and shrinkable boundary is used only for the x direction. After the relaxation, one of the edges parallel to the grain boundary with the width 0.5nm is fixed. The other edge is moved with a constant loading speed with 0.02Å/ps (2m/s). The stress-strain data are recorded during the loading.

To estimate the defect formation energy, we perform DFT calculation with Quantum-Espresso package using PBE functional and norm-conserving type pseudopotential. The pristine dislocation core obtained from MD relaxation with the geometries from TEM. The energy cutoff for the wave functions is 60 Ry, and 1 x 15 x 1 Monkhost-Pack grids are adopted for the K space sampling. For modeling the isolated ribbon, 15 Å vacuum is inserted to avoid undesirable interaction between periodic images in both x and z directions. The structure is relaxed with the fixation of boundary atoms movement in x and z directions and fully relaxed along the y direction. There is residual strain due to the fixed boundary atoms, but the 4|6 dislocation and its nearest atoms are fully relaxed under a given grain boundary. The sulfur vacancies at A, B, Ref-A, and Ref-B are introduced to compare the vacancy formation energy of A and B to the nearest vacancy position. The defect formation energy (E_f) is obtained by

$$E_f(\alpha) = E_V + E_S - E_0 \tag{4.2}$$

where E_0 is the total energy of the reference system; E_V is the total energy of the system with a sulfur vacancy, E_S is the energy of isolated sulfur atom; α is vacancy type with a single sulfur vacancy. For example, A1 is the first vacancy at the position A from pristine, and A2 is the second vacancy at the position A from A1. Here, we do not consider the detailed values of chemical potentials due to S/W rich limit or temperature [152]. Instead, we compare the formation energy at A and B sites with that of the nearest sulfur vacancy position.

4.3.3 Results and Discussions

At the exposed monolayer regions where the secondary layers have not merged in Figure 4-7(a)-(f), the tilt monolayer GB structures with common dislocation cores can be distinguished, where the intersecting angle of the two films is 23.5°. The extended GB has meandering pathways rather than atomically straight lines. It has the combination of two steps with turning angles of 60°. Taking the W-zigzag direction as the reference axis, the GB mostly develops along the direction of ~20.5° and at some points have steps along the ~80.5° (20.5°+60°) direction (Figure 4-7(c)). This monolayer GB is connected by a series of dislocation cores, which can be classified to be two categories subject to the extending directions. According to the previous classification of dislocation cores in monolayer TMDs, these two types on ~20.5° and ~80.5° are sulfur-polar and metal-polar dislocations, respectively, based on two unit vectors along the zigzag node motifs. The one on ~20.5° GB is composed of four- and six-fold (4|6) rings and their variations, whose detailed atomic structures are shown in Figure 4-7(g). While the other on ~80.5° consists of five- and seven-fold rings (5|7) rings with W-W bonds. Note that all these dislocation cores are W-rich, and the 4|6 rings including the variants make up the majority in this GB (Figure 4-7(d)-(f)), as the overall GB is extending along this direction in large scale. The 4|6 metal-rich GB can be derived from 5|7 S-S defects at the metal-rich condition by removing 2S or adding metal atoms, which has been observed in MoS_2 and WS_2 monolayers [153, 154]. In particular, the 4|6 (Figure 4-7(g), I) and 4|6+V_{2S} GB (Figure 4-7 (g), II and III) are more likely to form over 5|7 S-S GB in W-rich conditions. The high concentration of W-rich dislocation cores manifests a local W-rich environment during CVD growth of this material. Figure 4-8 shows the results of DFT calculation for the sulfur vacancy formation energy at A (dislocation core II) and B (dislocation core III) sites compared to the nearest sulfur position. The results show the formation energy of A and B are both lower than the reference positions. Also, the formation of the next vacancy at the same location becomes smaller than the first one. The energy difference between 1st and 2nd vacancies with the position A (core type II) is about

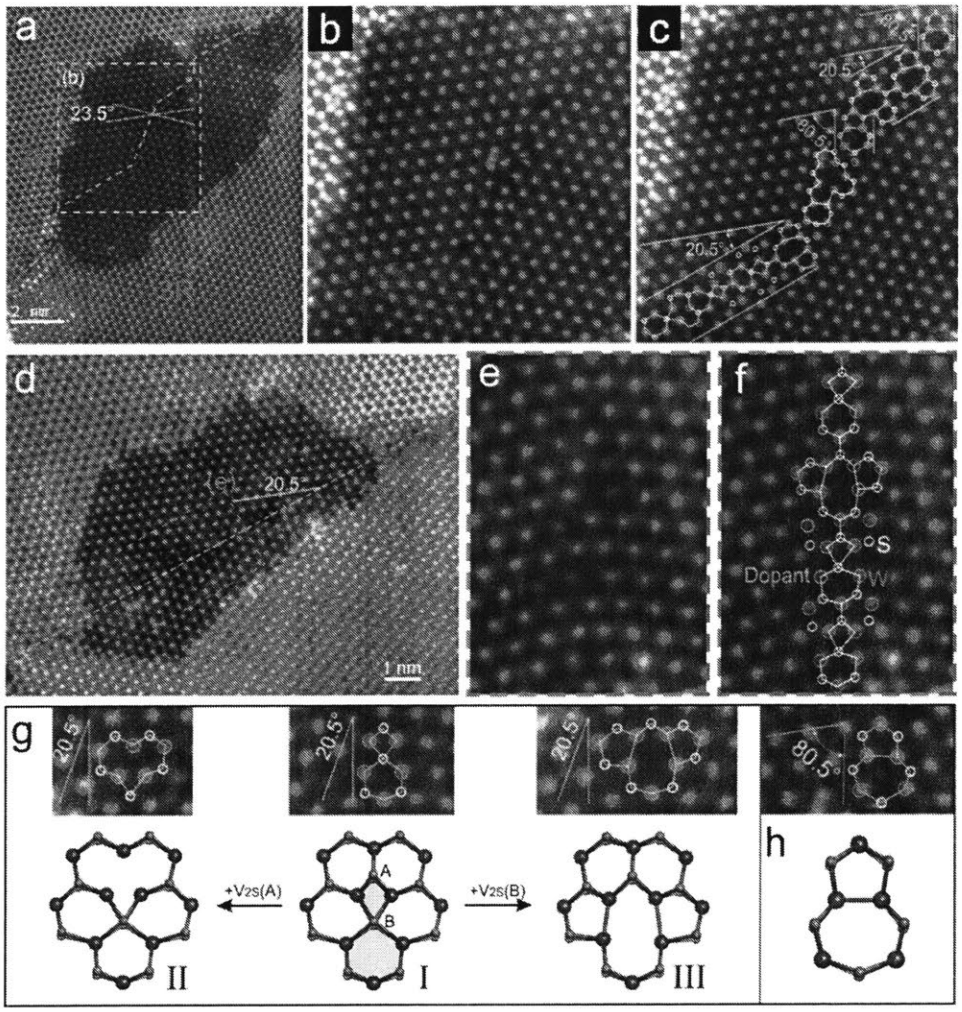

Figure 4-7: Grain boundaries (GBs) in the monolayer WS_2 region. (a) ADF-STEM showing a GB formed by two monolayer WS_2 crystal with orientations angle of 23.5°. (b) Enlarged view of the boxed region in (a), with (c) overlaid by atomic models of W (orange) and 2S (yellow) atoms showing the GB connected by dislocation cores structure. (d) Another GB formed in monolayer WS_2 area. (e) Enlarged view of the boxed region in (d), with (f) overlaid by atomic models showing the GB connected by dislocation cores structure. (g, h) Two categories of dislocation cores in monolayer WS_2 GBs

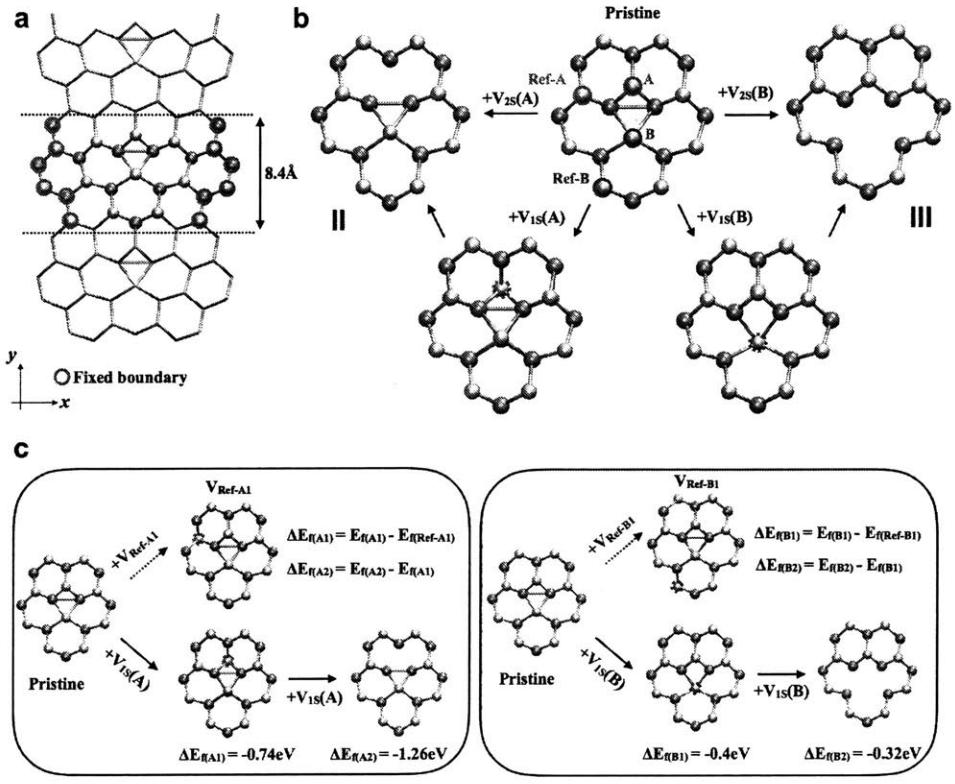

Figure 4-8: DFT calculation for defect formation energy (a) Unit cell (25Å x 8.4Å x 15Å) of the grain boundary with a dislocation core, the red-circled atoms are fixed in both x and z direction. (b) Schematic of dislocation core and its derivatives by introducing sulfur vacancies. The atomic geometries obtained from the structural relaxation through DFT calculations (c) The defect formation energy of type II and III, compared to the nearest sulfur vacancy (V_{Ref-A1} or V_{Ref-B1}). The defect formation energy of II and III are lower than that from the hexagonal lattices. Once, the monovacancy forms at A or B position, the second sulfur vacancy becomes easier to form.

1.3eV while the difference is not such significant about 0.3eV with the position B (core type III). Interestingly, Ref-A and Ref-B also show the difference between the 1st and 2nd vacancy formation energy about 1.3eV, indicating that the sulfur divacancy at the same position is likely to form near the grain boundary. More importantly, the grain boundary is the location of stress concentration. Once the sulfur is lost at the dislocation core, the other sulfur is under severe atomic stress and deformation compared to the other regions having both sulfurs, which can be another reason for the predominant divacancy observation in TEM. In this specific example of a bilayer dual GB area, we did not find overlaying GB sections or any The dual GB, Figure 4-9, shows specific periodic contrast features, in particular 6-member half-rings, similar to the stacked GB region. The dual GB structure has different atomic configurations along the nanoscale meandering pathway (Figure 4-9 (b)), so we classify them into type 1 and type 2 (i and ii), according to the atoms from which stacking (3R or 2H) taking the dominance. Type 1 dual GB (Figure 4-9 (c)) has the 6-member half-rings, due to alternating W atoms from the two layers (Figure 4-9(f)). The other type of dual GBs including two configurations, type 2i (Figure 4-9 (d)) and type 2ii (Figure 4-9 (e)), are 2H dominated, which means the structures are mainly 2H stacked at the bilayer GB region. Figures 4-10, C-1, and C-2 show rebuilt MD models and the results of tensile tests. The marked atomic positions of the models after relaxation show good agreement with those from TEM while some other bonds and angles are more relaxed in MD simulations. Under the tensile loading, the crack nucleation and propagation occur along the grain boundaries. There are several stages of stress-strain curves with drops caused by breaking atomic bonds in the 1st or 2nd layers. Before the catastrophic failure, the atomic bonds in the defects at the grain boundary fail first. The detailed information of the bonds is described in the figures. Overall, the 2nd layer completely breaks at the strain around 8% and the 1st layer holds the loading slightly longer with the strain around 9%. Only the 2nd layer of type I can elongate as much as the other layer due to the split sulfur atoms. It is intriguing to see how the dislocation cores deform or fail during the loading. The dislocation core I, II and III in Figure 4-8 are in the grain boundary of the 1st layer in Type 1, Type 2ii, and

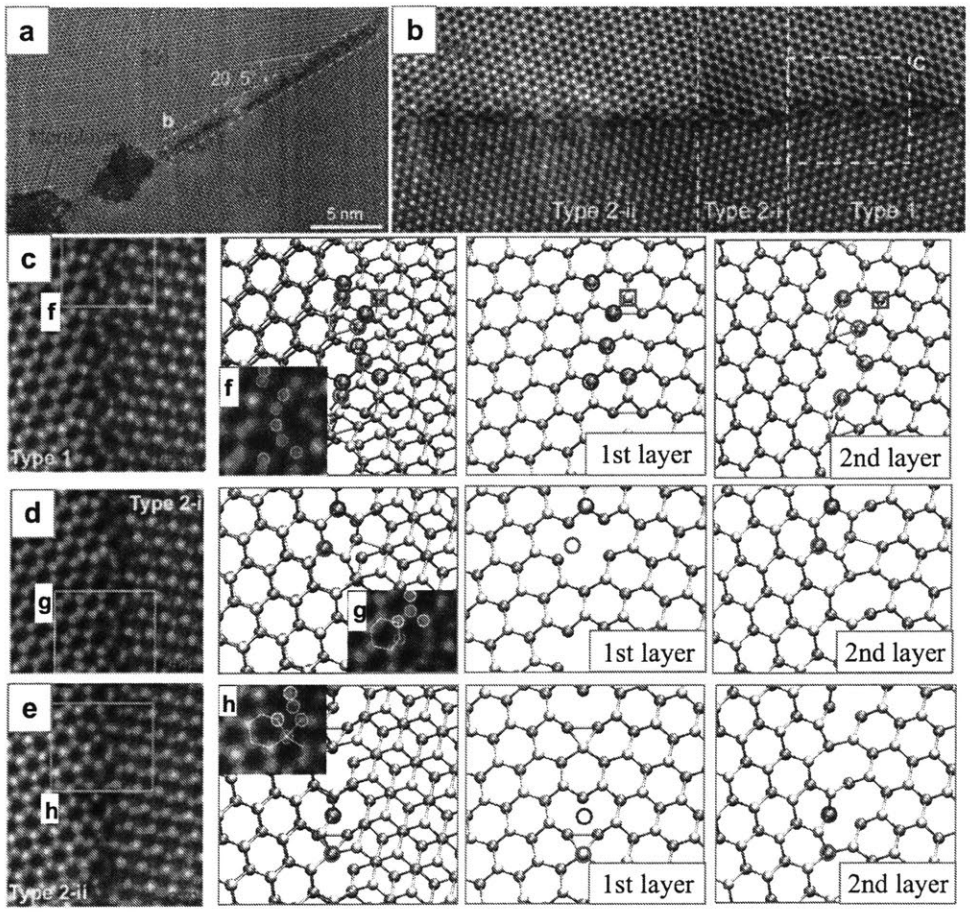

Figure 4-9: Dual GBs in the bilayer WS_2 region. (a) ADF-STEM showing the GB formed by two bilayer WS_2 crystal with different stacking registries (2H and 3R) and tilt angle. (b) Enlarged view of the dual bilayer GB highlighted in (a), showing three different configurations (type 1, type2i/ii). (c) Enlarged view of the yellow boxed region in (b) showing the periodic semicircle structure at the GB (Type 1). (d) Type 2i GB, (e) Type 2ii and their atomic structures with W atom position in the top and bottom from MD simulations.

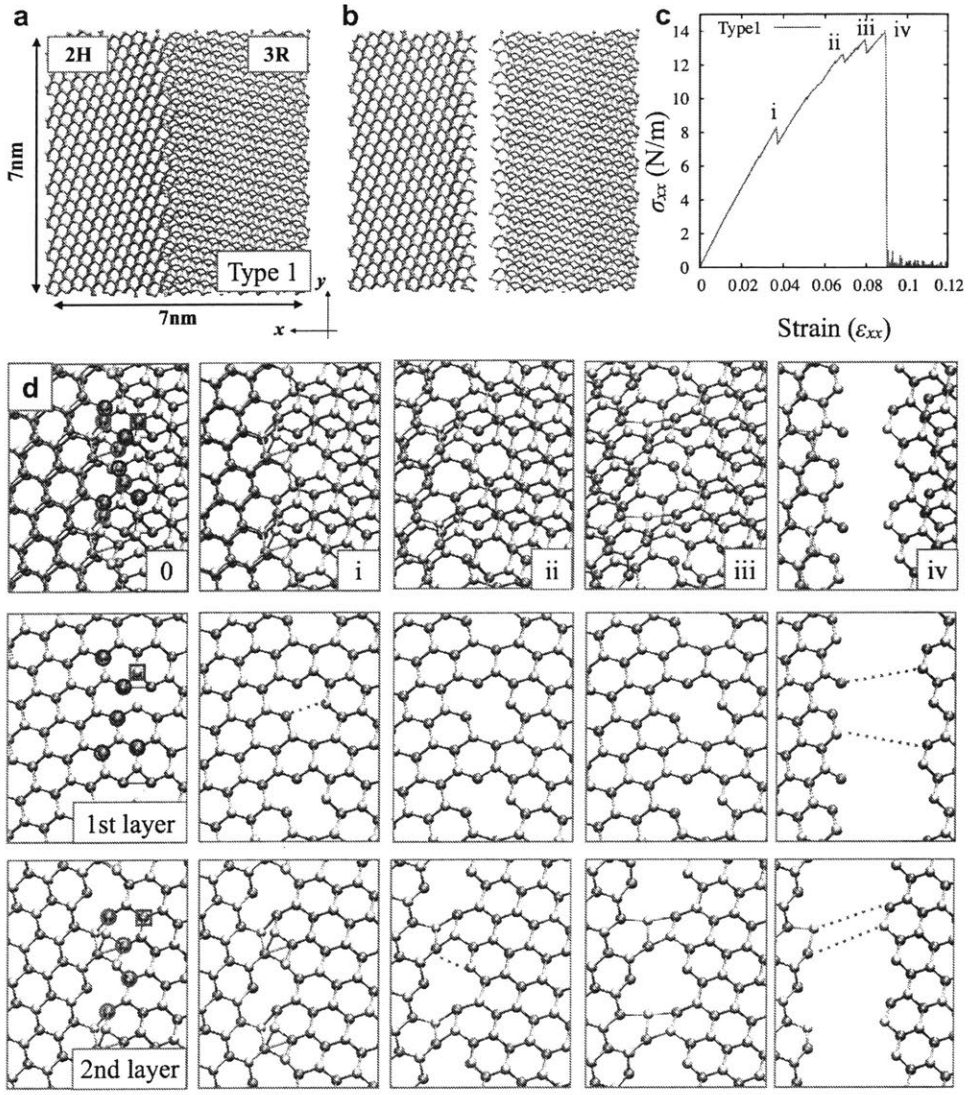

Figure 4-10: (a) Rebuilt model of Type1 through MD simulations with 7nm x 7nm size. (b) Snapshot of the model after both layers fail. (c) Stress-strain curve of the bilayer under tensile loading. There are several stages of failure (i- iv), which described more detail in d. (d) Detailed atomic structures of the MD model. The marked positions of atoms (red and blue circles and square) are well matched with TEM observation. The red lines indicate the bond breaks at the failure stage from i to iv described in the stress-strain curve.

Type 2i models, respectively. From the snapshots of models under tensile loading in Figure 4-10, C-1, and C-2, we can find the dislocations have different stability under mechanical loading. The dislocations I, II and III change their structures or fail at 1%, 4%, and 9% of the tensile strains, respectively. They are mechanically stable while they have different failure strain.

4.3.4 Conclusions

In summary, by using MD simulations and ADF-STEM we showed that dual GBs can exist in 2D crystals and that special types of W-rich dislocation cores are needed to enable such atomically precise GB structure. Our *in-situ* heating and tensile MD simulation show these structures are stable. We resolved the W and S positions within the atomically sharp dual GBs in the bilayers, enabling studies of 2H-3R and 2H-2H interfaces. The dual GBs exhibit voids in their structure, similar to those of monolayer TMDs grown by CVD, which enables the GB structure of both monolayer and bilayer regions to be deduced. These GB interfaces may have different semiconducting behavior compared to the overlapping GB types commonly found and further studies may help reveal new band gap behaviors to stimulate ways to increase the density and controlled growth of these 2D bilayer interfaces.

4.4 1D channel growth from lateral heterojunction

4.4.1 Introduction

Reducing the lateral scale of atomically thin 2D devices is crucial not only to realize competitive electronic device applications, but also for reaching the length scales needed for quantum confinement. Thus far, the many 2D heterostructure devices rely on the lithographic patterning of one 2D layer followed by the growth of another in the patterned areas [155, 156, 20, 157]. While this technique provides spatial control down to below a hundred nanometers or so, the nature of the lithographic patterning creates atomic defects and contamination. Consequently, the atomic junctions

in these heterostructures contain electronic defect states, impacting device performance. Recently, the growth of micron sized in-plane epitaxial interfaces between 2D materials has been reported using chemical vapor deposition (CVD) methods [21, 22, 23, 24, 158, 159, 160].

Theory predicts a tunable carrier confinement [161] and formation of 1D electron gas [162] at the abrupt and coherent interfaces in heterostructures of 2D materials that are just a few atoms wide. The atomic-scale heterostructures are usually chosen for computational convenience, but there would be benefits to realizing such narrow physical structures. For example, in contrast to broad in-plane heterostructures which ultimately generate misfit dislocations to release the lattice strain, thin channels can sustain large strains without relaxation and hence access a wider range of electronic band structures. Just as in bulk materials, dislocation formation can be suppressed below a critical film width [163], which scales inversely with the desired strain - several nanometers are typical for mismatch in the family of 2D transition metal dichalcogenides (TMDs). The thin channels always have one dimension below their critical thickness, ensuring stability against dislocation formation at the strained epitaxial interfaces. Eliminating interfacial dislocations, whose cores are 4|8 or 5|7 member ring structures, is key as these are generally expected to introduce undesirable mid-gap states [161, 164, 165].

This section shows how to model the fabricating coherent 1D channels within 2D heterostructures (Figure 4-11). These channels possess sub-nanometer widths and atomically coherent sidewalls free of misfit dislocations and dangling bonds. We start with a lateral interface between two 2D TMDs, MoS_2 and WSe_2, whose lattice mismatch provides an array of interfacial misfit dislocations (Figure 4-11(b)). Our experimental collaborator (David Muller's Group at Cornell University) introduce growth precursors that provide a high chemical potential for the channel material. The higher reactivity in the core of the misfit dislocations allows the channel atoms (Mo and S) to be inserted into the dislocation core, thus pushing the dislocations away from the original interface, forming 1D MoS_2 channels in a trail behind the advancing core (Figure 4-11(c)). The dislocation-catalyzed growth is essentially the

flat analog of the semiconductor nanowires whose growth from seeded catalysts has played an important role in semiconductor nanoscience.

4.4.2 Methods

Molecular dynamics model for 1D channels.

The computational model is a heterojunction composed of MoS_2 (4 nm x 7 nm) and WSe_2 (6 nm x 7 nm) with an interface along the zigzag edge of the 2D lattice. The 7 nm as the length of the material interface of this heterojunction is naturally given by the ~5% lattice mismatch between MoS_2 and WSe_2 (Table E.13). Periodic boundary conditions were applied to the zigzag direction along the interface of the heterojunction. Perpendicular to the interface, the model has 2 nm spacing between the simulation box boundary and the MoS_2 edge, and 2 nm spacing for the WSe_2 edge from the simulation box boundary. In addition, we set a 10 nm void region in the out-of-plane direction of the 2D material. These margins are large enough to guarantee that MoS_2 and WSe_2 only interact at the interface of the heterojunction.

We applied an interaction between the bottom layer of S/Se atoms and the substrate by using a Lennard-Jones (LJ) intermolecular potential with the 9-3 form [166] of

$$E_{sub} = \epsilon \left[\frac{2}{15} \left(\frac{\sigma}{r} \right)^9 - \left(\frac{\sigma}{r} \right)^3 \right], \tag{4.3}$$

where r is the distance from an atom to the surface of substrate; σ and ϵ are parameters that relates to the equilibrium distance $r = 0.858\sigma$ and adhesion energy 1.054ϵ per atom. The form is related to the integration over a half-lattice of particles with LJ 12-6 intermolecular potential. In the simulation, we used σ=2.3 Å and ϵ=0.1 eV through our simulations. We chose the adhesion energy as the system is stabilized during the annealing process (See more details in the next section). We note that the substrate model is simplified as an infinite wall to prevent the out-of-plane deformation and the penetration of atoms, which is similar to the sapphire substrate we used in experiments.

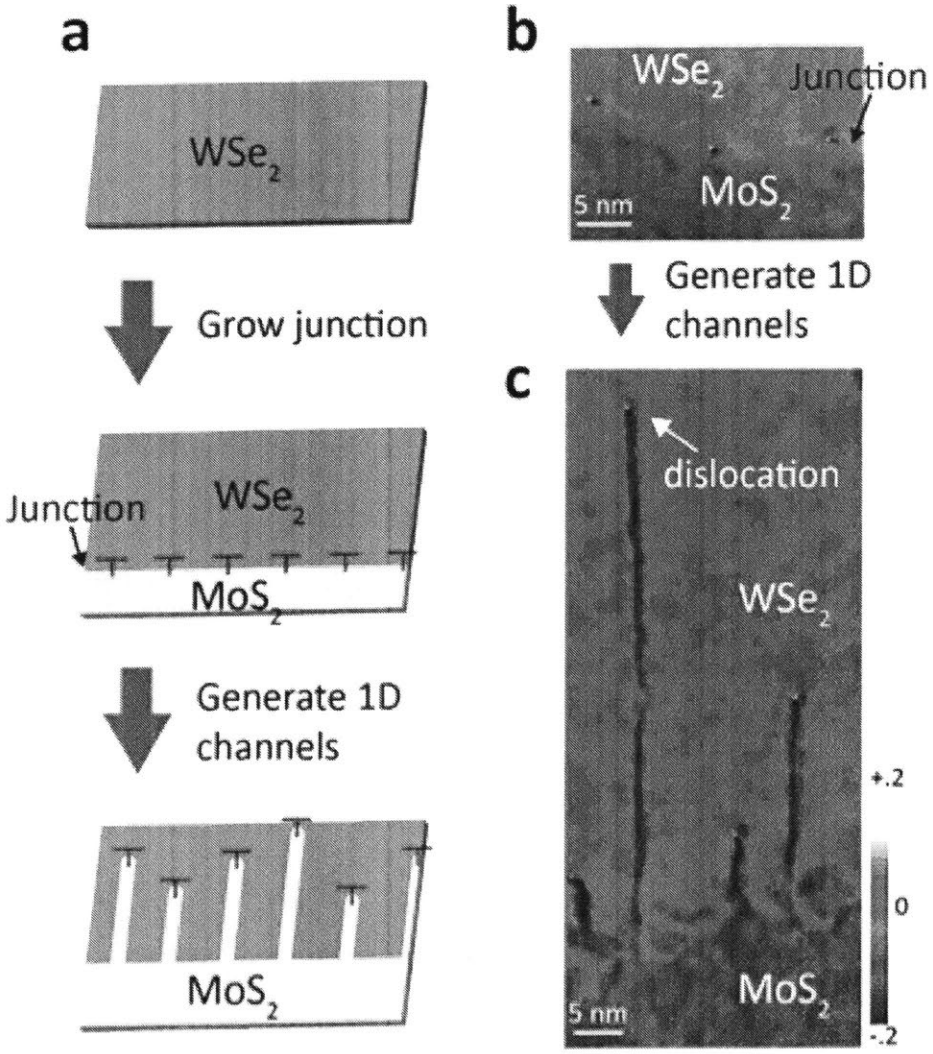

Figure 4-11: Formation of 1D channels. (a) Schematic of the patterning process guided by misfit dislocations (marked as 'T') at the MoS_2-WSe_2 lateral heterojunction. (b) and (c), atomic resolution ADF-STEM images overlaid with its ϵ_{xx} strain maps (see Figure 4-12 for more details) identifying the periodic dislocations at the interface of MoS_2 and WSe_2 (b) and the 1D channels created by chemically-driven migration of the interfacial dislocations as additional S and Mo atoms are added (c). Strain maps refer to the WSe_2 lattice.

We applied a number of cyclic annealing processes to study the behaviors of the dislocations. As a result, the pentagon-heptagon dislocations clearly climb towards the heptagon direction after hundreds of iterations, which matches our experimental results and represents the dynamic process for 1D MoS_2 formation.

Molecular dynamics model for 1D channels.

A number of cyclic annealing processes with adding or deleting atoms near the dislocation equilibrate the MoS_2-WSe_2 model, which is an algorithm combining MC and MDto accelerate the evolutions of the structures. Each of the cycles is composed of 4 stages by using NPT or NVT ensemble: heating, relaxing at high temperature, cooling, and relaxing at low temperature. The periodic condition and NPT ensemble are applied during the 2nd stage (relaxing at high temperature) to allow the structural relaxation along the junction direction. We have T_{low}=600 K for all atoms, and T_{high}=1100 K for W, T_{high}=900 K for Mo and Se, and T_{high}=600 K for S with 25 ps for the 2nd stage and 5 ps for the others. Before the 1st stage (heating) and after the 4th stage (relaxing at low temperature), conjugate gradient minimizations are applied for 5,000 steps. To simulate the experimental process of depositing Mo and S precursors at high temperature, we add MoS_2 nanoparticles 3 Å above the Mo/W plane over the dislocation with random variations less than 1.0 Å in both lattice directions, which allows both simulation efficiency and natural reaction between the nanoparticles and the MoS_2-WSe_2 heterojunction to be possible.

After every annealing process, we estimate a position of the next Mo for the most spacious region. When an estimated Mo position is located 2.4 Å away from the Mo/W atoms, the precursor nanoparticle (MoS_2) is added on the top of the system for the next cycle. The S2 or S4 is added based on the total number of sulfur and selenium atoms. After the 2nd stage, we check the out-of-plane displacements of atoms, and delete S/Se above 3.0 Å and Mo/W above 1.5 Å away from the Mo/W plane. We note that all these processes are setup to accelerate the reactions without forcibly forming bonds or other structures. The result confirms the generation of a straight 1D channel from the catalyst 5|7 dislocation with atomic thickness and

reveals the physics behind the growing process in atomic scale. To predict whether the approach can be applied to other TMDs, similar annealing process was conducted during the simulation in WS2-WSe_2 and MoS_2-$MoSe_2$ as well.

DFT calculation of 1D MoS_2 channel embedded in WSe_2

To demonstrate possible applications of 1D MoS_2 channel embedded in WSe_2, we obtained orbital projected band structures and projected density of state (PDOS) of six different models by QE package using the same functional and pseudopotential used for geometric parameters in Section 4.4.2. The rectangular shape unit cells in replicated in the x direction containing 60 atoms with the periodic boundary condition in x (along the zigzag edge) and y (along the armchair edge) directions. The energy cutoff for the wave functions is set to 60 Ry and 2 x 8 x 1 and 4 x 32 x 1 Monkhost-Pack grids are adopted for the K space sampling for structure relaxation and PDOS, respectively. We prepare 6 models with different ratios of MoS_2 and WSe_2 to represent 1D MoS_2 channels. The cells and atomistic structures are fully relaxed with convergence thresholds of 0.5 kbar and 10^{-3} (a.u.) for the pressure and atomic forces, respectively. Due to the rectangular unit shape of the system, we used Γ-K-Y-Γ for the bands structure to see the difference between the gap at the Γ the K points in hexagonal Brillouin zone (BZ) as suggested in the previous study [167]. Absolute conduction band minimum (CBM) and valence band maximum (VBM) relative to the vacuum level are calculated for all models. The obtained energy levels of pristine MoS_2 and WSe_2 show good agreement with those from the previous study [168], confirming the reliability of our calculation.

4.4.3 Results and Discussions

Atomic resolution annular dark field scanning transmission electron microscopy (ADF-STEM) imaging shows that the epitaxial interface between the body of the channel and the host matrix is coherently connected (Figure 4-12(a) and (b)). Meanwhile, a pentagon-heptagon (5|7) dislocation (heptagon pointing up) is found at the terminus

of all 1D channels (Figure 4-12(b)). The difference in the atomic number between Mo and W provides high contrast between the WSe_2 template and the newly grown MoS_2 channels in the ADF-STEM images.

The as-grown heterostructures of the TMDs must contain strain, due to the bond mismatch to create an epitaxial interface. Applying a geometric phase analysis (GPa) to the ADF-STEM image in Figure 4-12(a), we are able to elucidate the strain distribution in and around this 1D channel in its 2D matrix, as plotted in Figure 4-12(c)-(f).For GPa, the WSe_2 lattice parameter was chosen as the reference or zero strain (-.036 would correspond to relaxed MoS_2 sheets, consistent with the 3.6% lattice difference measured from the electron diffraction of the MoS_2 and WSe_2 layers in Figure C-3(a)). Along the x axis, there is significant difference in the strain map between the 2D WSe_2 and 1D MoS_2 channels, arising mainly from the lattice mismatch (Figure 4-12(c)). In contrast, the y-axis strain map reveals that MoS_2 channels have an identical lattice spacing with the host WSe_2 (Figure 4-12(d)), indicating a high uniaxial tensile strain along the y direction for detailed strain analysis on a single channel). Therefore, the newly synthesized 1D channel maintains coherency with the WSe_2 matrix and is strain accommodated, which effectively avoids the generation of misfit dislocations along the channel. The shear map and rotation map (Figure 4-12(e) and (f)) display the position and orientation of the dislocations as dipole fields, confirming all dislocations have the same orientation and migrate upwards (*e.g.* away from the original hetero-interface).

Growth of the 1D channels is not limited to the interfacial misfit dislocations at the heterostructure interface of the two 2D materials. They can also be generated from intrinsic 5|7 dislocations implanted within the WSe_2 film. The ADF-STEM image and corresponding ϵ_{xx} strain map (Figure 4-12(g)) of a MoS_2 1D channel show that it was formed from an intrinsic catalyst dislocation migrating in the direction of the heptagon. The isolated 1D channel is 70 nm in length and 1.5 nm in width, surrounded by monolayer WSe_2 on all sides, showing a high-aspect-ratio of about 47:1 (length to width).

To understand the catalytic role of 5|7 dislocations, we utilized a reactive force field

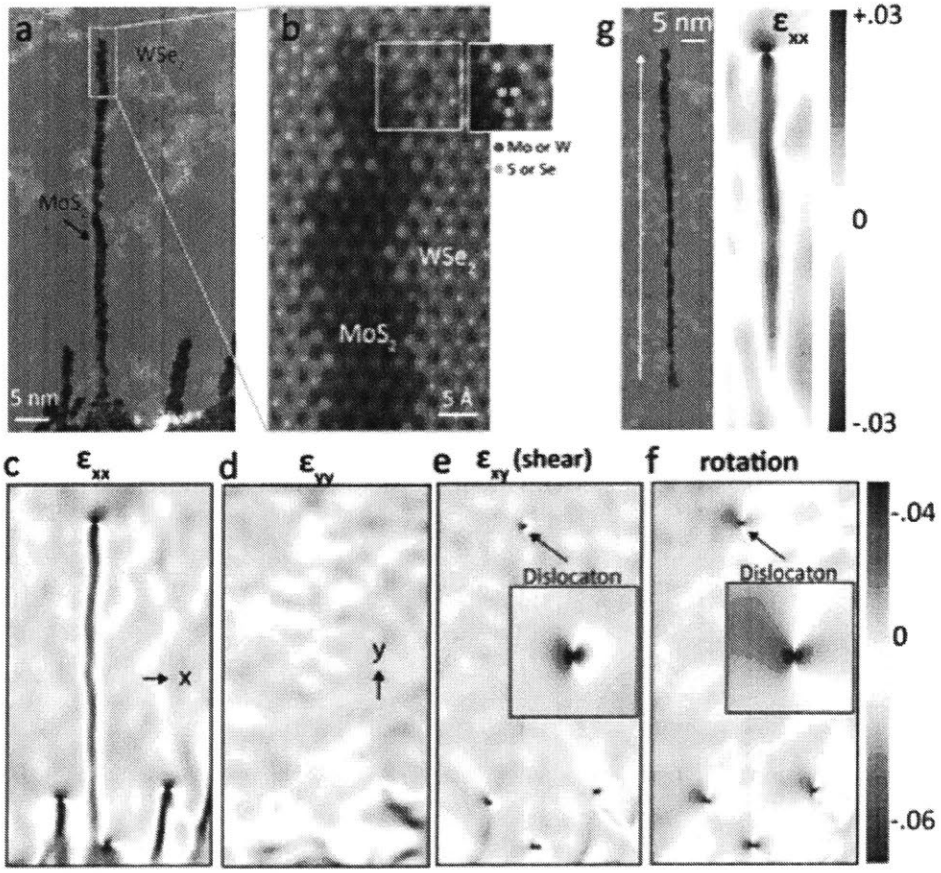

Figure 4-12: Strain maps of the 1D channels. (a) and (b), ADF-STEM image of MoS_2 1D channels embedded within WSe_2. The channel ends with the 5|7 dislocation (white box in (b)). The same section is shown to the right with the atoms labeled. (c) and (d), Geometric phase analysis (GPa) of the 1D MoS_2 in a with uniaxial strain components ϵ_{xx} (c) and ϵ_{yy} (d). All the strain is in reference to the WSe_2 lattice. The ϵ_{xx} clearly distinguishes the two lattices mainly due to the lattice mismatch, while the ϵ_{yy} indicates a high uniaxial tensile strain in the 1D MoS_2 which is lattice mismatched from the WSe_2. (e) and (f) display the shear strain and the rotation map (in radians) indicating the position and orientation of the dislocations. (g) ADF-STEM image and its ϵ_{xx} strain map of a MoS_2 1D channel formed from an intrinsic 5|7 dislocation in WSe_2, which matches the results found in channels arising from the heterojunction interface.

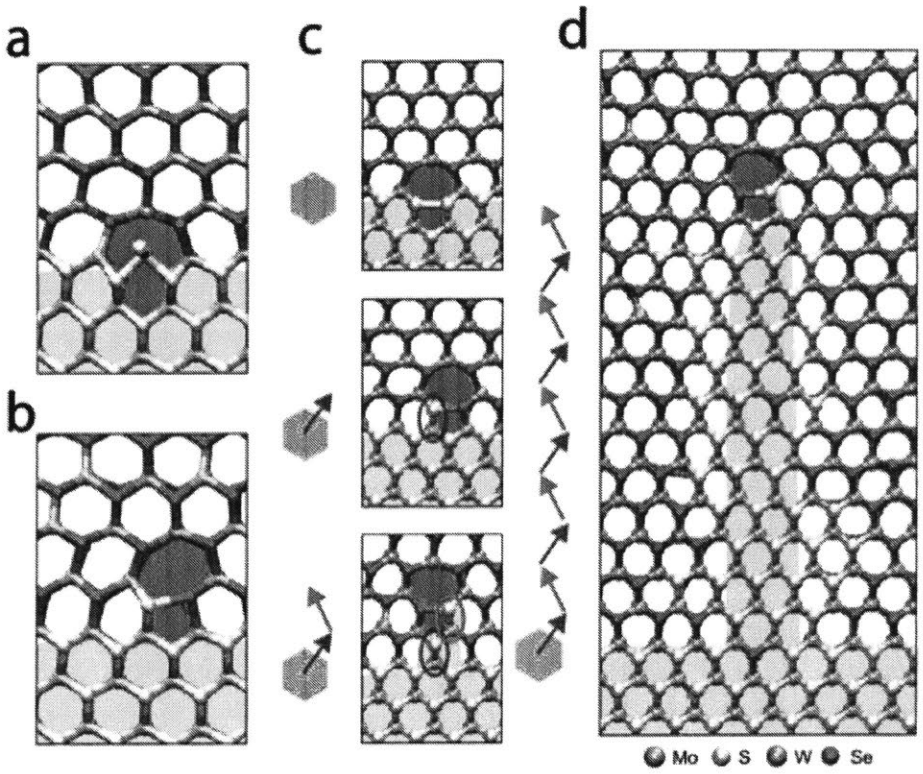

Figure 4-13: MD simulation of the 1D channel formation. (a) and (b) MD simulation of the process of Mo inserting into pentagon ring of 5|7 dislocation (a) and the formation of the next 5|7 dislocation (b). (c) MD simulation of each step for the patterning process. The 5|7 dislocation can migrate 30° to the right (blue arrow) or 30° to the left (red arrow). (d) The iteration of adding excess Mo and S atoms forms the 1D MoS_2 channel in WSe_2, unveiling the chemically driven mechanism for the formation of the 1D channels.

with newly developed parameters based on DFT calculations and an accelerated MD simulation. Our method captures the dynamics of the chemical bonds breaking and reforming, which is difficult to model using conventional non-reactive MD simulations. We found that unlike other hexagonal rings, the dislocation core allows the precursor atoms to be inserted, which acts as the driving force for the dislocation-catalyzed growth. The precursors first open the catalyst 5|7 dislocation, which admits the Mo insertion (Figure 4-13(a)). This step makes S atoms insufficient to finish the dislocation migration, leaving unsaturated dangling bonds in the system, and hence the lattice around the dislocation core reconstructs to find more energetically favorable structures. Afterwards, as more S atoms are absorbed from the environment, the lattice relaxes and forms the next dislocation (Figure 4-13(b)). While repeating these two key steps, the previously occupied W and Se atoms near the dislocation core have a certain probability to leave the 2D sheet, and those sites are replaced by the Mo and S precursors during the reconstruction and relaxation. Altogether, the entire process eventually leaves a narrow MoS_2 trail behind it.

The circles in Figure 4-13(c) indicate the additional Mo and S atoms placed at the dislocation during each migration step of the catalyst. The additional Mo and S atoms contribute to a 1.4% compressive strain in the x-direction within the channels (Figure C-4(c)).

Due to the crystal geometry of the hexagonal lattice, the migration of the dislocation has two choices: 30° to the right or left (blue or red arrows in Figure 4-13(c)), where the reference lattice orientation is shown as the gray hexagons. MD simulation shows the lateral strain field provides a local restoring force that guides dislocations back towards a straight line along the interface normal, as shown in Figure C-5. Thus, the dislocation zigzags about a straight line perpendicular to the macroscopic interface and is ultimately oriented in the heptagon direction, as shown in Figure 4-13(d).

The dislocation movement out of its slip plane also occurs in a 3D epitaxial interface, due to the diffusion of vacancies or interstitial atoms. In the bulk, this typically does not produce any major effects. In contrast, misfit dislocations in 2D materials

can directly take (release) atoms from (to) the environment, suggesting persistent climbs that can be used to pattern 1D channels by controlling the precursors and growth time. Statistically, 76% of dislocations tend to migrate and form 1D channels under our optimized growth conditions. Dislocations that did not move tended to have complicated local interface geometries (Figure C-3). After measuring 150 1D channels, we achieved an averaged distance between neighboring 1D channels of 10.9 ($\pm$ 0.9) nm, indicating a density of 92 ($\pm$ 8) 1D channels per micron along the interface between MoS_2 and WSe_2. The longest channels reached 80 nm. The length of the 1D channels was strongly correlated with the width of the MoS_2 layer around the WSe_2 triangles, which is mainly determined by the precursor ratio (S:Mo) and the growth time,suggesting these are two key underlying control parameters. However, there is a limit to how long the MoS_2 channels can be grown. As the surrounding MoS_2 layer continues to grow, the channel growth ultimately becomes unstable - the 1D channels have possibility to branch repeatedly and recursively, leading to tree-like structures that eventually consume the host material.

Despite a variety of lengths, more than 90% of the 1D channels have widths that are less than 2 nm, confirming the high accuracy of the dislocation-guided patterning process. For these ultra-narrow MoS_2 channels in WSe_2, DFT calculations show a type II band alignment useful for highly-localized carrier confinement and charge separation (Figure 4-15). Moreover, the strained 1D MoS_2 shows a direct band gap, distinct from the indirect band gap found in uniaxially strained 2D MoS_2 thin films. In addition, the 1D channel sidewalls should be free of undesirable mid-gap states that occur due to dislocations and dangling bonds. Both are desirable properties for ultra-small monolayer electronic and optoelectronic applications.

From the orbital projected band structures and PDOS shown in Figure 4-15, the 1D channel of MoS_2 mainly contributes to the CBM and the major contribution for the VBM comes from WSe_2. To estimate the local band gaps of MoS_2, we evaluated the contributions of MoS_2 for each eigenvalue in the band structures from the orbital projected band structure. As shown in Figure 4-15, the blue dot lines are corresponding to the weighted contribution from 1D MoS_2, where the dot size is proportional

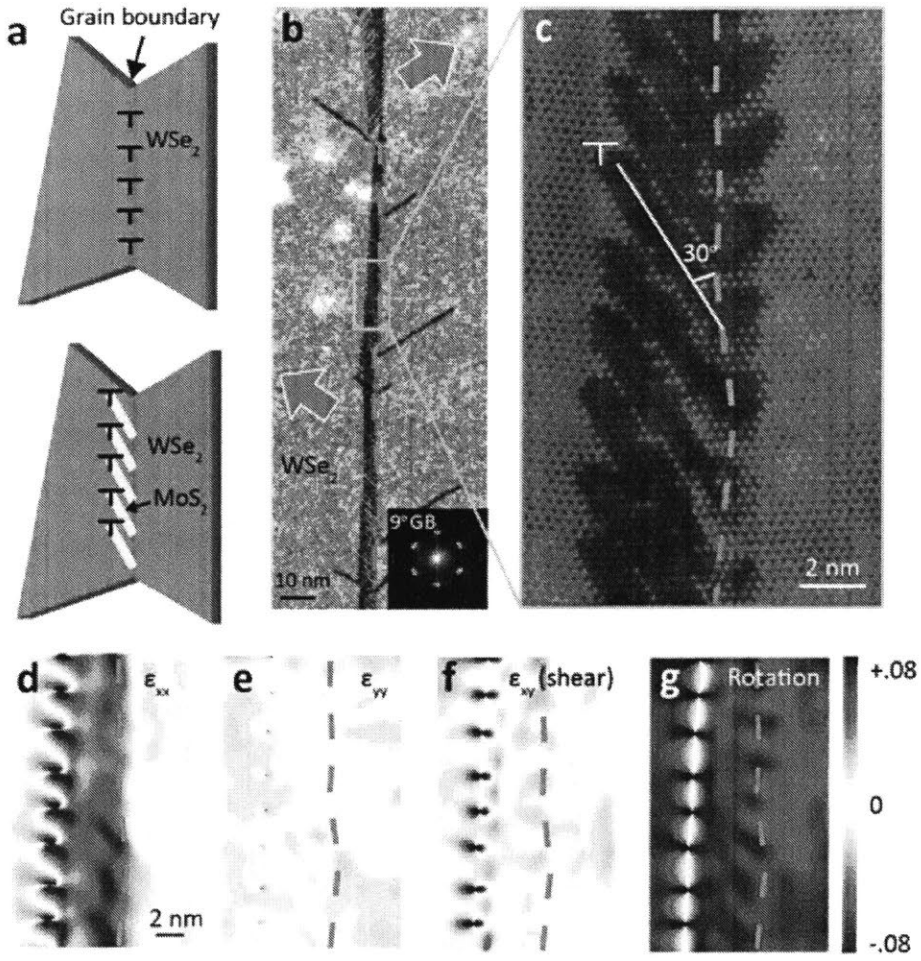

Figure 4-14: Generation of a super lattice at a grain boundary. (a) Schematic of the superlattice formation where the top (bottom) panel depicts the grain boundary before (after) the patterning process. (b) ADF-STEM image of a superlattice grown from the periodic dislocations at the WSe_2 grain boundary with 9° rotation (2 nm spacing between dislocations). All blue dashed lines indicate the position of the original curved grain boundary. The dislocations migrate in different directions (indicated by the green arrows), thus forming a shifted but straight grain boundary. (c) Magnified ADF-STEM image with one of the identical dislocations marked by a 'T'. (d)-(g), GPa of (c) showing that dislocations preserve their periodicity and orientations during the migration.

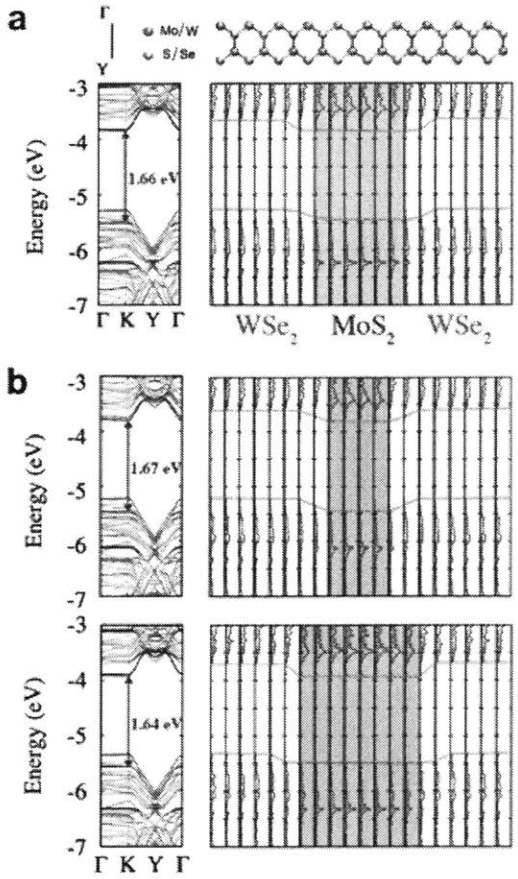

Figure 4-15: Electronic properties of 1D MoS_2 channels embedded within WSe_2 monolayer. (a) DFT calculation of the orbital projected band structure (left) and the projected density of state (PDOS) (right) of three-unit-cell wide MoS_2 1D channel embedded within WSe_2. In the orbital projected band structures, the blue dot lines are corresponding to the weighted contribution from 1D MoS_2, where the dot size is proportional to the MoS_2 contribution. Our calculations show our 1D MoS_2 forms a direct band gap, which is different from the indirect band gap of uniaxially strained MoS_2 that has been reported before [114]. The gray dot lines are corresponding to the weighted contribution from the WSe_2, while the red lines show the total band structure. Moreover, the PDOS plots show clear type II band alignment (blue lines) that can potentially be used for charge separation. (b) DFT calculations of 1D MoS_2 channels with two-unit-cell and four-unit-cell width. The band structure and PDOS show little difference from the three-unit-cell 1D channel, indicating robust 1D confinement even in the presence of small width variations. We chose the vacuum level as reference (0 eV). The spin-orbital coupling is not considered in this calculation.

to the MoS_2 contribution. The DFT calculations show that the gap of 1D MoS_2 is direct band gap even if we consider both K and Γ points while the uniaxial strain applied to MoS_2 results in the transition from the direct to indirect band gap. Due to the 1D confinement, the uniqueness of the band structure of 1D MoS_2 becomes more distinct, considering only K-Y or Γ-Y path in the BZ, where K-Γ path is ignored due to the translational symmetry broken in that path. The detailed values are listed in Table E.18.

The nature of the 1D growth can be used to create lateral 1D superlattices in 2D materials starting from a periodic dislocation chain, as illustrated in Figure 4-14(a). The most common structures with periodic dislocations are the grain boundaries of 2D materials. At a typical low-angle WSe_2 grain boundary, where two grains with small rotation angles connect laterally to form a classic low-angle tilt boundary, the periodic arrays of 5|7 dislocation cores line up with a spacing $\sim b/\theta$. Here, b is the Burger's vector and θ is the tilt angle between the two grains, suggesting grain boundary tilt angle can be used to control the 1D channel spacing. In theory, the dislocations are most stable when they lie vertically above one another with equal spacing [169]. To attain the lowest energy over large scales, the dislocations at the originally curved grain boundary (blue dashed line in Figure 4-13(b)) migrate with an angle of 30° to the left (or to the right) of the heptagon direction (as indicated in Figure 4-13(a)) to form a straight grain boundary. For example, in Figure 4-13(b), dislocations at the top migrate to the right while dislocations in the bottom migrate to the left, forming a straighter grain boundary.

The magnified ADF-STEM image, Figure 4-13(c), shows a region where all catalyst dislocations migrate 30° to the left forming ~1 nm nanowire arrays with sub-nanometer spacing. Figure 4-13(d) to 4-13(g) present the strain maps of Figure 4-13(c), indicating that dislocations keep their periodicity and orientations after the translation, and the right-side lattice orientation is inherited. We note that in Figure 4-13(c), short branches appear also on the right side of the original grain boundary, but they have no dislocations at the ends. This can be understood as arising from individual dislocation wandering before they are propelled towards the left by other

dislocations, suggesting a strong collective interaction between dislocations that can be used to control the patterning of 1D superlattices. This 1D superlattice formation is commonly observed at low-angle tilt grain boundaries lower than 10°.

4.4.4 Conclusions

Our strategy to produce dislocation-free 1D channels suggests a general set of search criteria for other 2D materials. First, candidate materials need a source of dislocations such as low-angle grain boundary or lattice mismatched hetero-interface. Secondly, while the dislocations allow for an easier insertion and exchange of atoms, the substitutions need to be energetically favorable (*e.g.* S for Se). We used MD simulations to identify another two candidate systems for 1D channels formation: 1D WS_2 in WSe_2 (a different 1D channel material) and 1D MoS_2 in $MoSe_2$ (a different matrix material), both of which are lattice mismatched (Figure C-6 for simulation details). However, combinations of materials that have little lattice mismatch, such as MoS_2 and WS_2, will not form 1D channels due to the lack of an initial source of catalyst dislocations. The lattice mismatch and displacement criteria allows us to predict candidate systems for 1D channel formation, and also provides a way to engineer the strain in the 1D channels by changing the 2D hosts.

Chapter 5

Three-Dimensional Designs from Two-dimensional Materials

5.1 Introduction

This Chapter introduces atomic models of 2D materials with three-dimensional designs utilizing triply periodic minimal surfaces (TPMS). The mechanical and thermal properties of 3D graphene are systematically studied based on developed models in the first and second sections. Also, the MD-based crystal Growth models for TMD materials are designed for flat and curved surfaces. The works presented here are the collaboration with Jamie H. Warner group in Oxford University and Jiwoong Park group in Chicago University and published papers [38, 33, 34, 40].

5.2 Mechanical properties of 3D graphene with TPMS

5.2.1 Introduction

Graphene, a two-dimensional (2D) single layer of graphite, is known as one of the stiffest and strongest materials [7, 5]. Along with its excellent mechanical properties, its unique thermal and electrical contuctivity [136] have placed graphene as one of the leading materials for innovation in several fields of materials science. Like

carbon atoms in other allotropes discovered in the last three decades (*e.g.*, carbon nanotubes and fullerenes), carbon atoms in graphene are covalently bonded with sp^2 hybridization. This 2D carbon layer is considered a fundamental building block for sp^2 structures with other dimensionalities: 0D fullerene, 1D nanotube, and 3D graphite, where the graphite layers are bound by weak van der Waals (vdW) interactions.

In the early 1990s, three-dimensional (3D) covalently bonded carbon networks were proposed by introducing triply periodic minimal surfaces (TPMSs), where all sp^2-hybridized carbon atoms form structures with zero mean curvature and negative Gaussian curvature [170, 171], through the inclusion of topological defects [172]. These TPMSs, called Schwarzites, can be classified into P (primitive), D (diamond) and G (gyroid) types [173]. Theory predicted that Schwarzites are mechanically stable and can have diverse electronic properties such as semiconducting, insulating or metallic, depending on their specific structures and sizes [174, 175]. Although the successes of synthesis of Schwarzites has been very limited, different synthetic methods have been utilized to form Schwarzite-like graphene foams with various porosities. Benedek *et al.* have reported carbon spongy foams with under few-hundreds of nanometer-scale pores from pulsed microplasma cluster source (PMCS) technique, showing distorted P and D type topologies [176, 177]. While the surface topologies are not clearly defined one nanometer-size porous carbon networks (sp^2 hybridization) have been synthesized by utilizing a zeolite [178]. Also, hydrothermal and chemical reductions from graphene oxide have been widely used to produce macroscale graphene foams with microscale pores, showing interesting mechanical properties, *e.g.*, near-zero Poisson's ratios and high compressive strength [179, 180, 181]. Additionally, the template-directed chemical vapor deposition (CVD) technique with nickel foams is a promising method to fabricate well-connected graphene foams [182]. Recently, sub-60 nm ordered graphene foams with gyroid surfaces have been synthesized using the directed CVD method [183].

The recent progress and intriguing features of the 3D graphene foams, *e.g.*, lightweight and excellent electrical and mechanical properties, have brought interest back to idealized Schwarzites in order to better understand their promising properties [184, 185].

Also, G type surface or atomic models of Schwarzites can be 3D printed to design innovative lightweight engineering materials to have a high-load bearing ability, where mechanical properties can be identified via atomic models [33, 186]. In previous studies performed to characterize the mechanical properties of Schwarzites, the number of atoms and lattice sizes are limited to a few hundred and under 5 nm sizes [175, 185, 187] or fail to generate appropriate models to sustain curved surfaces after structural relaxation [184]. Although the mechanical and thermal properties of G type surface from 3 nm to 20 nm lattice sizes were made and studied [33, 34] the relations between the other TPMS topologies (P and D types) and their mechanical properties are still mostly unknown.

5.2.2 Methods

In this study, we investigate the mechanical properties of P, D and G types of graphene foams using reactive molecular dynamics (MD) simulations [64, 63]. The elastic moduli, Poisson's ratios, strengths, and fracture energies with the power laws are obtained to predict mechanical properties at different scales. Our work sheds light on the roles of structures on the elastic and fracture properties with different failure mechanisms arising from TPMS topology, which might be applicable not only to porous carbon materials but also 3D printed engineering materials. [33] The atomic structures of 3D graphene with TPMSs were proposed based on Euler's law or Monte Carlo method with Ising models in the early 1990s while the lattice sizes were limited to a few nanometers [171, 187]. Larger scale Schwarzites with the P surface up to 12 nm lattice size were generated in the previous study [184] using Surface Evolver [188]. However, the structures of TPMSs were not conserved after structural relaxation because the building process considered only geometries without atomic stress and energy of carbon atoms.

Phase field crystal method can be utilized to build centroid surfaces and sinusoidal ruga graphene surfaces by considering total energy [172, 89]. This method was able to generate only small sizes of TPMSs under 5 nm [185]. Recently, we proposed a novel method that accounts for both local energy and stress to systematically construct

3D graphene foams with G type up to 20 nm lattice size, showing preserved curved surfaces after structural relaxation [33]. Here, we utilized the same approach to generate TPMS P and D types from 3 nm to 20 nm to study and compare their mechanical properties. We utilized previous models of G type from the references [33, 34]. All carbon atoms in our models are designed to have sp^2 bonds without any dangling bond or surface passivation that may play a significant role in the mechanical properties.

5.2.3 Results and Discussions

Figure 5-1 demonstrates 3D graphene models with different TPMSs. Each surface fits the cubic unit cell, and five models with different lattice sizes of L from 3 nm to 20 nm are systematically generated by three steps as shown in Figure 5-1(b) and Figure D-1. The open-shell structures of TPMSs describe critical features of experimentally synthesized graphene foams from PMCS and CVD methods in Figure 5-1(c). The densities of the models range from 100 to 1000mg/cm^3 in the current study, listed in Table E.19 where the number of atoms ranges from 800 to 60,000 in Table E.20. The pore sizes of our models do not fit both one nanometer [178] and the sub-hundreds nanometer [183] scales. However, our study can provide meaningful insight for the 3D graphene foams with pore sizes that have not been synthesized. As will be discussed later, our models cover the density ranges where the defect ratios change significantly from about 20% to 5% with different distributions. The models can capture the essential features for multiscale mechanics of 3D graphene foams with various TPMSs.

Based on the spanned area in the unit cell, P type shows the lightest weight with the assigned lattice size, while D type model is the heaviest. The area is $S = aL^2$, and the obtained factors, a, of P, D, and G types are 2.32, 3.78, and 3.06, respectively (Table E.20). To reflect the difference of surface areas for analysis, we utilized a relative density, ρ/ρ_0, where ρ and ρ_0 are the densities of TPMSs and pristine graphene (2.3g/cm^3), respectively. All three models show similar topological defect (pentagon and heptagon) distributions in Figures D-2-D-4. As the lattice size increases the defect ratios decreases from around 20% to 5% in Figure D-5. They are likely to form

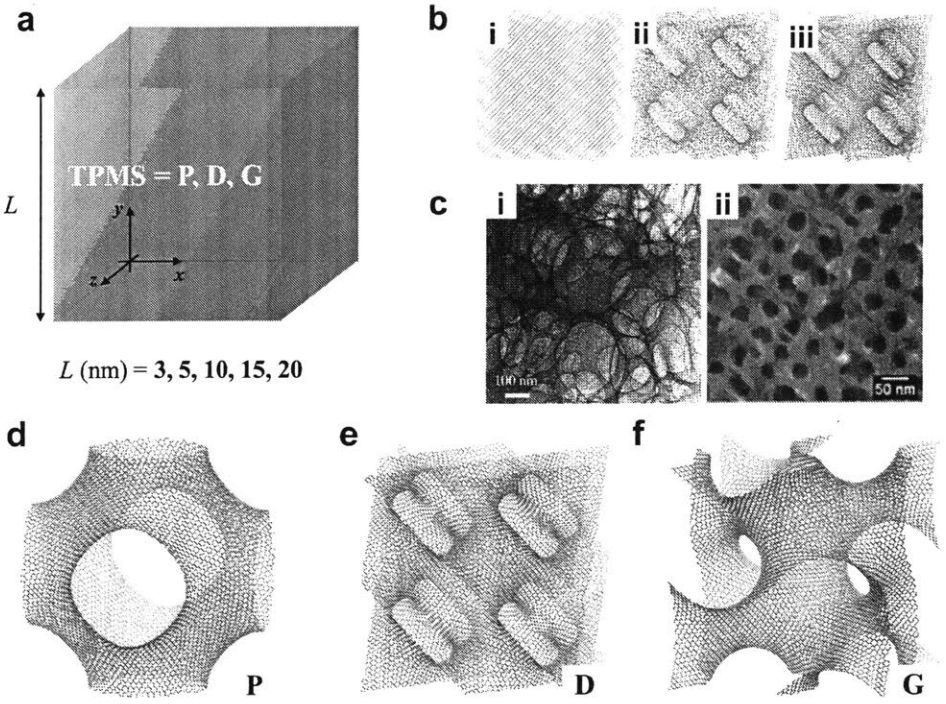

Figure 5-1: (a) Schematic figure for 3D graphene models with triply periodic minimal surfaces (TPMSs) P (primitive), D (diamond) and G (gyroid). All models have a cubic symmetry with varying lattice sizes (L): 3, 5, 10, 15, 20 nm. (b) Snapshots present a summary of three-step process, including (i) generation of initial template from FCC solid structure of Lennard-Jones (LJ) particles with external potentials, (ii) transformation to hexagonal carbon lattice from triangular LJ lattice, and (iii) refinement of geometries by adding and removing atoms based on the bond number (c) Different topologies from experimental synthesis including (i) a TEM image of randomly distorted P and D surfaces using the PMCS technique and (ii) a SEM image of well-ordered 60 nm gyroid surface using the directed CVD method (d)-(f) Snapshots of 3D graphenes with TPMS P, D, and G types with L=10 nm. The randomly oriented grains and boundaries with topological defects (mainly pentagons and heptagons) shape the curved surfaces.

grain boundaries with aggregated topological defects as the lattice sizes increase, which results in converged values of defects ratios to sustain the curved surfaces of TPMSs. This polycrystalline feature of graphene can cause softening or non-linear responses with a small deformation as shown in the previous polycrystalline graphene studies due to the out-of-plane deformation [88, 31, 101]. The models conserve the curved surfaces as defined after structural relaxation in Figure D-6, which is crucial for the derivation of power laws to systematically understand multiscale mechanical properties of 3D graphene foams. Firstly, to understand the effects of surface topol-

Figure 5-2: The components of stiffness (C_{11}, C_{12}), two shear moduli (C_{44} and $(C_{11} - C_{12})/2$), Young's modulus (E), and Poisson's ratios (ν) of 3D graphene foams with TPMS P, D, and G types. The values are averaged based on a cubic symmetry where the error bars represent the standard deviation. The elasticity is strongly affected by the structures, which provides an opportunity to design the elasticity with different TPMSs. The Poisson's ratios show the strong dependence on the relative density under 0.1 because the bending stiffness change as the density decreases. The defects distributions are more likely localized and form grain boundaries, changing the local mechanical properties. Solid lines in graphs are fitted functions described in Table E.21.

ogy on the elastic properties, elastic constants are obtained (See refch2:2:6:1). As all TPMSs have cubic symmetry, the three components of stiffness tensor (C_{11}, C_{12}, C_{44}) are enough to describe the elastic properties. We note that all our models are elastically stable based on the Born elastic criterion for cubic crystals [189]. The cubic shear modulus C_{44} represents the resistance to shear deformation across the (100) plane in the [010] direction while $(C_{11} - C_{12})/2$ represents the resistance to shear deformation across the (110) plane in the [11 $\bar{0}$] direction [79]. Figure 5-2 shows the obtained elastic moduli and Poisson's ratios for P, D, and G types as a function of the relative densities. The fitted functions for the properties of unit lattices are listed in Table E.21.

The elastic properties are strongly affected by the TPMS topology, providing a chance to design the properties from structures. The TPMS of D and G types have relatively higher Young's modulus and $(C_{11} - C_{22})/2$ than P type while the Poisson's ratio and C_{44} of P type are higher than those of D and G types. Two factors affect

the elastic properties: one is the topological defect (mainly pentagon and heptagon) distribution, and the other is the TPMS itself. From the previous study based on the isotropic linear material with the finite element method (FEM) [190], the trends of density dependence (exponent n from the scaling law) of TPMS are similar with those from our models. For example, the exponents of Young's modulus of P type and G type from FEM are 1.52 and 1.4, respectively. P and G types of graphene foams from our MD simulations have 1.62 and 1.57, respectively. Also, the exponents of other elasticity such as shear modulus of graphene foams have higher values than those from FEM. The higher dependency on the density than FEM can come from the defect distribution and its softening effect. Quantitatively decoupling the effects of defect distributions and structures is challenging and would be possible by utilizing FEM with careful set-up for graphene properties. Also, we note that there are nonlinear responses due to the softening in small strain ranges. The behaviors are observed in the polycrystalline graphene because of the out of plane deformation around the topological defects. Our models have the same essential features of polycrystalline in the regime of the relative densities below 0.1. This nonlinear response makes the elastic properties less sensitive to the topology.

Secondly, the macroscopic effects of polycrystalline structures are investigated. In general, the 3D graphene foams generated from the hydrothermal and chemical reductions feature the randomly assembled structures [181]. The well-ordered 3D graphene foams with G type TPMS from the directed CVD method [183] also shows polycrystalline features. Therefore, it is worth identifying macroscale effects with randomly oriented and distributed lattices from 3D graphene cubic crystals. Figure 5-3 shows the obtained elastic moduli based on Voigt-Reuss-Hill (VRH) approach (See Method 2.2.6, which is a macroscale average with randomly distributed polycrystalline structures from unit crystals). The average makes Young's modulus and shear modulus of D and P types converge into those of G type as shown in Table E.22 while both coefficients and exponents of G type change little compared to the others. This is because G type has nearly perfect isotropic elasticity confirmed by the Zener ratio (A_Z) and the universal anisotropy index (A_U) in Figure 5-3 and Table E.23. The

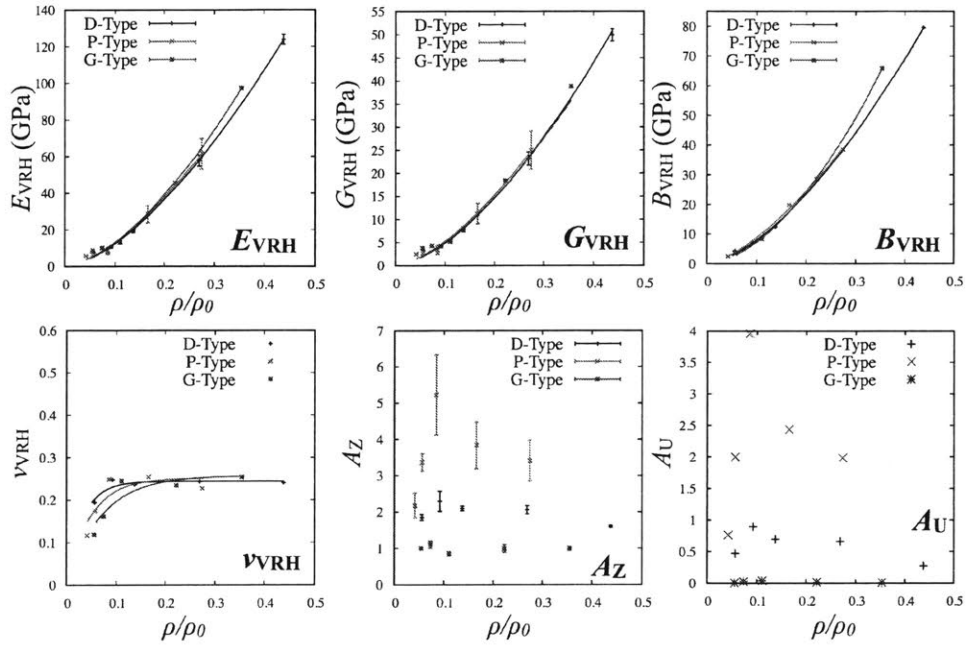

Figure 5-3: Young's modulus (E_{VRH}), shear modulus (G_{VRH}), bulk modulus (B_{VRH}), and Poisson's ratios (ν_{VRH}) based on Voigt-Reuss-Hill approach. The approach is to estimate isotropic properties from randomly oriented polycrystalline structures. The error bars indicate the upper and lower bounds from Voigt and Reuss averages. While the values do not change much for G type, those of P and D types vary significantly from their properties because G type has isotropic elasticity even with the geometrically cubic symmetry, which is confirmed by two anisotropy indexes A_Z and A_U (A_Z is a Zener ratio, and A_U is a universal anisotropy index). If a material is isotropic, A_Z is 1, and A_U is 0. The anisotropies of G and D types do not much depend on their density, while the anisotropy of P changes much. Solid lines in graphs are fitted functions described in Table E.23.

D and P types show the larger upper and low bounds of Young's and shear moduli than G type (more than one order of magnitude in Table E.24). The randomly oriented crystals in polycrystalline structures experience different strains under the uniform stress. The different strains are associated with the shear stress concentration at the grain boundaries, and the magnitude of the stress concentration depends on the elastic anisotropy. Therefore, G type has an advantage with polycrystalline structures than the others. Also, this means that the deformation of polycrystalline foams with G type is homogeneous under macroscopic loadings. The gyroid structure is often observed in nature such as in the microstructure in butterfly wings known for their unique structural colors [191]. Those structures have a thickness to form lattice networks with polycrystalline features [192] (expressed as $V_G <$ thickness in eq(2.25)). Although the materials properties and lattice scale are different, our finding of isotropic elasticity of G type with atomically thin thickness implies that the gyroid structure selected by nature may have an advantage for the polycrystalline structures than the other structures.

Poisson's ratios demonstrate strong density dependence when the relative density is under 0.1 (ρ=230mg/cm^3), which has not been captured with small size models in the previous studies. A possible explanation for the decrease of Poisson's ratios is a change of defect distribution at different scales. The spatial distributions of defects and their ratios as a function of lattice size and relative density are shown in Figures D-2-D-5 by utilizing the previously developed method [34]. As the lattice size increases, the defects to sustain the curvature are more localized and gathered at grain boundaries (converged to around 95% of hexagonal ring under the relative density 0.1), which basically changes the local mechanical properties of graphene including topological defects, to the level of pristine graphene as the system size increases. From the obtained scaling law for G type, Poisson's ratio decreases to 0.04 at ρ/ρ_0= 0.01 while a finite element model for G type has predicted ν=0.2 at the same relative density [190]. Our results explain the reported near-zero Poisson's ratios of graphene foams at the very low densities [181].

Finally, strengths under tension, shear, and compression are obtained to gain

Figure 5-4: (a) Tensile, (b) shear and (c) compressive strengths of 3D graphene models as a function of the relative densities and snapshots of failure with the models of L =10 nm. Compared to the elasticity, strengths are relatively less affected by surface topology. However, the failure mechanism remarkably changes. For tensile and shear loadings, multiple cracks (red arrows) are observed at different places in D and G types while a single crack at the failing point grows to fracture the entire system of P type. For compression, high values of Von Mises stress of D and G types (σ_{von}) are distributed in entire regions with complicated crumpled geometries while P type shows localized buckling. Solid lines in graphs are fitted functions described in Table E.25.

further insights into mechanical properties and fracture properties in Figure 5-4. The results reveal that the strengths are relatively less dependent on the TPMS topology compared to elasticity. However, the behaviors of failure differ under the tensile loading significantly. Multiple cracks nucleate in the D and G types while a crack grows to fracture in P type in Figure 5-4(a). Similar behaviors are observed under shear loading in Figure 5-4(b). The behaviors affect the stress-strain curves after the maximum stress as shown in Figures D-7 and D-8. P type shows brittle failure while D and G types have saw-like tails. In this section, the failure mechanism of the TPMS unit cell was mainly investigated in the current study. One may question whether the brittle failure of P type originates from a finite size effect. Thus, the tensile tests are performed with multiple unit cells (2x2x2) and confirmed the difference is still valid as shown in Figure D-9. As the number of the unit cell increases further, the failure will happen only near the region where the crack initially nucleated due to the stress concentration. How the fracture toughness of the TPMSs and crack propagation with a predefined crack change due to the TPMS topology would be an interesting topic in the future. Under compression, the geometries of models at a strain of -0.5 are demonstrated in Figure 5-4(c), showing complex crumpled geometries of D and G types with well-distributed high atomic Von Mises stress (σ_{von}) in the entire regions while P type collapsed with a localization of the stress. The stress-strain curves in Figure D-10 demonstrate that P type has several points abruptly losing the load-bearing ability, while G type has fewer points with continuously increasing compressive stress. At the high compressive strain, regions of TPMSs parallel to

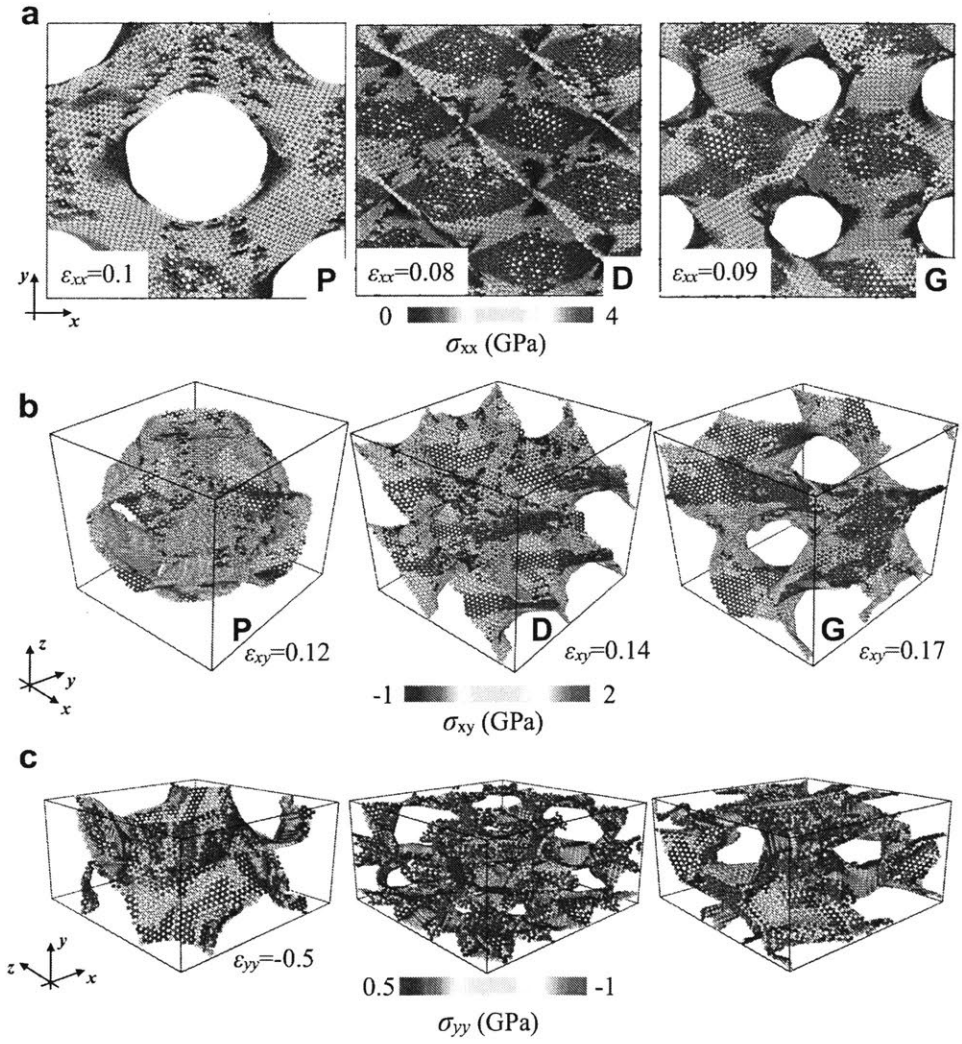

Figure 5-5: Snapshots of atomic stress distributions with (a) tensile (σ_{xx}) and (b) shear (σ_{xy}) loadings before the failure point and (c) compressive (σ_{yy}) stress at highly compressed state ($\epsilon_{yy} = -0.5$). Under the tension, D and G types show notable stress distributions compared to P type. The higher stress bands (red) are isolated from lower stress regions (blue). The twisted stress bands are observed in D type, and the spiral stress bands are found in G type. Similar isolated stress bands in D and G types are observed under shear loading. For compression, the parts parallel to loading direction mainly support the compression as indicated by red regions.

the loading direction mainly support the compression in Figure 5-5(c). As discussed, there are non-linear regions with a small deformation in stress-strain curves. The tensile and compressive moduli were obtained from the stress-strain curves, showing that the exponents of both tensile and compressive moduli are less sensitive to the topology as around 1.0 and 2.2, respectively. D and G types show higher moduli than P type, and its difference comes from the coefficients of the scaling laws as in Table E.29.

For the better insight of fracture properties, the atomic stress is calculated for tensile and shear loadings in Figure 5-5. We found that the different behaviors result from distinct stress distributions under the tensile and shear loadings between D and G types and P type. Figures 5-5(a) and (b) demonstrate that there are higher stress bands that are isolated by lower stress regions in D and G types. The atomic stress distributions in Figure D-12 also clearly show that there are high and low stresses in D and G for both tensile and shear loadings, preventing a single crack becoming dominant due to the stress concentration while P type fails by growing of a nucleated crack. Also, the atomic stresses of the high-stress bands of D and G types are higher than atomic stress in P type, making the strengths less dependent on the structures compared to the elastic properties. The isolated bands allow multiple nucleated cracks to be trapped and then, stress to transfer to lower stress regions. The redistributed atomic stress due to deformation makes the stress increase from the failing point, which makes a stress-strain curve in a saw-like shape by occurring multiple times. Eventually, multiple crack paths are possible with the more significant amount of energy dissipation as depicted in Figures 5-6(a) and (b). The saw-like stress-strain curves and the localized cracks were also observed with 3D printed G type polymers in the previous study [33]. To quantify the difference, we further obtained fracture energy from stress-strain curves under tensile loading in Figures5-6(c)-(e). The results show that D type can dissipate fracture energy almost three times larger than that of P type while the portion of fracture energy from the elastic region is similar.

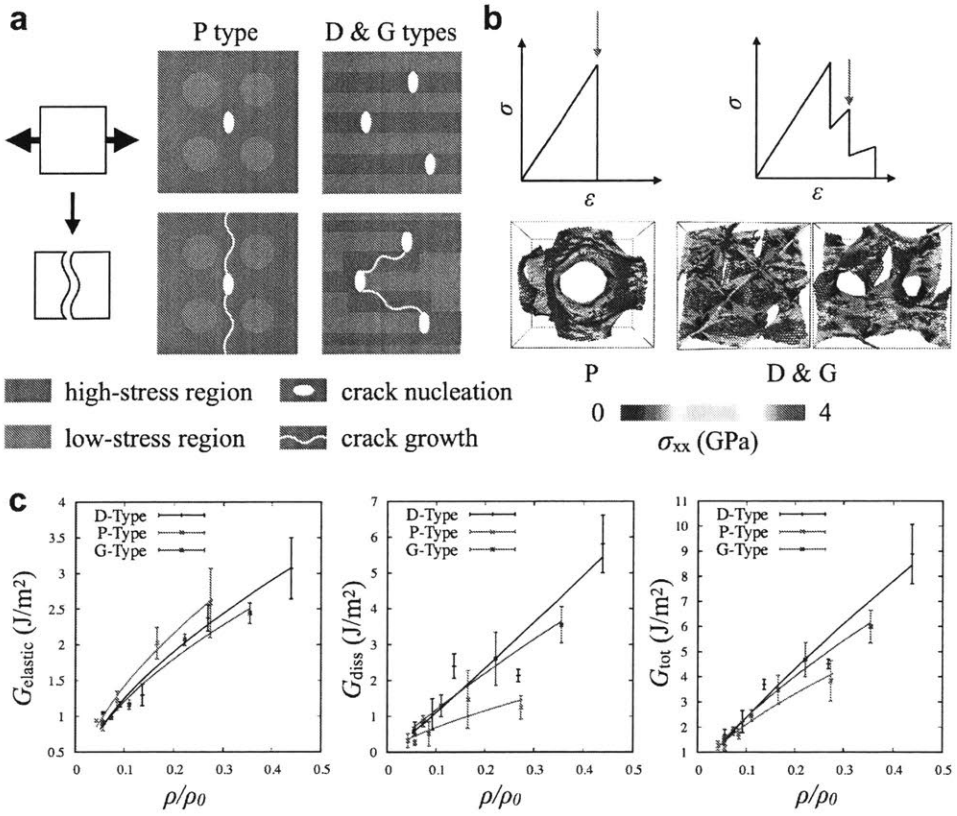

Figure 5-6: Schematic of different fracture behaviors between P type and D and G types. Due to the isolated high-stress bands, the stress-strain curves of D and G show a saw-like shape while P shows brittle failure as described in panel (b). Inset atomic stress shows how D and G types increase the intermediate stress by isolated cracks. (c) Fracture energy is calculated from the stress-strain curves under tensile loading. For the analysis, the total fracture energy is divided into elastic energy and dissipated energy. D type shows approximately three times higher dissipated energy than P type while both types have similar elastic energy. Solid lines in graphs are fitted functions described in Table E.26.

5.2.4 Conclusions

We note that these kinds of failure mechanisms are also observed in bio-inspired 3D printed composites [32] by mixing two different soft and stiff materials. On the other hand, our results demonstrate that the failure mechanisms with more energy dissipation can be useful even with a brittle and homogenous material based on complex 3D porous structures by controlling stress distribution, which can open the opportunities of designs for a novel class of lightweight crystal structures with excellent mechanical performance. In summary, we systematically studied the mechanical properties of triply periodic minimal surfaces (TPMSs) with 3D graphene foams: P (primitive), D (diamond), and G (gyroid) types. The five different models (P and D) from 3 nm to 20 nm for each type are generated, and their elasticity, strengths, and failure mechanisms are compared. We summarize our findings as below:

1. The defect distributions change with aggregation of defects forming grain boundaries as the density decreases, which causes a transition of the defect ratios at $\rho/\rho_0 \sim 0.1$.

2. Elastic properties are strongly affected by the types while strengths are less sensitive.

3. As the density decreases, Poisson's ratios significantly decrease from the transition ($\rho/\rho_0 \sim 0.1$); near-zero Poisson's ratio is possible at very low density.

4. Failure mechanism under tension or shear loading is strongly affected by the types.

5. Only G type has isotropic elasticity despite the structural cubic symmetry, which may have an advantage for stress concentration with polycrystalline structures than P and D types.

6. The isolated high-stress regions of D and G types allow saw-like stress-strain curves, which require more energy to break the unit cell of D and G types than P type.

Our findings provide the fundamental understanding of 3D graphene foams and insights to design lightweight materials with tailored mechanical properties from sophisticated 3D structures.

5.3 Thermal properties of gyroid graphene

5.3.1 Introduction

Graphene is a well-known two-dimensional (2D) material that has excellent mechanical, thermal and electrical properties [7, 193]. There is growing interest to utilize graphene in three-dimensional (3D) architectures because monolayers of graphene are constrained by their size, and because they are mechanical fragile with limited large-scale mechanical engineering applications. Several different methods have been developed to synthesize graphene-based porous materials with pore sizes ranging from nano- to micro-meters in diameter [179, 180, 182]. Recently, 3D graphene structures with sub-nanometer pore sizes have been developed based on a zeolite template [178]. Although the mechanical and thermal properties of graphene per se have been well characterized, the relationship between porous structures derived from graphene and their mechanical or thermal properties are not well defined [194, 195, 25, 196, 197, 198, 199, 200].

A gyroidal shape, one of triply periodic minimal surfaces as shown in Figure 5-7, has been proposed through atomistic computational modeling to represent the typical features of porous 3D graphene [33]. The scaling law derived from that study shows a great possibility of applying gyroid graphene to broad mechanical applications for high strength and low density. Such a gyroid graphene model enables rigorous evaluation of the thermal property of the 3D graphene structures.

Previous experimental studies have investigated thermal conductivities of graphene foams and aerogels [201, 202, 203], where extremely low thermal conductivities compared to the pristine graphene were reported. However, the quality of samples was dependent on processes much and thus, the mechanism reducing the thermal conduc-

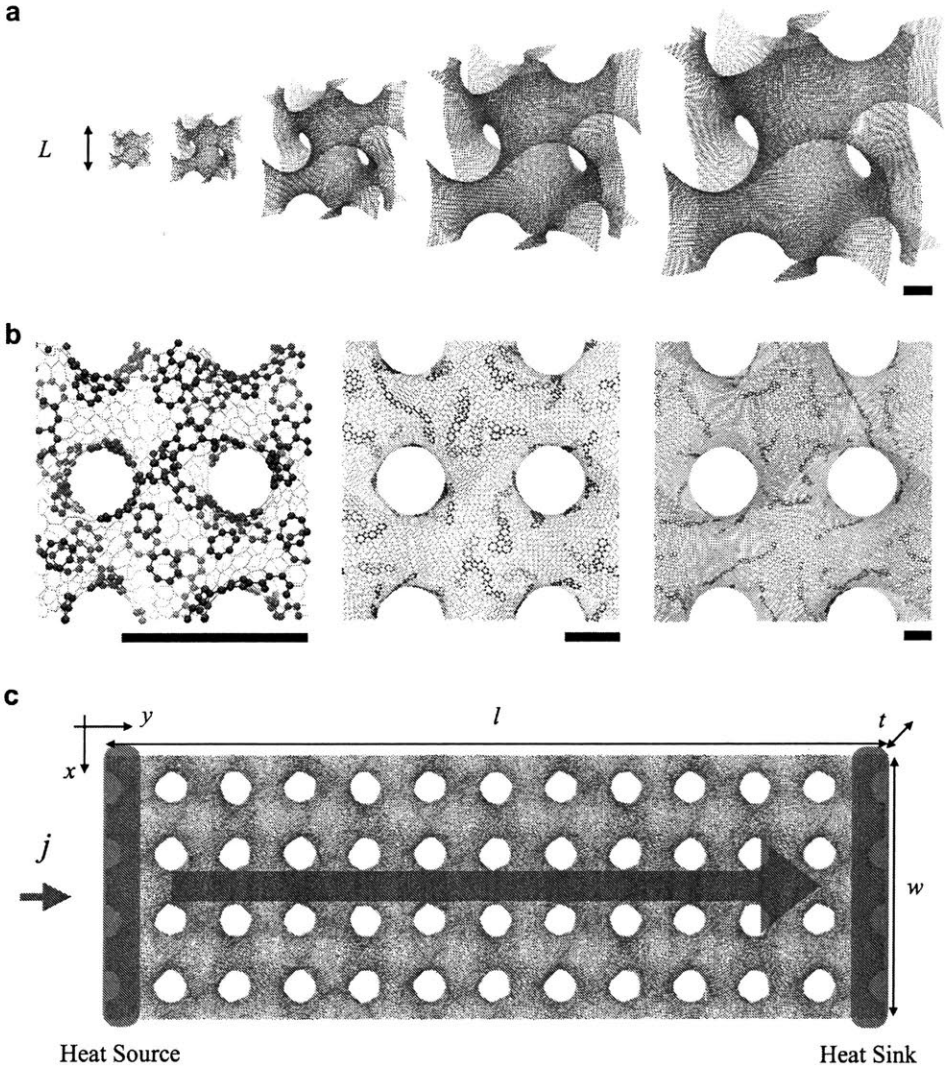

Figure 5-7: 3D gyroid graphene models and schematic for non equilibrium MD (a) Five models of gyroid graphene with different unit cell length, L =3, 5, 10, 15, 20 nm from left to right. Scale bar: 2.5 nm. (b) Spatial distribution of defects in the gyroid models: L = 3,10, and 20 nm. Red atoms indicate the atoms belong to non-hexagonal ring defects. The scale bar represents 2 nm for each model. The defects are dispersed for smooth-curves in the system (Figure D-15). (c) NEMD with a gyroid model (L =10 nm) for l = 60 nm, w=20 nm, and t=10 nm. The heat flux energy, j, is selected based on the temperature gradient. The cross-sectional areas (wt) are selected based on the standard deviation of temperatures of the temperature gradient with different system lengths (l) (Figure D-18 (b))

tivity was not clear. The porosity, defect ratios, and their distributions are possible reasons for the reduction, which cannot be individually controlled in experiments. It is intriguing to investigate how each factor plays a role in the reduction of the thermal conductivity of the 3D foam of graphene. Also, it is valuable to derive an ideal relation between the densities and thermal conductivities of graphene-based porous materials for materials design perspective. Models for mechanics and thermal properties derived from computational modeling can guide design strategies to control mechanical performance and thermal properties of such materials.

5.3.2 Methods

We relax the systems in the NPT ensemble together with the Langevin thermostat and Berendsen barostat at a low temperature of 10K to 300K for the cell parameters. Next, the Nosé-Hoover thermostat is applied to equilibrate the system at 300K for 5ps with a time step of 0.5 fs. Thereafter, the heat flux is imposed in the NVE ensemble for 0.5 ns or 1.0 ns with a timestep of 0.25 fs (0.5fs for L=15 nm and 20 nm) until steady state is obtained. The short time step is required for conserving the system's total energy while performing ensemble averaging, and the longer relaxation time is required for the longer system to attain a linear temperature gradient. Subsequently, averaged temperature gradients are obtained for 0.5 ns. Since a small cross sectional area and heat flux result in large standard deviations of temperature, we set up the system with replicated units for all simulations and scale the heat flux based on the length of the simulation box, which gives a net temperature drop of approximately 10K. Detailed information including lateral dimension, thickness, heat flux and the length is shown in Figure D-18. The temperature gradient is obtained by linear regression of the temperature profile of the system at steady state as shown in Figure D-19. All temperature gradients of models are shown in Figure D-20-D-24. The thermal conductivity is simply obtained from eq(2.8).

All models are relaxed in the NPT ensemble with the Langevin thermostat and Berendsen barostat from 10K to 300K. Next, sequential NPT, NVT, and NVE ensembles are applied at 300K for 10^6 steps for each. Finally, the data of heat current

vectors (eq(2.10)) are accumulated for 10^7 steps with the NVE ensemble. The heat current A_U tocorrelation functions (HCACF) are obtained by utilizing Fast Fourier Transform in the West (FFTW) library with C++ code and the thermal conductivities for all directions are calculated from eq(2.9). The widths of the systems are greater than 9 nm in each orthogonal direction, and the size dependence of the thermal conductivity is checked with doubled widths or thicknesses for each model.

All atomistic MD simulations and modeling are performed on the LAMMPS package. For interatomic potential, we utilize the optimized Tersoff parameters for better agreement with experimental data, as these parameters show improved fits to graphene's in-plane phonon-dispersion curves (Figure D-17).

All models are relaxed in the NPT ensemble with the Langevin thermostat and Berendsen barostat from 10K and 300K. Next, sequential NPT, NVT, and NVE ensembles are applied at 300K for 10^6 steps each. Finally, the data of heat flux vectors are accumulated for 10^7 steps with the NVE ensemble.

Detailed information including lateral dimension, thickness, heat flux and the length is shown in Figure D-18. The temperature gradient is obtained by linear regression of the temperature profile of the system at steady state as shown in Figure D-19. All temperature gradients of models are shown in Figure D-20-D-24. The HCACF and thermal conductivities of gyroid models are shown in Figure D-26.

5.3.3 Results and Discussions

In NEMD simulations, heat flux is imposed across the system in the y-direction as shown in Figure 5-7(c). The thermal conductivities of each model as a function of the system lengths are shown in Figure 5-8(a) and Table E.31. Compared to the reference value of 2D pristine graphene (1200~2000W/mK), the thermal conductivities of gyroid graphene with bulk density 5.5%~35.4% that of 2D graphene (ρ=2.3 g/cm^3) are 300 to 400 times lower. We carefully checked the convergence with respect to the lateral size because the results from NEMD vary with the simulation system lengths in the direction of the heat flux if the phonon MFP is bigger than the system length along the heat conduction direction. However, the thermal conductivity is insensitive

to the widths or thickness in the directions orthogonal to the heat flux. The models are constructed with thicknesses and widths that are greater than 9 nm because the dependence of graphene sheet's thermal conductivity on its width with NEMD is negligible if the width is larger than 5 nm. To verify that this is true, the longest system of each model is tested with twice the width or thickness. The results in Table E.33 show no significant difference.

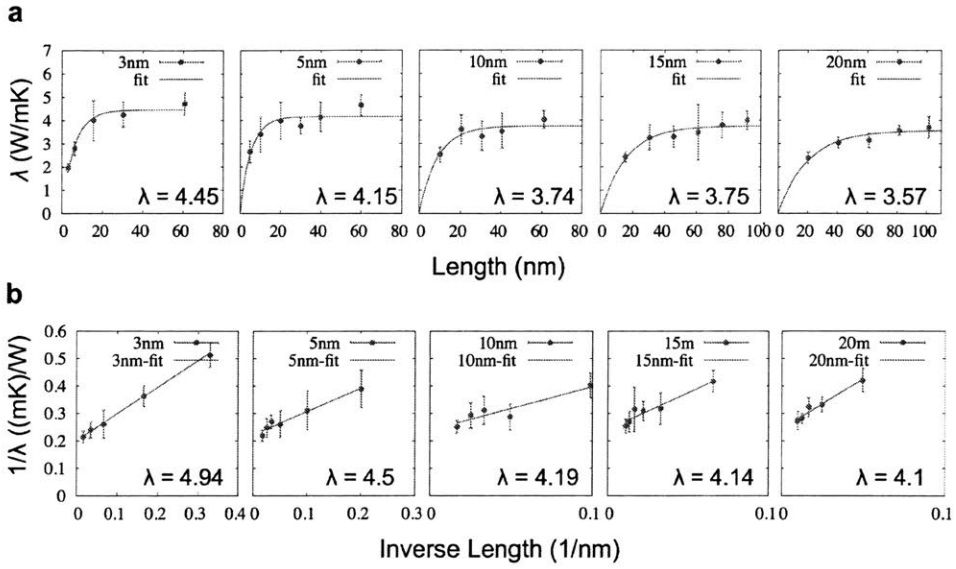

Figure 5-8: Thermal conductivities of gyroid graphene. (a) Thermal conductivities of five different models with various lengths and their fits. (b) The linear relation between the inversed thermal conductivity and inversed system lengths. The detailed data of fitted parameters are shown in Table E.31 and E.32.

A widely-used approach to obtain converged bulk limit values with NEMD is based on the linear fit of the inversed thermal conductivities and inversed system lengths as shown in Figure 5-8(b). In addition to NEMD data, the thermal conductivities calculated from equilibrium molecular dynamics (EMD) are also shown in Figure 5-9(a) and Table E.32. Comparing to pristine graphene, both methods produce very low values of thermal conductivities with similar density-insensitive trends. We note that the isotropic gyroid graphene is constructed from randomly oriented flakes with grain boundaries, which means that there should be no directional dependency in principle. However, the thermal conductivities of our models can have small variation along

different axes due to their specific geometries. The averaged standard deviation for all samples in the three directions from EMD results is sufficiently small (<0.2W/mK, Table E.32), hence the directional effects in gyroid graphene are negligible.

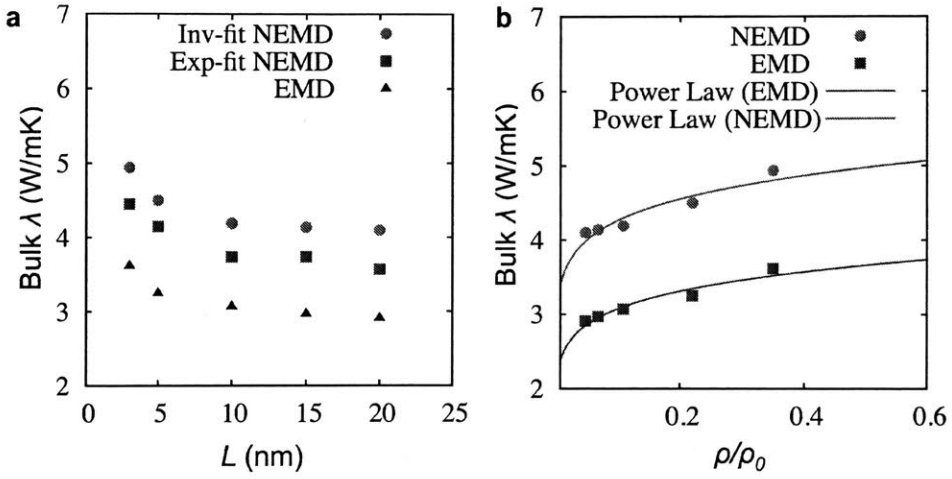

Figure 5-9: Summary of results and power laws. (a) Bulk limit of thermal conductivities of gyroid graphene with different method and fits. The detailed data of EMD are shown in Table E.32. (b) The scaling law of thermal conductivity of gyroid graphene. The obtained power laws are $\lambda = 4.0(\rho/\rho_0)^{0.11}$ and $5.3(\rho/\rho_0)^{0.097}$ for EMD and NEMD, respectively

Notably, EMD underestimates the thermal conductivities by approximately 30% in comparison to NEMD. We note here that the thermal conductivity obtained from EMD can vary based on the heat flux equation given in eq(2.10). The difference in the heat flux formulation can give a wide range of thermal conductivity of pristine graphene, ranging from 400W/mK to 1800W/mK [73]. We obtained the thermal conductivity of pristine graphene as 1200W/mK in the current study with the formulation assuming that the potential is equally divided between two atoms. Studying the effects of different formulations considering many body terms is not considered here, but the variation (from the current formulation, approximately 50% $\sim$ 150%) can explain the underestimation compared to NEMD because the thermal conductivity of pristine graphene from NEMD reaches around 2000W/mK for a 1000 nm strip [204]. Thus, both methods predict significant drops of thermal conductivity compared to the pristine graphene.

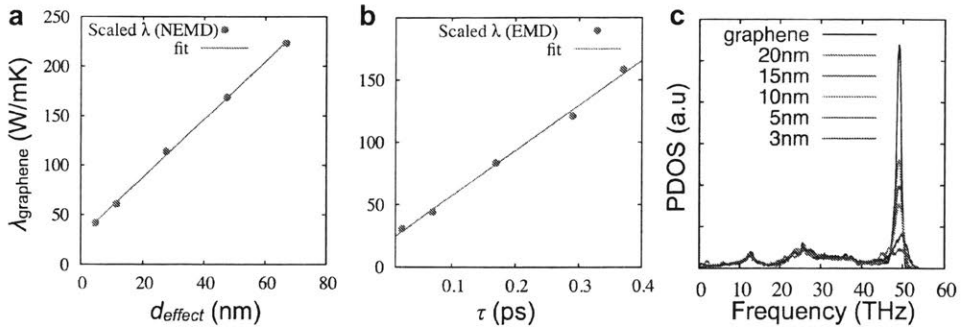

Figure 5-10: (a) The linear relation between the effective distance (deffect) between defects and the scaled thermal conductivity from NEMD based on the eq(5.3). (b) The linear relation between the relaxation time (τ) and the scaled thermal conductivity from EMD. (c) Phonon density of states obtained from PDOS

The results from our study suggest a scaling law for the thermal conductivity of gyroid graphene or porous foams of 3D graphene as a function of scaled density. The thermal conductivity of conventional porous materials such as silica aerogel follows the power law as [205]

$$\lambda = C\left(\frac{\rho}{\rho_0}\right)^{\alpha}, \tag{5.1}$$

where C is a parameter including the effects of the porosity; ρ_0 is the density of bulk silica; ρ is the density of silica aerogel; and α is approximately 1.6 for the densities between 0.3 to 1.0g/cm^3. However, 3D porous structures composed of monolayer graphene show significantly different behaviors, because the thermal conductivity of the 2D graphene that constitutes the gyroid graphene changes significantly with varying density as well. The power law we obtained from the five gyroid models is shown in Figure 5-9(b). The obtained α is around 0.1, showing little dependency on the scaled density. The exact expressions are $4.0(\rho/\rho_{graphene})^{0.11}$ and $5.3(\rho/\rho_{graphene})^{0.097}$ from EMD and NEMD, respectively. Based on the volume fraction ($\phi = V_{graphene}/V_{total}$), we can estimate the thermal conductivity of the graphene with defects as suggested from the previous study [202] as

$$\lambda_{graphene} = (3/\phi)\lambda \tag{5.2}$$

where ϕ is volume fraction ($V_{graphene}/V_{total}$) and can be obtained from $\rho/\rho_{graphene}$, where $\rho_{graphene}$=2.3 g/cm^3 is the density of planar graphene. The thermal conductivity of defected and curved graphene ($\lambda_{graphene}$) is reduced to 13% (L =20 nm) to 2% (L =3 nm) that of pristine graphene. Based on the obtained power law, the thermal conductivity of graphene recovers from 2% of the pristine graphene at ρ ~800mg/cm^3 to 2000W/mK, approximately at ρ ~10mg/cm^3.

There are several possible reasons for the reduction of the thermal conductivity of the graphene sheet that makes up gyroid graphene. One reason is that the disorder ratio (β) depends on the density as shown in the Table E.30. Previous studies have reported that the grain boundaries and various defects can reduce the thermal conductivity of graphene. Wu *et al.* have reported a 70% reduction in thermal conductivity, with grain boundaries in the polycrystalline graphene and approximately 10% defects, due to the reduction of the phonon life-time [78]. In that study, the polycrystalline graphene was considered to be a two-phase composite consisting of defects and pristine regions. The disordered grain boundary regions possessed only 5% of the thermal conductivity of the pristine graphene. Other studies also show significant drops of the thermal conductivity due to various defects such as Stone-Thrower-Wales (STW) defects, 5-7, and 5-8 pairs [206, 207]. We note that the defects of the gyroid graphene are dispersed more uniformly (Figure 5-7 (b) and Figure D-15) compared to polycrystalline graphene. Since the vibration of atoms near defects is influenced by the defects, more atoms are affected by the defects with well-dispersed defects, which can decrease the thermal conductivity more than polycrystalline graphene with the same defect ratio. Also, the dependence of thermal conductivity on temperature is determined at 200K, 300K, and 400K, showing that the trend with different disorder ratios (grain sizes) in Table E.34 agrees with that of polycrystalline graphene in recent simulations [75] and experiments [208].

Another feature of gyroid graphene is the curvatures induced by the defects. The dislocations and pentagon-heptagon defects will cause curvatures in pristine portions of the graphene sheet as they undergo torsional deformation and changing lattice direction along the direction of heat flux. Limited studies reported the effects of

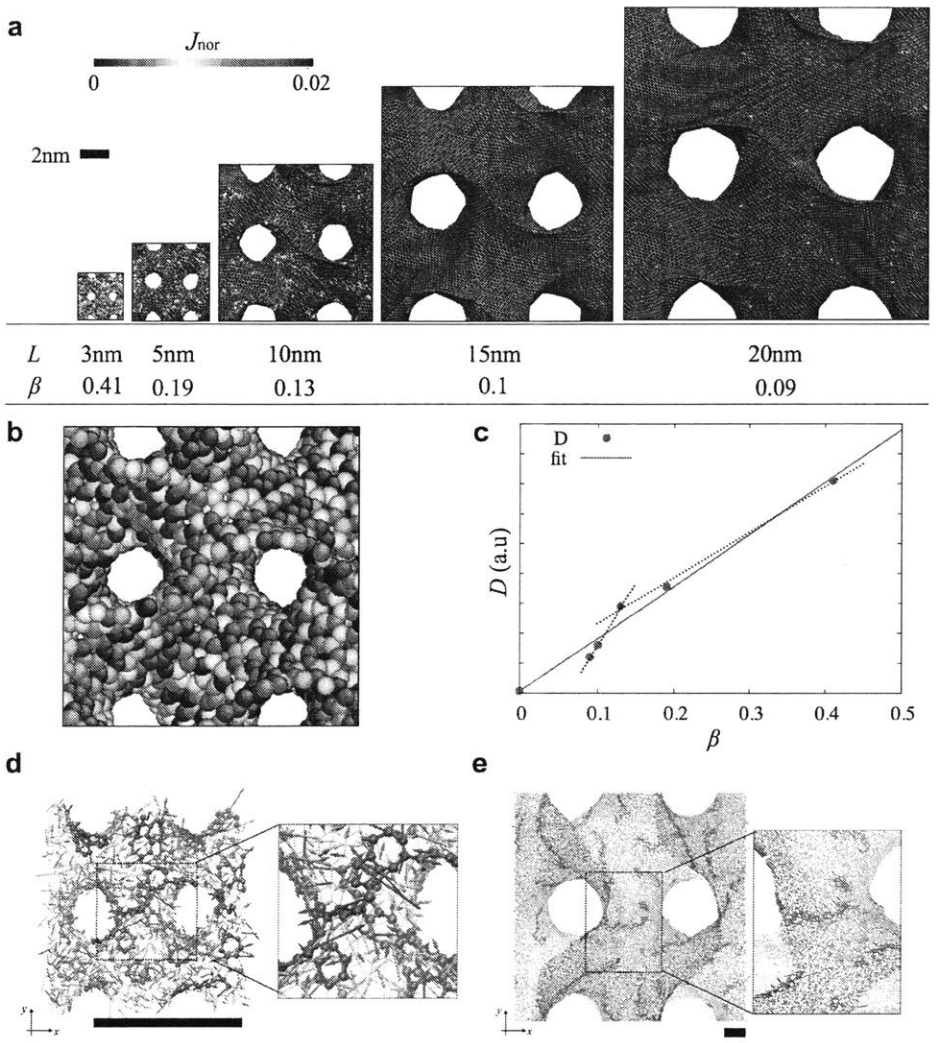

Figure 5-11: (a) The spatial distribution of the norm of the normalized atomic heat flux (J_{nor}) for gyroid graphenes. The higher value means more localization of heat flux and more energy dissipation. As the level of disorder increases, the system has more atoms having high J_{nor}. Also, the distribution of high J_{nor} changes from localizing near the defect to dispersing all over the system. (b) The spatial distribution of the atomic heat flux for the smallest gyroid graphene ($L = 3$ nm). (c) Dissipation factor (arbitrary unit) as a function of the level of disorder (β). The factor increases faster at a low level of disorder than at a high level of disorder because the localization already happens with non-defect atoms with highly disordered system. The dashed blue lines show different gradients in two different regions ($\beta < 0.13$ and $\beta > 0.13$). Normalized atomic heat flux vectors of gyroid model for $L = 3$ nm (d) and for $L = 20$ nm (e); Red colors indicate defects. The pristine graphene shows homogenous and clear directionality of the heat flux in the y-direction compared to gyroid models. The difference of norms between the defect and non-defect atoms is not clear with highly disordered system ($L = 3$ nm), while distinct localization of heat flux is observed with less disordered system ($L = 20$ nm). The scale bar represents 2 nm for each model.

graphene curvature or folding [209, 34], which can decrease the thermal conductivity by approximately 30% to 70%. Although the effects of strain and various defects have been separately studied in previous work, the effects of the curvatures induced by dislocations and 5-7 defects have not been systematically studied and need to be scrutinized. A similar three dimensional systems called Schwarzites having triply periodic minimal surfaces, have been studied by Pereira *et al* [210]. The thermal conductivities of Schwarzites are reported to be as low as 20W/mK. The main reason for the reduction of the thermal conductivities is much smaller phonon MFP. Although the system sizes of our models are prohibitively large for analyzing the phonon properties with anharmonic lattice dynamics, we can estimate the effects of the shortened MFP from the averaged distances between defects and a single-mode relaxation time approximation.

Firstly, we estimate the averaged distances between defect atoms to obtain insights into the phonon MFP due to the defects. The defects of the gyroid graphene are uniformly distributed in the system to sustain the structural features as shown in Figure 5-7 (b). The area of gyroid graphene sheet is proportional to L^2. Assuming the defects are homogenously distributed in the sheet, the averaged distances between defects can be expressed as

$$d_{defect} \propto \frac{L}{\sqrt{\beta}} \tag{5.3}$$

where L and β are the unit length of the model and defect ratio, respectively. For gyroid graphene structures, since the shorter L requires more defects for the higher curvatures, L decreases as β increases, leading to smaller ddefect. We note that ddefect is proportional to the effective distance between defects and MFP. The averaged distance ddefect has a strong linear relation (R^2=0.999) with $\lambda_{graphene}$ from eq(5.2) as shown in Figure 5-10 (a), which means that the major drop of the thermal conductivity of graphene sheet is caused by shortened MFP due to the distributed defects in the system.

Secondly, the acoustic mode relaxation time is obtained from the heat current au-

tocorrelation function (HCACF). The relaxation times for the slow acoustic mode are obtained from fitting functions and listed in Table E.32. Based on the single-mode approximation36, the overall phonon scattering is proportional to $1/\tau$. The relaxation time of the gyroid samples are 20 to 400 times shorter than that of graphene, which means the phonons are scattered much more frequently and thus, there is more localization of thermal energy transfer in gyroid graphene. The relaxation time and the $\lambda_{graphene}$ obtained from the eq(5.2) also have a linear relation (R^2=0.99) as shown in Figure 5-11 (b), meaning the scattering is a critical factor of the reduction. Since the reduction of relaxation time results in shortening MFP (eq(2.7)), the reduction comes from the shortened MFP, consistent with the discussion in the previous section.

Finally, we examine the phonon density of states (PDOS) of the gyroid graphene to investigate the contribution of the heat capacity to the thermal conductivity in eq(2.7). Both gyroid graphene and monolayer graphene over 5 ps are shown in Figure 5-10 (c) (separated graphs are provided in Figure D-16). The overall peaks and shape does not change much except around 50 THz. This trend is very similar with those of polycrystalline graphene reported in the previous study. Although there is a significant change around 50THz, the contribution of high frequencies to the specific heat is not important (Only 2.5%, compared to that of 10THz). Considering the fact that the thermal conductivity has a linear relation with the relaxation time (Figure 5-10 (b) and eq(2.7)), and the effect of specific heat is not significant from PDOS, we can deduce that the effect of group velocity is negligible compared to the effect of the relaxation time. Thus, we can conclude that the main reduction of $\lambda_{graphene}$ comes from the short MFP due to the high scattering rate (shorten relaxation time) and dispersed defects, which appears with localization of heat flux [211].

For better insight into the localization of thermal energy transfer, we obtain the atomic heat flux from NEMD as $J_i = -S_i v_i$, where v_i, and S_i are the atomic energy, velocity, and stress tensors. We need to normalize the atomic heat flux because the values vary with factors like the total heat flux energy, system size, and the thermal conductivity. The normalized spatial distributions of the atomic heat flux in the gyroid models are shown in Figure 5-11 (a) and (b). Then, we define dissipation

factor (D) to understand how the localized heat flux changes with its density (See Method part). The D factors of gyroid models and pristine graphene as a function of the disorder ratio β are shown in Figure 5-11 (c), clearly showing that the defects cause more localized heat flux. The overall trend is linear between β and D, and notably the gradient of the region between β=0 and 0.13 is steeper than that of systems with higher disorder (β>0.13). As shown in Figure 5-11(a), the higher J_{nor} is localized near the defects in the systems with lower levels of disorder (β<0.13), but non-defect atoms also have high J_{nor} in the system with higher levels of disorder (β>0.13). Thus, the localization increases faster at a low level of disorder than at a high level of disorder because the localization already happens with non-defect atoms in the highly disordered system. The localization of thermal energy at non-defect atoms is induced by curvatures. This can be clearly seen from the vector maps of the models; the vector maps of gyroid models (L=3, 20 nm) are shown in Figure 5-11 (d) and (e) (Figure D-27-D-30 for other models and graphene). The atomic heat flux vectors (J) lie along the lattice direction of graphene, and the overall heat flux directionality of the whole system (Figure D-27) and the difference of norms between the defect and non-defect atoms are not clear with highly disordered system (β>0.13) compared to pristine graphene as shown in Figure 5-11 (d). Conversely, the localization of the heat flux (showing larger norms of the vectors than others) becomes distinct near the defects as the system size increases (β<0.13) as shown in Figure 5-11 (e). The disturbed directionality of the heat flux vectors due to the curved lattices can cause the localization of heat flux with the non-defect atoms, which explains why the thermal conductivity show much lower values than planar systems with defects. This is the common feature of the 3D structures generated from 2D materials and thus our understanding of the thermal conductivity gain from the current work may be applicable to other 2D materials with 3D porous structures.

5.3.4 Conclusions

In this section, the thermal conductivities of 3D gyroid graphene are studied on the basis of molecular dynamics. Both non-equilibrium and equilibrium MD methods

show that these gyroid graphenes have extremely low thermal conductivities (more than 300 times lower with one-third the density of graphene) compared to those of pristine graphene and carbon nanotubes. From the derived power law, we have revealed that the thermal conductivity does not depend on the density as much as conventional porous materials, such as silica aerogels, because the thermal conductivity of the constitutive graphene sheets decreases significantly. Based on the low thermal conductivity and the mechanical stability with a very low density, the gyroid graphene can be one of the best candidates for superior construction or composite materials. We find that the main reasons for the reduction are the porosities and shorter phonon mean free paths due to dispersed defects. Also, the curved lattice direction can increase the scattering even at sites with the non-defect atoms, which is the key feature of the 3D structures assembled from 2D materials. This study can provide a design rule for higher thermal conductivity of 3D graphene foam. For example, we can design 3D graphene structures with heterogeneous material density distribution as well as anisotropic thermal conductivity for efficient thermal management and mechanical function such as facades with energy efficiency.

5.4 3D surface of TMD materials

5.4.1 Introduction

In this section, MD based growth models of TMD monolayers are proposed. Various substrates are utilized for CVD method for TMD such as silicon nitride (Si_3N_4), silica(SiO_2), and sapphire (aluminum oxide). The unveiled growth mechanisms are the chemical reaction with the precursors of metal and chalcogenide and diffusion on the substrates. The lattice orientation of the substrates is less critical, but the lattice directions of initial seed play a vital role in the crystal growth. Therefore, the details of diffusion can be ignored to obtain the grown crystals from the initial seed. The morphology of grain shape depends on the chemical environments such as dependent the local metal-rich or S-rich conditions. The defects and structures at the grain

boundary depend on at the mismatching angles between grains. When the substrate is corrugated with positive and negative curvatures, the crystal growing process can be affected by the accumulated strain energy from the substrates. First, the proposed models show the grain boundary from two tilted grains can be formed. Second, the models show how the single grain can branch on the negative or positive curvatures.

5.4.2 Methods

Growth of tilted triangular WS_2 seeds on the flat surface

MD simulations for crystal growth and grain boundary formation in this study are performed via a LAMMPS package. The crystal growth model utilizes the previously proposed method of building atomic structures of polycrystalline graphene by combining MD and Monte Carlo (MC) method. In the process, energetically favored structures are selected by geometries and bond numbers, and further relaxed by MD runs. It can quickly accept or decline the new configuration based on the geometries of defects and has successfully generated well-stitched polycrystalline graphene. In the same way, models iteratively apply a growth algorithm for WS_2 monolayer based on the bond number. Figure 5-12(a) presents four steps of the algorithm for the one iteration from a given WS_2 seed to the next seed to be relaxed by MD simulations. Different from graphene, WS_2 has three atoms-thick structures (i). To obtain a correct bond number, we project sulfide atoms positions on flat surfaces by averaging the locations of the top and bottom sulfides, which allows us to calculate the bond number based on the distance between W and S atoms (ii). Then, we add the W or S atoms to the desired position based on newly tuned criterions (iii) will be described in the following section. Finally, 3D structures are reconstructed from the projected positions for the next structural relaxation MD (iv). The relaxation of each step uses the NVT ensemble more than 2000 steps with 1fs time step and energy minimization. The most important part of the growth method is adding or removing the atoms in the step (iii). After removing the atoms having the bond number more than four, atoms are added only near to the reference atoms having the bond number one or

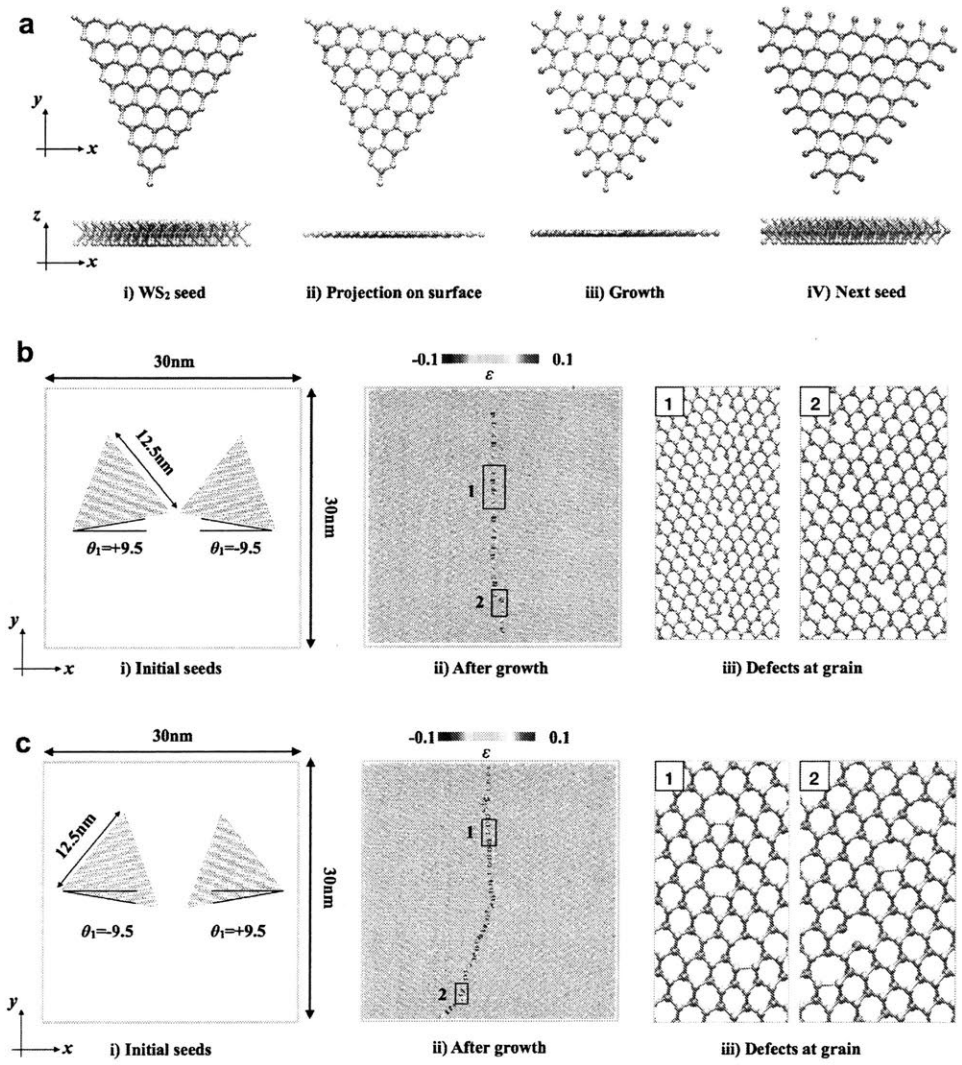

Figure 5-12: (a) The schematic of the growth algorithm from a relaxed seed of WS_2 (i) to the next seed (iv). To obtain accurate bond information of each atom, the projection the 3D geometries on the flat surface (ii) is required. After adding W or S atoms on the surface (iii), the three-atom-thick structure (iv) is generated from the 2D geometries. (b)-(c) Crystal growth and grain boundary structures with two different angles for 19° mismatching. The strain (ϵ) is calculated from the relative bond lengths between W-S projected into the x-y plane. The defects at the grain boundary structures are obtained from further relaxation of MD simulations.

two. If the bond number of the atom is one, two atoms (W or S, as an opposite type of the reference atoms) are added. If the bond number of the reference atom is two, one atom is attached. In this case, if two bonded atoms are the same type, the additional atom follows the atom type while if the two bonded atoms are different; the new atom type is randomly selected. The variance on the position of new atoms is added based on the Monte Carlo method. If the distances between the added atom and pre-existing atoms are not long enough, the atoms are rejected. Unlike polycrystalline graphene, there are more kinds of defects at the grain boundary in CVD grown TMD monolayer. We only remove S atoms having bond number two and larger angle than 150° to have reported defect types in previous studies [164, 212, 213, 154]. A box of 30 nm x 30 nm x 10 nm is prepared to obtain the structure of grain boundary with 19° mismatch with S edge triangular seeds. The lateral length of the triangular seed is 12.5nm.

MoS_2 growth on curved surfaces

Several studies have been reported for models of grain boundaries or defects in two-dimensional materials on a curved surface. Mostly, the proposed methods are based on total energy estimation or energy barrier between transition states. Wang *et al.*, report a finite length of grain boundaries of graphene and MoS_2 on a non-zero Gaussian curvature based on kinetic Monte Carlo method [214]. Phase field methods have been utilized to build curved atomic structures of graphene [172, 185]. While those methods do not require pre-knowledge of defect types, the system sizes are limited because one needs to evaluate energy of randomly selected states to evolve and the other needs to minimize the total energy of the entire system. The growth models on the flat surface are extended to describe the various defects at the grain boundaries of MoS_2 and see how the defects and grains are evolved due to the strain coming from the curved substrates. The REBO potential is utilized to describe the interatomic interaction of MoS_2 monolayer. To constrain surface during the evolution,

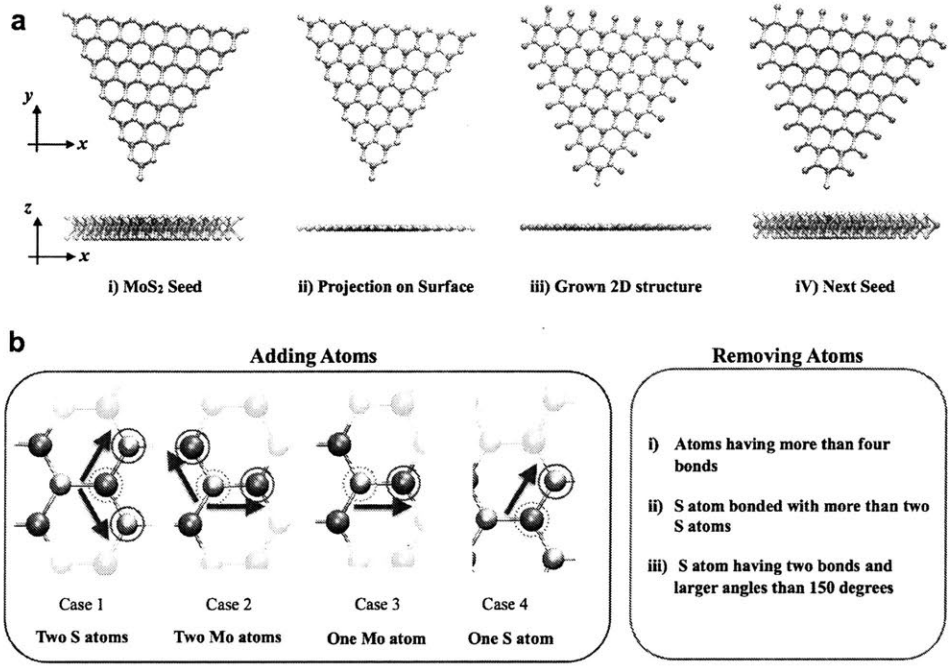

Figure 5-13: The schematic of the curved surface with two mathematical functions. The sphere function cannot exist on the flat surface because there is a discontinuity of the first derivative that makes singularity between two surfaces. The Gaussian function is introduced between the sphere and flat surface to remove the discontinuity.

analytical forms of a sphere and Gaussian curve are utilized ($V_{Surface}$):

$$V_{Sphere} = z - \sqrt{R^2 - r^2}, \qquad r^2(= x^2 + y^2) < r_t^2,$$
$$V_{Gaussian} = z - \sqrt{(R^2 - r_t^2)\exp(-b(r^2 - r_t^2))}, \qquad r^2 > r_t^2, \tag{5.4}$$

where the R is the radius of a sphere; r_t is the transition point from sphere function to Gaussian function; b is a coefficient related to dispersion of the Gaussian function in Figure 5-13. The Gaussian function plays a role in the transition function from the flat surface to positive curvature. The constraint function is applied on Mo atoms:

$$E_{Mo} = E_{REBO} + \lambda \sum V_{surface}^2, \tag{5.5}$$

where λ was set as 50eV while S atoms are controlled by E_{REBO}; $V_{Surface}$ is the surface equations of the sphere and Gaussian. The modified potential allows Mo atoms deform only on the surface during the structural relaxation. Then, the same iterative growth algorithm of WS_2 on the flat surface is applied in Figure 5-14.

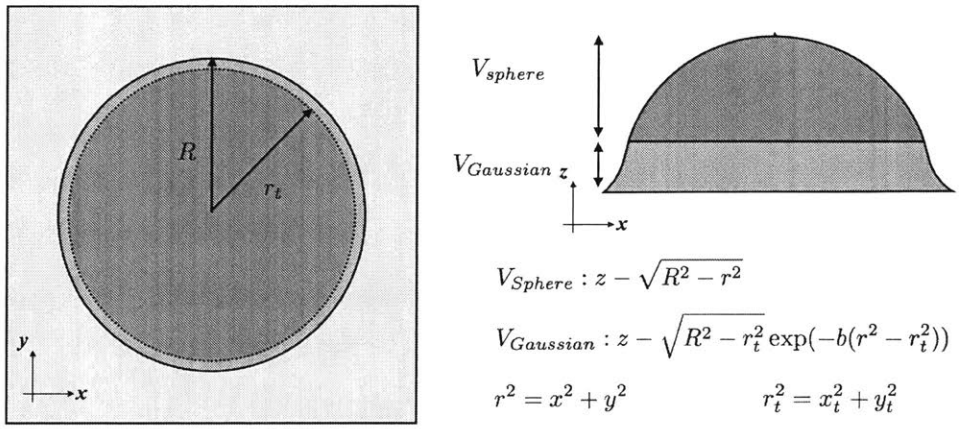

Figure 5-14: (a) The schematic of the growth algorithm from the relaxed seed (i) to the next seed (iv) for relaxation. To obtain accurate bond information of each atom, the projection the 3D geometries on the surface (ii) is required. After adding Mo or S atoms on the surface, the 2D geometries are transferred to have three-atom-thick structures (iii). (b) The adding and removing atoms based on the bond information in panel (a)-(iii).

5.4.3 Results and Discussions

Figure 5-12(b) and (c) show the grain boundary and defects from the initial angles of WS_2 monolayer seeds. A central part of each seed is fixed during the MD relaxation to prevent undesired rotation. The only mirrored seeds are considered in the examples while the relative displacement along the y direction can change the grain boundary to have meandering paths. Figures 5-15 and (Figure D-31) show the results of crystal

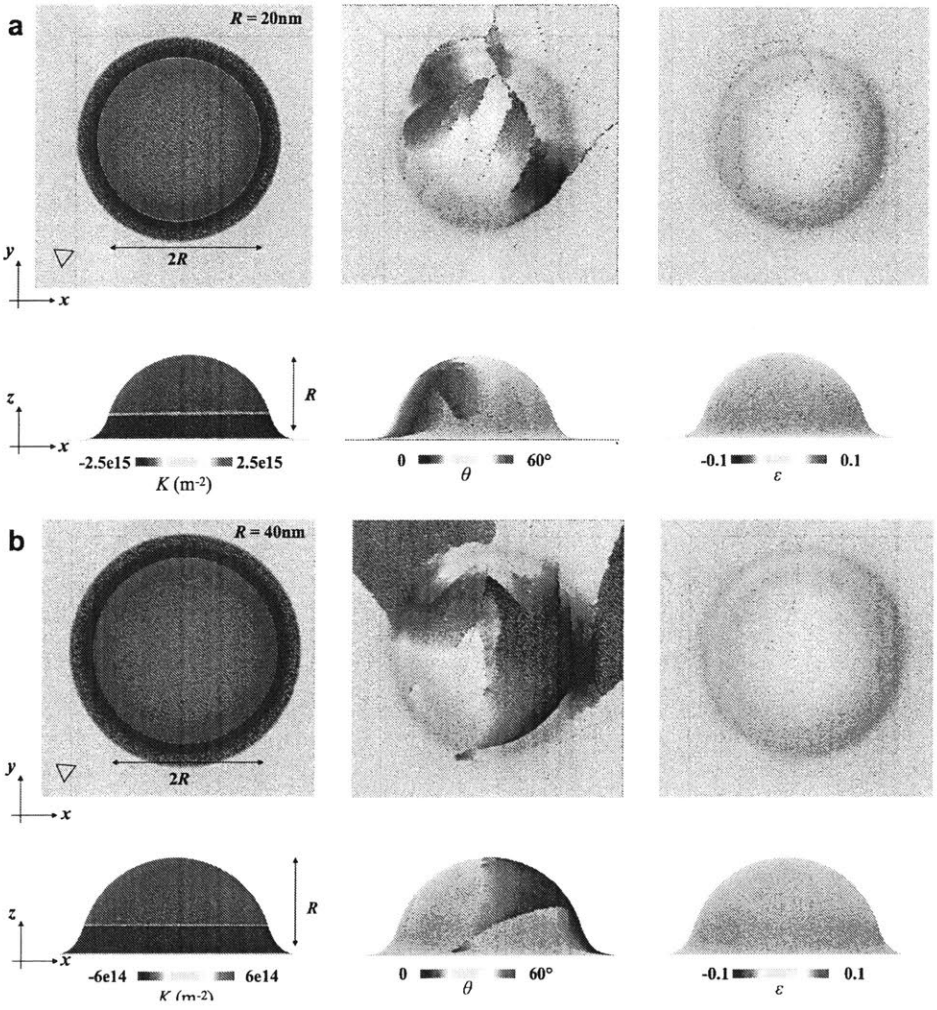

Figure 5-15: Crystal growth of MoS_2 with R=20 nm (a) and R=40 nm (b) curvature. K is the Gaussian curvature of the surface; θ is the lattice angle obtained from projected lattice on the flat surface; ϵ is strain calculated from bond length between Mo and S where the S position is projected on the curved surface. Triangles represent the positions and orientation of initial seeds.

growth of MoS_2 from the flat surface. The initial triangular seed is located on the flat surface. As the crystal growth, it edge of triangle first meet the negative curvature on the Gaussian surface. The negative curvature on the Gaussian surface allows the grain branches into multiple regions by Mo-S bond breaking. When the grain grows on the positive curvature of the sphere surface, other grains are generated by the deletion of lattice and the formation of dislocation. The generated dislocations change the angle of grains and form a long grain boundary. In the end, complicated grain distributions are obtained Next, the initial seed is located on the center of the half sphere to see the effect of curvature on the initiation of the deletion. Figure 5-16 (Figure D-32) shows the results after the seed grows. The results show a clear tendency that pristine grain size depends on the curvatures. As the positive curvature increases, the grain size gets smaller. The grains from the center show more symmetric distribution compared with those from the flat region in Figure 5-15.

5.4.4 Conclusions

The MD-based crystal growth models are proposed and utilized to predict the grain boundary structure with tilted angles with monolayer WS_2. The types of defects formed at the grain boundary show good agreement with previously reported defects. The models are further extended to understand and model the grains on the curved surface. The grain distributions on the curved surface actively interact with curvatures, and the behaviors are different between positive and negative curvatures. The initial locations of seeds govern the overall geometries of grains, and the curvature controls the size of the pristine region.

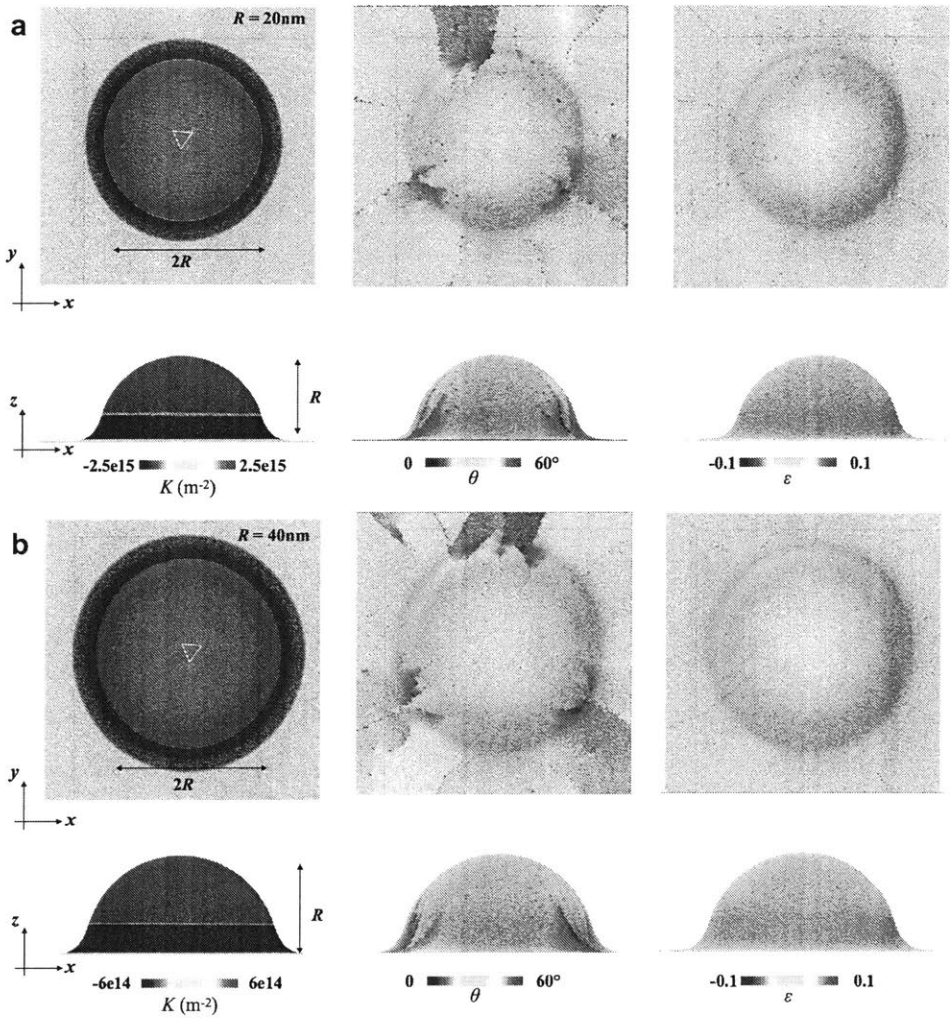

Figure 5-16: Crystal growth of MoS_2 with R=20 nm (a) and R=40 nm (b) curvature from the center of the sphere. K is the Gaussian curvature of the surface; θ is the lattice angle obtained from projected lattice on the flat surface; ϵ is strain calculated from bond length between Mo and S where the S position is projected on the curved surface. Triangles represent the positions and orientation of initial seeds.

Chapter 6

Conclusion, Discussions, and Future

6.1 Review of key findings and their significance

Two-dimensional (2D) materials provide not only provide exciting new material properties, but also excellent platforms to validate theoretical models by direct comparing atomic structures from DFT (density functional theory) calculations, reactive MD (molecular dynamics), CGMD (coarse-grained MD), KMC (kinetic monte carlo), to FEM (finite element method) including phase field models with their intrinsically multiscale features having atomically thin thickness but wafer scale area. The multiscale modeling paradigm becomes more critical when the available macroscale models are not accurate enough, but microscale models are not efficient enough. The typical strategy is a bottom-up approach by deriving parameters required for the macroscale models from the microscale models. In principle, the interaction of atoms in quantum mechanics based on many-body electrons can provide sufficient information to understand most of chemistry, physics, biology, materials science and engineering problems. However, the development of a scaled-up model (e.g., molecular dynamics from quantum mechanics) should be validated because the approximation of the many-body effects for scaling up is not straightforward, and some information is dropped.

In this thesis, I developed reactive MD models for transition metal dichalcogenides *e.g.*, MoS_2, WS_2, $MoSe_2$, and WSe_2. The models can innately describe not only their mechanical behaviors of single crystals but also those of the bilayers and covalently

bonded heterostructures. The key strategy in my development is matching the non-linearity of stress-strain and failure strains of single crystals of MD to DFT calculations. The non-linearity of mechanical properties is critical to validate the developed models by comparison with advanced TEM images conducted by experimental work [35, 37, 103, 36]. I also devise methods to generate well-stitched polycrystalline crystals based on reported dislocation and defects at the grain boundary. The method is further extended to create intricate three-dimensional surface structures such as three different types of triply minimal surfaces, and roughened surfaces with non-zero and non-negative Gaussian curvature.

The validated models are utilized to understand mechanical, thermal and electronic properties related to the structures of 2D materials through further calculations of DFT for electronics and accurate defect formation energy, reactive MD with well-controlled boundary conditions, and comparison with continuum theory. I summarize the important mechanisms unveiled in the thesis as follows:

1. Fracture is one of the most foundational concerns in physical science and engineering governing a wide range of material failure. In this thesis, the atomic-scale mechanisms of crack-tip behaviors in 2D MoS_2 and WS_2 crystals are studied including the effects from the sulfur vacancies and bilayer. The crack propagation becomes slower because the sulfur vacancies make the system metallic and plastic. Different from graphene, TMD materials have a three-atomic thickness, which causes geometrical interlocking to enhance the layer-to-layer friction. The friction plays a critical role in the crack propagation, and the friction mechanisms can explain various fracture patterns experimentally observed in the bilayer MoS_2. The lattice structures of TMD materials have a different symmetry (D_{3h}) [215] from monoatomic 2D crystal such as graphene [216] (D_{6h}) although they have the primitive hexagonal cell. The loss of inversion symmetry allows the propagation anisotropy along the armchair direction in WS_2 monolayer. Conventional linear elastic fracture mechanics (LEFM) cannot explain the mechanisms because such anisotropy has not been considered as a parameter in LEFM framework.

2. The grain boundary and topological defects at the boundary are essential fea-

tures of 2D materials. The prediction of the atomic structures at the grain boundary is a challenging task in atomic scale modeling. The advanced TEM provides representative structures of topological defects at the grain boundary, *e.g.*, pentagon and heptagon in graphene. I propose a method for the generation of polycrystalline graphene with randomly distributed grains by merely utilizing the reported geometries. The fracture toughness from the developed models agrees with the previous experimental measurement, which was not realized in the former MD studies. Also, the models reveal the crucial role of out-of-plane deformation on the fracture toughness. The reactive MD models are utilized to unveil the catalytic function of 5|7 dislocation at the border of a hetero-junction between MoS_2 and WSe_2 for 1D MoS_2 channel growth in WSe_2.

3. One of the main goals of this thesis is to provide an efficient design tool for 2D materials. By utilizing the developed MD models and methods, I propose a method to generate three-dimensional graphene. Three different types of triply periodic minimal surface (TPMS), *e.g.*, D, P, and G, are made to derive scaling laws of mechanical and thermal properties. The results provide the mechanisms for how the newly designed structures behave differently from conventional porous materials and 2D materials. Finally, the crystal growth method of TMD materials on the arbitrary surface is proposed. The method can predict the grain boundary structures from two tilted grains on the flat surface. Furthermore, the models can provide grain distributions on the curved surface.

6.2 Possibilities for future research

Fracture is one of the most prominent multiscale phenomena, including atomic bond breaking and macroscale crack propagation [104, 105, 106, 119]. Several models have been developed to understand the crack-tip behaviors and fracture patterns of various materials [30]. This thesis provides insights into the mechanics including crack propagations in the crystalline materials, which were not captured in the conventional fracture theory and bulk crystals.

The unveiled atomic-scale mechanisms such as the anisotropic propagation due to the atomic lattice distortion, are not limited to the nanoscale. Also, the importance of local inelasticity is aligned with the findings in the previous studies [118]. Many earlier studies including 2D material failure have been performed based on different types of forcefields or potentials without carefully checking the non-linearity of stress-strain curves with DFT calculations. Instead, elasticity and ground state energy have been the standards to describe failure. Results in this thesis clearly show that atomic-scale non-linearity comparable with quantum mechanics would be mandatory to develop macroscale models, such as CGMD and FEM. In this section, I discuss possible research directions in the future.

MD is a useful tool to investigate nanoscale to microscale deformation and dynamics such as wrinkles, ripples, crumples, and crack propagation of 2D materials [217, 218]. In this thesis, the REBO can provide relatively larger size and comparable behaviors of failure and deformation with DFT calculations and experimental observations. While there are many emerging nano- and low-dimensional materials and their heterostructures the development of the forcefields is limited due to the complexity of the forcefield.

One direction is to develop a multiscale framework utilizing the genetic algorithm and coarse-grained models. The critical bottleneck of up-scaling from DFT to MD is a parameterization. The genetic algorithm with a large amount of training data can provide a systematic, reliable and automated way for parameterization. The availability of increasingly reliable parameters of various 2D materials offer more opportunities to reveal atomic structures, deformation, and mechanisms of failure and synthesis process for multiple applications at least up to the 100 nm scale. The REBO potential can be further simplified if one considers only bond breaking and failure of pristine crystals. The simplified formulations can provide accessibility to larger scale system sizes in 2D materials. To handle larger systems, it is also possible to use coarse-grained models.

Regarding three-dimensional designs of materials, exploring the electronics and optical properties coupled with mechanics is an intriguing direction. It is difficult to

investigate the scaling laws of optoelectronic properties due to the sizes that DFT can handle. However, the smallest one is possible to manage with DFTB method. A more feasible way is to build different curvatures of surfaces as a component of entire structures and study the properties of the parts. One may find a general relation between a certain electronic or optical properties and the given curvatures. Then, it would be possible to build FEM models by connecting parts. Since 2D materials are very thin and flexible, coupling with mechanical deformation can provide opportunities for various applications, *e.g.*, energy, filtration, and semiconducting devices.

For the crystal growth model, the current model assumes an optimal growth condition such as triangular morphology and defect types at boundaries of TMD materials missing synthesis conditions such as precursors and temperatures. It is possible to include the effects of synthesis conditions by exploring the impact of chemical enviro nments and temperatures. Then, the growth models can predict the quality of grain boundary structures at the different chemical enviro nments, for example, metal-rich condition or chalcogenide-rich condition. The predicted atomic structure would provide not only the mechanical properties but also electron transfer, band structures, and chemical reaction at the defects. The growth models also can provide useful information such as the critical elastic energy for branching grains on the surfaces with different curvatures, which was not possible to obtain directly from the experiments. The data can be up-scaled to the continuum level theory such as phase field theory for grain boundary and growth.

Appendix A

Supplementary Figures for Chapter 2: Methodology

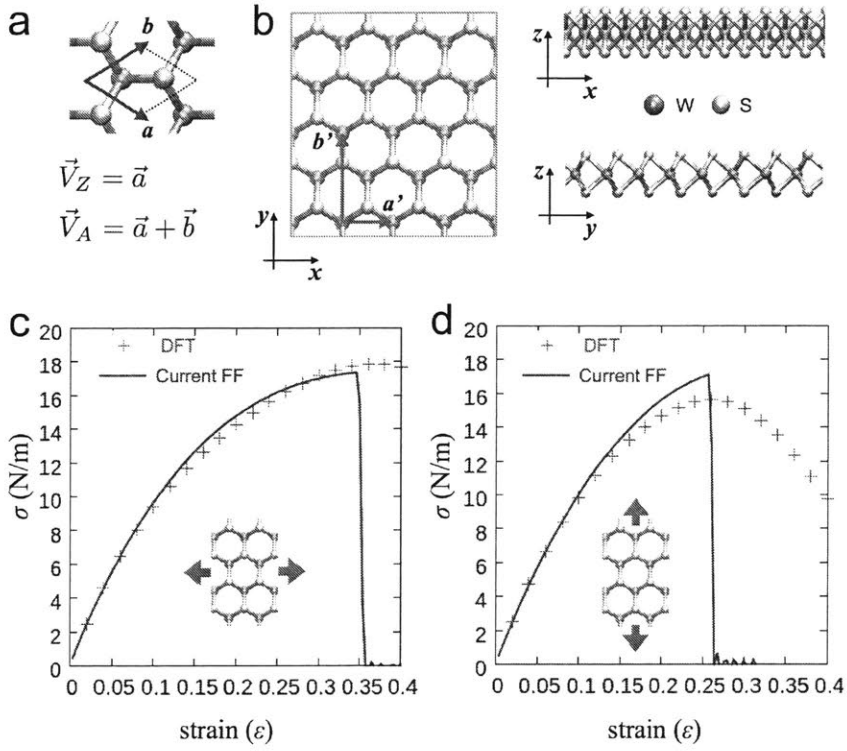

Figure A-1: (a) The hexagonal unit cell of WS_2 with lattice parameters a and b. For simplicity, we define the crack propagation directions as V_Z= a (zigzag, [100]) and V_A= a + b (armchair, [110]). We only distinguish the crack propagation direction V_A and from $-V_A$, because they show different crack propagation patterns but do not distinguish $-V_Z$ from V_Z. (b) The geometries of monolayer MD simulations in the current study. The x and y directions are aligned along V_Z and V_A directions, respectively. To distinguish the crack propagation direction from the loading direction, we define the loading directions in the x and y direction as 'zz' (zigzag) and 'ac' (armchair), respectively. The stress-strain curves under the uniaxial tensile loadings in the zz (c) and ac (d) directions with a plane strain condition. The failure strain and strength from the current REBO are well matched with those from DFT calculations. The stress unit (N/m) is used to ignore the uncertainty of the thickness.

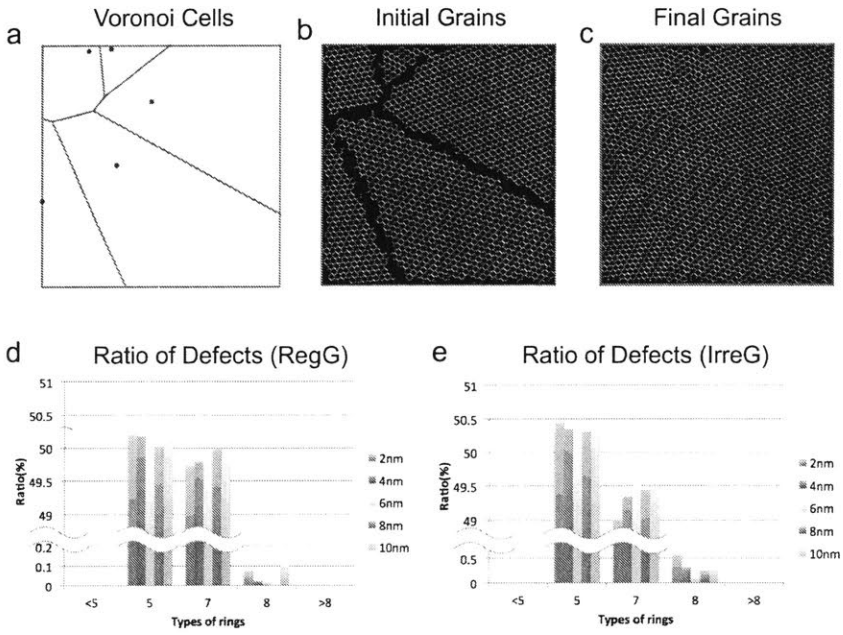

Figure A-2: The process of a building polycrystalline graphene and the evaluation of our models. From randomly generated Voronoi cells (a), the randomly rotated initial grains form the initial geometry (b). The final geometry is obtained after about 1500 times of iterations with mainly pentagon-heptagon defects (c). The ratios of defects in our RegG Model (d) and IrreG Model (e).

Appendix B

Supplementary Figures for Chapter 3: Single Crystals

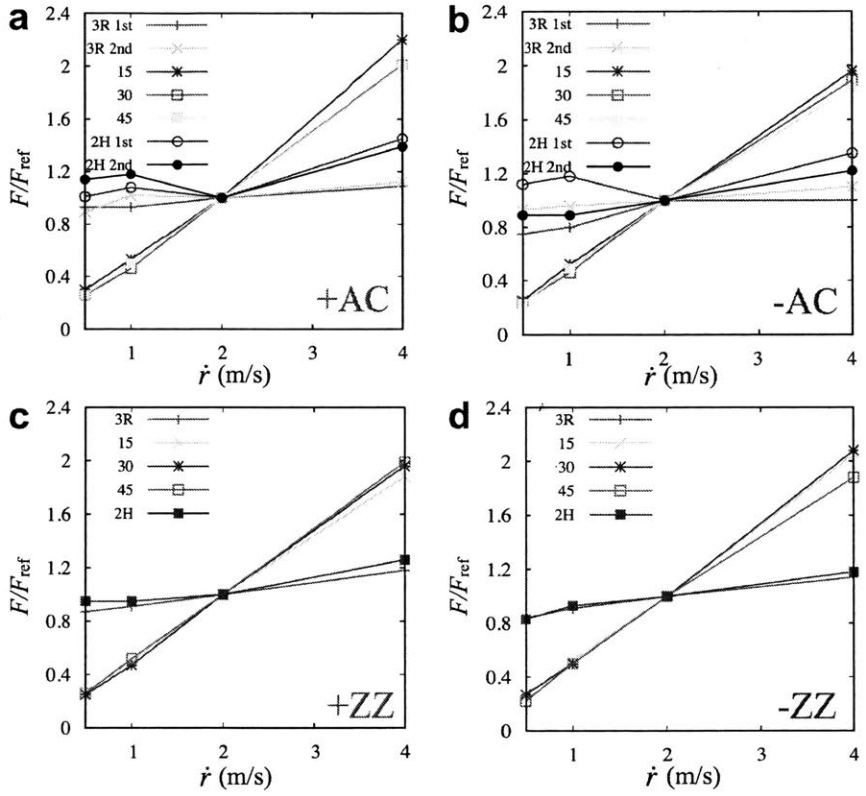

Figure B-1: Strain effects on frictions. The normalized factors are shown with the different loading rates of +AC, -AC, +ZZ and -ZZ for (a)-(d) The frictions of turbostratic stacks show a linear relation with the loading rates while the frictions of 2H and 3R are less sensitive to the loading rate slower than 0.02Å/ps (2m/s).

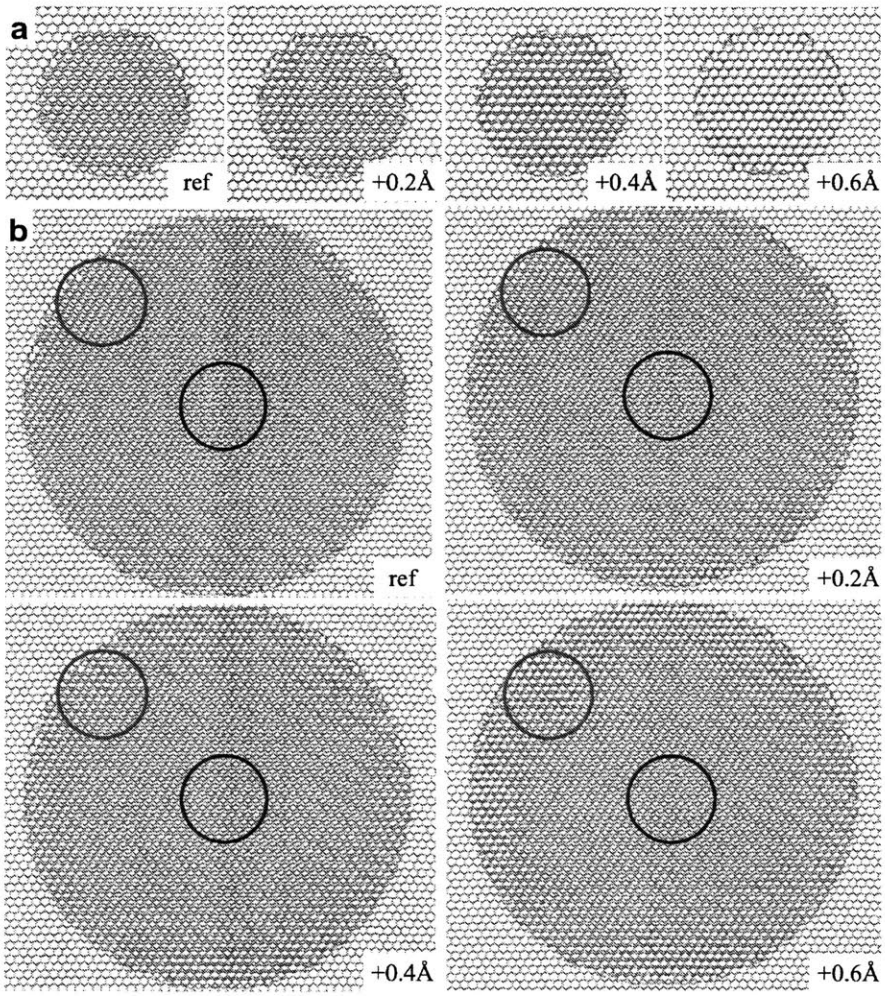

Figure B-2: Snap shots of the friction test in the +AC direction in Figure 3-8(a) with R=50 Å(a) and 150 Å (b). As the size of the radius increases, the friction is likely to decrease by utilizing local deformation. The two circles indicate the locally different geometries between the two regions during the loading.

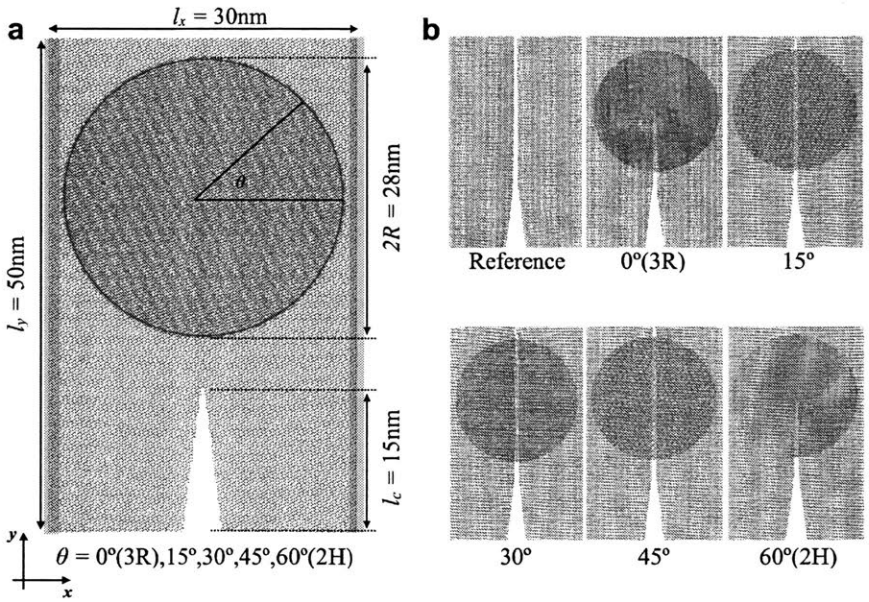

Figure B-3: (a) Schematic figure for crack propagation into bilayer region. (b) Results of crack propagations. The stack conditions significantly affect the crack-tip propagation. Only 2H and 3R stacks show that the crack propagation is disturbed and blocked.

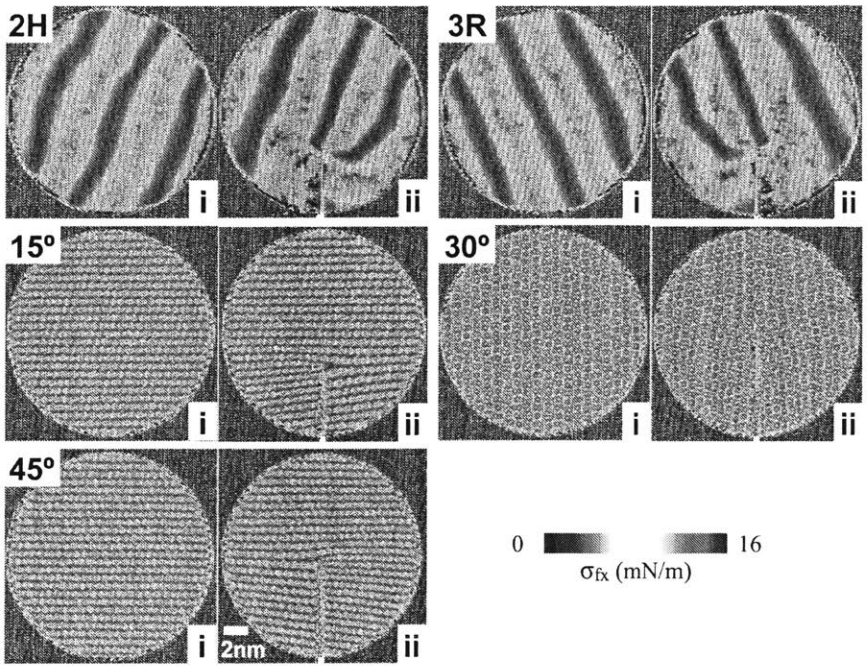

Figure B-4: The interlocking friction distribution from vdW terms of sulfur atoms in the top and bottom layers with different stacks: 2H, 3R, 15°, 30°, and 0°. The sulfur atoms are colored according to their relative geometries estimated by the vdW terms (See Method). The two panels (i) and (ii) represent the distributions before and during the crack propagation, respectively. It can be assumed that the friction is applied to the opposite direction of the movement. Therefore, the distribution near the crack tip provides the crucial information to understand the crack behaviors. The two well ordered stacks (2H and 3R) show significantly different interaction before and during the propagation while the other stacks show weaker interaction. The 30° shows symmetric distribution while the 15° and 45° show asymmetric distribution, which results in the asymmetric moiré pattern during the propagation in Figure 3-9.

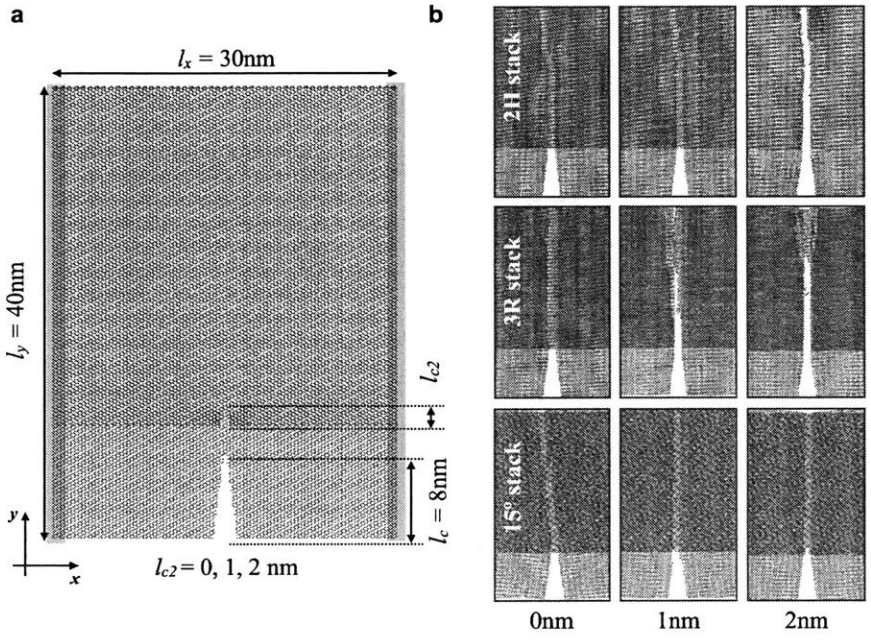

Figure B-5: (a) Schematic figure for crack propagation in the bottom layer into semi-infinite bilayer regions with different lengths of flaws of the top layer (b) Results of crack propagations. The coherent fracture occurs with small flaws with 3R and 2H stacks but does not occur with 15° turbostratically-stacked bilayer.

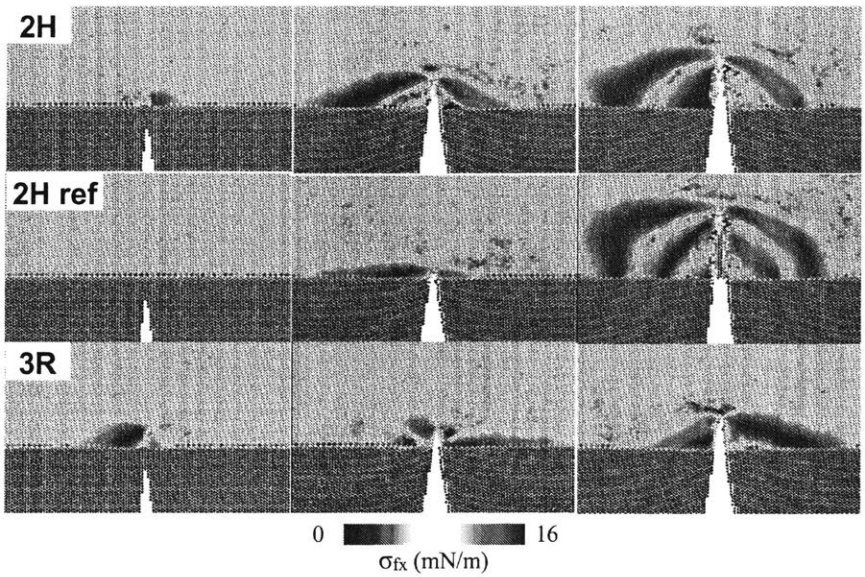

Figure B-6: The interlocking friction distribution from vdW terms of the two sulfur atoms in the top and bottom layers to demonstrate the coherent fracture with different conditions. The sulfur atoms are colored according to their relative geometries estimated by the vdW terms. The top layers of 2H and 3R have a small flaw of 2 nm length on the crack path of the bottom layer. The highly activated frictions near the flaw are observed in both 2H and 3R while no activation of the friction without the small flaw in 2H ref. The initial interlocking friction causes effective tensile stress near the crack tip and coherent fracture occurs.

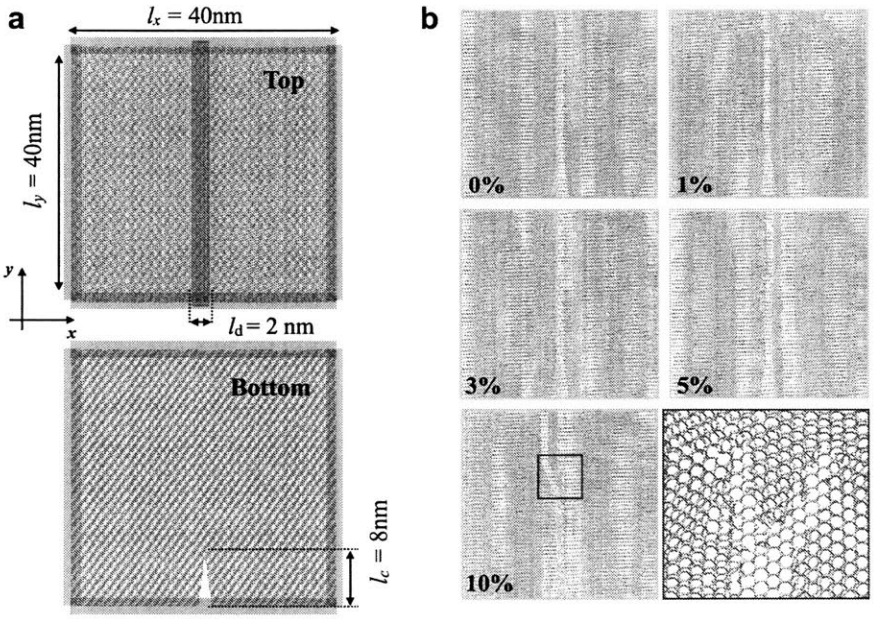

Figure B-7: (a) Schematic figure for crack propagation in semi-infinite bilayer regions with different ratio of defects along the crack path. All edges are fixed with non-periodic boundary condition. The different ratios of defects are introduced in the top layer with a width ld. (b) Results of crack propagations for different ratio from 0% to 10%. The crack is branched with 10% defects in the top layer. The coherent fracture occurs with 20% defect ratio.

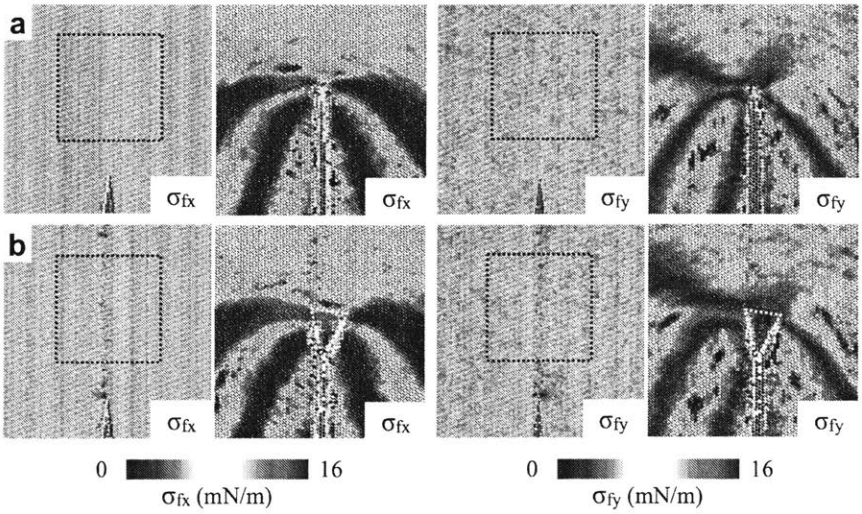

Figure B-8: The interlocking friction distribution from vdW terms of sulfur atoms in the top and bottom layers without sulfur vacancies (a) and 10% sulfur vacancies (b) in the second layer. The sulfur atoms are colored according to their relative geometries estimated by the vdW terms (See method). There is asymmetric distribution of σ_{fy} in the x direction with 0%, which decides the branching direction when the crack branches. Highly activated friction is observed in the triangular island region.

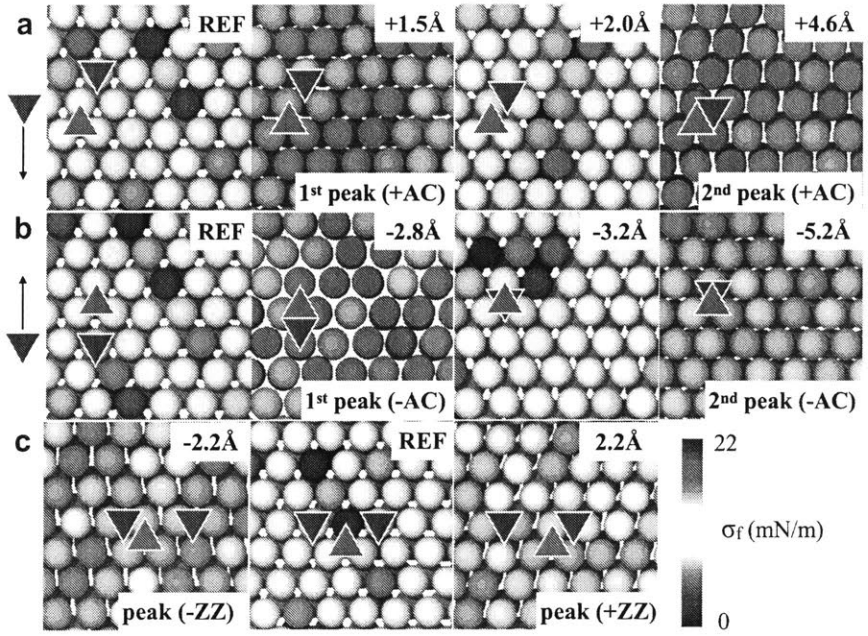

Figure B-9: Snap shots of friction distribution of 2H stacks during the interlayer friction tests with four different loading directions. (a) positive and (b) negative armchair directions (+AC and -AC), and (c) the two zigzag directions (+ZZ and -ZZ) in Figure 3-8. The red and blue triangles represent the sulfur triangles in the top and bottom layers, respectively. The atomic stress from vdW terms between the bottom sulfurs in the top layer and the top sulfurs in the bottom layer, describe sulfurs' relative positions and therefore, it can be a good indicator for the interlocking friction (high friction distributions correspond to the friction peaks in Figure 3-8).

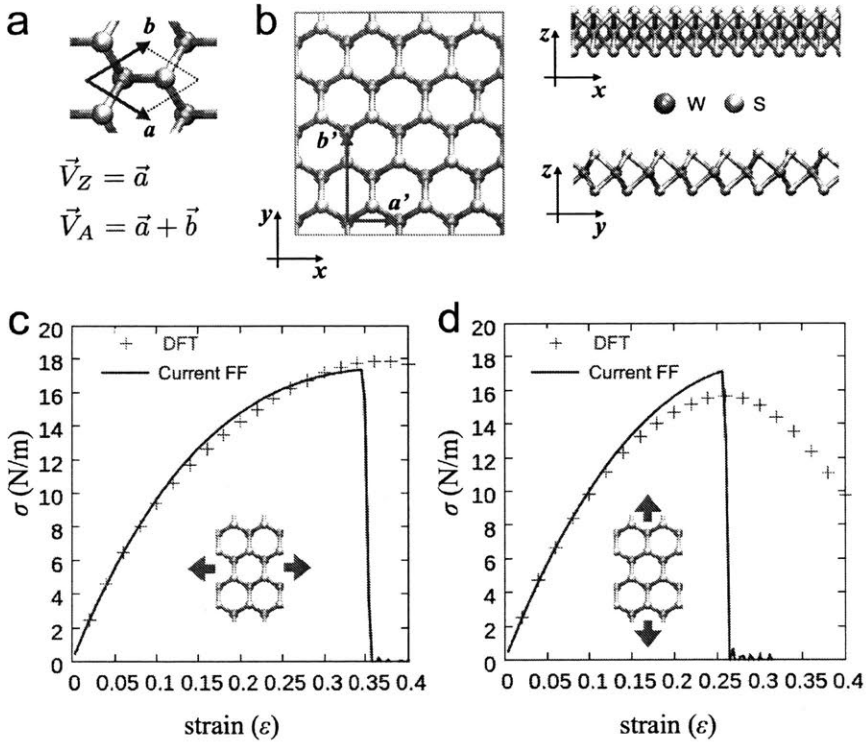

Figure B-10: (a) The hexagonal unit cell of WS_2 with lattice parameters a and b. For simplicity, we define the crack propagation directions as $V_Z = a$ (zigzag, [100]) and $V_A = a + b$ (armchair, [110]). We only distinguish the crack propagation directionV_A and from $-V_A$, because they show different crack propagation patterns but do not distinguish V_Z from $-V_Z$. (b) The geometries of monolayer MD simulations in the current study. The x and y directions are aligned along V_Z and $-V_A$ directions, respectively. To distinguish the crack propagation direction from the loading direction, we define the loading directions in the x and y direction as 'zz' (zigzag) and 'ac' (armchair), respectively. The stress-strain curves under the uniaxial tensile loadings in the zz (c) and ac (d) directions with a plane strain condition. The failure strain and strength from the current REBO are well matched with those from DFT calculations. The stress unit (N/m) is used to ignore the uncertainty of the thickness.

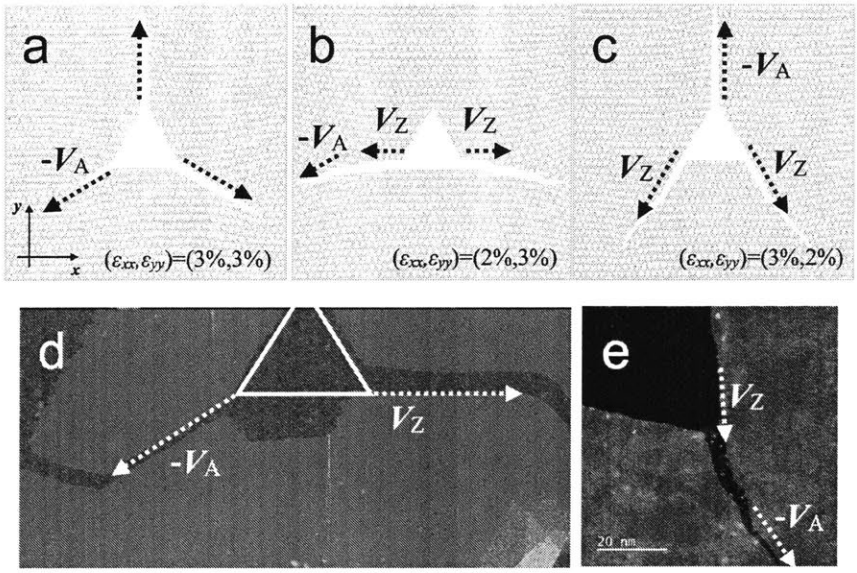

Figure B-11: (a)-(c)$V_A$rious crack propagation patterns due to the different pre-strains around the triangular voids with the size of $R = 6$ nm in MD simulation. The size, R, is defined as the distance between the centroid and vertex of the equilateral triangle. (d)-(e) Crack patterns observed by TEM after transferring process. There are distinct V_Z and $-V_A$ crack patterns and the mixtures of both crack direction during the propagation.

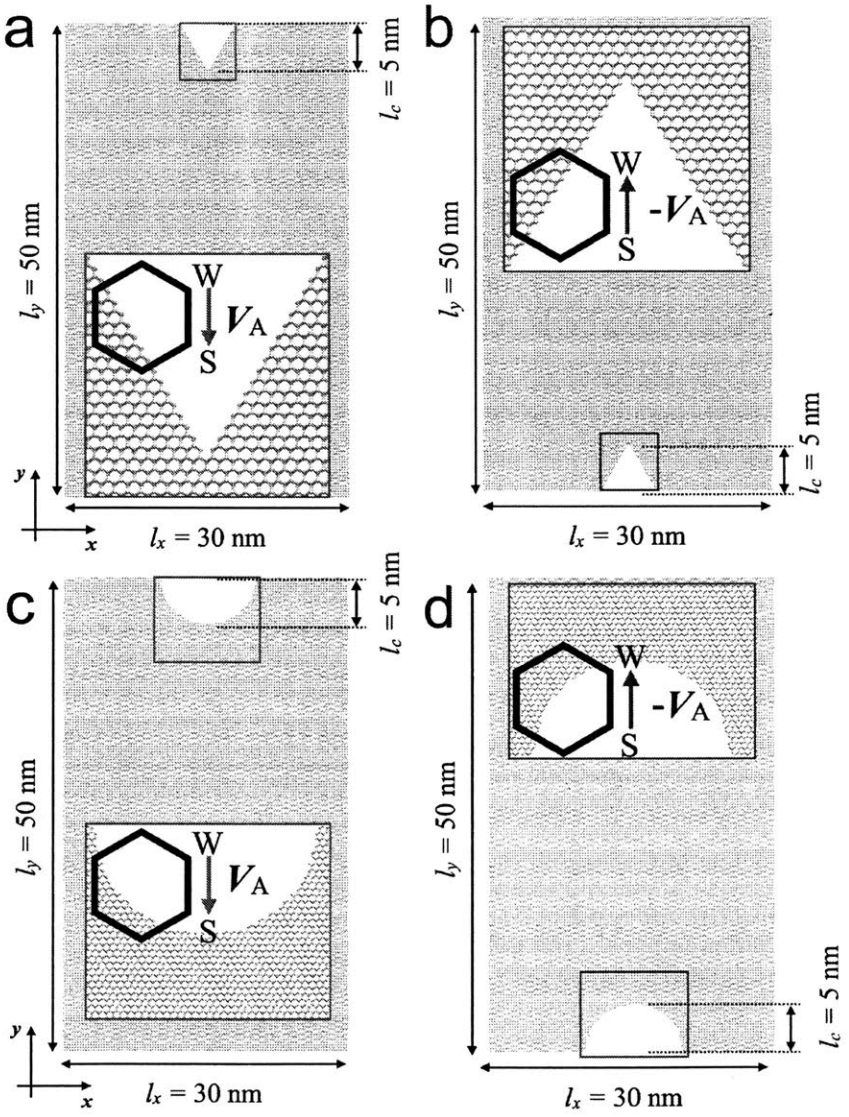

Figure B-12: Schematics of the edge-located half-circular and triangular voids for the tensile loading in the zz direction. A triangle with the crack length of $l_c = 5$ nm is introduced in both the top and bottom edges in pristine WS_2 monolayer (30 nm by 50 nm), which corresponds to the crack directions in V_A(a) and $-V_A$ (b). A half-circular void is introduced in both crack directions in V_A(c) and $-V_A$ (d).

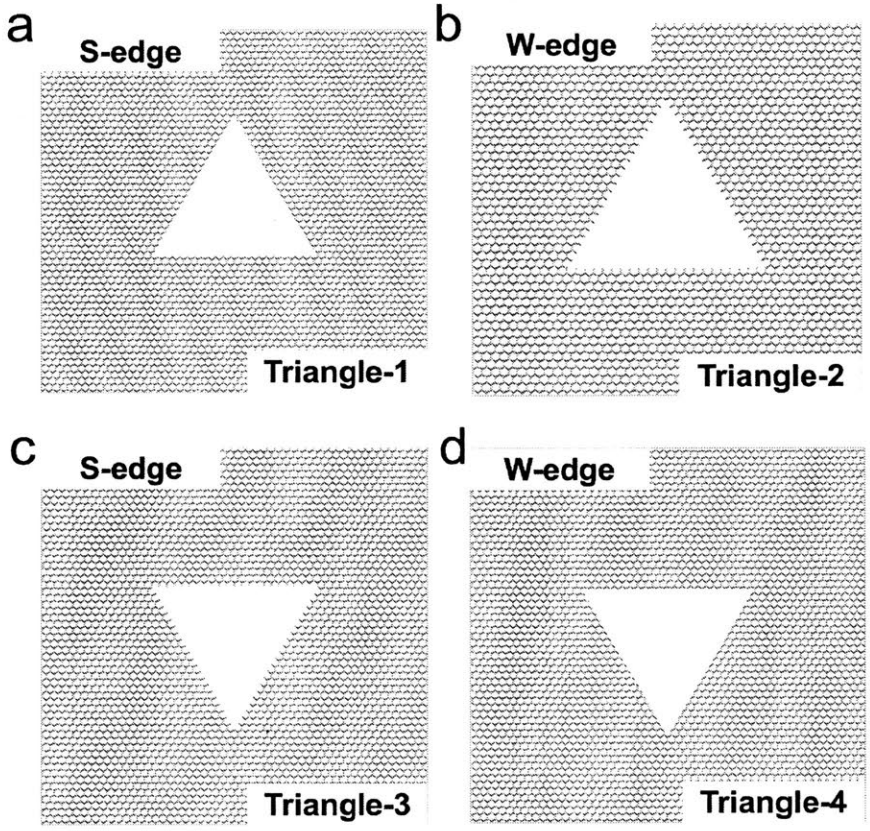

Figure B-13: Schematic of triangular void structures. (a)-(b) S atom and W atoms are located on edge with the crack direction $-V_A$. (c)-(d) S atom and W atoms are located on edge with the crack direction V_A.

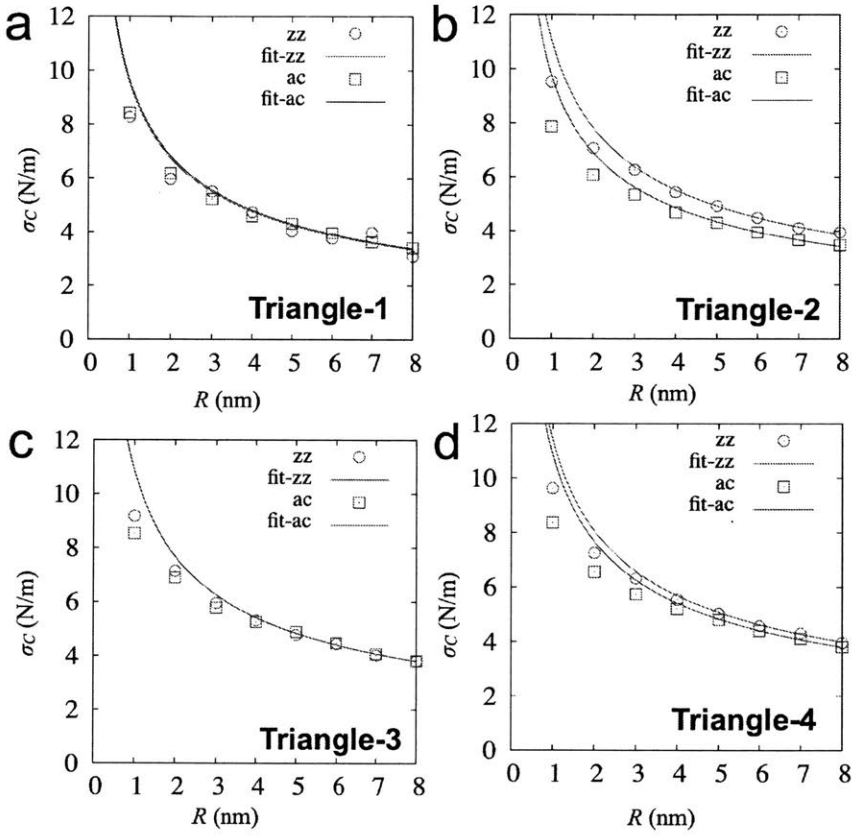

Figure B-14: Strengths of the WS_2 monolayer with triangular voids under the loading in both zz and ac directions with the plane strain conditions. The equations from the linear elastic fracture mechanics describe the trend well.

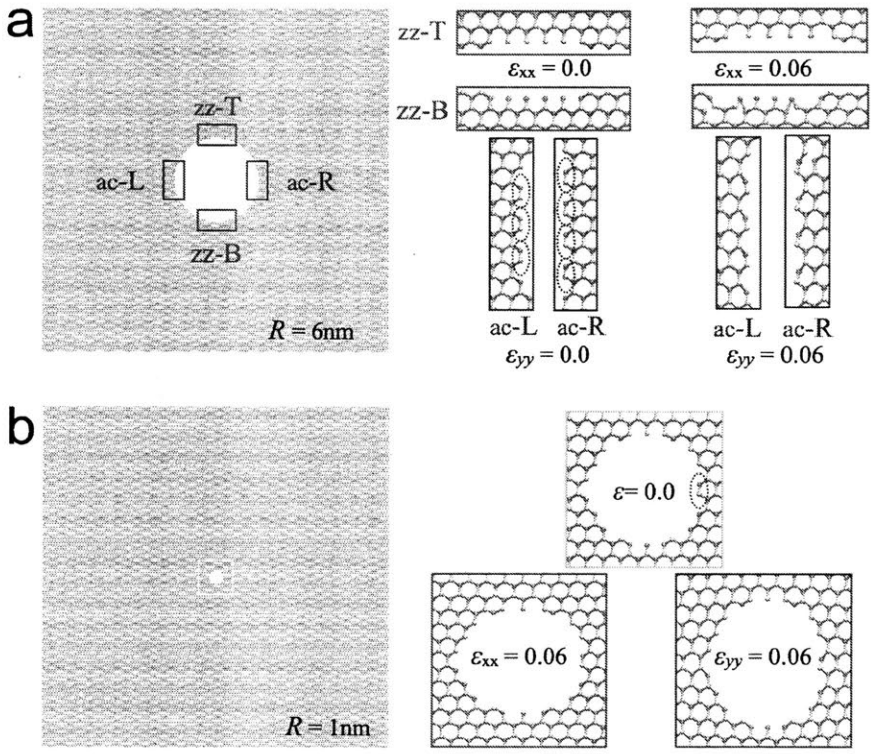

Figure B-15: The deformation of edge structure in the circular void with different size of $R = 6$ nm (a) and 1 nm (b). W-S atom pairs (blue dotted circles) play a protective role in elongating the failure strains as the size of R increases.

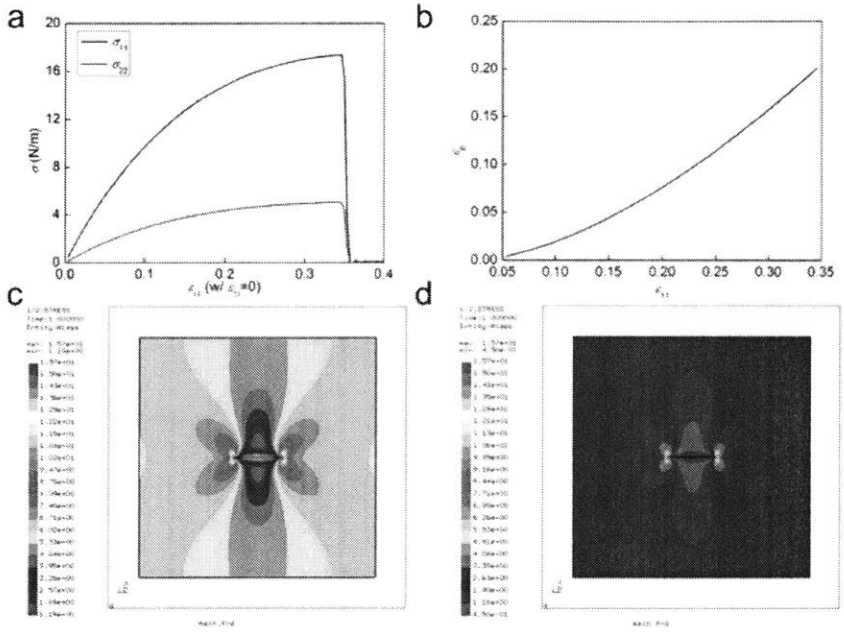

Figure B-16: Derivation of the elastic-plastic model of WS_2 before material failure for FEM model and the stress distribution of the sample with a line crack. (a) The stress-strain curve of a piece of WS_2 under tensile loading in the x direction ($\epsilon_{11}>0$) with plane strain condition ($\epsilon_{22}=0$) in MD simulation. (b) The plastic deformation of WS_2 computed by using the results in panel. By using the elastic-plastic model, we apply simple boundary conditions by uniformly stretch the upper and lower edge of a piece of WS_2 model (with 50x50 nm and a line crack of a length of 10 nm) and gradually increase the deformation until the maximum von Mises stress of all the elements reach σ_C value. (c) The stress distribution within the sample by using the elastic-plastic model. (d) The stress distribution within the sample by using only the linear elastic model.

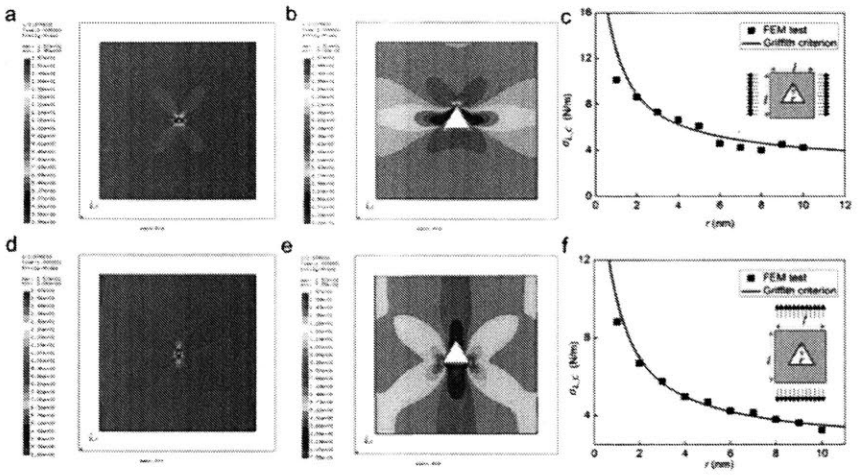

Figure B-17: The FEM result of the stress distribution at the critical point before failure from the initial triangle crack of different sizes and different orientations with different loading directions. The triangular cracks with one edge in parallel with the loading direction for (a) $R = 1$ nm and (b) $R = 5$ nm. The triangle cracks with one edge in vertical with the loading direction for (d) r=1 nm and (e) $R = 5$ nm. The summary of the FEM results of $\sigma_{(L_C)}$ as a function of the crack length r for the triangle cracks with one edge in parallel with the loading direction (c). (panel (c), the fitting function with $F_{zz}(\phi) = 1.041 - 0.60223\phi$) and the triangle cracks with one edge in vertical with the loading direction (panel (f), the fitting function with $F_{ac}(\phi) = 1.341 - 1.138\phi$).

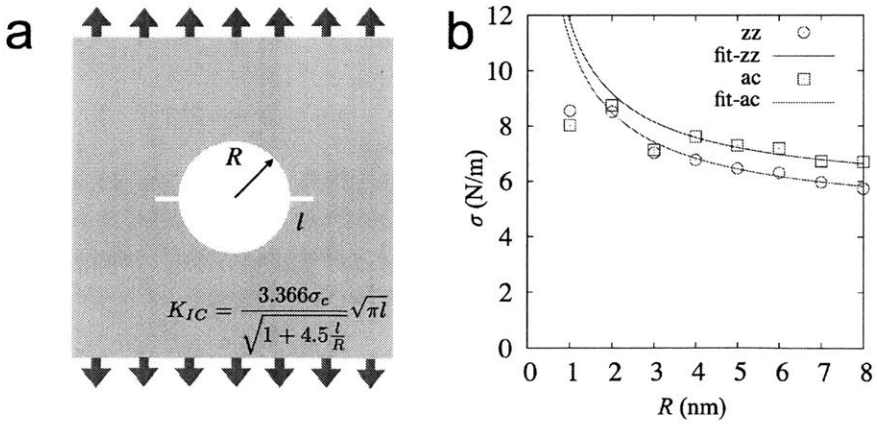

Figure B-18: (a) We approximate the system with a circle with a radius R under tension with the symmetrical cracks of length l normal to the loading direction based on Lukáĺ model. (b) The strengths under the loadings in the zz and ac directions with the fitted functions.

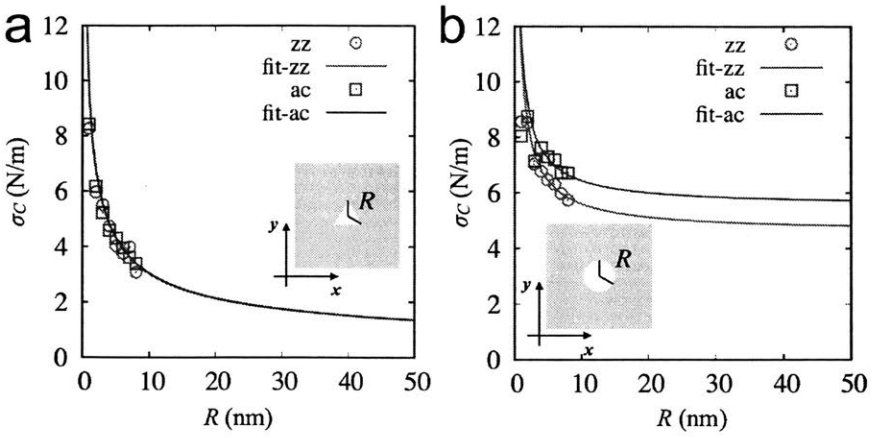

Figure B-19: The extrapolations of the strengths from the MD simulation data for triangular (a) and circular (b) voids.

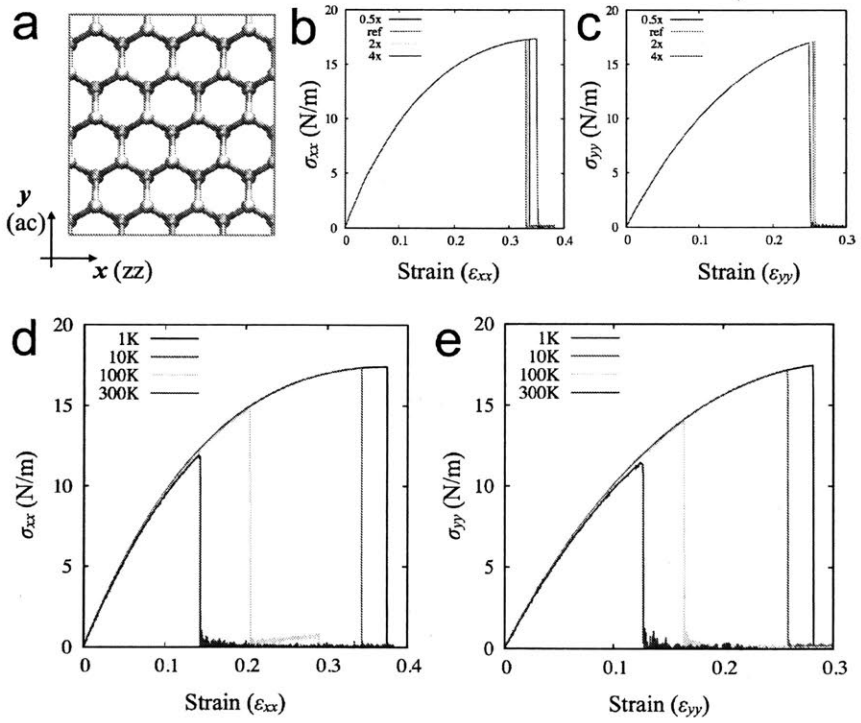

Figure B-20: Strain rate and temperature effects on the strength of the pristine WS_2 monolayer. (a) Schematic of WS_2 with the lattice direction. (b)-(c) The stress-strain curves of pristine WS_2 with the different strain rate (ref: 0.02Å/ps) in both the zz (x) and ac (y) directions. (e)-(f). The stress-strain curves of the pristine WS_2 monolayer with the different temperature from 1K to 300K.

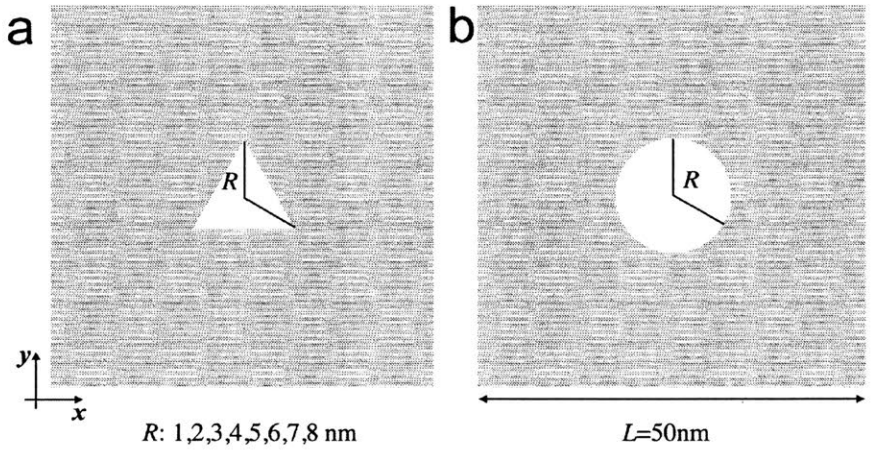

Figure B-21: Schematics of triangular (a) and circular (b) voids for strengths. The size, R, is defined by the distance from the centroid to the vertex for a triangular void and radius for a circular void.

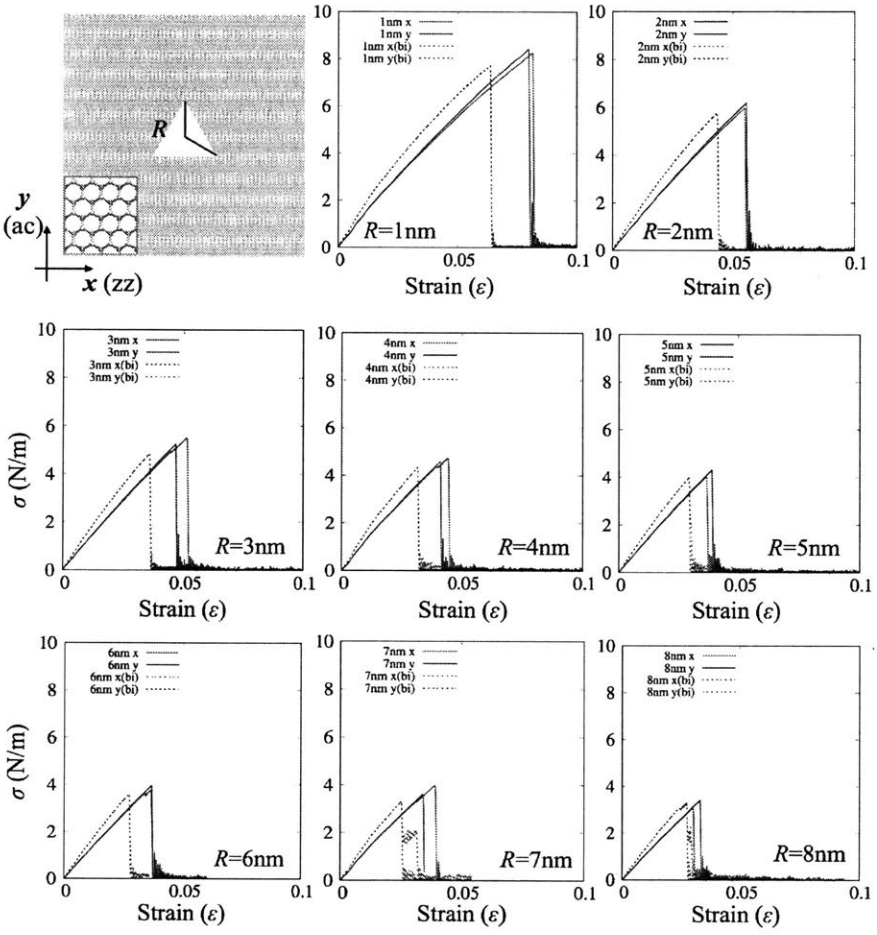

Figure B-22: Stress-strain curves of the WS_2 monolayer with a triangular void under the tensile loadings in zz (x) and ac (y), and both with a plane strain condition.

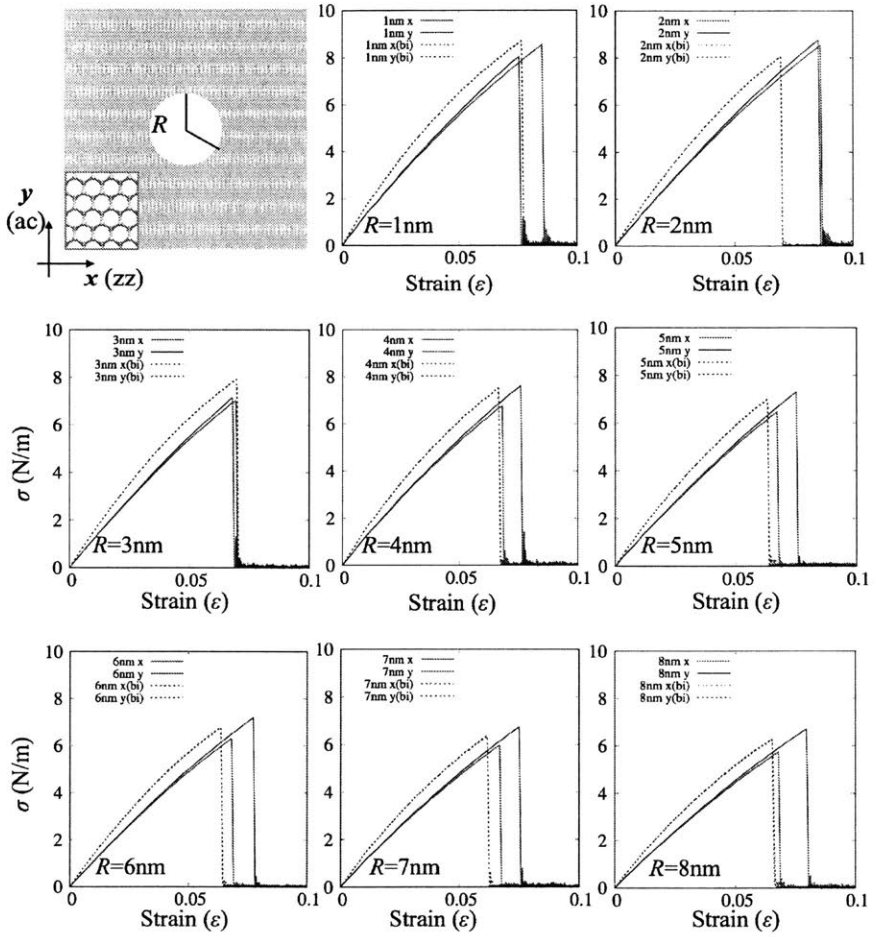

Figure B-23: Stress-strain curves of the 50 nm by 50 nm WS_2 monolayer with a circular void under the tensile loadings in zz (x) and ac (y), and both with a plane strain condition.

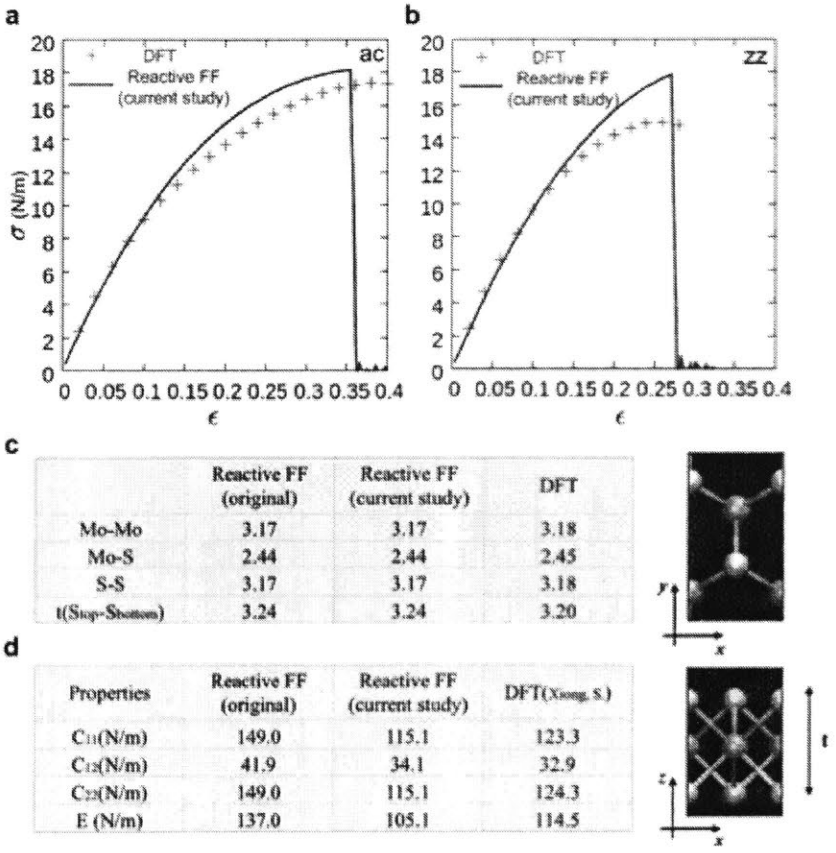

	Reactive FF (original)	Reactive FF (current study)	DFT
Mo-Mo	3.17	3.17	3.18
Mo-S	2.44	2.44	2.45
S-S	3.17	3.17	3.18
t(S_{top}-S_{bottom})	3.24	3.24	3.20

Properties	Reactive FF (original)	Reactive FF (current study)	DFT(X_{voigt} S.)
C_{11}(N/m)	149.0	115.1	123.3
C_{12}(N/m)	41.9	34.1	32.9
C_{22}(N/m)	149.0	115.1	124.3
E (N/m)	137.0	105.1	114.5

Figure B-24: (a,b) The stress-strain curves of the reactive FF used in the current study (blue line) and DFT calculation (red points) in the armchair and zigzag directions. The original potential has artificial stiffening due to the switching functions as the same as the REBO potential for graphene. Our new parameters remove the stiffening effects and can describe the failure strains for both zigzag and armchair directions, which have not been achieved in the previous studies. (c) The equilibrated geometries of MoS_2. (d) The elastic constant and Young's modulus of the current study and DFT calculation. The reactive FF used in the current study well describes geometries, mechanical properties and failure behaviors of MoS_2.

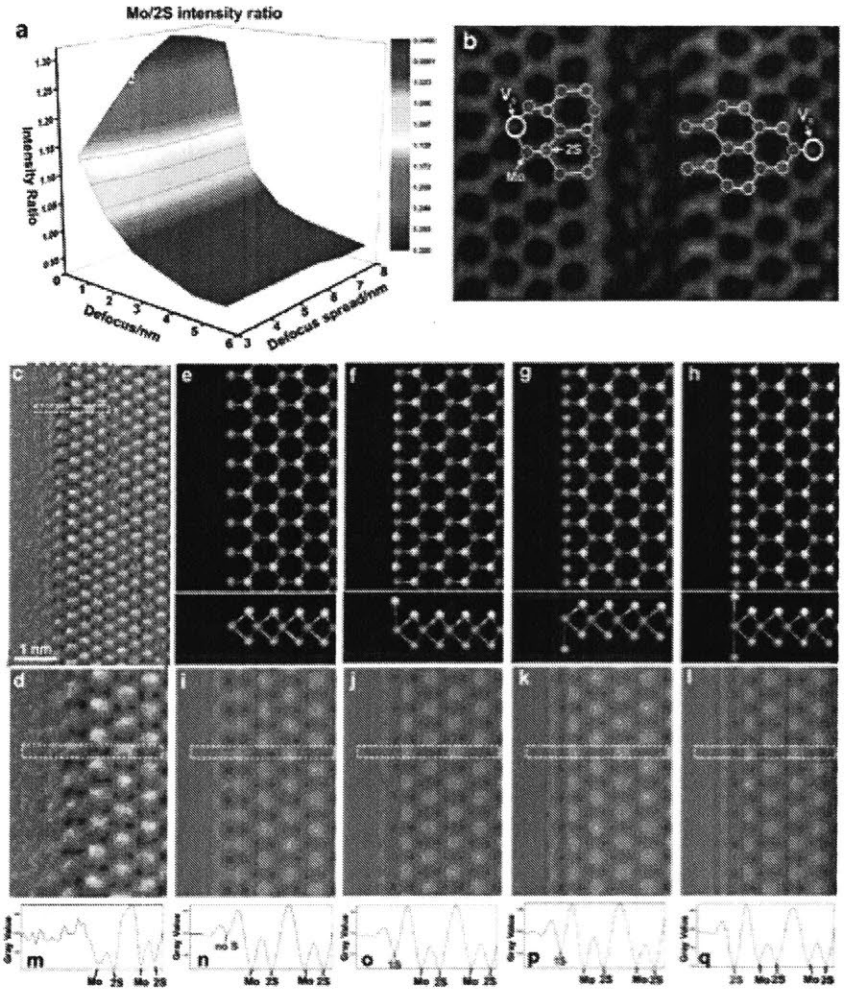

Figure B-25: (a) 3D plot showing the dependence of the Mo/2S intensity ratio in the AC-TEM on the parameters of defocus (nm) and defocus spread (nm) by performing a series of simulations on the atomic model of pristine monolayer MoS_2. (b) AC-TEM image showing cracked MoS_2 edges with white circles highlighting the mono-sulfur vacancies as reference points, as well as blue and yellow circles representing Mo and 2S sites, respectively, which are deduced by counting atoms from either reference points. (c) AC-TEM image of one side of the long and straight zigzag edges, which is the right part of Figure 3-4(a). (d) Magnified view of the structure of the MoS_2 edge from the region indicated by the orange dashed box in panel c. (e)-(h) Atomic models of four possible edge configurations. Each of them is having both the top and bottom S atoms lost, having the bottom S atoms lost and the top S atoms move to places above the MoS_2 lattice plane, having the top S atoms lost and the bottom S atoms move to places below the MoS_2 plane, and having no S atoms on the edge lost but both the top and the bottom S atoms move to out-of-plane places, respectively. The upper parts show the top views of the atomic models, while the bottom parts show the side views. (i)-(l) Multi-slice image simulations of the edge structure based on corresponding atomic models shown in panel e-h, respectively. (m)-(q) Boxed line profile analysis across the edge region shown in yellow dashed boxed in panel d, i-l, respectively.

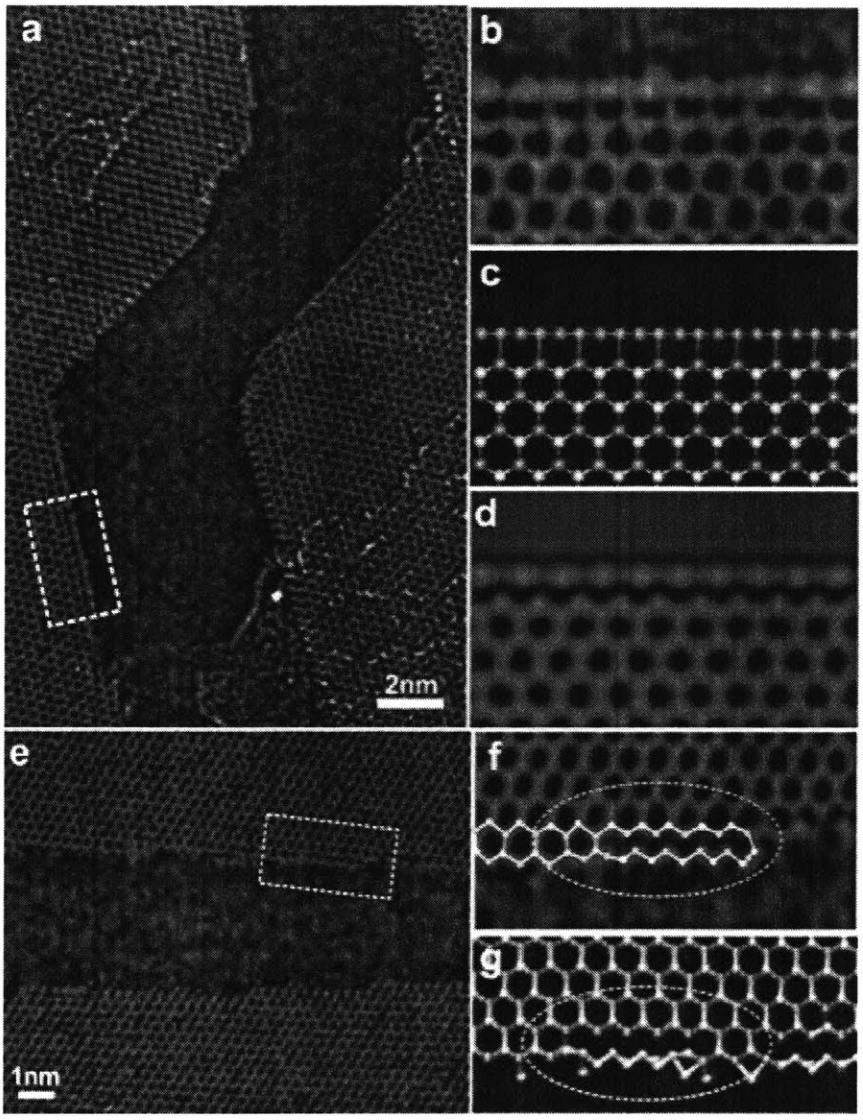

Figure B-26: (a) AC-TEM image of the MoS_2 torn edges with a path deflection. (b) Detailed structure of a segment of the MoS_2 edge from the region indicated by the white dashed box in panel a, where a configuration reconstruction of the outermost Mo and S atom takes place. (c) Atomic model of the edge structure in panel b. The blue, yellow and orange spheres represent the single Mo atom, double S atoms and the single S atom, respectively. (d) Multi-slice image simulation using the atomic model in panel c in a supercell. (e) AC-TEM image of the long and straight MoS_2 zigzag edge. (f) Detailed edge structure from the region marked in the white dashed box in panel e with an atomic model overlaid. (g) Simulation snapshot of the MoS_2 edge structure after performing a penetration test in a MoS_2 model, which is cropped from Fig 3-4 (g). The regions marked by orange ellipses in panel f and g show a good configuration match on edges between the AC-TEM image and the simulation results via a penetration test.

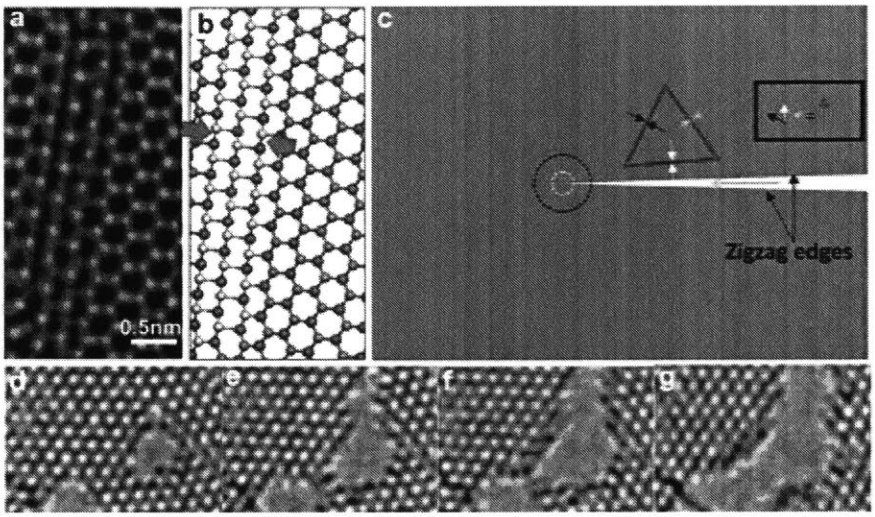

Figure B-27: (a) AC-TEM image showing the line defects formation in monolayer MoS_2 due to the missing of three S lines along the zigzag lattice orientation under the electron beam irradiation. (b) Atomic model of the line defect structure. The pair of red arrows shows the lattice contraction along the armchair direction due to the generation of line defects. The blue, yellow and orange spheres indicate the single Mo atom, the single S atom and double S atoms, respectively. (c) Schematic illustration showing the direction of the strain and mechanical stress generated around the crack tip due to the line defects formation under the electron beam irradiation at the slow crack stage. (d)-(g)Time series of AC-TEM images showing the generation, extension and rupture of the residual chain after the crack propagation in a defective region of the MoS_2 lattice.

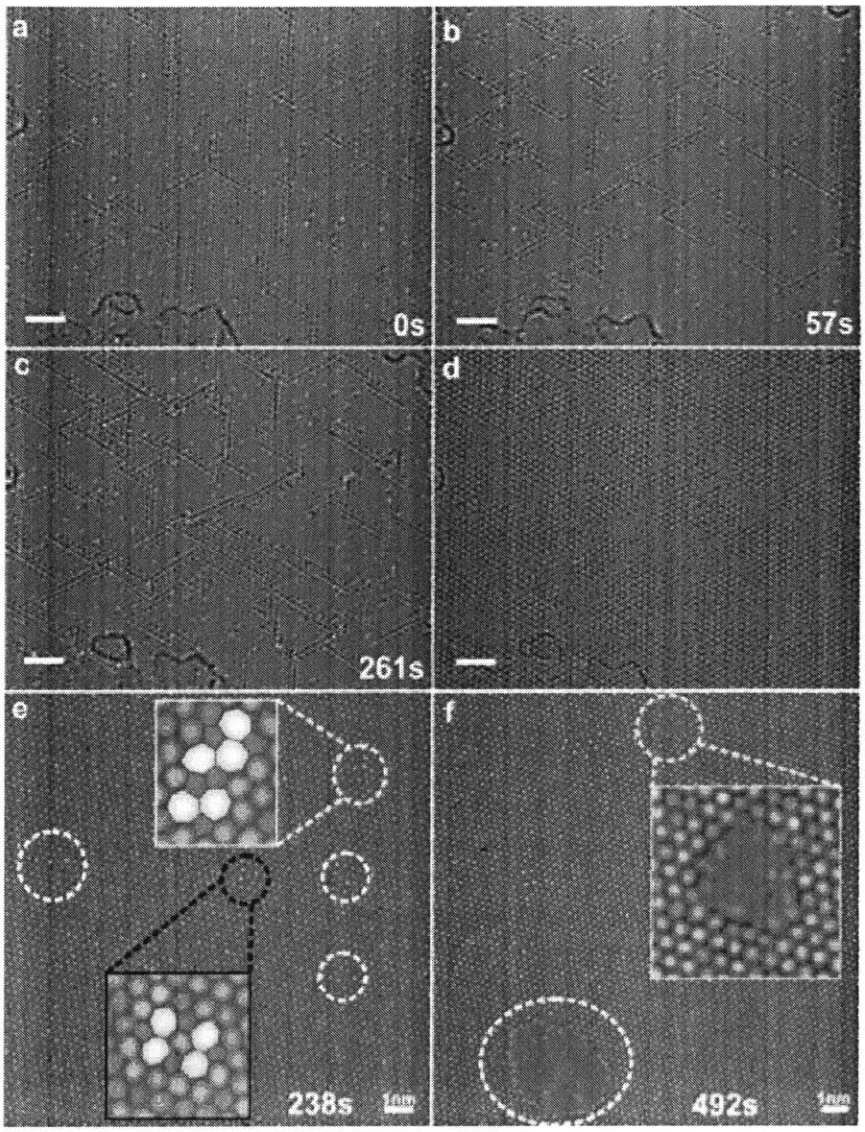

Figure B-28: (a-c) AC-TEM images showing the configuration evolution of monolayer MoS_2 under the same electron dose as that we used when imaging the crack propagation. We applied a nonstandard defocus value rather than the 'optimal' Scherzer focus to 'filter' the pristine MoS_2 but highlight the defect structures like vacancies and line defects. (d) AC-TEM image taking under the standard defocus value close to the Scherzer focus, which proves that those highlighted configurations in panel a to c are vacancies and line defects rather than dislocation pools. Scale bar: 2 nm. (e-f) AC-TEM images showing the generation of vacancy clusters, dislocation pairs and small holes on graphene under a prolonged electron beam illumination, which is different from the lattice evolution on monolayer MoS_2, where S vacancies are prone to aggregate into line defect networks.

Appendix C

Supplementary Figures for Chapter 4: Grain Boundary and Heterostructures

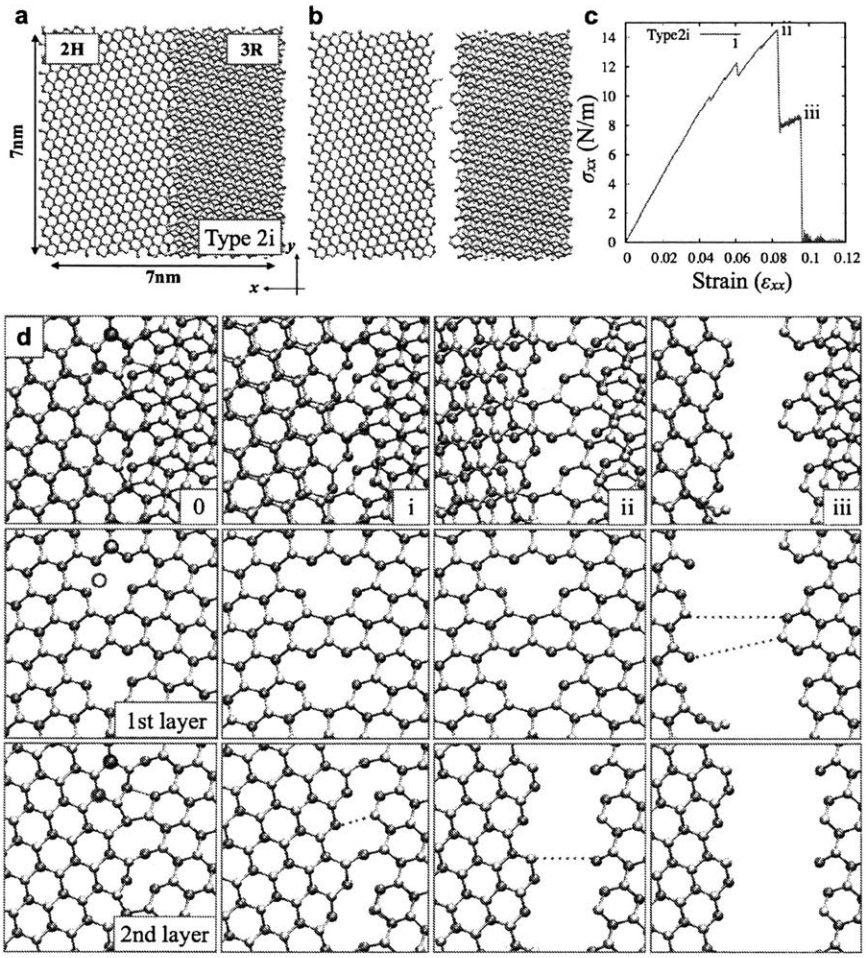

Figure C-1: (a) Rebuilt model of Type2i through MD simulations with 7nm x 7nm size. (b) Snapshot of the model after both layers fail. (c) Stress-strain curve of the bilayer under tensile loading. There are several stages of failure (i- iii), which described more detail in d. (d) Detailed atomic structures of the MD model. The marked positions of atoms (red and blue circles) are well matched with TEM observation. The red lines indicate the bond breaks at the failure stage from i to iii described in the stress-strain curve.

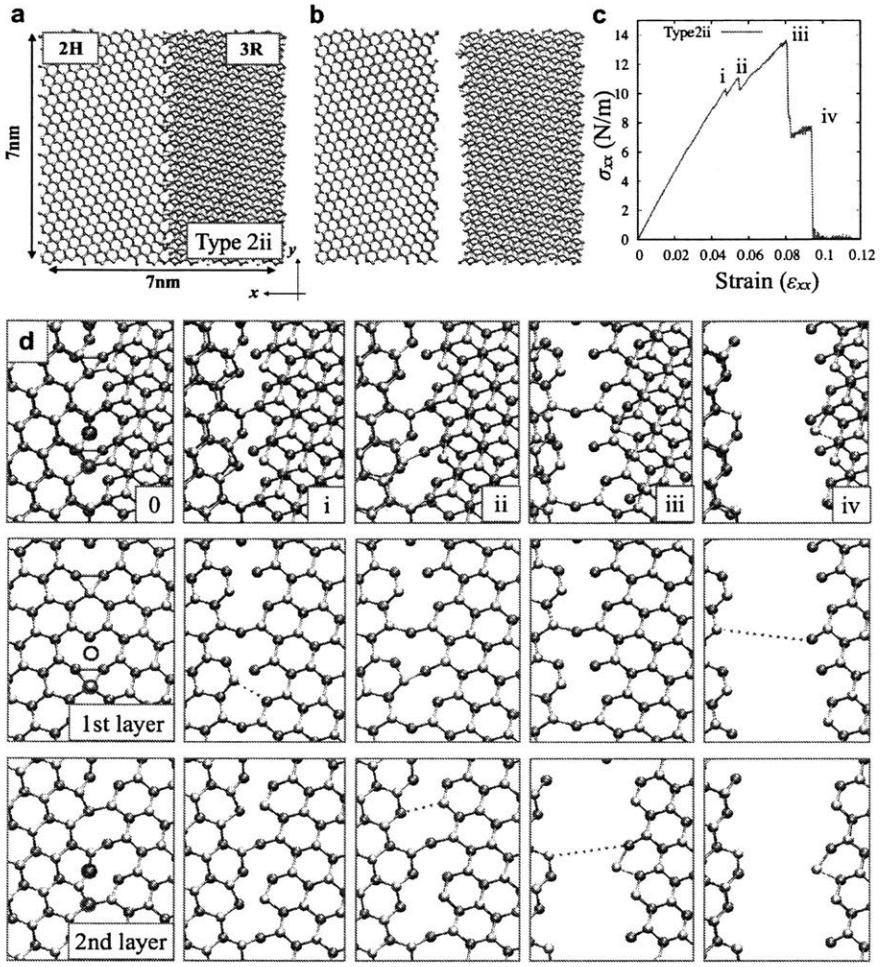

Figure C-2: (a) Rebuilt model of Type2ii through MD simulations with 7 nm x 7 nm size. (b) Snapshot of the model after both layers fail. (c) Stress-strain curve of the bilayer under tensile loading. There are several stages of failure (i- iv), which described more detail in d. (d) Detailed atomic structures of the MD model. The marked positions of atoms (red and blue circles) are well matched with TEM observation. The red lines indicate the bond breaks at the failure stage from i to iv described in the stress-strain curve.

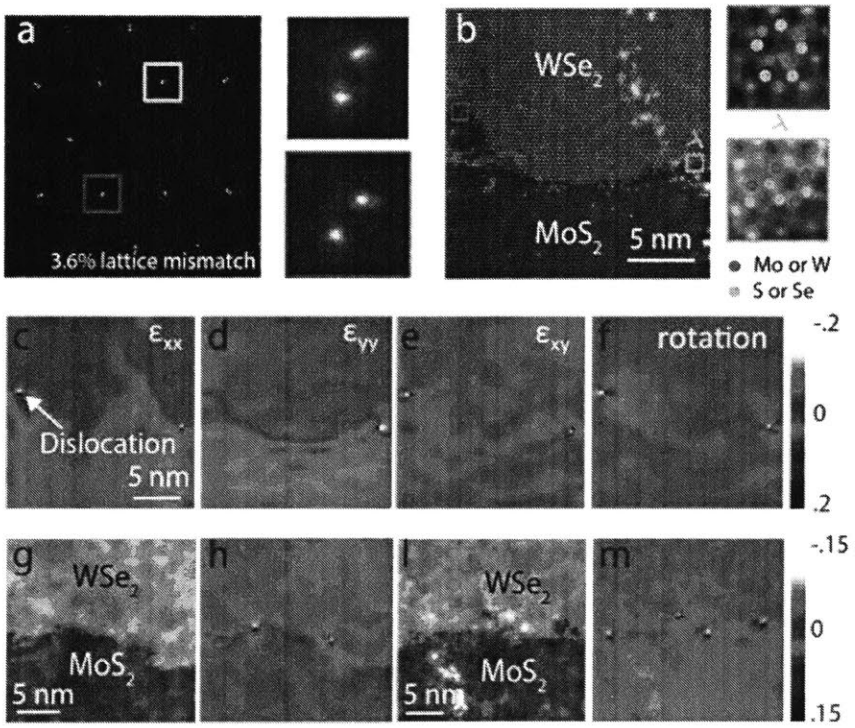

Figure C-3: Dislocations at abrupt MoS_2-WSe_2 junctions. (a) Diffraction pattern of the abrupt junction from a micron-sized area with magnified diffracted spots on the right, indicating that the two materials are flat and fully relaxed. We fit the peaks to Gaussian and located the centers, showing a 3.6% lattice mismatch between MoS_2 and WSe_2. (b) Atomic resolution ADF-STEM image of the abrupt MoS_2-WSe_2 junction with two misfit dislocations appearing at the interface. The magnified images of the dislocations are shown on the right with the atoms marked. They are pentagon-heptagon pair dislocations with Mo-Mo bonds (red border) or S-S bonds (yellow border). In the formation of 1D MoS_2, both types of the 5|7 dislocations behave similarly as catalysts. c-f, GPA maps of (b), indicating the lattice strain, in addition to the location and orientation of the misfit dislocations. (g-m), Additional ADF images (g, l) and the overlay with ϵ_{xx} strain maps (h, m) of abrupt junctions with dislocations at the interface.

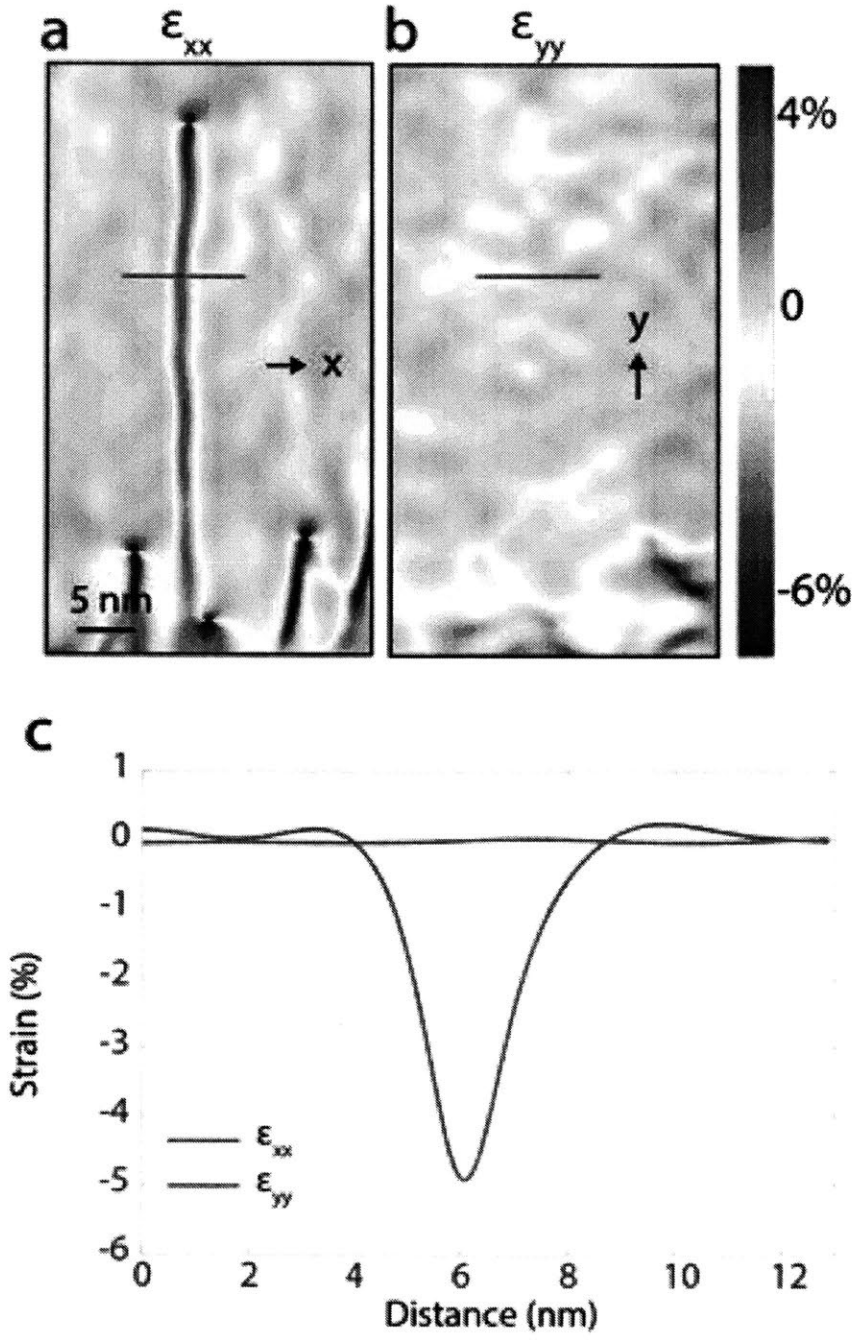

Figure C-4: (a, b) The uniaxial strain ϵ_{xx} and ϵ_{yy} maps shown in Figure 4-12 in the main manuscript. (c) The line profile from the blue line region in a and red line region in (b) respectively. The minimum (blue line) shows a ~5% lattice difference in the MoS_2 from the surrounding WSe_2, indicating a small compressive strain (~1.4%) along the x direction in the MoS_2 1D channels, which can be calculated from the 3.6% lattice mismatch between MoS_2 and WSe_2. Along the y direction, the MoS_2 and WSe_2 are lattice matched, showing a 3.6% tensile ϵ_{yy} strain in the MoS_2 1D channel to form the coherent structure.

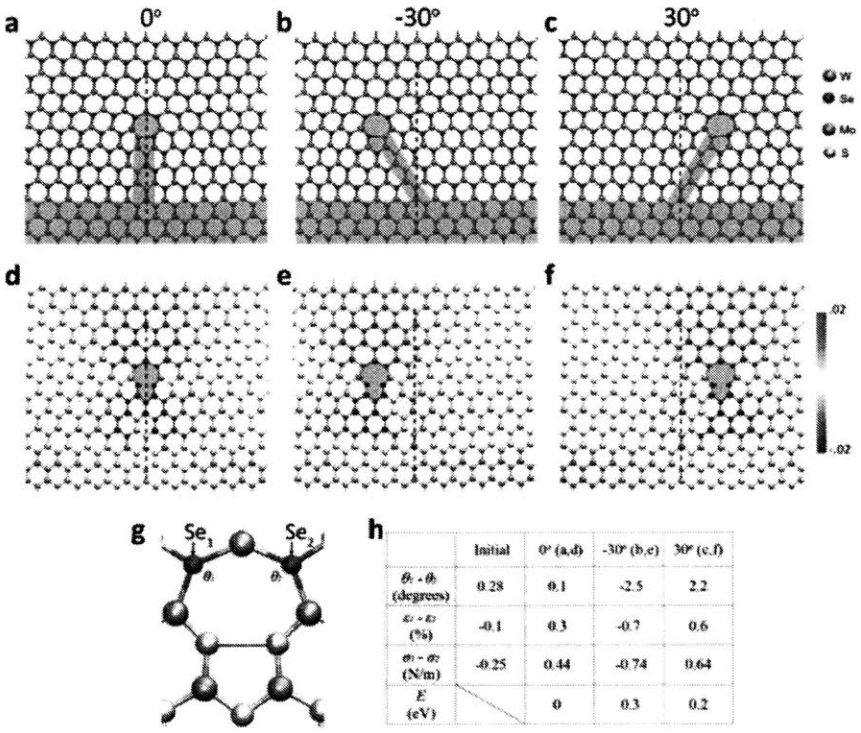

	Initial	0° (a,d)	-30° (b,e)	30° (c,f)
$\theta_1 - \theta_2$ (degrees)	0.28	0.1	-2.5	2.2
$\epsilon_1 - \epsilon_2$ (%)	-0.1	0.3	-0.7	0.6
$\sigma_1 - \sigma_2$ (N/m)	-0.25	0.44	-0.74	0.64
E (eV)		0	0.3	0.2

Figure C-5: Strain guides the migration direction. (a-c), Schematic of the 1D channels migrating *via* a zigzag path perpendicular to the interface (a), path 30° to the left (b) and right (c). (d-f), The corresponding strain maps of (a), (b), and (c). The strain map of 0° 1D channel (d) shows a symmetric strain, while (e) and (f) show clear asymmetric strain. (g) Schematic of the catalyst dislocation. (h) Table of the local bond angle (θ), atomic strain (ϵ), atomic stress (σ) and total energy (E) differentiations between Se1 and Se2 selenium atoms (g) for the three migrating paths shown in (a)-(c). The initial one is calculated from the case where the dislocation is at the interface without migrating. The bond angle, strain, and stress differences between the two W-Se bonds reveal a local asymmetry in the dislocation core. This asymmetry affects the breaking of left or right W-Se bonds (*i.e.*, migrating toward left or right) when the precursors insert into the lattice. The comparison of total energy confirms the dislocation prefers to form a zigzag path that is perpendicular to the interface.

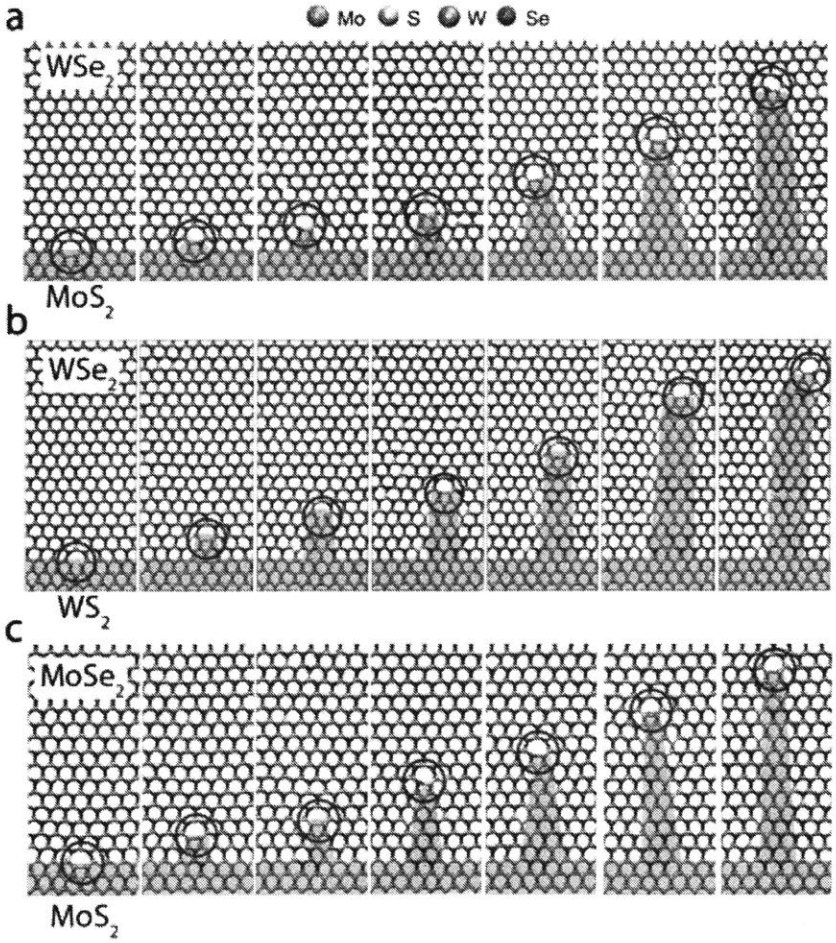

Figure C-6: MD simulations of different combinations of TMDs that grow 1D channels. (a- c) MD simulation of the formation of 1D MoS_2 embedded within 2D WSe_2 (a), 1D WS_2 embedded within 2D WSe_2 (b), and 1D MoS_2 embedded within 2D $MoSe_2$ (c). The results prove that this approach can extend to different combinations of TMDs other than MoS_2-WSe_2, although the widths of the 1D channels show small variations, which is due to the difference in optimized growth conditions for different cases.

Appendix D

Supplementary Figures for Chapter 5: Three-Dimensional Designs

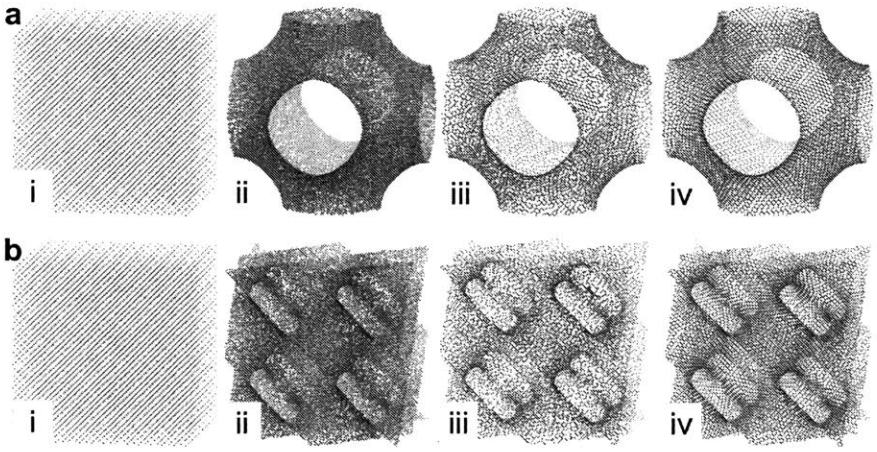

Figure D-1: Generation of atomic TPMS P(a) and D(b) types, representing critical steps including (i) Lennard-Jones (LJ) particles distributed with fcc structure, (ii) generation of TPMSs with triangular LJ lattice with external potentials $\lambda(V_X)^2$, X = P and D, (iii) transformation from triangular lattice to hexagonal one, and (iv) refinement of the geometries for all carbons to have sp^2 bonds.

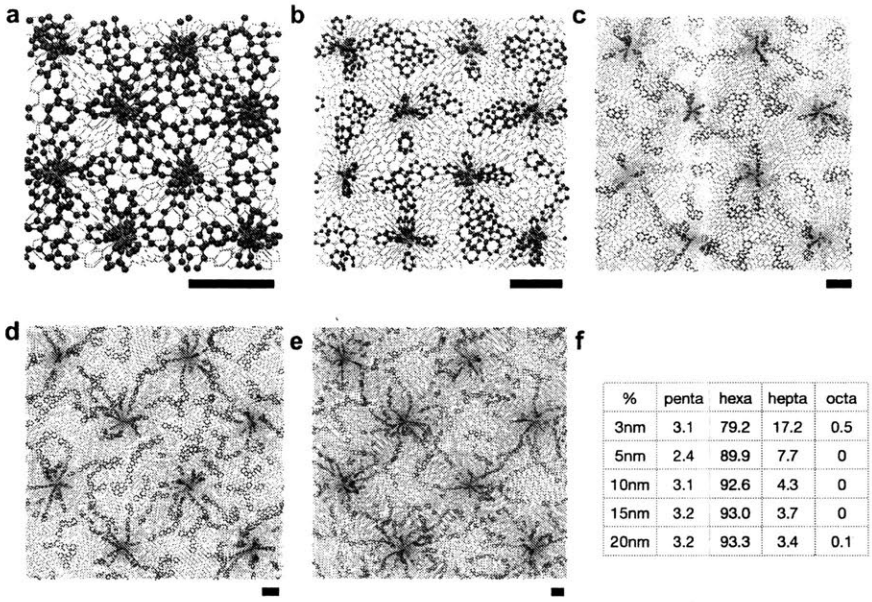

%	penta	hexa	hepta	octa
3nm	3.1	79.2	17.2	0.5
5nm	2.4	89.9	7.7	0
10nm	3.1	92.6	4.3	0
15nm	3.2	93.0	3.7	0
20nm	3.2	93.3	3.4	0.1

Figure D-2: (a-e) The spatial distribution of topological defects (pentagon, heptagon, and octagon) in the D type models from L=3 nm to 20 nm. The red atoms indicate the atoms belong to non-hexagonal ring defects. The ratios of defects and hexagon ring are listed in table f.

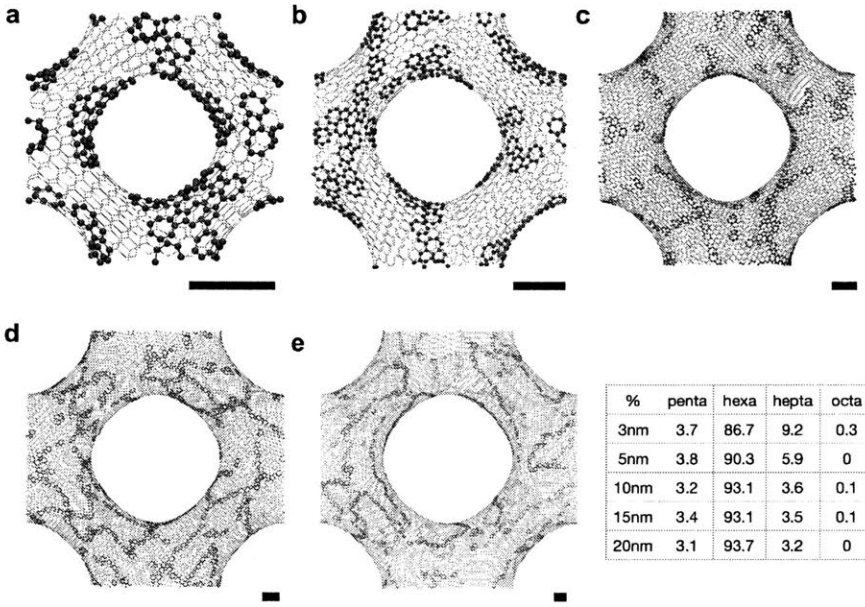

%	penta	hexa	hepta	octa
3nm	3.7	86.7	9.2	0.3
5nm	3.8	90.3	5.9	0
10nm	3.2	93.1	3.6	0.1
15nm	3.4	93.1	3.5	0.1
20nm	3.1	93.7	3.2	0

Figure D-3: The spatial distribution of topological defects (pentagon, heptagon, and octagon) in the P type models from L=3 nm to 20 nm. The red atoms indicate the atoms belong to non-hexagonal ring defects. The ratios of defects and hexagon ring are listed in table (f). The scale bar represents 1 nm for each model.

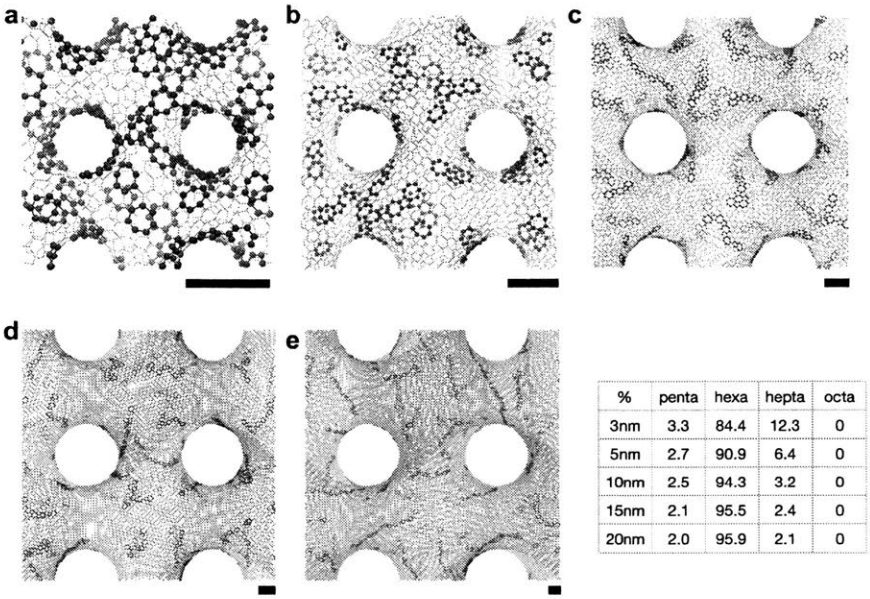

%	penta	hexa	hepta	octa
3nm	3.3	84.4	12.3	0
5nm	2.7	90.9	6.4	0
10nm	2.5	94.3	3.2	0
15nm	2.1	95.5	2.4	0
20nm	2.0	95.9	2.1	0

Figure D-4: (a-e) The spatial distribution of topological defects (pentagon, heptagon, and octagon) in the G type models from L=3 nm to 20 nm. The red atoms indicate the atoms belong to non-hexagonal ring defects. The ratios of defects and hexagon ring are listed in table (f). The scale bar represents 1 nm for each model.

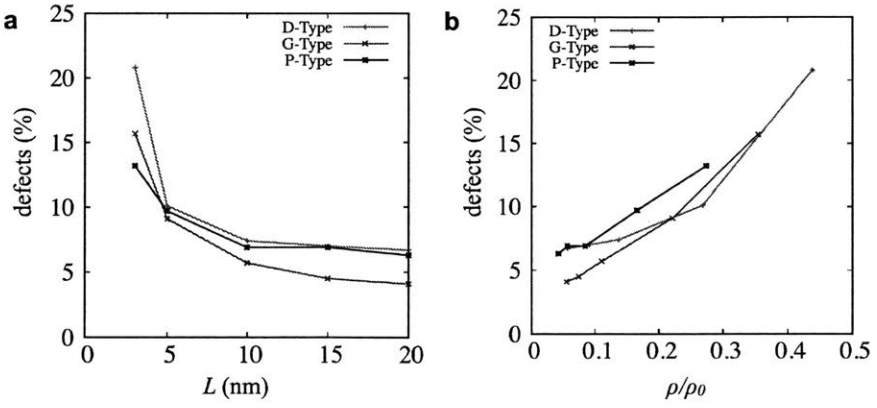

Figure D-5: The ratios of hexagons (a) and defects (b) as a function of relative density. The ratios of hexagons are closed to 95% where the relative density is below the 0.1.

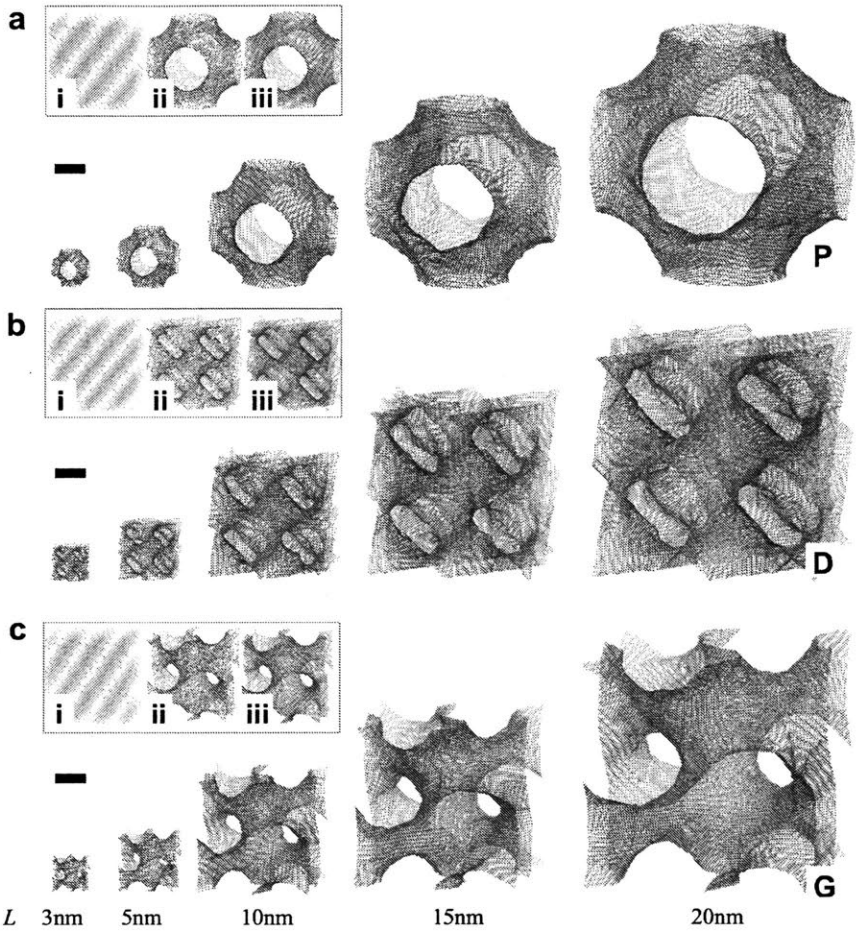

Figure D-6: (a-c) Five different models of P, D, and G types with different lattice sizes of L=3, 5, 10, 15, 20 nm. Scale bar, 2.5 nm. Inset panels present a summary of the three-step process, including (i) generation of the initial template from FCC structure of LJ particles with external potentials, (ii) transformation from triangular LJ lattice to hexagonal carbon lattice, and (iii) refinement of geometries by adding and removing atoms based on bond number. The randomly oriented grains and boundaries with topological defects (mainly pentagons and heptagons) shape the curved surfaces.

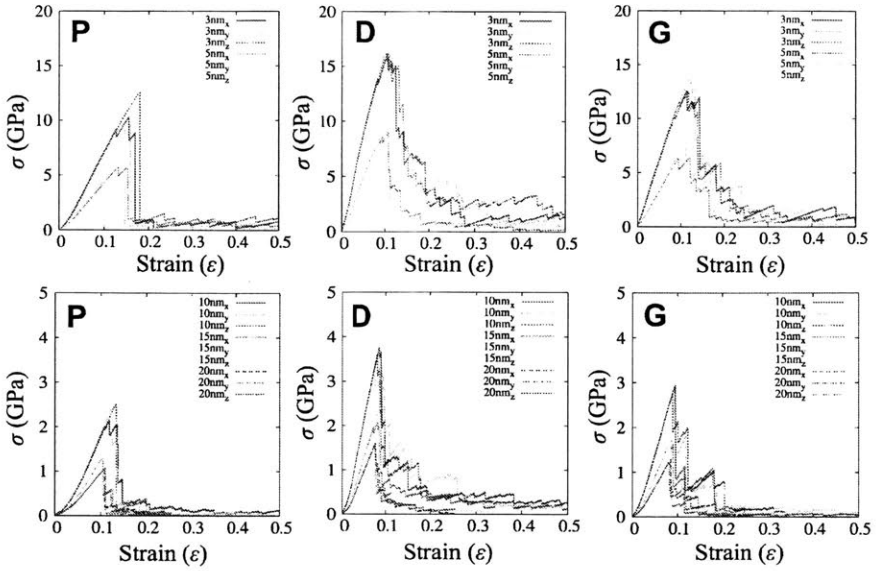

Figure D-7: Stress-strain curves under tensile loading with a plane strain condition. Top Panels include the data for L=3 and 5 nm sizes, and bottom panels show the data for L=10, 15, and 20 nm. The P type clearly shows brittle behavior while the D and G types show multiple breaks with a saw-like shape. The maximum stresses (strengths) are recorded in all three directions and averaged.

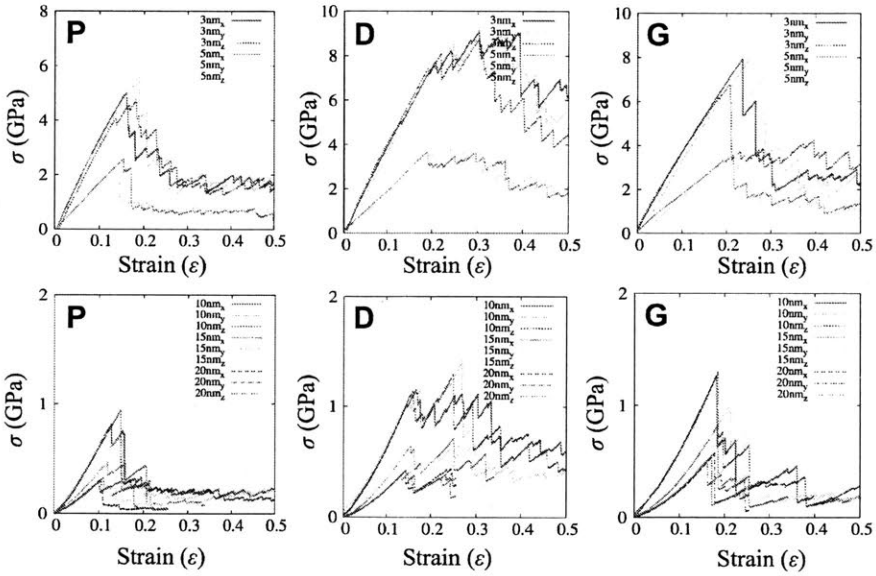

Figure D-8: Stress-strain curves under shear loading with a plane strain condition. Top panels include the data for L=3 and 5 nm, and bottom panels show the data for L=10, 15, and 20 nm. D and G types show multiple breaks with saw-like stress-strain curves.

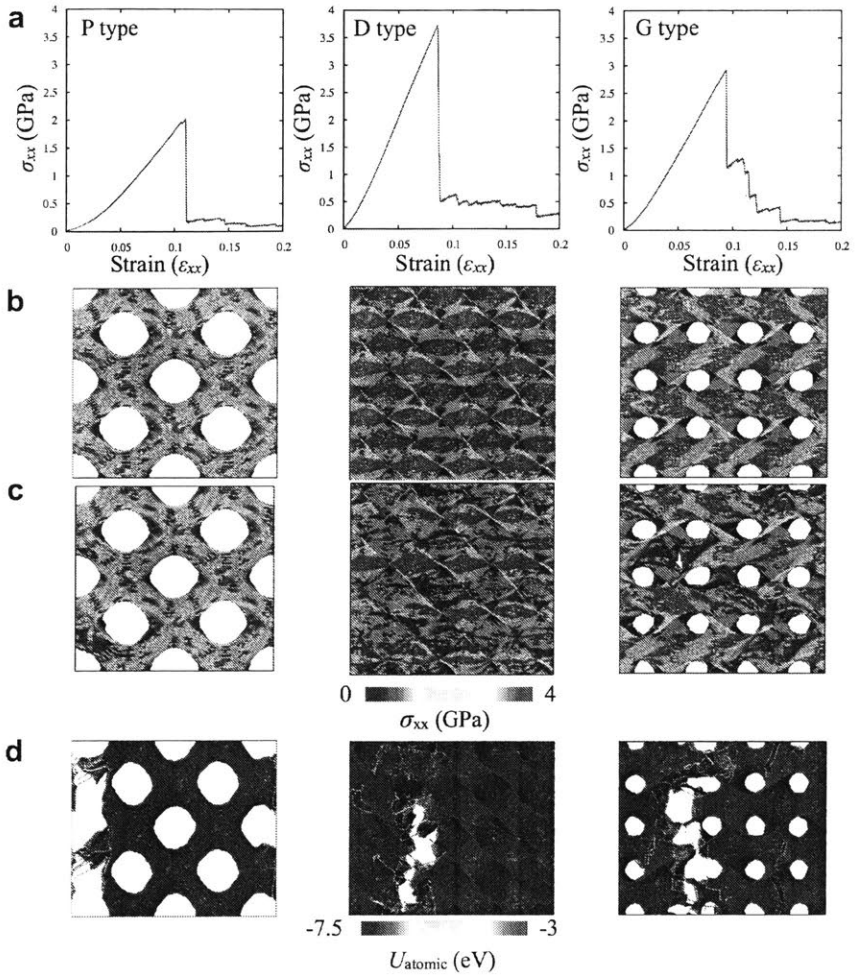

Figure D-9: Finite size effects on failure mechanisms of 3D graphene foams with TPMSs. The tensile tests were performed with 8 unit cells (2x2x2) (a) The stress-strain curves of 3D graphene foams with P, D and G types. (b) The atomic stress distributions before crack nucleation. (c) The atomic stress distribution after crack nucleation. (d) The atomic energy at ϵ_{xx}=0.2 to show the spatial distribution of bond breaking. The bond breaks of P type are spatially localized, which is distinctly different from G and D types as shown in the unit cell study.

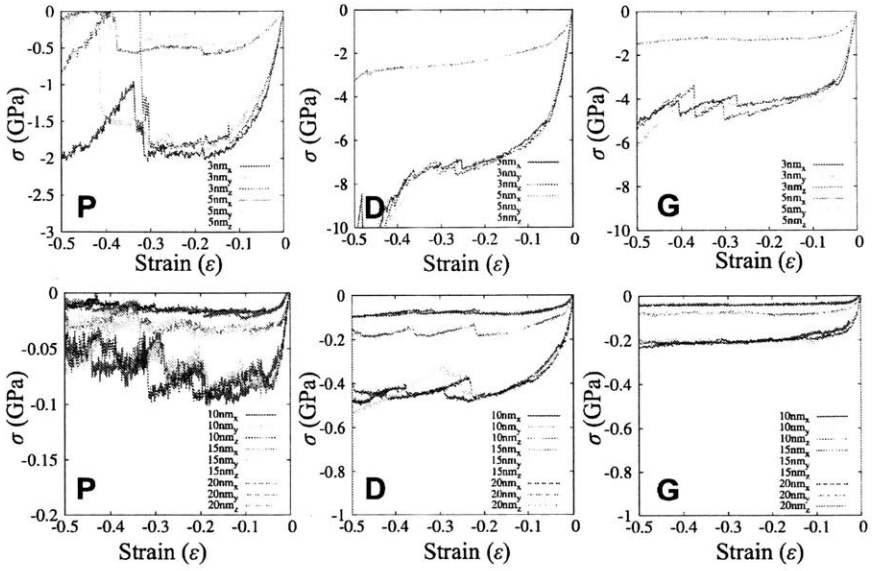

Figure D-10: Stress-strain curves under compressive loading with a plane strain condition. Top panels include the data for L=3 and 5 nm, and bottom panels show the data for L=10, 15, and 20 nm. The compressive stresses are estimated with a fitting function, and the averaged.

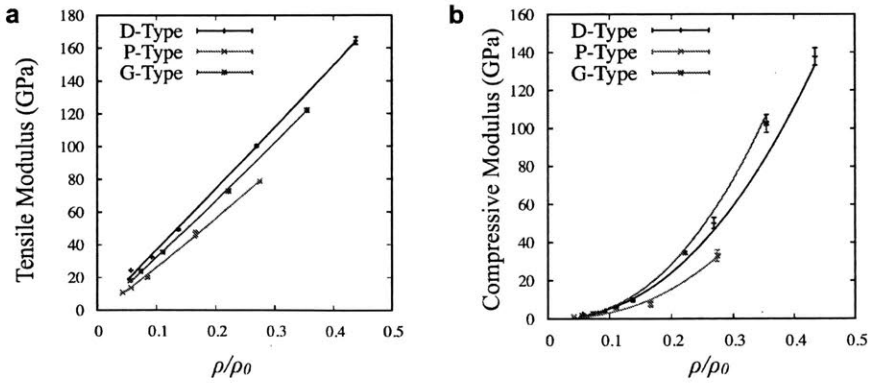

Figure D-11: Tensile (a) and compressive (b) moduli obtained from stress-strain curves. The exponents of both tensile and compressive moduli are less sensitive to the topology as around 1.0 and 2.2, respectively. D and G types show higher moduli than P type, and its difference comes from the coefficients of the scaling laws as in Table E.29.

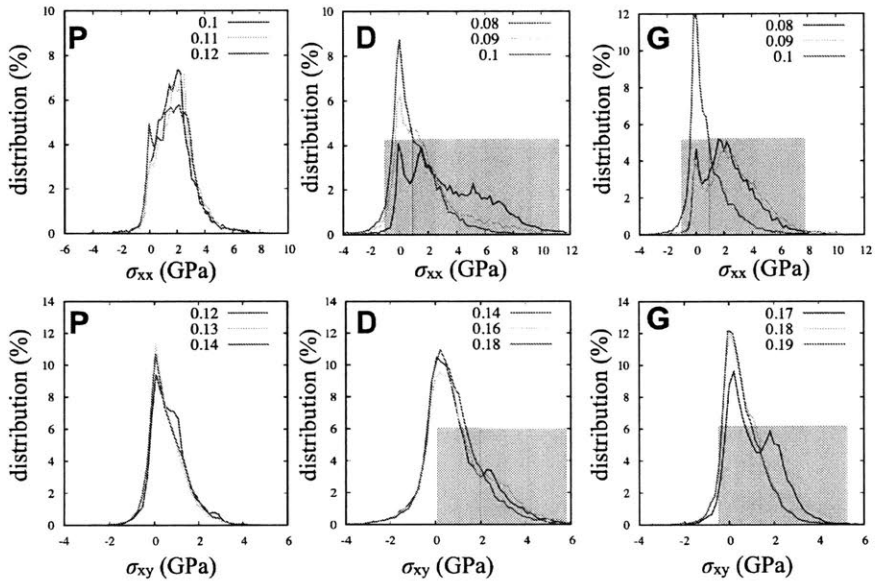

Figure D-12: Distributions of atomic stress at different strains. The blue lines indicate the distributions before the initial crack; the green and red lines show the distributions after initiation of cracks. Compared to P type, D and G types show the two regions of stress distribution (highlighted in red and blue). After initial crack formation, the portion of higher stress region decreases.

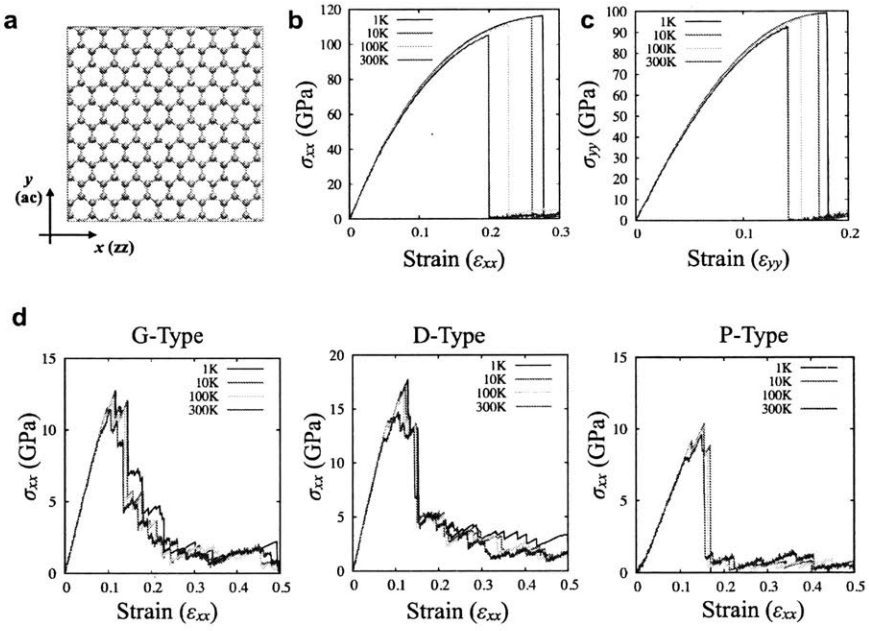

Figure D-13: Temperature effects on the strength of the pristine graphene and 3D graphene foams with TPMS. (a) Schematic of graphene with the lattice direction. (b-c) The stress-strain curves of pristine graphene with the temperatures from 1K to 300K in both zigzag (x) and armchair (y) directions. The strength of pristine graphene strongly depends on the temperature with AIREBO potential. (d) The stress-strain curves in the x direction of 3D graphene foams (L=3 nm) with TMPS (G, D, and P) with the temperatures from 1K to 300K. The temperature does not affect the linear region.

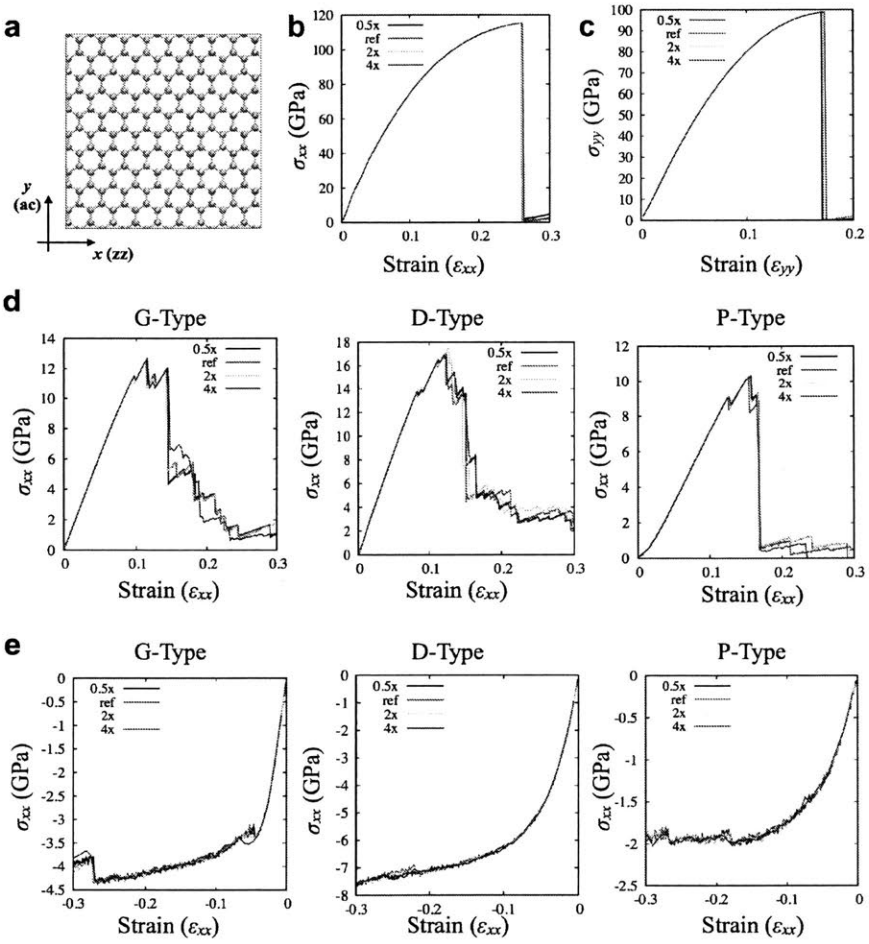

Figure D-14: Strain rate effects on the strength of the pristine graphene and 3D graphene foams with TPMS. (a) Schematic of graphene with the lattice direction. (b-c) The stress-strain curves of pristine graphene with the different strain rate (ref: 0.02Å/ps) in both zigzag (x) and armchair (y) directions. (d) The stress-strain curves in the x direction of 3D graphene foams (L=3 nm) with TMPS (G, D, and P) under various tensile loading rate (ref: 0.02Å/ps). (e) The stress-strain curves in the x direction of 3D graphene foams (L=3 nm) with TMPS (G, D, and P) under various compressive loading rate (ref: -0.05Å/ps).

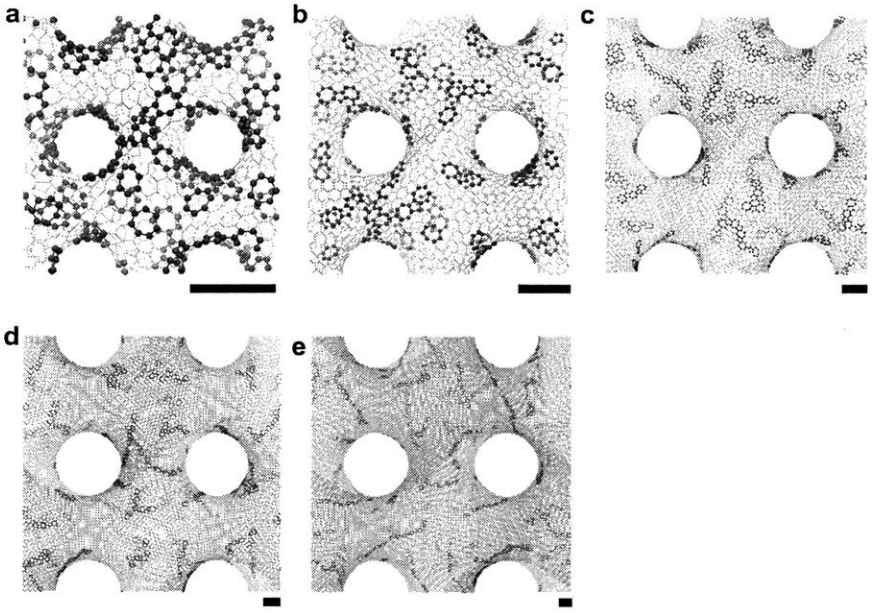

Figure D-15: a-f. The spatial distribution of defects in the gyroid models: L= 3, 5, 10, 15 and 20 nm. Red atoms indicate the atoms belong to non-hexagonal ring defects. The scale bar represents 1 nm for each model.

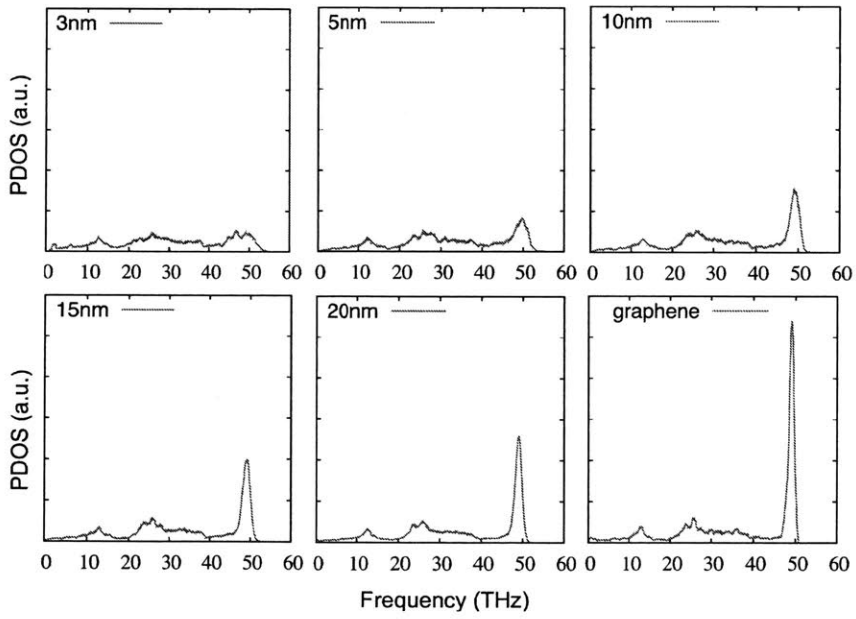

Figure D-16: Phonon density of states of gyroid graphene and graphene (Separated images)

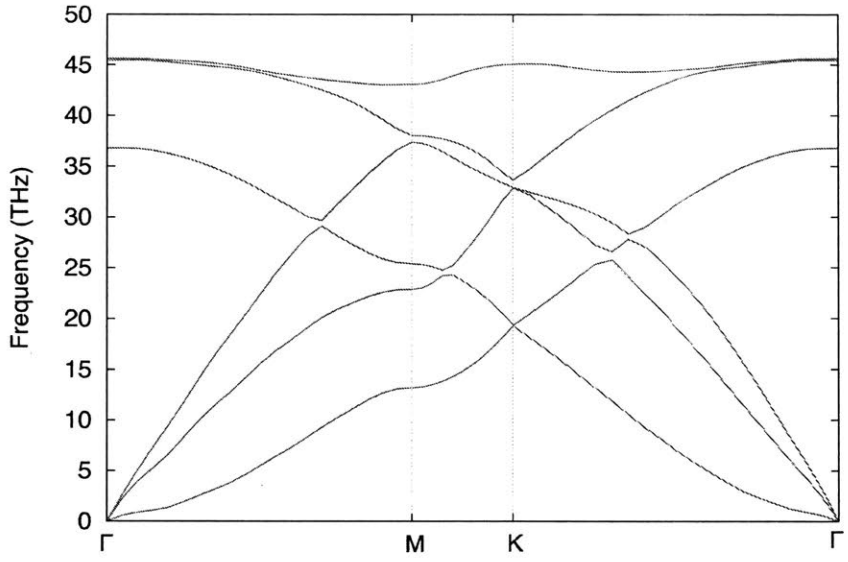

Figure D-17: Phonon dispersion curves of graphene (10 nm x 10 nm) obtained from lattice dynamics with the optimized Tersoff potential.

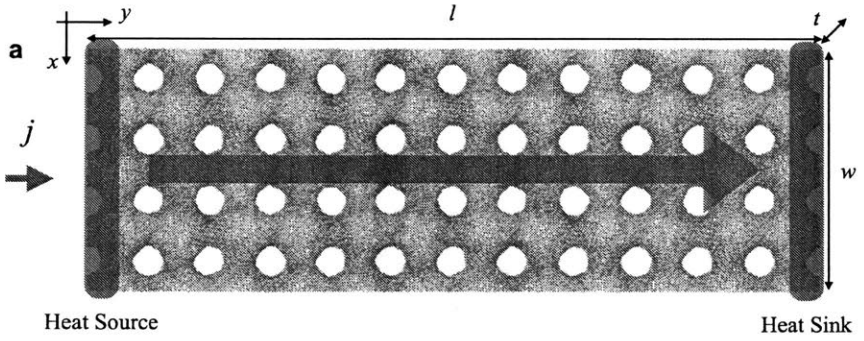

b

L (nm)	3	5	10	15	20
l (nm)	3,6,15,30,60	5,10,20,30,40,60	10,20,30,40,60	15,30,45,60,75,90	20,40,60,80,100
w (nm)	9	10	20	15	20
t (nm)	9	10	10	15	20
j (eV/ps)	0.4 ~ 8.0	0.5 ~ 4.0	1.0 ~ 4.0	0.6 ~ 2.8	1.0 ~ 5.0

Figure D-18: (a) An example of the NEMD setup with a gyroid model (L=10 nm) for l = 60 nm, w=20 nm, and t=10 nm. (b) The table of the detailed NEMD configurations for all models. The heat flux energy, j, is selected based on the temperature gradient. Also, the cross-sectional areas (wt) are selected based on the standard deviation of temperatures of the temperature gradient.

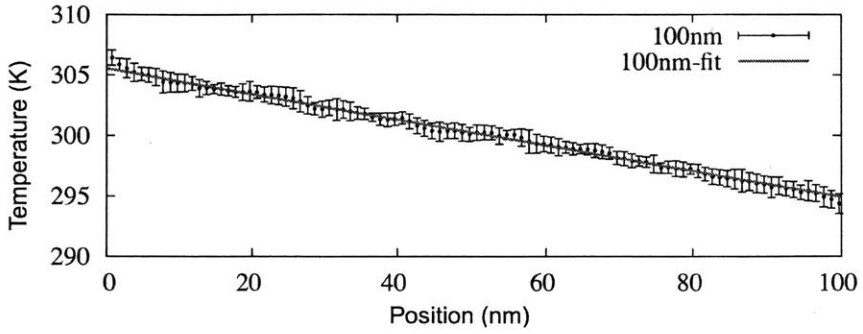

Figure D-19: Typical temperature distribution of gyroid graphene with L=20 nm and L=100 nm).

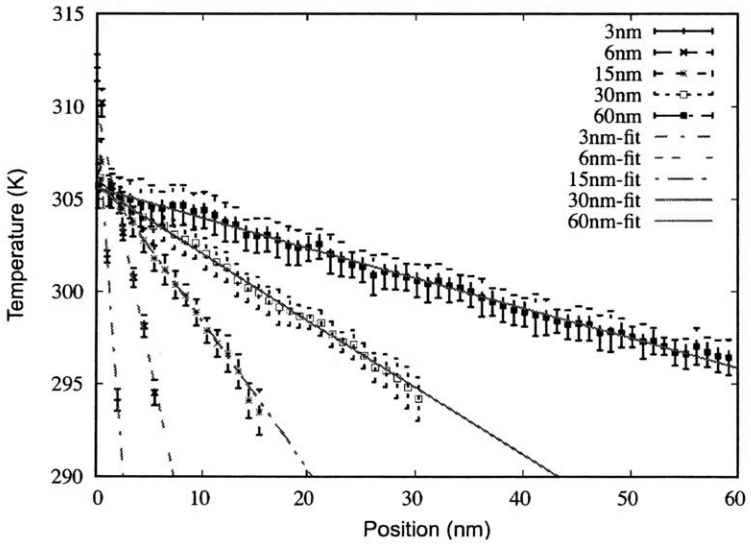

Figure D-20: Typical temperature distribution of gyroid graphene with L=20 nm and L=100 nm).

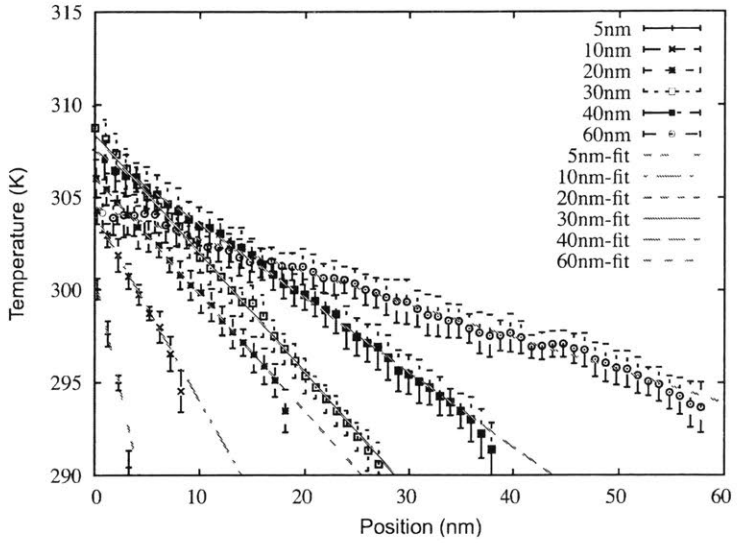

Figure D-21: Temperature distribution of gyroid graphene with L=5 nm with various lengths.

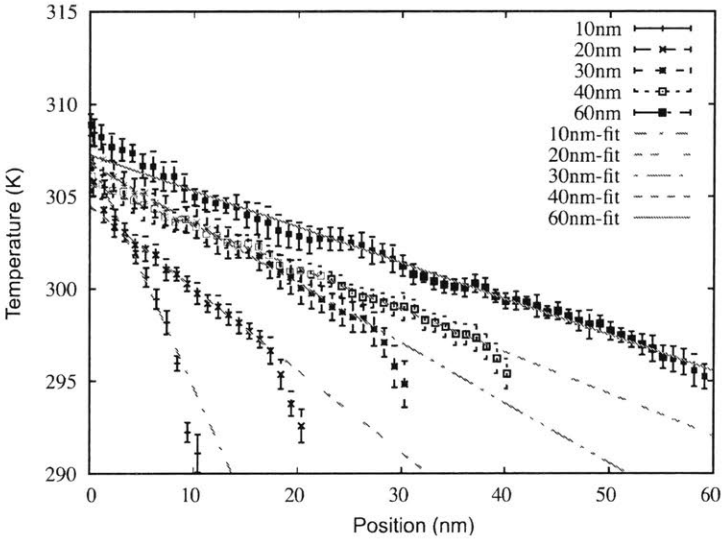

Figure D-22: Temperature distribution of gyroid graphene with L=10 nm with various lengths.

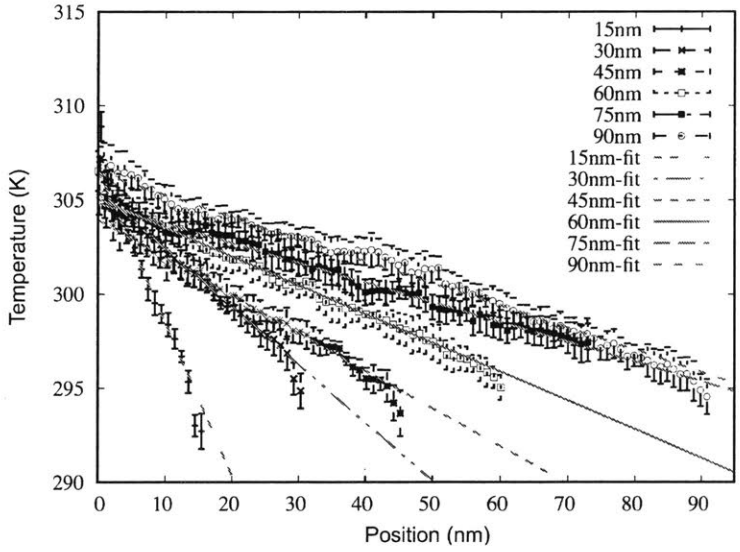

Figure D-23: Temperature distribution of gyroid graphene with L=15 nm with various lengths.

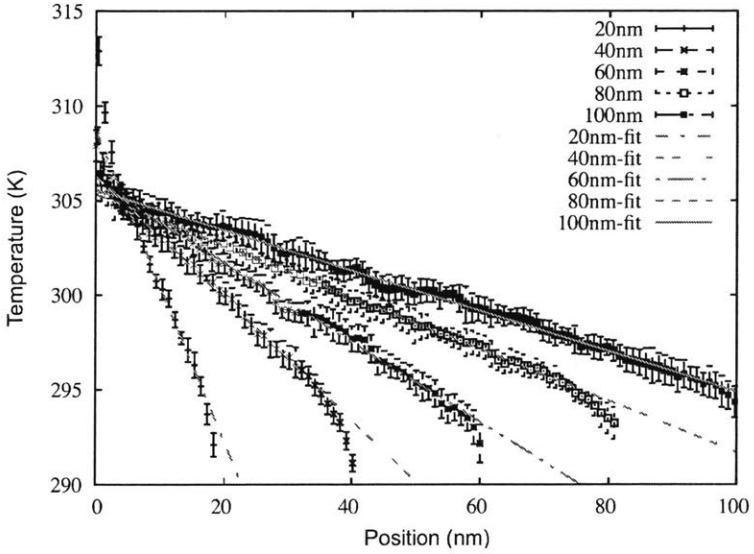

Figure D-24: Temperature distribution of gyroid graphene with L=20 nm with various lengths.

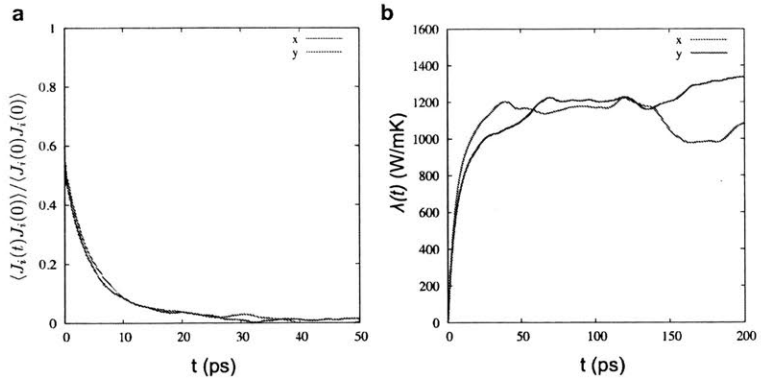

Figure D-25: The HCACF (a) and thermal conductivity (b) and from EMD (Green-Kubo) of graphene (10 nm x 10 nm).

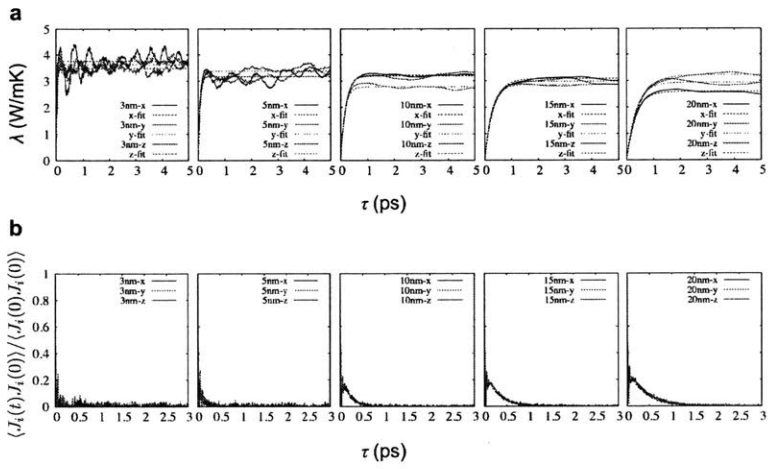

Figure D-26: The thermal conductivity (a) and HCACF (b) from EMD (Green-Kubo) of gyroid graphene.

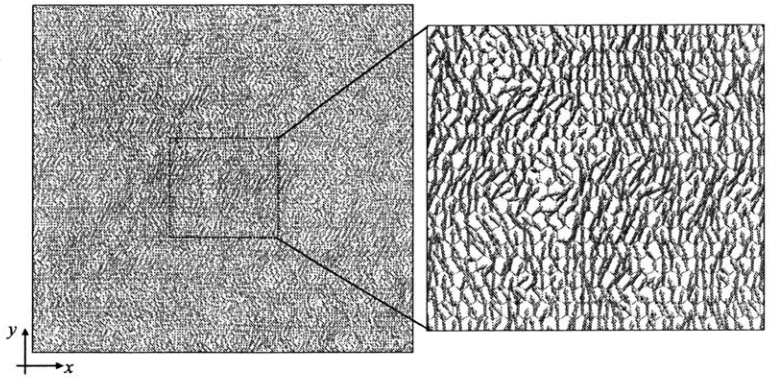

Figure D-27: Atomic heat flux vectors of graphene: homogeneous distribution and clear directionality in the heat flux direction (in the y direction)

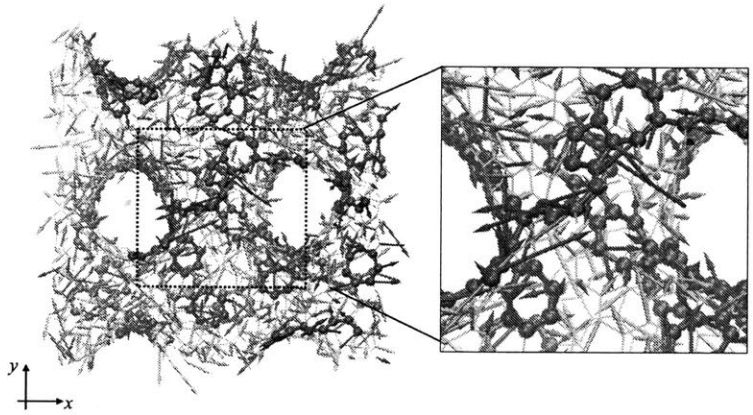

Figure D-28: Atomic heat flux vectors of gyroid model (L=3 nm), NEMD applied in the y direction: non-homogeneous and complicated directionality. The red atoms indicate defects. The vectors of hexagonal atoms show large variation as those of detect atoms.

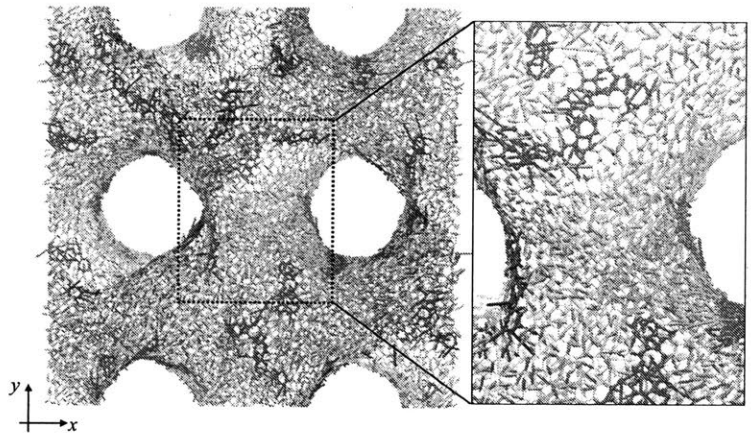

Figure D-29: Atomic heat flux vectors of gyroid model (L=10 nm), NEMD applied in the y direction: The red atoms indicate defects. The vectors of hexagonal atoms show slightly less deviation than those of 3 nm model. The directionality is still unclear.

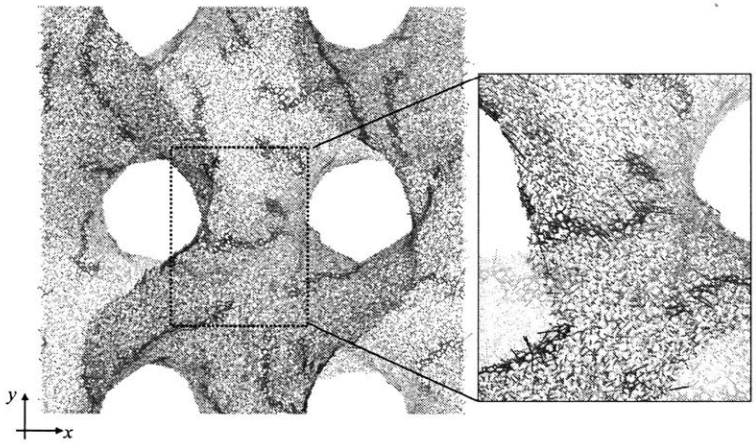

Figure D-30: Atomic heat flux vectors of gyroid model (L=20 nm), NEMD applied in the y direction: The red atoms indicate defects. The vectors of hexagonal atoms show much less deviation than those of hexagonal atoms, clearly showing the difference between defects and hexagonal atoms. The directionality is still unclear because the vector basically follows the lattice directions.

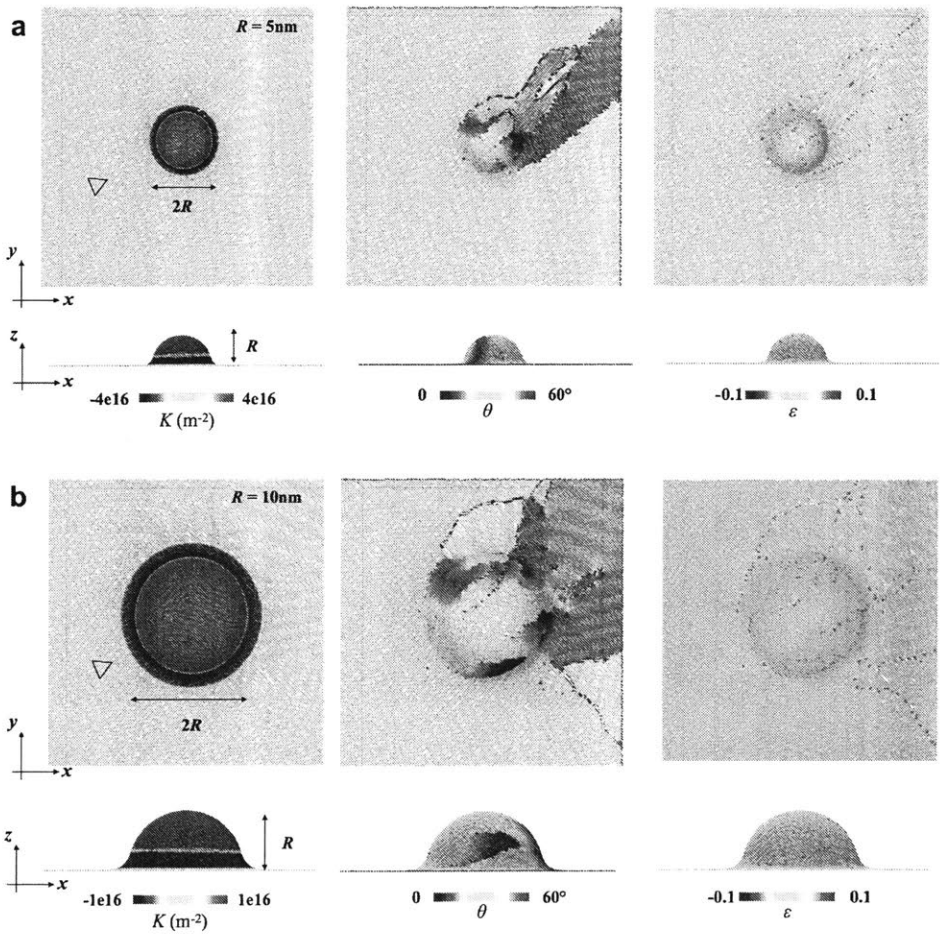

Figure D-31: Crystal growth of MoS_2 with R=5 nm (a) and R=10 nm (b) curvature. K is the Gaussian curvature of the surface; θ is the lattice angle obtained from projected lattice on the flat surface; ϵ is strain calculated from bond length between Mo and S where the S position is projected on the curved surface. Triangles represent the positions and orientation of initial seeds.

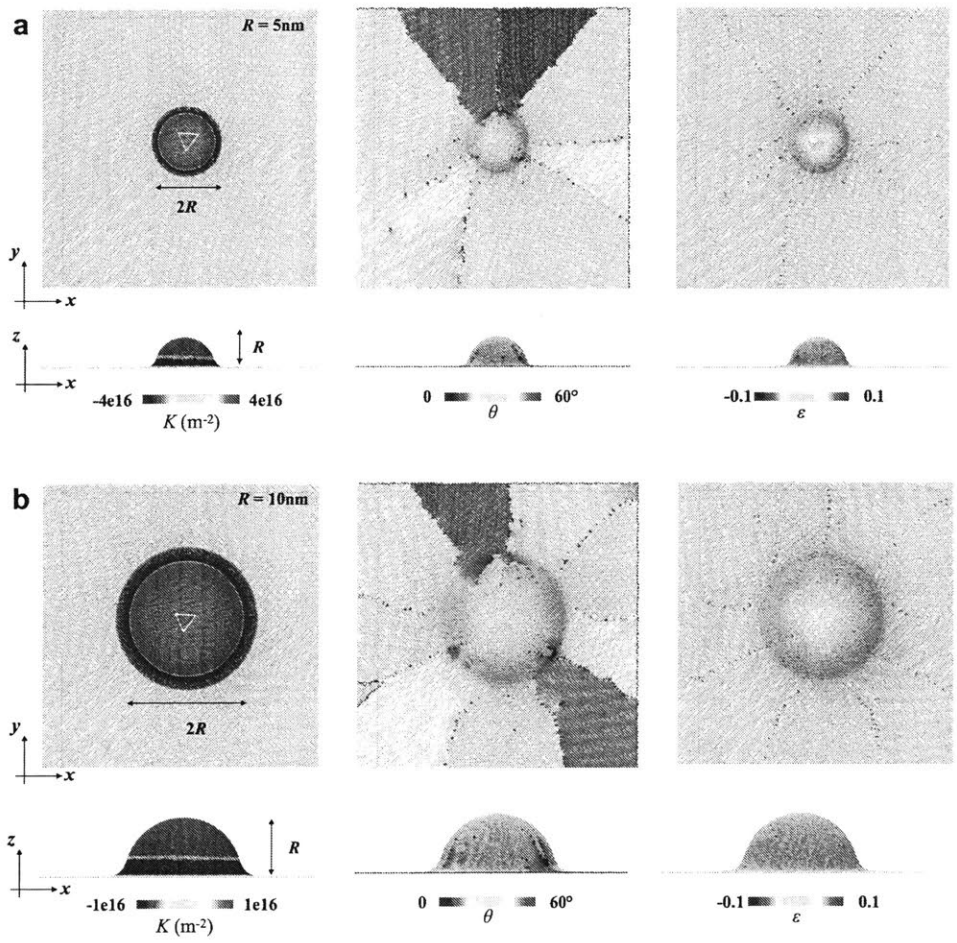

Figure D-32: Crystal growth of MoS_2 with R=5 nm (a) and R=10 nm (b) curvature from the center of the sphere. K is the Gaussian curvature of the surface; θ is the lattice angle obtained from projected lattice on the flat surface; ϵ is strain calculated from bond length between Mo and S where the S position is projected on the curved surface. Triangles represent the positions and orientation of initial seeds.

Appendix E

Supplementary Tables

E_b (meV/atom)	AA	AA' (2H)	AB (3R)
DFT-D2	14.1	24.1	23.8
Original FF	11.6	16.2	16.3
Optimized FF	15.6	22.0	21.7

Table E.1: The binding energy obtained from DFT calculation with Grimme's vdW-D2 correction and MD with both original and optimized reactive FFs. The difference of the binding energy between 2H and 3R are improved.

h_{equil} (Å)	AA	AA' (2H)	AB (3R)
DFT-D2	6.7	6.2	6.3
Original FF	6.5	6.1	6.1
Optimized FF	6.7	6.3	6.3

Table E.2: The equilibrium distance obtained from DFT calculation with Grimme's vdW-D2 correction and MD with both original and optimized reactive FFs. The difference of the equilibrium distance between 2H and 3R are improved.

LJ parameters	σ_{MM} (Å)	σ_{MS} (Å)	σ_{SS} (Å)	ε_{MM} (eV)	ε_{MS} (eV)	ε_{SS} (eV)
Original FF	4.2	3.665	3.13	0.00058595	0.0028498	0.01386
Optimized FF	3.6	3.165	3.25	0.00093752	0.00455965	0.022176

Table E.3: The original and optimized Lennard-Jones parameters for the layer-to-layer interaction. Explicit parameters for σ_{MS} and ϵ_{MS} are utilized instead of conventional mixing rules.

	Original FF	Optimized FF (current study)	DFT (current study)	DFT[15] (reference)
Mo-Mo (S-S)	3.17	3.21	3.18	3.18
Mo-S	2.44	2.46	2.45	2.41
t(S_{top}-S_{bottom})	3.24	3.24	3.20	3.11
C_{11} (N/m)	149.0	127.9	129.9	123.3
C_{12} (N/m)	41.9	38.5	29.3	32.9
C_{22} (N/m)	149.0	127.9	130.2	124.3
E (N/m)	137.0	116.3	123.5	114.5

Table E.4: The geometric parameters and elastic constant of monolayer MoS_2 from DFT calculations and MD.

2R	0° (3R or AB)	15°	30°	45°	60° (2H or AA')
5 nm	0.38	0.081	0.068	0.076	0.41
7 nm	0.41	0.071	0.066	0.063	0.36
10 nm	0.34	0.069	0.060	0.032	0.32
15 nm	0.30	0.063	0.061	0.032	0.28
Avg (nN/nm^2)	0.37 ± 0.04	0.071 ± 0.008	0.064 ± 0.003	0.065 ± 0.004	0.34 ± 0.06

Table E.5: Friction forces per area in the +ZZ direction for the rotational stacking from 2H stack: $\theta = 0°$ (3R) 15°, 30°, 45°, 60° (2H) with four different sizes: $2R = 5$, 7, 10, 15 nm.

2R	0° (3R or AB)	15°	30°	45°	60° (2H or AA')
5 nm	0.34	0.049	0.054	0.051	0.37
7 nm	0.35	0.057	0.060	0.055	0.37
10 nm	0.32	0.056	0.054	0.058	0.34
15 nm	0.29	0.057	0.056	0.061	0.31
Avg (nN/nm^2)	0.33 ± 0.03	0.055 ± 0.003	0.056 ± 0.003	0.056 ± 0.005	0.35 ± 0.03

Table E.6: Friction forces per area in the -ZZ direction for the rotational stacking from 2H stack: $\theta = 0°$ (3R) 15°, 30°, 45°, 60° (2H) with four different sizes: $2R = 5$, 7, 10, 15 nm.

2R	0° (3R or AB)	15°	30°	45°	60° (2H or AA')
5 nm	0.50 / 0.15	0.060	0.059	0.065	0.26 / 0.52
7 nm	0.54 / 0.16	0.055	0.055	0.058	0.24 / 0.57
10 nm	0.53 / 0.15	0.056	0.055	0.060	0.24 / 0.52
15 nm	0.48 / 0.13	0.054	0.060	0.058	0.23 / 0.47
Avg (nN/nm^2)	0.52 ± 0.03 0.15 ± 0.01	0.056 ± 0.003	0.057 ± 0.003	0.060 ± 0.003	0.24 ± 0.01 0.52 ± 0.04

Table E.7: Friction forces per area in the +AC direction for the rotational stacking from 2H stack: $\theta = 0°$ (3R) 15°, 30°, 45°, 60° (2H) with four different sizes: $2R = 5$, 7, 10, 15 nm. For 2H and 3R, two peak forces are recorded.

2R	0° (3R or AB)	15°	30°	45°	60° (2H or AA')
5 nm	0.27 / 0.54	0.066	0.064	0.066	0.53 / 0.11
7 nm	0.25 / 0.53	0.071	0.062	0.066	0.59 / 0.15
10 nm	0.23 / 0.51	0.066	0.066	0.064	0.52 / 0.14
15 nm	0.25 / 0.48	0.064	0.063	0.064	0.50/ 0.14
Avg (nN/nm^2)	0.25 ± 0.01 0.52 ± 0.03	0.067 ± 0.003	0.064 ± 0.002	0.065± 0.002	0.53 ± 0.04 0.14 ± 0.02

Table E.8: Friction forces per area in the -AC direction for the rotational stacking from 2H stack: $\theta = 0°$ (3R) 15°, 30°, 45°, 60° (2H) with four different sizes: $2R = 5$, 7, 10, 15nm. For 2H and 3R, two peak forces are recorded.

R (nm)	Circle K_{IC} (MPam$^{1/2}$)		Triangle-1 K_{IC} (MPam$^{1/2}$) S-edge (Exp)		Triangle-2 K_{IC} (MPam$^{1/2}$) W-edge		Triangle-3 K_{IC} (MPam$^{1/2}$) S-edge (invT)		Triangle-4 K_{IC} (MPam$^{1/2}$) W-edge (invT)	
	zz	ac	zz	ac	zz	ac	zz	ac	zz	ac
1	0.78	0.73	0.75	0.77	0.87	0.72	0.88	0.76	0.84	0.78
2	1.10	1.13	0.77	0.80	0.91	0.78	0.94	0.85	0.92	0.89
3	1.11	1.13	0.87	0.83	1.00	0.85	1.01	0.9	0.94	0.91
4	1.24	1.39	0.87	0.84	1.00	0.86	1.03	0.95	0.97	0.96
5	1.32	1.49	0.82	0.88	1.01	0.88	1.03	0.98	0.98	1.00
6	**1.41**	**1.62**	**0.84**	**0.88**	**1.01**	**0.89**	**1.03**	**0.99**	**1.00**	**1.00**
7	**1.45**	**1.64**	**0.97**	**0.88**	**1.00**	**0.89**	**1.05**	**1.0**	**0.98**	**0.99**
8	**1.49**	**1.75**	**0.80**	**0.89**	**1.03**	**0.9**	**1.03**	**0.99**	**0.99**	**0.99**
Avg. (std.)	1.45 (0.04)	1.67 (0.07)	0.87 (0.1)	0.88 (0.01)	1.01 (0.02)	0.89 (0.01)	1.04 (0.01)	0.99 (0.01)	0.99 (0.01)	0.99 (0.01)

Table E.9: The fracture toughness (K_{IC}) of the WS_2 monolayer with the different radius of crack and its failure strength (σ_C). The effective thickness is set as 0.615 nm for monolayer WS_2.

R (nm)	Triangle-1 K_{IC} (MPam$^{1/2}$) S-edge (Exp)		Triangle-2 K_{IC} (MPam$^{1/2}$) W-edge		Triangle-3 K_{IC} (MPam$^{1/2}$) S-edge (invT)		Triangle-4 K_{IC} (MPam$^{1/2}$) W-edge (invT)	
	zz	ac	zz	ac	zz	ac	zz	ac
1	0.77	1.01	0.89	0.95	0.9	1.01	0.86	1.03
2	0.78	1.03	0.93	1.02	0.95	1.10	0.94	1.15
3	0.87	1.05	0.99	1.08	1.00	1.16	0.94	1.16
4	0.86	1.04	0.99	1.07	1.00	1.19	0.96	1.20
5	0.80	1.08	0.99	1.08	1.00	1.20	0.95	1.22
6	**0.81**	**1.06**	**0.97**	**1.06**	**0.99**	**1.18**	**0.96**	**1.20**
7	**0.92**	**1.03**	**0.95**	**1.04**	**0.99**	**1.17**	**0.93**	**1.16**
8	**0.75**	**1.01**	**0.96**	**1.03**	**0.96**	**1.14**	**0.93**	**1.14**
Avg. (std.)	0.83 (0.09)	1.03 (0.01)	0.96 (0.01)	1.04 (0.01)	0.98 (0.02)	1.16 (0.02)	0.94 (0.02)	1.16 (0.03)

Table E.10: The fracture toughness (K_{IC}) of the WS_2 monolayer with the different R of crack and its failure strength (σ_C) based on the empirical equations from FEM simulations. We use the effective thickness as 0.615 nm for monolayer WS_2.

Circular void R (nm)	zz (N/m)	ac (N/m)
1	8.6	8.0
2	8.5	8.7
3	7.0	7.1
4	6.8	7.6
5	6.5	7.3
6	6.3	7.2
7	6.0	6.7
8	5.7	6.7
K_{IC} (MPam$^{1/2}$)	1.46	1.5
l (nm)	1.07	0.78

Table E.11: The strengths (N/m) of WS_2 monolayer from the stress-strain curves from $R = 1$ nm to 8 nm. The fracture toughness (K_{IC}) of the WS_2 monolayer with the different radius of crack. We used the effective thickness as 0.615 nm for monolayer WS_2.

Q_{MM}	3.68313	α_{MM}	0.995132
β_{MM}	1.07603	A_{MM}	121.276952699
B_{MM}	478.479101848	A_{MS}	388.7777704834
B_{MS}	908.2375325272	R^{min}_{MS}	2.91
R^{max}_{MS}	2.91	R^{max}_{SS}	2.9

Table E.12: The parameters for interatomic interaction in the current study. Subscripts M and S refer metal and chalcogen, respectively.

DFT (Å)	MoS_2	WS_2	$MoSe_2$	WSe_2
Mo/W-Mo/W	3.18	3.23	3.32	3.36
Mo/W-S/Se	2.45	2.45	2.55	2.58
S/Se-S/Se	3.18	3.23	3.32	3.36
t(top-bottom)	3.20	3.19	3.35	3.40

Table E.13: The geometric parameters obtained from DFT calculations.

REBO (Å)	MoS_2	WS_2	$MoSe_2$	WSe_2
Mo/W-Mo/W	3.17	3.24	3.28	3.33
Mo/W-S/Se	2.46	2.46	2.55	2.56
S/Se-S/Se	3.17	3.24	3.28	3.33
t(top-bottom)	3.23	3.21	3.41	3.38

Table E.14: The geometric parameters obtained from REBO potential

DFT (N/m)	MoS_2	WS_2	$MoSe_2$	WSe_2
C11	129.9	129.3	104.7	113.1
C22	130.2	132.6	105.6	112.2
C12	29.25	30.15	24.9	25.8
E	123.5	124	99.2	106.7

Table E.15: Elastic constants and Young's modulus (averaged in the x and y directions) from DFT calculations

REBO (N/m)	MoS_2	WS_2	$MoSe_2$	WSe_2
C11	115.1	118.3	90.1	96.3
C22	115.1	118.3	90.1	96.3
C12	34.1	34.8	26.7	28.6
E	105.0	108.1	82.2	87.8

Table E.16: Elastic constants and Young's modulus (averaged in the x and y directions) from the current REBO potential

	$(MoS_2)_{10}$	$(WSe_2)_{10}$	$(MoS_2)_1$ $(WSe_2)_9$	$(MoS_2)_2$ $(WSe_2)_8$	$(MoS_2)_3$ $(WSe_2)_7$	$(MoS_2)_4$ $(WSe_2)_6$
A in x (Å)	31.86	33.60	33.43	33.24	33.07	32.90
B in y (Å)	5.52	5.82	5.79	5.76	5.73	5.70
ε_y in MoS_2	0	-	4.9%	4.3%	3.8%	3.2%
ε_y in WSe_2	-	0	-0.5%	-1.0%	-1.5%	-2.0%
CBM (eV)	-4.21 (-4.29)[17]	-3.64 (-3.69)[17]	-3.72	-3.8	-3.85	-3.92
VBM (eV)	-5.92 (-5.98)[17]	-5.09 (-5.20)[17]	-5.15	-5.21	-5.27	-5.33
Gap (eV)	1.71 (1.69)[17]	1.45 (1.51)[17]	1.43	1.41	1.42	1.41

Table E.17: The relaxed lattice parameters (A in the x direction and B in the y direction), CBM, VBM and band gap of each model. The reference values of pristine MoS_2 and WSe_2 are obtained from the previous study[17] [168]. Here we use the foot notation to indicate the width of the materials in rectangular unit cells. For example, $(MoS_2)_3(WSe_2)_7$ indicate a three-unit-cell wide MoS_2 1D channel embedded within a seven-unit-cell WSe_2 matrix, which is schematically described in Figure **??**(a).

	$(MoS_2)_1$ $(WSe_2)_9$	$(MoS_2)_2$ $(WSe_2)_8$	$(MoS_2)_3$ $(WSe_2)_7$	$(MoS_2)_4$ $(WSe_2)_6$
CBM@MoS_2 (eV)	-3.72	-3.80	-3.85	-3.92
VBM@MoS_2 (eV)	-5.24	-5.47	-5.51	-5.56
Gap@MoS_2 (eV)	1.52	1.67	1.66	1.64

Table E.18: The estimation of localized band-edge of MoS_2 from the orbital projected band structures. With widths from one rectangular unit cell to four unit cells, the MoS_2 channels all present direct band gaps even if we consider the Γ point in the calculation.

L (nm)	P	D	G
3	630.3	1008.0	814.8
5	381.0	618.2	510.1
10	195.3	315.3	253.9
15	129.7	211.8	169.4
20	97.3	129.0	126.8

Table E.19: Densities (mg/cm^3) of 3D graphene foams with different TPMSs after structural relaxation.

L (nm)	P	D	G
3	810	1304	1062
5	2266	3658	2846
10	9116	14802	11972
15	20582	33412	27018
20	36526	59478	48172
a	2.32±0.004	3.78±0.009	3.06±0.01

Table E.20: The number of atoms in 3D graphene foams with different TPMSs (2.546Å^2/atom). The surface area is $S = aL^2$ and the factor, a, is obtained by averaging from 10 to 20 nm models where the defects ratios are low enough.

	P	D	G
C_{11} (GPa)	384.9 $(\rho/\rho_0)^{1.50}$	590.1 $(\rho/\rho_0)^{1.49}$	643.5 $(\rho/\rho_0)^{1.64}$
C_{12} (GPa)	196.6 $(\rho/\rho_0)^{1.43}$	165.3 $(\rho/\rho_0)^{1.87}$	284.9 $(\rho/\rho_0)^{1.89}$
C_{44} (GPa)	275.1 $(\rho/\rho_0)^{1.48}$	167.7 $(\rho/\rho_0)^{1.70}$	194.5 $(\rho/\rho_0)^{1.55}$
$(C_{11}$-$C_{12})/2$ (GPa)	99.9 $(\rho/\rho_0)^{1.63}$	206.2 $(\rho/\rho_0)^{1.37}$	188.8 $(\rho/\rho_0)^{1.53}$
E (GPa)	266.8 $(\rho/\rho_0)^{1.62}$	499.9 $(\rho/\rho_0)^{1.41}$	494.2 $(\rho/\rho_0)^{1.57}$
ν	0.378(1-exp(-29.6ρ/ρ_0))	0.156(1-exp(-16.6ρ/ρ_0))	0.25(1-exp(-15.4ρ/ρ_0))

Table E.21: Elastic constants as a function of the relative densities. The density of pristine graphene (ρ_0) is 2.3g/cm^3.

	P	D	G
E (GPa)	266.8 $(\rho/\rho_0)^{1.62}$	499.9 $(\rho/\rho_0)^{1.41}$	494.2 $(\rho/\rho_0)^{1.57}$
E_{VRH} (GPa)	466.2 $(\rho/\rho_0)^{1.53}$	446.5 $(\rho/\rho_0)^{1.56}$	502.1 $(\rho/\rho_0)^{1.58}$
C_{44} (GPa)	275.1 $(\rho/\rho_0)^{1.48}$	167.7 $(\rho/\rho_0)^{1.70}$	194.5 $(\rho/\rho_0)^{1.55}$
$(C_{11}$-$C_{12})/2$ (GPa)	99.9 $(\rho/\rho_0)^{1.63}$	206.2 $(\rho/\rho_0)^{1.37}$	188.8 $(\rho/\rho_0)^{1.53}$
G_{VRH} (GPa)	182.9 $(\rho/\rho_0)^{1.54}$	179.8 $(\rho/\rho_0)^{1.55}$	192.4 $(\rho/\rho_0)^{1.55}$

Table E.22: Young's modulus and Shear modulus from the cubic lattices and VRH average (ρ_0= 2.3g/cm^3). Due to cubic symmetry, there are two shear moduli: C_{44} and $(C_{11} - C_{12})/2$.

	P	D	G
E_{VRH} (GPa)	446.2 $(\rho/\rho_0)^{1.53}$	446.5 $(\rho/\rho_0)^{1.56}$	502.1 $(\rho/\rho_0)^{1.58}$
G_{VRH} (GPa)	182.9 $(\rho/\rho_0)^{1.54}$	179.8 $(\rho/\rho_0)^{1.55}$	192.4 $(\rho/\rho_0)^{1.55}$
B_{VRH} (GPa)	257.4 $(\rho/\rho_0)^{1.46}$	286.8 $(\rho/\rho_0)^{1.55}$	398.8 $(\rho/\rho_0)^{1.74}$
ν_{VRH}	0.251(1-exp(-21.3ρ/ρ_0))	0.245(1-exp(-30.9ρ/ρ_0))	0.257(1-exp(-14.6ρ/ρ_0))
A_Z (GPa)	3.60±0.51	1.98±0.11	0.99±0.04
A_U (GPa)	2.23±0.51	0.6±0.1	0.02±0.007

Table E.23: The elasticity based on Voigt-Reuss-Hill approach as a function of the relative densities ($\rho_0 = 2.3\text{g/cm}^3$). Two anisotropy indexes: a Zenar ratio and a universal anisotropic index.

L (nm)	P ($\Delta E/\Delta G/\Delta B$)	D ($\Delta E/\Delta G/\Delta B$)	G ($\Delta E/\Delta G/\Delta B$)
3	8.4/2.0/0.1	2.7/0.3/0.01	0.03/0.004/0.03
5	4.7/2.4/0.04	3.0/0.7/0.01	0.04/0.01/0.04
10	2.0/4.0/0.02	1.0/0.7/0.005	0.04/0.04/0.002
15	0.8/2.0/0.001	0.7/0.9/0.01	0.02/0.03/0.004
20	0.3/0.8/0.01	0.3/0.5/0.003	0.005/0.007/0.005

Table E.24: The variance of Young's modulus (E_{VRH}), shear modulus (G_{VRH}), and bulk modulus (B_{VRH}) based on VRH average. The variance of the bulk modulus is small (<0.1) because the values from cubic symmetry have to be the same as the isotropic average. The unit is GPa.

	P	D	G
σ_T (GPa)	55.6 $(\rho/\rho_0)^{1.25}$	46.6 $(\rho/\rho_0)^{1.26}$	49.2 $(\rho/\rho_0)^{1.28}$
σ_C (GPa)	57.4 $(\rho/\rho_0)^{2.62}$	64.1 $(\rho/\rho_0)^{2.65}$	50.0 $(\rho/\rho_0)^{2.37}$
σ_S (GPa)	34.1 $(\rho/\rho_0)^{1.46}$	34.4 $(\rho/\rho_0)^{1.65}$	36.6 $(\rho/\rho_0)^{1.53}$

Table E.25: Strengths as a function of the relative densities with different structures.

	P	D	G
$G_{elastic}$ (J/m^2)	5.8 $(\rho/\rho_0)^{0.61}$	5.1 $(\rho/\rho_0)^{0.61}$	4.6 $(\rho/\rho_0)^{0.58}$
$G_{dissipation}$ (J/m^2)	3.8 $(\rho/\rho_0)^{0.74}$	13.3 $(\rho/\rho_0)^{1.1}$	9.2 $(\rho/\rho_0)^{0.89}$
G_{total} (J/m^2)	9.6 $(\rho/\rho_0)^{0.66}$	17.1 $(\rho/\rho_0)^{0.86}$	13.4 $(\rho/\rho_0)^{0.75}$

Table E.26: Fracture energies under tensile loading as a function of the relative densities.

Deformation strain	C_{11} (GPa)	C_{12} (GPa)	E (GPa)
0.01%	954.5	350.0	826.2
0.05%	945.6	348.4	827.4
0.1%	956.1	346.2	830.8
0.5%	971.64	332.3	858
1.0%	987.6	317.3	885.7

Table E.27: The deformation strain for elastic constants of graphene. The range between 0.01% and 0.1% shows relatively constant elastic constants and 0.1% was chosen to measure the elastic constants for TPMS models.

	P		D		G	
	Orthotropic	Cubic	Orthotropic	Cubic	Orthotropic	Cubic
3nm	0.35±0.03	0.36	0.17±0.01	0.17	0.25±0.01	0.25
5nm	0.37±0.01	0.38	0.14±0.01	0.14	0.23±0.02	0.23
10nm	0.41±0.01	0.40	0.13±0.01	0.13	0.22±0.02	0.22
15nm	0.32±0.03	0.33	0.13±0.02	0.13	0.17±0.03	0.17
20nm	0.23±0.05	0.23	0.09±0.01	0.09	0.12±0.01	0.12

Table E.28: Two different methods obtain Poisson ratios. One is calculating averaged Poisson ratios obtained from orthotropic symmetry. The other one is calculating Poisson ratios from averaged C_{11} and C_{12}, utilizing the equation from cubic symmetry, $C_{12}/(C_{11}+C_{12})$.

	Tensile modulus (GPa)			Compressive modulus (GPa)		
Types	P	D	G	P	D	G
3nm	78.5±0.6	164.5±2.3	122.2±1.3	33.0±3.1	137.7±4.6	102.5±4.7
5nm	46.7±2.2	100.5±0.7	72.9±1.3	7.7±1.6	50.1±2.9	34.5±0.7
10nm	20.1±0.6	49.4±0.5	35.5±0.2	3.1±0.2	9.7±0.9	5.9±0.7
15nm	13.7±0.1	32.5±0.3	23.8±0.2	1.5±0.1	4.1±0.2	2.7±0.2
20nm	10.7±0.03	24.3±0.2	18.1±0.1	1.1±0.1	2.5±0.2	1.7±0.3
Power laws	$329.2\,(\rho/\rho_0)^{1.1}$	$377.7\,(\rho/\rho_0)^{1.01}$	$362.6\,(\rho/\rho_0)^{1.05}$	$633.2\,(\rho/\rho_0)^{2.3}$	$835.6\,(\rho/\rho_0)^{2.2}$	$1165.5\,(\rho/\rho_0)^{2.3}$

Table E.29: Tensile and compressive moduli from stress-strain curves. The tensile and compressive moduli were fitted from strain 4 $\sim$ 6% and 0 $\sim$ -2%, respectively.

L (nm)	5 rings	6 rings	7 rings	8 rings	Disorder ratio by #type (%)	Disorder ratio (β) by #atom (%)
3	17	439	64	0	15.58	41.0
5	30	1002	70	0	9.07	18.8
10	147	5635	192	1	5.69	13.0
15	279	12896	321	3	4.47	10.0
20	473	23086	413	4	3.71	9.0

Table E.30: Defect types and disorder ratios of three-dimensional gyroid graphene models.

L (nm)	λ_0 (W/mK)	l_0 (nm)	A	Λ_0 (W/mk)
3	4.45	58.9	9.66	4.94
5	4.15	84.0	8.46	4.50
10	3.74	88.15	15.82	4.19
15	3.75	157.7	26.66	4.14
20	3.57	200.5	36.52	4.1

Table E.31: Fitted parameter data for thermal conductivity (exponential fit), $\lambda(x) = \lambda_0(1 - \exp(-x/l_0))$, and inversed thermal conductivities (inverse linear fit), $\frac{1}{\Lambda}\left(\frac{1}{x}\right) = A\left(\frac{1}{x}\right) + \frac{1}{\Lambda_0}$, as a function of the length and the inverse length from NEMD.

L (nm)	λ_0 (W/mK)	τ_0 (ps)	*Doubled size* λ_0 (W/mK)
3	3.62 ± 0.14	0.02	3.52 ± 0.03
5	3.25 ± 0.12	0.07	3.07 ± 0.15
10	3.07 ± 0.25	0.17	3.00 ± 0.07
15	2.97 ± 0.11	0.29	2.91 ± 0.09
20	2.91 ± 0.32	0.37	2.69 ± 0.15
Reference (graphene)	1218 (zz), 1121(ac)	8.78	-

Table E.32: Fitted parameter data for thermal conductivity (exponential fit), as a function of correlation time (ps) from EMD (zz: zigzag direction, ac: armchair direction). The parameter, τ_0, is a relaxation time of the fast acoustic modes. The size effects are tested with doubled size

L (nm)	λ (t, w, l)	λ_{tested} (t, w, l)
3	4.71 ± 0.47 (9,9,60)	5.08 ± 0.39 (18,9,60)
5	4.64 ± 0.44 (10,10,60)	4.32 ± 0.31 (20,10,60)
10	4.03 ± 0.38 (20,10,60)	3.73 ± 0.17 (20,20,60)
15	3.99 ± 0.4 (15,15,90)	4.07 ± 0.48 (30,15,90)
20	3.7 ± 0.46 (20,20,100)	3.2 ± 0.2 (40,20,100)

Table E.33: The effects of width and thickness. We have tested doubled width or thickness with the longest sample in the y direction (l). The results show the thermal conductivities from the Fourier law. Increasing the width or thickness from the current setting does not affect thermal conductivities.

L (nm)	λ_0 (W/mK) @200K	λ_0 (W/mK) @300K	λ_0 (W/mK) @400K	α
3	3.65 ± 0.14	3.52 ± 0.03	3.49 ± 0.07	0.005
10	3.19 ± 0.04	3.00 ± 0.07	2.98 ± 0.04	0.008
20	2.77+0.1	2.69 ± 0.15	2.64 ± 0.02	0.06

Table E.34: Temperature dependency obtained from EMD with doubled sizes due to their small standard deviations. Fitted data for thermal conductivity (exponential fit), as a function of correlation time (ps) from EMD. The dependency parameter, α, is fitted to $\lambda \sim T^{-\alpha}$ in the range between 200K to 400K.

Appendix F

Codes, REBO Parameters, and Visualization

In this appendix, the developed codes and parameters are listed and explained.

F.1 Polycrystalline graphene generation

The sources codes include (C++, intel compiler, and openmpi with fftw and voro++ libraries): main.cpp, atominfo.cpp, readfile.cpp, lmpinput.cpp, graphene.cpp, cell.cpp, grained.cpp etc. While the other codes are utilities for readfile, atom information for positions and types, gereration of lammps input, and cell-linked list, the key code is "grained.cpp". Initially, I designed to run the lammps package as a library and parallelize the functions I built.

Figure F-1 shows the main function. First, the GenVoro() in the gb (Grained) class generates the voronoi seeds from the voro++ library. The number of seeds and graphene sizes (min and max of l_x, l_y, and l_z) are defined in grained.cpp. The pristine graphene is generated with $2l_x$ by $2l_y$ and cut out by the Voronoi cells after randomly rotated. Then, iterative algorithm are applied in the for loop.

The structures are relaxed by running lammps through "relax.in" input file. The input simply relax the given structures with several hundreds steps. The function (gb->rnd_cut()) adds variance for the adding and deleting process.

```
int main(int argc, char *argv[]){
  MPI_Init(&argc, &argv);
  myComm=MPI_COMM_WORLD;

  ReadFile *readf;
  AtomInfo *atominfo;
  LMPInput *lmpinp;
  Grained *gb;

  gb = new Grained;
  gb->GenVoro();

  using namespace LAMMPS_NS;
  LAMMPS *lmp = new LAMMPS(argc,argv,MPI_COMM_WORLD);
  for(int i=0;i<10000;i++){
   if(i!=0){
     gb->rnd_cut();
     gb->Readxyz1();//gen from voro
     gb->GenLMP();
   }

   delete lmp;
   lmp = new LAMMPS(argc,argv,MPI_COMM_WORLD);
   lmp->input->file("relax.in");

    gb->rnd_cut();
    gb->Readxyz2();//add voro
  }

  gb->Readxyz1();//gen from voro

  MPI_Finalize();
  return 0;

}
```

Figure F-1: main.cpp for the polycrystalline graphene generation

The "relax.in" generates "grained.xyz" after energy minimization through MD simulations. The function (gb->Readxyz2()) reads the geometries (grained.xyz), and adds carbon atoms based on the bond numbers described in the method.

Then, the function (gb->Readxyz1()) deletes the atoms that do not satisfy the conditions such as bond angles, length, and bond numbers. gb->GenLMP() generates the data file from the last step for the structural relaxation through MD.

The iteration number (the example is set to 10000) is set as large enough to refine the geometries without voids.

F.2 Source code for bilayer MoS_2

Here, I include the modified part of the original REBO code for MoS2. To obtain comparable binding energy profile with DFT calculation, I needed to change the cutoffs of the Lennard Jones parameters. Figure F-2 shows the modified code for the cutoff between Mo and S. The LJ parameters in the new version do not follow the

```
//This is original
/*rcLJmax[0][0] = 2.5*sigma[0][0];
rcLJmax[0][1] = 2.5*sigma[0][1];
rcLJmax[1][0] = rcLJmax[0][1];
rcLJmax[1][1] = 2.5*sigma[1][1];
*/

//This part is modfied by GS Jung for bilayer MoS2
rcLJmax[0][0] = 2.5*sigma[0][0];
rcLJmax[0][1] = 1.5*sigma[0][1];
rcLJmax[1][0] = rcLJmax[0][1];
rcLJmax[1][1] = 2.5*sigma[1][1];
```

Figure F-2: Modification of cutoff M-S for bilayer interaction of MoS_2

conventional rules. The values for the interaction between Mo and S are explicitly provided in the parameter file in Figure F-3. Then, the applying the conventional rules should be turned off as in Figure F-3(left). The final step is to modify the parameter file as the order shown in Figure F-3(right).

```
// LJ parameters
// Here modified by GS JUNG for explicit sigma and epsilon for MS
fgets(s,MAXLINE,fp);
sscanf(s,"%lg",&epsilon_MM);
fgets(s,MAXLINE,fp);
sscanf(s,"%lg",&epsilon_SS);
fgets(s,MAXLINE,fp);
sscanf(s,"%lg",&epsilon_MS);
fgets(s,MAXLINE,fp);
sscanf(s,"%lg",&sigma_MM);
fgets(s,MAXLINE,fp);
sscanf(s,"%lg",&sigma_SS);
fgets(s,MAXLINE,fp);
sscanf(s,"%lg",&sigma_MS);
```

```
// LJ modified by GS Jung

sigma[0][0] = sigma_MM;
//sigma[0][1] = (sigma_MM + sigma_SS)/2; //original version
sigma[0][1] = sigma_MS;
sigma[1][0] = sigma[0][1];
sigma[1][1] = sigma_SS;

epsilon[0][0] = epsilon_MM;
//epsilon[0][1] = sqrt(epsilon_MM*epsilon_SS); //original version
epsilon[0][1] = epsilon_MS;
epsilon[1][0] = epsilon[0][1];
epsilon[1][1] = epsilon_SS;
```

Figure F-3: (left) Modification of the 'read parameter' function, read_file, for explicit parameters for σ_{MS} and ϵ_{MS}. (right) Ignoring the conventional rules for the LJ parameters

F.3 Source code for MoS_2-WSe_2 heterostructures

Here, I introduce how to modify the original source code that handles only two atoms for MoS_2WSe_2 heterostructures. First, the code should recognize four different atoms and have memory for them in Figure F-4. When the REBO calculates the bond order parameters, the coordinate term is independent from the atom type. Therefore, what matters are mainly correct assignments for the interatomic parameters without modifying the bond order function. The major modifications of the source code come

```
double rcmin[4][4],rcmax[4][4],rcmaxsq[4][4],rcmaxp[4][4];
double Q[4][4],alpha[4][4],A[4][4],BIJc[4][4],Beta[4][4];
double b0[4],b1[4],b2[4],b3[4],b4[4],b5[4],b6[4];
double bg0[4],bg1[4],bg2[4],bg3[4],bg4[4],bg5[4],bg6[4];
double a0[4],a1[4],a2[4],a3[4];
double rcLJmin[4][4],rcLJmax[4][4],rcLJmaxsq[4][4];
double epsilon[4][4],sigma[4][4];
```

```
for (int i = 3; i < narg; i++) {
  if (strcmp(arg[i],"NULL") == 0) {
    map[i-2] = -1;
    continue;
  } else if (strcmp(arg[i],"M") == 0) {
    map[i-2] = 0;
  } else if (strcmp(arg[i],"S") == 0) {
    map[i-2] = 1;
  } else if (strcmp(arg[i],"W") == 0) {
    map[i-2] = 2;
  } else if (strcmp(arg[i],"Se") == 0) {
    map[i-2] = 3;
  }else error->all(FLERR,"Incorrect args for pair coefficients; this?");
}
```

Figure F-4: (top) Defining four atom variables in .h file. (bottom) adding W and Se atom types in .cpp

from the read_file. New variables are defined for REBO for inputs in Figure F-5 (left). Then, new par for LJ are defined in Figure F-5 (right).

```
// REBO Parameters (M-W REBO)
double rcmin_MW,rcmax_MW;
double rcmaxp_MW;
double Q_MW,alpha_MW,A_MW;
double BIJc_MW1;
double Beta_MW1;

// REBO Parameters (M-Se REBO)
double rcmin_MSe,rcmin_SeSe,rcmax_MSe,rcmax_SeSe;
double rcmaxp_MSe,rcmaxp_SeSe;
double Q_MSe,Q_SeSe,alpha_MSe,alpha_SeSe,A_MSe,A_SeSe;
double BIJc_MSe1,BIJc_SeSe1;
double Beta_MSe1,Beta_SeSe1;

// REBO Parameters (W-Se REBO)
double rcmin_WW,rcmin_WSe,rcmax_WW,rcmax_WSe;
double rcmaxp_WW,rcmaxp_WSe;
double Q_WW,Q_WSe,alpha_WW,alpha_WSe,A_WW,A_WSe;
double BIJc_WW1,BIJc_WSe1;
double Beta_WW1,Beta_WSe1;

// REBO Parameters (W-S REBO)
double rcmin_WS,rcmax_WS;
double rcmaxp_WS;
double Q_WS,alpha_WS,A_WS;
double BIJc_WS1;
double Beta_WS1;

// REBO Parameters (S-Se REBO)
double rcmin_SSe,rcmax_SSe;
double rcmaxp_SSe;
double Q_SSe,alpha_SSe,A_SSe;
double BIJc_SSe1;
double Beta_SSe1;

//REBO Common Parameters (Mo-S-W-Se REBO)
double M_bg0,M_bg1,M_bg2,M_bg3,M_bg4,M_bg5,M_bg6;
double S_bg0,S_bg1,S_bg2,S_bg3,S_bg4,S_bg5,S_bg6;
double M_b0,M_b1,M_b2,M_b3,M_b4,M_b5,M_b6;
double S_b0,S_b1,S_b2,S_b3,S_b4,S_b5,S_b6;
double M_a0,M_a1,M_a2,M_a3;
double S_a0,S_a1,S_a2,S_a3;
```

```
// LJ Parameters (W-Se REBO)
double rcLJmin_WW,rcLJmin_WSe,rcLJmax_WW,rcLJmax_WSe;
double epsilon_WW,epsilon_WSe;
double sigma_WW,sigma_WSe;

// LJ Parameters (W-S REBO)
double rcLJmin_WS,rcLJmax_WS;
double epsilon_WS;
double sigma_WS;
```

Figure F-5: (left) New variables in read_file function for REBO. (right) New variables in read_file function for LJ.

Then, reading parameters are simply extended from the original code, examples are in Figure F-6. The order of variables should be matched the order in the parameters file. Then, the parameters are assigned in the memories defined in Figure F-4. After the code assigns the parameters in the main load (MPI=0) from the 'read_file' function, the parameters should be transferred to other MPI node for parallelization in Figure F-7.

F.4 Generation of TPMS

Here, I introduce the codes for TPMS graphene generation. The basic process is the same as polycrystalline graphene with the periodic boundary conditions in the x, y, and z directions. The key part is how to constraint the geometries. I modify the "pair_lj_cut.cpp" for the constraint and utilize "hybrid" potential in LAMMPS to combine the REBO potential. Figure F-8 shows how to add the external potential for the G type. Once the equations for the surface are given, it is straightforward to obtain the derivative of the external potentials.

```
//self
fgets(s,MAXLINE,fp);
sscanf(s,"%lg",&rcmin_MM);
fgets(s,MAXLINE,fp);
sscanf(s,"%lg",&rcmax_MM);
fgets(s,MAXLINE,fp);
sscanf(s,"%lg",&rcmin_SS);
fgets(s,MAXLINE,fp);
sscanf(s,"%lg",&rcmax_SS);
fgets(s,MAXLINE,fp);
sscanf(s,"%lg",&rcmin_WW);
fgets(s,MAXLINE,fp);
sscanf(s,"%lg",&rcmax_WW);
fgets(s,MAXLINE,fp);
sscanf(s,"%lg",&rcmin_SeSe);
fgets(s,MAXLINE,fp);
sscanf(s,"%lg",&rcmax_SeSe);
//interaction
fgets(s,MAXLINE,fp);
sscanf(s,"%lg",&rcmin_MW);
fgets(s,MAXLINE,fp);
sscanf(s,"%lg",&rcmax_MW);
fgets(s,MAXLINE,fp);
sscanf(s,"%lg",&rcmin_MS);
fgets(s,MAXLINE,fp);
sscanf(s,"%lg",&rcmax_MS);
fgets(s,MAXLINE,fp);
sscanf(s,"%lg",&rcmin_MSe);
fgets(s,MAXLINE,fp);
sscanf(s,"%lg",&rcmax_MSe);
fgets(s,MAXLINE,fp);
sscanf(s,"%lg",&rcmin_WS);
fgets(s,MAXLINE,fp);
sscanf(s,"%lg",&rcmax_WS);
fgets(s,MAXLINE,fp);
sscanf(s,"%lg",&rcmin_WSe);
fgets(s,MAXLINE,fp);
sscanf(s,"%lg",&rcmax_WSe);
fgets(s,MAXLINE,fp);
sscanf(s,"%lg",&rcmin_SSe);
fgets(s,MAXLINE,fp);
sscanf(s,"%lg",&rcmax_SSe);
```

Figure F-6: Extension of the original code to get parameters for four atoms interactions.

```
rcmin[0][0] = rcmin_MM;    //MM
rcmin[0][1] = rcmin_MS;    //MS
rcmin[0][2] = rcmin_MW;    //MW
rcmin[0][3] = rcmin_MSe;   //MSe

rcmin[1][0] = rcmin_MS;    //SM
rcmin[1][1] = rcmin_SS;    //SS
rcmin[1][2] = rcmin_WS;    //SW
rcmin[1][3] = rcmin_SSe;   //SSe

rcmin[2][0] = rcmin_MW;    //WM
rcmin[2][1] = rcmin_WS;    //WS
rcmin[2][2] = rcmin_WW;    //WW
rcmin[2][3] = rcmin_WSe;   //WSe

rcmin[3][0] = rcmin_MSe;    //SeM
rcmin[3][1] = rcmin_SSe;    //SeS
rcmin[3][2] = rcmin_WSe;    //SeW
rcmin[3][3] = rcmin_SeSe;   //SeSe

rcmax[0][0] = rcmax_MM;    //MM
rcmax[0][1] = rcmax_MS;    //MS
rcmax[0][2] = rcmax_MW;    //MW
rcmax[0][3] = rcmax_MSe;   //MSe

rcmax[1][0] = rcmax_MS;    //SM
rcmax[1][1] = rcmax_SS;    //SS
rcmax[1][2] = rcmax_WS;    //SW
rcmax[1][3] = rcmax_SSe;   //SSe

rcmax[2][0] = rcmax_MW;    //WM
rcmax[2][1] = rcmax_WS;    //WS
rcmax[2][2] = rcmax_WW;    //WW
rcmax[2][3] = rcmax_WSe;   //WSe

rcmax[3][0] = rcmax_MSe;    //SeM
rcmax[3][1] = rcmax_SSe;    //SeS
rcmax[3][2] = rcmax_WSe;    //SeW
rcmax[3][3] = rcmax_SeSe;   //SeSe
```

```
MPI_Bcast(&rcmin[0][0],16,MPI_DOUBLE,0,world);
MPI_Bcast(&rcmax[0][0],16,MPI_DOUBLE,0,world);
MPI_Bcast(&rcmaxsq[0][0],16,MPI_DOUBLE,0,world);
MPI_Bcast(&rcmaxp[0][0],16,MPI_DOUBLE,0,world);

MPI_Bcast(&Q[0][0],16,MPI_DOUBLE,0,world);
MPI_Bcast(&alpha[0][0],16,MPI_DOUBLE,0,world);
MPI_Bcast(&A[0][0],16,MPI_DOUBLE,0,world);
MPI_Bcast(&BIJc[0][0],16,MPI_DOUBLE,0,world);
MPI_Bcast(&Beta[0][0],16,MPI_DOUBLE,0,world);

MPI_Bcast(&b0[0],4,MPI_DOUBLE,0,world);
MPI_Bcast(&b1[0],4,MPI_DOUBLE,0,world);
MPI_Bcast(&b2[0],4,MPI_DOUBLE,0,world);
MPI_Bcast(&b3[0],4,MPI_DOUBLE,0,world);
MPI_Bcast(&b4[0],4,MPI_DOUBLE,0,world);
MPI_Bcast(&b5[0],4,MPI_DOUBLE,0,world);
MPI_Bcast(&b6[0],4,MPI_DOUBLE,0,world);

MPI_Bcast(&a0[0],4,MPI_DOUBLE,0,world);
MPI_Bcast(&a1[0],4,MPI_DOUBLE,0,world);
MPI_Bcast(&a2[0],4,MPI_DOUBLE,0,world);
MPI_Bcast(&a3[0],4,MPI_DOUBLE,0,world);

MPI_Bcast(&bg0[0],4,MPI_DOUBLE,0,world);
MPI_Bcast(&bg1[0],4,MPI_DOUBLE,0,world);
MPI_Bcast(&bg2[0],4,MPI_DOUBLE,0,world);
MPI_Bcast(&bg3[0],4,MPI_DOUBLE,0,world);
MPI_Bcast(&bg4[0],4,MPI_DOUBLE,0,world);
MPI_Bcast(&bg5[0],4,MPI_DOUBLE,0,world);
MPI_Bcast(&bg6[0],4,MPI_DOUBLE,0,world);

MPI_Bcast(&rcLJmin[0][0],16,MPI_DOUBLE,0,world);
MPI_Bcast(&rcLJmax[0][0],16,MPI_DOUBLE,0,world);
MPI_Bcast(&rcLJmaxsq[0][0],16,MPI_DOUBLE,0,world);
MPI_Bcast(&epsilon[0][0],16,MPI_DOUBLE,0,world);
MPI_Bcast(&sigma[0][0],16,MPI_DOUBLE,0,world);
```

Figure F-7: (left) Examples of assignments from the input values. (right) Based on the memory sizes, the parameters are transferred to other MPI nodes by using MPI broadcast command.

```
//make outsource forces.
double Lxc=lx/3.141592*0.5;
double Lyc=ly/3.141592*0.5;
double Lzc=lz/3.141592*0.5;
double cosx = cos((xtmp-xlo)/Lxc);
double cosy = cos((ytmp-ylo)/Lyc);
double cosz = cos((ztmp-zlo)/Lzc);
double sinx = sin((xtmp-xlo)/Lxc);
double siny = sin((ytmp-ylo)/Lyc);
double sinz = sin((ztmp-zlo)/Lzc);

double vv0 = 20*(sinx*cosy+siny*cosz+sinz*cosx);
double addx =-vv0*(cosx*cosy-sinz*sinx);
double addy =-vv0*(-sinx*siny+cosy*cosz);
double addz =-vv0*(-siny*sinz+cosz*cosx);


f[i][0]+=addx;
f[i][1]+=addy;
f[i][2]+=addz;
//end of outsource force
```

Figure F-8: The code for the external potential for Gyorid (G type).

F.5 Crystal Growth TMD

The TMD materials have three-atom thickness. It is not possible to utilize the polycrystalline algorithm because the algorithm is based on the plane structure and bond number. Also, there are two types of atom. The polycrystalline code is modified to recognize the type of atoms from the xyz file. The projected bond length cuts are changed to 2.04 Å. The type is simply selected by the "if" statement. The two python codes, htom.py and mtoh.py, are utilized for converting 3D structures from 2D and vice versa. The key of the code is to build a function to distinguish top and bottom sulfur based on curved or flat surfaces. Only the distance from metal to sulfur cannot distinguish which sulfur is belong to the top or bottom. Therefore, the additional bond list for only sulfurs atoms is generated to distinguish which one is top and bottom. In this list, sulfur atoms can have one neighbor sulfur based on the distance less than 3.6 Å. Then, it becomes possible to distinguish which one is top or bottom based on the give surface equation. The projected positions are simply obtained from the averaging the positions of top and bottom sulfurs.

For recovering 3D structures from 2D geometries also requires surface equations and its normal vectors. Since the distance from the surface is known, the locations of top and bottom sulfurs are simply calculated from the normal vector.

F.6 Parameters of Bilayer MoS_2

F.7 Parameters of Mo-W-S-Se

The parameters for the heterostructures (MoS_2-WSe_2) are listed in Figure F-10. The vdW parameters are the same with original ones.

F.8 Visualization

It is essential to appropriately visualize data from MD for understanding mechanisms. VMD is mainly utilized for atomic structures and evolutions of crack propagation

```
4.50                rcmin_MM
2.9                 rcmin_MS
1.10                rcmin_SS
5.00                rcmax_MM
2.9                 rcmax_MS
2.9                 rcmax_SS
3.419129390005910   Q_MM
1.505537839153790   Q_MS
0.254959104053671   Q_SS
1.07500712999340    alpha_MM
1.19267902218820    alpha_MS
1.10775022439715    alpha_SS
119.6631465133      A_MM
384.7161867505      A_MS
691.5107873415      A_SS
472.1120839032      BIJc_MM1
898.7491227776      BIJc_MS1
843.6210395223      BIJc_SS1
1.16100322369589    Beta_MM1
1.26973752204290    Beta_MS1
1.12673623610320    Beta_SS1
0.1326842550663270  M_b0
-0.007642788338017  M_b1
0.0341395775059370  M_b2
0.2523050971380870  M_b3
0.1227287372225670  M_b4
-0.361387798398897  M_b5
-0.282577591351457  M_b6
0.120194301035280   M_bg0
0.045238287358190   M_bg1
0.067922807244030   M_bg2
-0.03672511378682   M_bg3
0.107516477513860   M_bg4
0.004964711984940   M_bg5
-0.12997598358652   M_bg6

0.006848761596750   S_b0
-0.02389964401024   S_b1
0.137457353311170   S_b2
0.033016467497740   S_b3
-0.31064291544850   S_b4
-0.08550273135791   S_b5
0.149252790306880   S_b6
-0.2850852          S_bg0
1.67102480          S_bg1
-3.5678516          S_bg2
3.45054990          S_bg3
-1.2186289          S_bg4
0.0                 S_bg5
0.0                 S_bg6
0.138040769883614   M_a0
0.803625443023934   M_a1
0.292412960851064   M_a2
0.640588078946224   M_a3
0.062978539843324   S_a0
2.478617619878250   S_a1
0.036666243238154   S_a2
2.386431372486710   S_a3
0.00093752          epsilon_MM
0.02217600          epsilon_SS
0.00455965          epsilon_MS
3.60000000          sigma_MM
3.25000000          sigma_SS
3.16500000          sigma_MS
```

Figure F-9: Parameters of Bilayer MoS_2. The vdW parameters are explicitly defined in the end.

[219]. It has a function to make movie from .xyz trajectory files from LAMMPS [220]. To visualize the atomic stress, Atomeye [221] and OVITO [222] are utilized. LAMMPS provides a dump commend with a cfg option to print out atomic position and data such as stress and potential though .cfg file format, which is readable for the visualization tools without any modification.

4.50	rcmin_MM		
5.00	rcmax_MM		
2.00	rcmin_SS		
3.00	rcmax_SS		
4.50	rcmin_WW	934.409018993	BIJc_MSe1
5.00	rcmax_WW	1067.80305510052	BIJc_SS1
2.00	rcmin_SeSe	934.409018993	BIJc_WS1
3.00	rcmax_SeSe	1067.80305510052	BIJc_SSe1
4.50	rcmin_MW	478.479101848	BIJc_WW1
5.00	rcmax_MW	910.869871192	BIJc_WSe1
2.85	rcmin_MS	1015.3259487	BIJc_SeSe1
2.85	rcmax_MS	1.16100322369589	Beta_MM1
3.00	rcmin_MSe	1.26973752204290	Beta_MS1
3.00	rcmax_MSe	1.16100322369589	Beta_MW1
2.90	rcmin_WS	1.21411	Beta_MSe1
2.90	rcmax_WS	1.12673623610320	Beta_SS1
3.05	rcmin_WSe	1.26973752204290	Beta_WS1
3.05	rcmax_WSe	1.12673623610320	Beta_SSe1
2.00	rcmin_SSe	1.07603	Beta_WW1
3.00	rcmax_SSe	1.21411	Beta_WSe1
3.419129390005910	Q_MM	1.12673623610320	Beta_SeSe1
1.505537839153790	Q_MS	0.1326842550663270	M_b0
3.419129390005910	Q_MW	-0.007642788338017	M_b1
1.57018	Q_MSe	0.0341395775059370	M_b2
0.254959104053671	Q_SS	0.2523050971380870	M_b3
1.505537839153790	Q_WS	0.1227287372225670	M_b4
0.254959104053671	Q_SSe	-0.361387798398897	M_b5
3.68313	Q_WW	-0.282577591351457	M_b6
1.57018	Q_WSe	0.120194301035280	M_bg0
0.254959104053671	Q_SeSe	0.045238287358190	M_bg1
1.07500712999340	alpha_MM	0.067922807244030	M_bg2
1.19267902218820	alpha_MS	-0.03672511378682	M_bg3
1.07500712999340	alpha_MW	0.107516477513860	M_bg4
1.13962	alpha_MSe	0.004964711984940	M_bg5
1.10775022439715	alpha_SS	-0.12997598358652	M_bg6
1.19267902218820	alpha_WS	0.006848761596750	S_b0
1.10775022439715	alpha_SSe	-0.02389964401024	S_b1
0.995132	alpha_WW	0.137457353311170	S_b2
1.13962	alpha_WSe	0.033016467497740	S_b3
1.10775022439715	alpha_SeSe	-0.31064291544850	S_b4
127.545150175833	A_MM	-0.08550273135791	S_b5
410.056773901736	A_MS	0.149252790306880	S_b6
127.545150175833	A_MW	-0.2850852	S_bg0
399.980668177	A_MSe	1.67102480	S_bg1
875.271356172441	A_SS	-3.5678516	S_bg2
399.980668177	A_WS	3.45054990	S_bg3
875.271356172441	A_SSe	-1.2186289	S_bg4
121.276952699	A_WW	0.0	S_bg5
389.904562452	A_WSe	0.0	S_bg6
832.256206642	A_SeSe	0.138040769883614	M_a0
503.209287034595	BIJc_MM1	0.803625443023934	M_a1
957.948166792925	BIJc_MS1	0.292412960851064	M_a2
503.209287034595	BIJc_MW1	0.640588078946224	M_a3
		0.062978539843324	S_a0
		2.478617619878250	S_a1
		0.036666243238154	S_a2
		2.386431372486710	S_a3

Figure F-10: Parameters of MoS_2-WSe_2 heterostructures. The vdW part is not included in but the same values of the original ones are utilized.

Bibliography

[1] J. Yeo, G. S. Jung, F. J. Martín-Martínez, S. Ling, G. X. Gu, Z. Qin, and M. J. Buehler, "Materials-by-design: computation, synthesis, and characterization from atoms to structures," *Physica Scripta*, vol. 93, no. 5, p. 053003, 2018.

[2] A. R. Brodtkorb, C. Dyken, T. R. Hagen, J. M. Hjelmervik, and O. O. Storaasli, "State-of-the-art in heterogeneous computing," *Scientific Programming*, vol. 18, no. 1, pp. 1–33, 2010.

[3] M. S. Dresselhaus and G. Dresselhaus, "Intercalation compounds of graphite," *Advances in Physics*, vol. 51, no. 1, pp. 1–186, 2002.

[4] O. Shenderova, V. Zhirnov, and D. Brenner, "Carbon nanostructures," *Critical Reviews in Solid State and Material Sciences*, vol. 27, no. 3-4, pp. 227–356, 2002.

[5] K. S. Novoselov, A. K. Geim, S. V. Morozov, D. Jiang, Y. Zhang, S. V. Dubonos, I. V. Grigorieva, and A. A. Firsov, "Electric field effect in atomically thin carbon films," *science*, vol. 306, no. 5696, pp. 666–669, 2004.

[6] A. A. Balandin, S. Ghosh, W. Bao, I. Calizo, D. Teweldebrhan, F. Miao, and C. N. Lau, "Superior thermal conductivity of single-layer graphene," *Nano Letters*, vol. 8, no. 3, pp. 902–907, 2008.

[7] C. Lee, X. Wei, J. W. Kysar, and J. Hone, "Measurement of the elastic properties and intrinsic strength of monolayer graphene," *Science*, vol. 321, no. 5887, pp. 385–388, 2008.

[8] P. Giannozzi, S. Baroni, N. Bonini, M. Calandra, R. Car, C. Cavazzoni, D. Ceresoli, G. L. Chiarotti, M. Cococcioni, I. Dabo, *et al.*, "Quantum espresso: a modular and open-source software project for quantum simulations of materials," *Journal of Physics: Condensed Matter*, vol. 21, no. 39, p. 395502, 2009.

[9] J. P. Perdew, K. Burke, and M. Ernzerhof, "Generalized gradient approximation made simple," *Physical Review Letters*, vol. 77, no. 18, p. 3865, 1996.

[10] N. Troullier and J. L. Martins, "Efficient pseudopotentials for plane-wave calculations," *Physical Review B*, vol. 43, no. 3, p. 1993, 1991.

[11] A. Geim, "Ak geim and ks novoselov, nat. mater. 6, 183 (2007).," *Nature Materials*, vol. 6, p. 183, 2007.

[12] X. Li, X. Wang, L. Zhang, S. Lee, and H. Dai, "Chemically derived, ultrasmooth graphene nanoribbon semiconductors," *Science*, vol. 319, no. 5867, pp. 1229–1232, 2008.

[13] Z. H. Ni, T. Yu, Y. H. Lu, Y. Y. Wang, Y. P. Feng, and Z. X. Shen, "Uniaxial strain on graphene: Raman spectroscopy study and band-gap opening," *ACS Nano*, vol. 2, no. 11, pp. 2301–2305, 2008.

[14] B. Radisavljevic, A. Radenovic, J. Brivio, i. V. Giacometti, and A. Kis, "Single-layer mos 2 transistors," *Nature Nanotechnology*, vol. 6, no. 3, p. 147, 2011.

[15] C. R. Dean, A. F. Young, I. Meric, C. Lee, L. Wang, S. Sorgenfrei, K. Watanabe, T. Taniguchi, P. Kim, K. L. Shepard, *et al.*, "Boron nitride substrates for high-quality graphene electronics," *Nature Nanotechnology*, vol. 5, no. 10, p. 722, 2010.

[16] A. K. Geim and I. V. Grigorieva, "Van der waals heterostructures," *Nature*, vol. 499, no. 7459, p. 419, 2013.

[17] C.-H. Lee, G.-H. Lee, A. M. Van Der Zande, W. Chen, Y. Li, M. Han, X. Cui, G. Arefe, C. Nuckolls, T. F. Heinz, *et al.*, "Atomically thin p–n junctions with van der waals heterointerfaces," *Nature Nanotechnology*, vol. 9, no. 9, p. 676, 2014.

[18] K. Novoselov, A. Mishchenko, A. Carvalho, and A. C. Neto, "2d materials and van der waals heterostructures," *Science*, vol. 353, no. 6298, p. aac9439, 2016.

[19] K. Kang, K.-H. Lee, Y. Han, H. Gao, S. Xie, D. A. Muller, and J. Park, "Layer-by-layer assembly of two-dimensional materials into wafer-scale heterostructures," *Nature*, vol. 550, no. 7675, p. 229, 2017.

[20] M. P. Levendorf, C.-J. Kim, L. Brown, P. Y. Huang, R. W. Havener, D. A. Muller, and J. Park, "Graphene and boron nitride lateral heterostructures for atomically thin circuitry," *Nature*, vol. 488, no. 7413, p. 627, 2012.

[21] Y. Gong, J. Lin, X. Wang, G. Shi, S. Lei, Z. Lin, X. Zou, G. Ye, R. Vajtai, B. I. Yakobson, *et al.*, "Vertical and in-plane heterostructures from ws 2/mos 2 monolayers," *Nature Materials*, vol. 13, no. 12, p. 1135, 2014.

[22] X. Duan, C. Wang, J. C. Shaw, R. Cheng, Y. Chen, H. Li, X. Wu, Y. Tang, Q. Zhang, A. Pan, *et al.*, "Lateral epitaxial growth of two-dimensional layered semiconductor heterojunctions," *Nature Nanotechnology*, vol. 9, no. 12, p. 1024, 2014.

[23] C. Huang, S. Wu, A. M. Sanchez, J. J. Peters, R. Beanland, J. S. Ross, P. Rivera, W. Yao, D. H. Cobden, and X. Xu, "Lateral heterojunctions within monolayer mose 2–wse 2 semiconductors," *Nature Materials*, vol. 13, no. 12, p. 1096, 2014.

[24] M.-Y. Li, Y. Shi, C.-C. Cheng, L.-S. Lu, Y.-C. Lin, H.-L. Tang, M.-L. Tsai, C.-W. Chu, K.-H. Wei, J.-H. He, *et al.*, "Epitaxial growth of a monolayer wse2-mos2 lateral pn junction with an atomically sharp interface," *Science*, vol. 349, no. 6247, pp. 524–528, 2015.

[25] H. N. Tien, N. T. M. Hien, E.-S. Oh, J. Chung, E. J. Kim, W. M. Choi, B.-S. Kong, S. H. Hur, *et al.*, "Synthesis of a highly conductive and large surface area graphene oxide hydrogel and its use in a supercapacitor," *Journal of Materials Chemistry A*, vol. 1, no. 2, pp. 208–211, 2013.

[26] P. Kim, "Graphene: Across the border," *Nature Materials*, vol. 9, no. 10, p. 792, 2010.

[27] S. Bae, H. Kim, Y. Lee, X. Xu, J.-S. Park, Y. Zheng, J. Balakrishnan, T. Lei, H. R. Kim, Y. I. Song, *et al.*, "Roll-to-roll production of 30-inch graphene films for transparent electrodes," *Nature Nanotechnology*, vol. 5, no. 8, p. 574, 2010.

[28] T. Wu, X. Zhang, Q. Yuan, J. Xue, G. Lu, Z. Liu, H. Wang, H. Wang, F. Ding, Q. Yu, *et al.*, "Fast growth of inch-sized single-crystalline graphene from a controlled single nucleus on cu–ni alloys," *Nature Materials*, vol. 15, no. 1, p. 43, 2016.

[29] P. A. M. Dirac, "Quantum mechanics of many-electron systems," *Proceedings of the Royal Society of London. Series A, Containing Papers of a Mathematical and Physical Character*, vol. 123, no. 792, pp. 714–733, 1929.

[30] D. Sen, K. S. Novoselov, P. M. Reis, and M. J. Buehler, "Tearing graphene sheets from adhesive substrates produces tapered nanoribbons," *Small*, vol. 6, no. 10, pp. 1108–1116, 2010.

[31] G. Jung, Z. Qin, and M. J. Buehler, "Molecular mechanics of polycrystalline graphene with enhanced fracture toughness," *Extreme Mechanics Letters*, vol. 2, pp. 52–59, 2015.

[32] G. S. Jung and M. J. Buehler, "Multiscale modeling of muscular-skeletal systems," *Annual Review of Biomedical Engineering*, vol. 19, pp. 435–457, 2017.

[33] Z. Qin, G. S. Jung, M. J. Kang, and M. J. Buehler, "The mechanics and design of a lightweight three-dimensional graphene assembly," *Science Advances*, vol. 3, no. 1, p. e1601536, 2017.

[34] G. S. Jung, J. Yeo, Z. Tian, Z. Qin, and M. J. Buehler, "Unusually low and density-insensitive thermal conductivity of three-dimensional gyroid graphene," *Nanoscale*, vol. 9, no. 36, pp. 13477–13484, 2017.

[35] S. Wang, Z. Qin, G. S. Jung, F. J. Martin-Martinez, K. Zhang, M. J. Buehler, and J. H. Warner, "Atomically sharp crack tips in monolayer mos2 and their enhanced toughness by vacancy defects," *ACS Nano*, vol. 10, no. 11, pp. 9831–9839, 2016.

[36] Y. Han, M.-Y. Li, G.-S. Jung, M. A. Marsalis, Z. Qin, M. J. Buehler, L.-J. Li, and D. A. Muller, "Sub-nanometre channels embedded in two-dimensional materials," *Nature Materials*, vol. 17, no. 2, p. 129, 2018.

[37] G. S. Jung, S. Wang, Z. Qin, F. J. Martin-Martinez, J. H. Warner, and M. J. Buehler, "Interlocking friction governs the mechanical fracture of bilayer mos2," *ACS Nano*, vol. 12, no. 4, pp. 3600–3608, 2018.

[38] G. S. Jung and M. J. Buehler, "Multiscale mechanics of triply periodic minimal surfaces of three-dimensional graphene foams," *Nano Letters*, vol. 18, no. 8, pp. 4845–4853, 2018.

[39] J. Yeo, G. S. Jung, F. J. Martín-Martínez, J. Beem, Z. Qin, and M. J. Buehler, "Multiscale design of graphyne-based materials for high-performance separation membranes," *Advanced Materials*, p. 1805665, 2019.

[40] Y. Zhou, S. G. Sarwat, G. S. Jung, M. J. Buehler, H. Bhaskaran, and J. H. Warner, "Grain boundaries as electrical conduction channels in polycrystalline monolayer ws2," *ACS Applied Materials & Interfaces*, 2019.

[41] M. J. Buehler and S. Keten, "Colloquium: Failure of molecules, bones, and the earth itself," *Reviews of Modern Physics*, vol. 82, no. 2, p. 1459, 2010.

[42] I. M. Georgescu, S. Ashhab, and F. Nori, "Quantum simulation," *Reviews of Modern Physics*, vol. 86, no. 1, p. 153, 2014.

[43] P. Hohenberg and W. Kohn, "Inhomogeneous electron gas," *Physical Review*, vol. 136, no. 3B, p. B864, 1964.

[44] W. Kohn and L. J. Sham, "Self-consistent equations including exchange and correlation effects," *Physical Review*, vol. 140, no. 4A, p. A1133, 1965.

[45] A. Szabo and N. S. Ostlund, *Modern quantum chemistry: introduction to advanced electronic structure theory*. Courier Corporation, 2012.

[46] B. J. Alder and T. E. Wainwright, "Studies in molecular dynamics. i. general method," *The Journal of Chemical Physics*, vol. 31, no. 2, pp. 459–466, 1959.

[47] A. Rahman, "Correlations in the motion of atoms in liquid argon," *Physical Review*, vol. 136, no. 2A, p. A405, 1964.

[48] A. D. MacKerell Jr, D. Bashford, M. Bellott, R. L. Dunbrack Jr, J. D. Evanseck, M. J. Field, S. Fischer, J. Gao, H. Guo, S. Ha, *et al.*, "All-atom empirical potential for molecular modeling and dynamics studies of proteins," *The Journal of Physical Chemistry B*, vol. 102, no. 18, pp. 3586–3616, 1998.

[49] W. D. Cornell, P. Cieplak, C. I. Bayly, I. R. Gould, K. M. Merz, D. M. Ferguson, D. C. Spellmeyer, T. Fox, J. W. Caldwell, and P. A. Kollman, "A second generation force field for the simulation of proteins, nucleic acids, and organic molecules," *Journal of the American Chemical Society*, vol. 117, no. 19, pp. 5179–5197, 1995.

[50] M. Christen, P. H. Hünenberger, D. Bakowies, R. Baron, R. Bürgi, D. P. Geerke, T. N. Heinz, M. A. Kastenholz, V. Kräutler, C. Oostenbrink, *et al.*, "The gromos software for biomolecular simulation: Gromos05," *Journal of Computational Chemistry*, vol. 26, no. 16, pp. 1719–1751, 2005.

[51] L. Verlet, "Computer" experiments" on classical fluids. i. thermodynamical properties of lennard-jones molecules," *Physical Review*, vol. 159, no. 1, p. 98, 1967.

[52] S. Nosé, "A unified formulation of the constant temperature molecular dynamics methods," *The Journal of Chemical Physics*, vol. 81, no. 1, pp. 511–519, 1984.

[53] W. G. Hoover, "Canonical dynamics: Equilibrium phase-space distributions," *Physical Review A*, vol. 31, no. 3, p. 1695, 1985.

[54] G. J. Martyna, M. L. Klein, and M. Tuckerman, "Nosé–hoover chains: The canonical ensemble via continuous dynamics," *The Journal of Chemical Physics*, vol. 97, no. 4, pp. 2635–2643, 1992.

[55] H. C. Andersen, "Rattle: A âĂIJvelocityâĂİ version of the shake algorithm for molecular dynamics calculations," *Journal of Computational Physics*, vol. 52, no. 1, pp. 24–34, 1983.

[56] G. Jung, Z. Qin, and M. J. Buehler, "Mechanical properties and failure of biopolymers: atomistic reactions to macroscale response," in *Polymer Mechanochemistry*, pp. 317–343, Springer, 2015.

[57] M. Buehler, "Hierarchical chemo-nanomechanics of proteins: Entropic elasticity, protein unfolding and molecular fracture," *Journal of Mechanics of materials and structures*, vol. 2, no. 6, pp. 1019–1057, 2007.

[58] A. C. Van Duin, S. Dasgupta, F. Lorant, and W. A. Goddard, "Reaxff: a reactive force field for hydrocarbons," *The Journal of Physical Chemistry A*, vol. 105, no. 41, pp. 9396–9409, 2001.

[59] T. P. Senftle, S. Hong, M. M. Islam, S. B. Kylasa, Y. Zheng, Y. K. Shin, C. Junkermeier, R. Engel-Herbert, M. J. Janik, H. M. Aktulga, *et al.*, "The reaxff reactive force-field: development, applications and future directions," *NPJ Computational Materials*, vol. 2, p. 15011, 2016.

[60] M. J. Buehler, A. C. Van Duin, and W. A. Goddard III, "Multiparadigm modeling of dynamical crack propagation in silicon using a reactive force field," *Physical Review Letters*, vol. 96, no. 9, p. 095505, 2006.

[61] J. Tersoff, "Modeling solid-state chemistry: Interatomic potentials for multicomponent systems," *Physical Review B*, vol. 39, no. 8, p. 5566, 1989.

[62] D. W. Brenner, "Empirical potential for hydrocarbons for use in simulating the chemical vapor deposition of diamond films," *Physical Review B*, vol. 42, no. 15, p. 9458, 1990.

[63] S. J. Stuart, A. B. Tutein, and J. A. Harrison, "A reactive potential for hydrocarbons with intermolecular interactions," *The Journal of Chemical Physics*, vol. 112, no. 14, pp. 6472–6486, 2000.

[64] D. W. Brenner, O. A. Shenderova, J. A. Harrison, S. J. Stuart, B. Ni, and S. B. Sinnott, "A second-generation reactive empirical bond order (rebo) potential energy expression for hydrocarbons," *Journal of Physics: Condensed Matter*, vol. 14, no. 4, p. 783, 2002.

[65] S. L. Mayo, B. D. Olafson, and W. A. Goddard, "Dreiding: a generic force field for molecular simulations," *Journal of Physical chemistry*, vol. 94, no. 26, pp. 8897–8909, 1990.

[66] A. K. Rappé, C. J. Casewit, K. Colwell, W. A. Goddard III, and W. Skiff, "Uff, a full periodic table force field for molecular mechanics and molecular dynamics simulations," *Journal of the American Chemical Society*, vol. 114, no. 25, pp. 10024–10035, 1992.

[67] A. K. Rappe and W. A. Goddard III, "Charge equilibration for molecular dynamics simulations," *The Journal of Physical Chemistry*, vol. 95, no. 8, pp. 3358–3363, 1991.

[68] T.-R. Shan, B. D. Devine, T. W. Kemper, S. B. Sinnott, S. R. Phillpot, *et al.*, "Charge-optimized many-body potential for the hafnium/hafnium oxide system," *Physical Review B*, vol. 81, no. 12, p. 125328, 2010.

[69] B. D. Jensen, K. E. Wise, and G. M. Odegard, "Simulation of the elastic and ultimate tensile properties of diamond, graphene, carbon nanotubes, and amorphous carbon using a revised reaxff parametrization," *The Journal of Physical Chemistry A*, vol. 119, no. 37, pp. 9710–9721, 2015.

[70] P. Rowe, G. Csányi, D. Alfè, and A. Michaelides, "Development of a machine learning potential for graphene," *Physical Review B*, vol. 97, no. 5, p. 054303, 2018.

[71] G. Rajasekaran, R. Kumar, and A. Parashar, "Tersoff potential with improved accuracy for simulating graphene in molecular dynamics environment," *Materials Research Express*, vol. 3, no. 3, p. 035011, 2016.

[72] D. L. Nika and A. A. Balandin, "Thermal transport in graphene, few-layer graphene and graphene nanoribbons," in *Thermal transport in low dimensions*, pp. 339–363, Springer, 2016.

[73] M. H. Khadem and A. P. Wemhoff, "Comparison of green–kubo and nemd heat flux formulations for thermal conductivity prediction using the tersoff potential," *Computational Materials Science*, vol. 69, pp. 428–434, 2013.

[74] J. J. Yeo, Z. S. Liu, and T. Y. Ng, "Enhanced thermal characterization of silica aerogels through molecular dynamics simulation," *Modelling and Simulation in Materials Science and Engineering*, vol. 21, p. 075004, aug 2013.

[75] Y. Wang, Z. Song, and Z. Xu, "Characterizing phonon thermal conduction in polycrystalline graphene," *Journal of Materials Research*, vol. 29, no. 3, pp. 362–372, 2014.

[76] R. Kubo, "The fluctuation-dissipation theorem," *Reports on Progress in Physics*, vol. 29, no. 1, p. 255, 1966.

[77] R. Kubo, "Statistical-mechanical theory of irreversible processes. i. general theory and simple applications to magnetic and conduction problems," *Journal of the Physical Society of Japan*, vol. 12, no. 6, pp. 570–586, 1957.

[78] P. Wu, S. Quek, Z. Sha, Z. Dong, X. Liu, G. Zhang, Q. Pei, and Y. Zhang, "Thermal transport behavior of polycrystalline graphene: A molecular dynamics study," *Journal of Applied Physics*, vol. 116, no. 20, p. 204303, 2014.

[79] S. I. Ranganathan and M. Ostoja-Starzewski, "Universal elastic anisotropy index," *Physical Review Letters*, vol. 101, no. 5, p. 055504, 2008.

[80] J. Den Toonder, J. Van Dommelen, and F. Baaijens, "The relation between single crystal elasticity and the effective elastic behaviour of polycrystalline materials: theory, measurement and computation," *Modelling and Simulation in Materials Science and Engineering*, vol. 7, no. 6, p. 909, 1999.

[81] A. A. Griffith, "Vi. the phenomena of rupture and flow in solids," *Philosophical Transactions of the Royal Society of London. Series A, Containing Papers of a Mathematical or Physical Character*, vol. 221, no. 582-593, pp. 163–198, 1921.

[82] G. R. Irwin, "Analysis of stresses and strains near the end of a crack traversing a plate," *J. appl. Mech.*, 1957.

[83] P. Lukáš, "Stress intensity factor for small notch-emanated cracks," *Engineering Fracture Mechanics*, vol. 26, no. 3, pp. 471–473, 1987.

[84] P. Weißgraeber, J. Felger, D. Geipel, and W. Becker, "Cracks at elliptical holes: stress intensity factor and finite fracture mechanics solution," *European Journal of Mechanics-A/Solids*, vol. 55, pp. 192–198, 2016.

[85] O. Shenderova, D. Brenner, A. Omeltchenko, X. Su, and L. Yang, "Atomistic modeling of the fracture of polycrystalline diamond," *Physical Review B*, vol. 61, no. 6, p. 3877, 2000.

[86] R. Grantab, V. B. Shenoy, and R. S. Ruoff, "Anomalous strength characteristics of tilt grain boundaries in graphene," *Science*, vol. 330, no. 6006, pp. 946–948, 2010.

[87] Y. Wei, J. Wu, H. Yin, X. Shi, R. Yang, and M. Dresselhaus, "The nature of strength enhancement and weakening by pentagon–heptagon defects in graphene," *Nature Materials*, vol. 11, no. 9, p. 759, 2012.

[88] T. Zhang, X. Li, S. Kadkhodaei, and H. Gao, "Flaw insensitive fracture in nanocrystalline graphene," *Nano Letters*, vol. 12, no. 9, pp. 4605–4610, 2012.

[89] T. Zhang, X. Li, and H. Gao, "Designing graphene structures with controlled distributions of topological defects: A case study of toughness enhancement in graphene ruga," *Extreme Mechanics Letters*, vol. 1, pp. 3–8, 2014.

[90] T. Liang, S. R. Phillpot, and S. B. Sinnott, "Parametrization of a reactive many-body potential for mo–s systems," *Physical Review B*, vol. 79, no. 24, p. 245110, 2009.

[91] J. A. Stewart and D. Spearot, "Atomistic simulations of nanoindentation on the basal plane of crystalline molybdenum disulfide (mos2)," *Modelling and Simulation in Materials Science and Engineering*, vol. 21, no. 4, p. 045003, 2013.

[92] S. Xiong and G. Cao, "Molecular dynamics simulations of mechanical properties of monolayer mos2," *Nanotechnology*, vol. 26, no. 18, p. 185705, 2015.

[93] R. C. Cooper, C. Lee, C. A. Marianetti, X. Wei, J. Hone, and J. W. Kysar, "Nonlinear elastic behavior of two-dimensional molybdenum disulfide," *Physical Review B*, vol. 87, no. 3, p. 035423, 2013.

[94] T. Li, "Ideal strength and phonon instability in single-layer mos 2," *Physical Review B*, vol. 85, no. 23, p. 235407, 2012.

[95] S. Goedecker, M. Teter, and J. Hutter, "Separable dual-space gaussian pseudopotentials," *Physical Review B*, vol. 54, no. 3, p. 1703, 1996.

[96] S. Grimme, "Semiempirical gga-type density functional constructed with a long-range dispersion correction," *Journal of Computational Chemistry*, vol. 27, no. 15, pp. 1787–1799, 2006.

[97] J. He, K. Hummer, and C. Franchini, "Stacking effects on the electronic and optical properties of bilayer transition metal dichalcogenides mos 2, mose 2, ws 2, and wse 2," *Physical Review B*, vol. 89, no. 7, p. 075409, 2014.

[98] T. Peng, G. Huai-Hong, Y. Teng, and Z. Zhi-Dong, "Stacking stability of mos2 bilayer: an ab initio study," *Chinese Physics B*, vol. 23, no. 10, p. 106801, 2014.

[99] S. Bertolazzi, J. Brivio, and A. Kis, "Stretching and breaking of ultrathin mos2," *ACS Nano*, vol. 5, no. 12, pp. 9703–9709, 2011.

[100] B. I. Yakobson and F. Ding, "Observational geology of graphene, at the nanoscale," *ACS Nano*, vol. 5, no. 3, pp. 1569–1574, 2011.

[101] J. Kotakoski and J. C. Meyer, "Mechanical properties of polycrystalline graphene based on a realistic atomistic model," *Physical Review B*, vol. 85, no. 19, p. 195447, 2012.

[102] C. Rycroft, "Voro++: A three-dimensional voronoi cell library in c++," tech. rep., Lawrence Berkeley National Lab.(LBNL), Berkeley, CA (United States), 2009.

[103] G. S. Jung, S. Wang, Z. Qin, S. Zhou, M. Danaie, A. I. Kirkland, M. J. Buehler, and J. H. Warner, "Anisotropic fracture dynamics due to local lattice distortions," *ACS Nano*, 2019.

[104] M. J. Buehler and H. Gao, "Dynamical fracture instabilities due to local hyperelasticity at crack tips," *Nature*, vol. 439, no. 7074, p. 307, 2006.

[105] J. Kermode, T. Albaret, D. Sherman, N. Bernstein, P. Gumbsch, M. Payne, G. Csányi, and A. De Vita, "Low-speed fracture instabilities in a brittle crystal," *Nature*, vol. 455, no. 7217, p. 1224, 2008.

[106] A. Livne, E. Bouchbinder, I. Svetlizky, and J. Fineberg, "The near-tip fields of fast cracks," *Science*, vol. 327, no. 5971, pp. 1359–1363, 2010.

[107] Q. H. Wang, K. Kalantar-Zadeh, A. Kis, J. N. Coleman, and M. S. Strano, "Electronics and optoelectronics of two-dimensional transition metal dichalcogenides," *Nature Nanotechnology*, vol. 7, no. 11, p. 699, 2012.

[108] D. Jariwala, V. K. Sangwan, L. J. Lauhon, T. J. Marks, and M. C. Hersam, "Emerging device applications for semiconducting two-dimensional transition metal dichalcogenides," *ACS Nano*, vol. 8, no. 2, pp. 1102–1120, 2014.

[109] A. Splendiani, L. Sun, Y. Zhang, T. Li, J. Kim, C.-Y. Chim, G. Galli, and F. Wang, "Emerging photoluminescence in monolayer mos2," *Nano Letters*, vol. 10, no. 4, pp. 1271–1275, 2010.

[110] C. Lee, Q. Li, W. Kalb, X.-Z. Liu, H. Berger, R. W. Carpick, and J. Hone, "Frictional characteristics of atomically thin sheets," *Science*, vol. 328, no. 5974, pp. 76–80, 2010.

[111] J. H. Warner, M. H. Rümmeli, L. Ge, T. Gemming, B. Montanari, N. M. Harrison, B. Büchner, and G. A. D. Briggs, "Structural transformations in graphene studied with high spatial and temporal resolution," *Nature Nanotechnology*, vol. 4, no. 8, p. 500, 2009.

[112] J. H. Warner, E. R. Margine, M. Mukai, A. W. Robertson, F. Giustino, and A. I. Kirkland, "Dislocation-driven deformations in graphene," *Science*, vol. 337, no. 6091, pp. 209–212, 2012.

[113] A. W. Robertson, C. S. Allen, Y. A. Wu, K. He, J. Olivier, J. Neethling, A. I. Kirkland, and J. H. Warner, "Spatial control of defect creation in graphene at the nanoscale," *Nature Communications*, vol. 3, p. 1144, 2012.

[114] K. He, C. Poole, K. F. Mak, and J. Shan, "Experimental demonstration of continuous electronic structure tuning via strain in atomically thin mos2," *Nano Letters*, vol. 13, no. 6, pp. 2931–2936, 2013.

[115] T. Shen, A. V. Penumatcha, and J. Appenzeller, "Strain engineering for transition metal dichalcogenides based field effect transistors," *ACS Nano*, vol. 10, no. 4, pp. 4712–4718, 2016.

[116] A. Castellanos-Gomez, R. Roldán, E. Cappelluti, M. Buscema, F. Guinea, H. S. van der Zant, and G. A. Steele, "Local strain engineering in atomically thin mos2," *Nano Letters*, vol. 13, no. 11, pp. 5361–5366, 2013.

[117] A. Kushima, X. Qian, P. Zhao, S. Zhang, and J. Li, "Ripplocations in van der waals layers," *Nano Letters*, vol. 15, no. 2, pp. 1302–1308, 2015.

[118] M. J. Buehler, F. F. Abraham, and H. Gao, "Hyperelasticity governs dynamic fracture at a critical length scale," *Nature*, vol. 426, no. 6963, p. 141, 2003.

[119] A. J. Pons and A. Karma, "Helical crack-front instability in mixed-mode fracture," *Nature*, vol. 464, no. 7285, p. 85, 2010.

[120] L. B. Freund, *Dynamic fracture mechanics*. Cambridge university press, 1998.

[121] K. B. Broberg, *Cracks and fracture*. Elsevier, 1999.

[122] L. I. Slepyan, *Models and phenomena in fracture mechanics*. Springer Science & Business Media, 2012.

[123] H. Gao, "A theory of local limiting speed in dynamic fracture," *Journal of the Mechanics and Physics of Solids*, vol. 44, no. 9, pp. 1453–1474, 1996.

[124] H. Gao, "Elastic waves in a hyperelastic solid near its plane-strain equibiaxial cohesive limit," *Philosophical Magazine Letters*, vol. 76, no. 5, pp. 307–314, 1997.

[125] F. F. Abraham, "Dynamics of brittle fracture with variable elasticity," *Physical Review Letters*, vol. 77, no. 5, p. 869, 1996.

[126] M. J. Buehler, H. Tang, A. C. Van Duin, and W. A. Goddard III, "Threshold crack speed controls dynamical fracture of silicon single crystals," *Physical Review Letters*, vol. 99, no. 16, p. 165502, 2007.

[127] R. Pérez and P. Gumbsch, "An ab initio study of the cleavage anisotropy in silicon," *Acta Materialia*, vol. 48, no. 18-19, pp. 4517–4530, 2000.

[128] J. Kermode, L. Ben-Bashat, F. Atrash, J. Cilliers, D. Sherman, and A. De Vita, "Macroscopic scattering of cracks initiated at single impurity atoms," *Nature Communications*, vol. 4, p. 2441, 2013.

[129] E. Bitzek, J. R. Kermode, and P. Gumbsch, "Atomistic aspects of fracture," *International Journal of Fracture*, vol. 191, no. 1-2, pp. 13–30, 2015.

[130] P. Gumbsch and R. M. Cannon, "Atomistic aspects of brittle fracture," *MRS Bulletin*, vol. 25, no. 5, pp. 15–20, 2000.

[131] S. Wang, A. Robertson, and J. H. Warner, "Atomic structure of defects and dopants in 2d layered transition metal dichalcogenides," *Chemical Society Reviews*, vol. 47, no. 17, pp. 6764–6794, 2018.

[132] A. W. Robertson, G.-D. Lee, K. He, Y. Fan, C. S. Allen, S. Lee, H. Kim, E. Yoon, H. Zheng, A. I. Kirkland, *et al.*, "Partial dislocations in graphene and their atomic level migration dynamics," *Nano Letters*, vol. 15, no. 9, pp. 5950–5955, 2015.

[133] S. Wang, H. Sawada, X. Han, S. Zhou, S. Li, Z. X. Guo, A. I. Kirkland, and J. H. Warner, "Preferential pt nanocluster seeding at grain boundary dislocations in polycrystalline monolayer mos2," *ACS Nano*, vol. 12, no. 6, pp. 5626–5636, 2018.

[134] P. Y. Huang, C. S. Ruiz-Vargas, A. M. Van Der Zande, W. S. Whitney, M. P. Levendorf, J. W. Kevek, S. Garg, J. S. Alden, C. J. Hustedt, Y. Zhu, *et al.*, "Grains and grain boundaries in single-layer graphene atomic patchwork quilts," *Nature*, vol. 469, no. 7330, p. 389, 2011.

[135] M. Plomp, W. Van Enckevort, and E. Vlieg, "Controlling crystal surface termination by cleavage direction," *Physical Review Letters*, vol. 86, no. 22, p. 5070, 2001.

[136] A. K. Geim and K. S. Novoselov, "The rise of graphene," in *Nanoscience and Technology: A Collection of Reviews from Nature Journals*, pp. 11–19, World Scientific, 2010.

[137] S. Stankovich, D. A. Dikin, G. H. Dommett, K. M. Kohlhaas, E. J. Zimney, E. A. Stach, R. D. Piner, S. T. Nguyen, and R. S. Ruoff, "Graphene-based composite materials," *Nature*, vol. 442, no. 7100, p. 282, 2006.

[138] C. Mattevi, H. Kim, and M. Chhowalla, "A review of chemical vapour deposition of graphene on copper," *Journal of Materials Chemistry*, vol. 21, no. 10, pp. 3324–3334, 2011.

[139] Z. Song, V. I. Artyukhov, B. I. Yakobson, and Z. Xu, "Pseudo hall–petch strength reduction in polycrystalline graphene," *Nano Letters*, vol. 13, no. 4, pp. 1829–1833, 2013.

[140] G.-H. Lee, R. C. Cooper, S. J. An, S. Lee, A. Van Der Zande, N. Petrone, A. G. Hammerberg, C. Lee, B. Crawford, W. Oliver, *et al.*, "High-strength chemical-vapor–deposited graphene and grain boundaries," *Science*, vol. 340, no. 6136, pp. 1073–1076, 2013.

[141] R. Wang, Z. Suo, A. Evans, N. Yao, and I. Aksay, "Deformation mechanisms in nacre," *Journal of Materials Research*, vol. 16, no. 9, pp. 2485–2493, 2001.

[142] M. E. Launey, M. J. Buehler, and R. O. Ritchie, "On the mechanistic origins of toughness in bone," *Annual Review of Materials Research*, vol. 40, pp. 25–53, 2010.

[143] S. Yip, "Nanocrystalline metals: Mapping plasticity," *Nature Materials*, vol. 3, no. 1, p. 11, 2004.

[144] Y. Zhu, N. Moldovan, and H. D. Espinosa, "A microelectromechanical load sensor for in situ electron and x-ray microscopy tensile testing of nanostructures," *Applied Physics Letters*, vol. 86, no. 1, p. 013506, 2005.

[145] P. Zhang, L. Ma, F. Fan, Z. Zeng, C. Peng, P. E. Loya, Z. Liu, Y. Gong, J. Zhang, X. Zhang, *et al.*, "Fracture toughness of graphene," *Nature Communications*, vol. 5, p. 3782, 2014.

[146] K. Kim, Z. Lee, W. Regan, C. Kisielowski, M. Crommie, and A. Zettl, "Grain boundary mapping in polycrystalline graphene," *ACS Nano*, vol. 5, no. 3, pp. 2142–2146, 2011.

[147] Y. Liu and B. I. Yakobson, "Cones, pringles, and grain boundary landscapes in graphene topology," *Nano Letters*, vol. 10, no. 6, pp. 2178–2183, 2010.

[148] Y. Liu, X. Zou, and B. I. Yakobson, "Dislocations and grain boundaries in two-dimensional boron nitride," *ACS Nano*, vol. 6, no. 8, pp. 7053–7058, 2012.

[149] S. Park, M. S. Kim, H. Kim, J. Lee, G. H. Han, J. Jung, and J. Kim, "Spectroscopic visualization of grain boundaries of monolayer molybdenum disulfide by stacking bilayers," *ACS Nano*, vol. 9, no. 11, pp. 11042–11048, 2015.

[150] S. Najmaei, Z. Liu, W. Zhou, X. Zou, G. Shi, S. Lei, B. I. Yakobson, J.-C. Idrobo, P. M. Ajayan, and J. Lou, "Vapour phase growth and grain boundary structure of molybdenum disulphide atomic layers," *Nature Materials*, vol. 12, no. 8, p. 754, 2013.

[151] J. Cheng, T. Jiang, Q. Ji, Y. Zhang, Z. Li, Y. Shan, Y. Zhang, X. Gong, W. Liu, and S. Wu, "Kinetic nature of grain boundary formation in as-grown mos2 monolayers," *Advanced Materials*, vol. 27, no. 27, pp. 4069–4074, 2015.

[152] H.-P. Komsa and A. V. Krasheninnikov, "Native defects in bulk and monolayer mos 2 from first principles," *Physical Review B*, vol. 91, no. 12, p. 125304, 2015.

[153] W. Zhou, X. Zou, S. Najmaei, Z. Liu, Y. Shi, J. Kong, J. Lou, P. M. Ajayan, B. I. Yakobson, and J.-C. Idrobo, "Intrinsic structural defects in monolayer molybdenum disulfide," *Nano Letters*, vol. 13, no. 6, pp. 2615–2622, 2013.

[154] A. Azizi, X. Zou, P. Ercius, Z. Zhang, A. L. Elías, N. Perea-López, G. Stone, M. Terrones, B. I. Yakobson, and N. Alem, "Dislocation motion and grain boundary migration in two-dimensional tungsten disulphide," *Nature Communications*, vol. 5, p. 4867, 2014.

[155] X. Ling, Y. Lin, Q. Ma, Z. Wang, Y. Song, L. Yu, S. Huang, W. Fang, X. Zhang, A. L. Hsu, *et al.*, "Parallel stitching of 2d materials," *Advanced Materials*, vol. 28, no. 12, pp. 2322–2329, 2016.

[156] M. Zhao, Y. Ye, Y. Han, Y. Xia, H. Zhu, S. Wang, Y. Wang, D. A. Muller, and X. Zhang, "Large-scale chemical assembly of atomically thin transistors and circuits," *Nature Nanotechnology*, vol. 11, no. 11, p. 954, 2016.

[157] L. Chen, L. He, H. S. Wang, H. Wang, S. Tang, C. Cong, H. Xie, L. Li, H. Xia, T. Li, *et al.*, "Oriented graphene nanoribbons embedded in hexagonal boron nitride trenches," *Nature Communications*, vol. 8, p. 14703, 2017.

[158] Y. Gong, S. Lei, G. Ye, B. Li, Y. He, K. Keyshar, X. Zhang, Q. Wang, J. Lou, Z. Liu, *et al.*, "Two-step growth of two-dimensional wse2/mose2 heterostructures," *Nano Letters*, vol. 15, no. 9, pp. 6135–6141, 2015.

[159] Z. Zhang, P. Chen, X. Duan, K. Zang, J. Luo, and X. Duan, "Robust epitaxial growth of two-dimensional heterostructures, multiheterostructures, and superlattices," *Science*, vol. 357, no. 6353, pp. 788–792, 2017.

[160] L. Liu, J. Park, D. A. Siegel, K. F. McCarty, K. W. Clark, W. Deng, L. Basile, J. C. Idrobo, A.-P. Li, and G. Gu, "Heteroepitaxial growth of two-dimensional hexagonal boron nitride templated by graphene edges," *Science*, vol. 343, no. 6167, pp. 163–167, 2014.

[161] J. Kang, H. Sahin, and F. M. Peeters, "Tuning carrier confinement in the mos2/ws2 lateral heterostructure," *The Journal of Physical Chemistry C*, vol. 119, no. 17, pp. 9580–9586, 2015.

[162] O. Rubel, "One-dimensional electron gas in strained lateral heterostructures of single layer materials," *Scientific Reports*, vol. 7, no. 1, p. 4316, 2017.

[163] R. People and J. Bean, "Calculation of critical layer thickness versus lattice mismatch for ge x si1- x/si strained-layer heterostructures," *Applied Physics Letters*, vol. 47, no. 3, pp. 322–324, 1985.

[164] A. M. Van Der Zande, P. Y. Huang, D. A. Chenet, T. C. Berkelbach, Y. You, G.-H. Lee, T. F. Heinz, D. R. Reichman, D. A. Muller, and J. C. Hone, "Grains and grain boundaries in highly crystalline monolayer molybdenum disulphide," *Nature Materials*, vol. 12, no. 6, p. 554, 2013.

[165] X. Zou, Y. Liu, and B. I. Yakobson, "Predicting dislocations and grain boundaries in two-dimensional metal-disulfides from the first principles," *Nano Letters*, vol. 13, no. 1, pp. 253–258, 2012.

[166] J. Magda, M. Tirrell, and H. Davis, "Molecular dynamics of narrow, liquid-filled pores," *The Journal of Chemical Physics*, vol. 83, no. 4, pp. 1888–1901, 1985.

[167] M. Ghorbani-Asl, N. Zibouche, M. Wahiduzzaman, A. F. Oliveira, A. Kuc, and T. Heine, "Electromechanics in mos 2 and ws 2: nanotubes vs. monolayers," *Scientific Reports*, vol. 3, p. 2961, 2013.

[168] Y. Liang, S. Huang, R. Soklaski, and L. Yang, "Quasiparticle band-edge energy and band offsets of monolayer of molybdenum and tungsten chalcogenides," *Applied Physics Letters*, vol. 103, no. 4, p. 042106, 2013.

[169] D. Hull and D. J. Bacon, *Introduction to dislocations*, vol. 37. Elsevier, 2011.

[170] A. Mackay and H. Terrones, "Diamond from graphite," *Nature*, vol. 352, no. 6338, p. 762, 1991.

[171] H. Terrones and A. Mackay, "The geometry of hypothetical curved graphite structures," *Carbon*, vol. 30, no. 8, pp. 1251–1260, 1992.

[172] T. Zhang, X. Li, and H. Gao, "Defects controlled wrinkling and topological design in graphene," *Journal of the Mechanics and Physics of Solids*, vol. 67, pp. 2–13, 2014.

[173] A. H. Schoen, "Infinite periodic minimal surfaces without self-intersections," 1970.

[174] M.-Z. Huang, W. Ching, and T. Lenosky, "Electronic properties of negative-curvature periodic graphitic carbon surfaces," *Physical Review B*, vol. 47, no. 3, p. 1593, 1993.

[175] T. Lenosky, X. Gonze, M. Teter, and V. Elser, "Energetics of negatively curved graphitic carbon," *Nature*, vol. 355, no. 6358, p. 333, 1992.

[176] G. Benedek, H. Vahedi-Tafreshi, E. Barborini, P. Piseri, P. Milani, C. Ducati, and J. Robertson, "The structure of negatively curved spongy carbon," *Diamond and Related Materials*, vol. 12, no. 3-7, pp. 768–773, 2003.

[177] E. Barborini, P. Piseri, P. Milani, G. Benedek, C. Ducati, and J. Robertson, "Negatively curved spongy carbon," *Applied Physics Letters*, vol. 81, no. 18, pp. 3359–3361, 2002.

[178] K. Kim, T. Lee, Y. Kwon, Y. Seo, J. Song, J. K. Park, H. Lee, J. Y. Park, H. Ihee, S. J. Cho, *et al.*, "Lanthanum-catalysed synthesis of microporous 3d graphene-like carbons in a zeolite template," *Nature*, vol. 535, no. 7610, p. 131, 2016.

[179] L. Jiang and Z. Fan, "Design of advanced porous graphene materials: from graphene nanomesh to 3d architectures," *Nanoscale*, vol. 6, no. 4, pp. 1922–1945, 2014.

[180] H. Bi, K. Yin, X. Xie, Y. Zhou, N. Wan, F. Xu, F. Banhart, L. Sun, and R. S. Ruoff, "Low temperature casting of graphene with high compressive strength," *Advanced Materials*, vol. 24, no. 37, pp. 5124–5129, 2012.

[181] Y. Wu, N. Yi, L. Huang, T. Zhang, S. Fang, H. Chang, N. Li, J. Oh, J. A. Lee, M. Kozlov, *et al.*, "Three-dimensionally bonded spongy graphene material with super compressive elasticity and near-zero poissonâĂŹs ratio," *Nature Communications*, vol. 6, p. 6141, 2015.

[182] Z. Chen, W. Ren, L. Gao, B. Liu, S. Pei, and H.-M. Cheng, "Three-dimensional flexible and conductive interconnected graphene networks grown by chemical vapour deposition," *Nature Materials*, vol. 10, no. 6, p. 424, 2011.

[183] T. Cebo, A. I. Aria, J. A. Dolan, R. S. Weatherup, K. Nakanishi, P. R. Kidambi, G. Divitini, C. Ducati, U. Steiner, and S. Hofmann, "Chemical vapour deposition of freestanding sub-60 nm graphene gyroids," *Applied Physics Letters*, vol. 111, no. 25, p. 253103, 2017.

[184] D. C. Miller, M. Terrones, and H. Terrones, "Mechanical properties of hypothetical graphene foams: Giant schwarzites," *Carbon*, vol. 96, pp. 1191–1199, 2016.

[185] J. Lei and Z. Liu, "The structural and mechanical properties of graphene aerogels based on schwarz-surface-like graphene models," *Carbon*, vol. 130, pp. 741–748, 2018.

[186] S. M. Sajadi, P. S. Owuor, S. Schara, C. F. Woellner, V. Rodrigues, R. Vajtai, J. Lou, D. S. Galvão, C. S. Tiwary, and P. M. Ajayan, "Multiscale geometric design principles applied to 3d printed schwarzites," *Advanced Materials*, vol. 30, no. 1, p. 1704820, 2018.

[187] S. Townsend, T. Lenosky, D. Muller, C. Nichols, and V. Elser, "Negatively curved graphitic sheet model of amorphous carbon," *Physical Review Letters*, vol. 69, no. 6, p. 921, 1992.

[188] K. A. Brakke, "The surface evolver," *Experimental Mathematics*, vol. 1, no. 2, pp. 141–165, 1992.

[189] F. Mouhat and F.-X. Coudert, "Necessary and sufficient elastic stability conditions in various crystal systems," *Physical Review B*, vol. 90, no. 22, p. 224104, 2014.

[190] D. W. Abueidda, R. K. A. Al-Rub, A. S. Dalaq, D.-W. Lee, K. A. Khan, and I. Jasiuk, "Effective conductivities and elastic moduli of novel foams with triply periodic minimal surfaces," *Mechanics of Materials*, vol. 95, pp. 102–115, 2016.

[191] K. Michielsen and D. G. Stavenga, "Gyroid cuticular structures in butterfly wing scales: biological photonic crystals," *Journal of The Royal Society Interface*, vol. 5, no. 18, pp. 85–94, 2007.

[192] M. Saba, B. D. Wilts, J. Hielscher, and G. E. Schröder-Turk, "Absence of circular polarisation in reflections of butterfly wing scales with chiral gyroid structure," *Materials Today: Proceedings*, vol. 1, pp. 193–208, 2014.

[193] K. S. Novoselov and A. Geim, "The rise of graphene," *Nature Materials*, vol. 6, no. 3, pp. 183–191, 2007.

[194] Z. Xu, Y. Zhang, P. Li, and C. Gao, "Strong, conductive, lightweight, neat graphene aerogel fibers with aligned pores," *ACS Nano*, vol. 6, no. 8, pp. 7103–7113, 2012.

[195] J. Li, S. Zhao, G. Zhang, Y. Gao, L. Deng, R. Sun, and C.-P. Wong, "A facile method to prepare highly compressible three-dimensional graphene-only sponge," *Journal of Materials Chemistry A*, vol. 3, no. 30, pp. 15482–15488, 2015.

[196] M. A. Worsley, S. O. Kucheyev, H. E. Mason, M. D. Merrill, B. P. Mayer, J. Lewicki, C. A. Valdez, M. E. Suss, M. Stadermann, P. J. Pauzauskie, *et al.*, "Mechanically robust 3d graphene macroassembly with high surface area," *Chemical Communications*, vol. 48, no. 67, pp. 8428–8430, 2012.

[197] X. Zhang, Z. Sui, B. Xu, S. Yue, Y. Luo, W. Zhan, and B. Liu, "Mechanically strong and highly conductive graphene aerogel and its use as electrodes for electrochemical power sources," *Journal of Materials Chemistry*, vol. 21, no. 18, pp. 6494–6497, 2011.

[198] A. Nieto, B. Boesl, and A. Agarwal, "Multi-scale intrinsic deformation mechanisms of 3d graphene foam," *Carbon*, vol. 85, pp. 299–308, 2015.

[199] H. Sun, Z. Xu, and C. Gao, "Multifunctional, ultra-flyweight, synergistically assembled carbon aerogels," *Advanced Materials*, vol. 25, no. 18, pp. 2554–2560, 2013.

[200] X. Xie, Y. Zhou, H. Bi, K. Yin, S. Wan, and L. Sun, "Large-range control of the microstructures and properties of three-dimensional porous graphene," *Scientific Reports*, vol. 3, p. 2117, 2013.

[201] Z. Fan, A. Marconnet, S. T. Nguyen, C. Y. Lim, and H. M. Duong, "Effects of heat treatment on the thermal properties of highly nanoporous graphene aerogels using the infrared microscopy technique," *International Journal of Heat and Mass Transfer*, vol. 76, pp. 122–127, 2014.

[202] M. T. Pettes, H. Ji, R. S. Ruoff, and L. Shi, "Thermal transport in three-dimensional foam architectures of few-layer graphene and ultrathin graphite," *Nano Letters*, vol. 12, no. 6, pp. 2959–2964, 2012.

[203] Y. Xie, S. Xu, Z. Xu, H. Wu, C. Deng, and X. Wang, "Interface-mediated extremely low thermal conductivity of graphene aerogel," *Carbon*, vol. 98, pp. 381–390, 2016.

[204] J. J. Yeo and Z. Liu, "Molecular dynamics analysis of the thermal conductivity of graphene and silicene monolayers of different lengths," *Journal of Computational and Theoretical Nanoscience*, vol. 11, no. 8, pp. 1790–1796, 2014.

[205] J. Fricke and T. Tillotson, "Aerogels: production, characterization, and applications," *ThinSsolid Films*, vol. 297, no. 1-2, pp. 212–223, 1997.

[206] Z. G. Fthenakis, Z. Zhu, and D. Tománek, "Effect of structural defects on the thermal conductivity of graphene: From point to line defects to haeckelites," *Physical Review B*, vol. 89, no. 12, p. 125421, 2014.

[207] Y. J. Jie, L. Zishun, and N. T. Yong, "Comparing the effects of dispersed stone–thrower–wales defects and double vacancies on the thermal conductivity of graphene nanoribbons," *Nanotechnology*, vol. 23, no. 38, p. 385702, 2012.

[208] W. Lee, K. D. Kihm, H. G. Kim, S. Shin, C. Lee, J. S. Park, S. Cheon, O. M. Kwon, G. Lim, and W. Lee, "In-plane thermal conductivity of polycrystalline chemical vapor deposition graphene with controlled grain sizes," *Nano Letters*, vol. 17, no. 4, pp. 2361–2366, 2017.

[209] B. Mortazavi, A. Rajabpour, S. Ahzi, Y. Rémond, and S. M. V. Allaei, "Nitrogen doping and curvature effects on thermal conductivity of graphene: A non-equilibrium molecular dynamics study," *Solid State Communications*, vol. 152, no. 4, pp. 261–264, 2012.

[210] L. F. C. Pereira, I. Savić, and D. Donadio, "Thermal conductivity of one-, two- and three-dimensional carbon," *arXiv preprint arXiv:1307.6203*, 2013.

[211] Y. Wang, Z. Song, and Z. Xu, "Mechanistic transition of heat conduction in two-dimensional solids: A study of silica bilayers," *Physical Review B*, vol. 92, no. 24, p. 245427, 2015.

[212] J. Hong, Z. Hu, M. Probert, K. Li, D. Lv, X. Yang, L. Gu, N. Mao, Q. Feng, L. Xie, *et al.*, "Exploring atomic defects in molybdenum disulphide monolayers," *Nature Communications*, vol. 6, p. 6293, 2015.

[213] T. H. Ly, D. J. Perello, J. Zhao, Q. Deng, H. Kim, G. H. Han, S. H. Chae, H. Y. Jeong, and Y. H. Lee, "Misorientation-angle-dependent electrical transport across molybdenum disulfide grain boundaries," *Nature Communications*, vol. 7, p. 10426, 2016.

[214] Y. Wang and V. H. Crespi, "Theory of finite-length grain boundaries of controlled misfit angle in two-dimensional materials," *Nano Letters*, vol. 17, no. 9, pp. 5297–5303, 2017.

[215] A. Molina-Sanchez and L. Wirtz, "Phonons in single-layer and few-layer mos 2 and ws 2," *Physical Review B*, vol. 84, no. 15, p. 155413, 2011.

[216] L. Malard, M. Guimaraes, D. Mafra, A. Jorio, *et al.*, "Group-theory analysis of electrons and phonons in n-layer graphene systems," *Physical Review B*, vol. 79, no. 12, p. 125426, 2009.

[217] J. Zang, S. Ryu, N. Pugno, Q. Wang, Q. Tu, M. J. Buehler, and X. Zhao, "Multifunctionality and control of the crumpling and unfolding of large-area graphene," *Nature Materials*, vol. 12, no. 4, p. 321, 2013.

[218] S. Deng and V. Berry, "Wrinkled, rippled and crumpled graphene: an overview of formation mechanism, electronic properties, and applications," *Materials Today*, vol. 19, no. 4, pp. 197–212, 2016.

[219] W. Humphrey, A. Dalke, and K. Schulten, "Vmd: visual molecular dynamics," *Journal of molecular graphics*, vol. 14, no. 1, pp. 33–38, 1996.

[220] S. Plimpton, "Fast parallel algorithms for short-range molecular dynamics," *Journal of Computational Physics*, vol. 117, no. 1, pp. 1–19, 1995.

[221] J. Li, "Atomeye: an efficient atomistic configuration viewer," *Modelling and Simulation in Materials Science and Engineering*, vol. 11, no. 2, p. 173, 2003.

[222] A. Stukowski, "Visualization and analysis of atomistic simulation data with ovito–the open visualization tool," *Modelling and Simulation in Materials Science and Engineering*, vol. 18, no. 1, p. 015012, 2009.